

Dissertation zur Erlangung des Doktorgrades
der Fakultät für Chemie und Pharmazie
der Ludwig-Maximilians-Universität München

**Exploring Multinary
(Oxide) Nitride Materials by
the Ammonothermal Approach**

Mathias Mallmann

aus

Hutthurm, Deutschland

2020

Erklärung

Diese Dissertation wurde im Sinne von § 7 der Promotionsordnung vom 28. November 2011 von Herrn Prof. Dr. Wolfgang Schnick betreut.

Eidesstattliche Versicherung

Diese Dissertation wurde eigenständig und ohne unerlaubte Hilfe erarbeitet.

München, den 21.07.2020

.....

(Mathias Mallmann)

Dissertation eingereicht am	13.03.2020
1. Gutachter:	Prof. Dr. Wolfgang Schnick
2. Gutachter:	Prof. Dr. Rainer Niewa
Mündliche Prüfung am	16.07.2020

Für meine Familie

*“Our greatest weakness lies in giving up.
The most certain way to succeed is always
to try just one more time.”*

(Thomas A. Edison)

Acknowledgements

Zuallererst möchte ich Herrn Prof. Dr. Wolfgang Schnick für die Möglichkeit danken, meine Dissertation in seinem Arbeitskreis anfertigen zu können. Sowohl das spannende und abwechslungsreiche Themengebiet, als auch die erstklassigen Arbeitsbedingungen waren optimale Voraussetzungen für meine Promotion. Darüber hinaus möchte ich mich für die Freiheit bei der Umsetzung meiner Forschungsideen, für die förderlichen Fachgespräche und Anregungen zu diesen Themen, sowie für die Gelegenheit an sehr lehrreichen Fachtagungen teilnehmen zu können bedanken.

Bei Herrn Prof. Dr. Rainer Niewa möchte ich mich sehr herzlich für die Übernahme des Koreferats meiner Dissertation, sowie für die hilfreichen Diskussionen während der Zusammenarbeit im Rahmen unserer Forschergruppe bedanken.

Herrn Prof. Dr. Eberhard Schlücker, Herrn Prof. Dr. Hans-Christian Böttcher, Herrn Prof. Dr. Konstantin Karaghiosoff und Herrn Prof. Dr. Stefan Schwarzer möchte ich herzlich für ihre Bereitschaft, der Prüfungskommission meiner Doktorarbeit anzugehören danken.

Ferner danke ich meinen internen und externen Kooperationspartnern Prof. Dr. Ján Minár, Prof. Dr. Dirk Johrendt, Dr. Robin Niklaus, Dr. Christian Maak, Dr. Philipp Strobel, Dr. Peter Schmidt, Tobias Rackl und Sebastian Wendl, die wesentlich zum Erfolg dieser Arbeit beigetragen haben.

Besonders bedanken möchte ich mich außerdem bei meinem Vorgänger Dr. Jonas Häusler, der mir das Thema der Ammonothermalsynthese bereits im Rahmen meines F-Praktikums nähergebracht hat und mich sowohl während meiner Masterarbeit als auch zum Anfang meiner Promotion stets mit Rat und Tat unterstützt hat.

Bei meinen Laborkollegen Dr. Peter Wagatha, Dr. Jonas Häusler, Dr. Niklas Cordes, Dr. Claudia Lerner, Dr. Stefan Rudel, Kerstin Gotschling, Lisa Gamperl und Florian Engelsberger, sowie bei meinen Kollegen in der Schreibstube Sebastian Wendl, Otto Zeman und Jonathan Sappl möchte ich mich recht herzlich für die schöne Zeit und die angenehme Arbeitsatmosphäre bedanken.

Ein großer Dank gilt meinen Arbeitskollegen und Freunden Dr. Sebastian Vogel, Dr. Christian Maak, Dr. Simon Kloß, Sebastian Wendl und Tobias Giftthaler für deren unermüdliche Hilfsbereitschaft, die tolle Zeit und die vielen lustigen Abende innerhalb und außerhalb der Uni.

Außerdem möchte ich mich bei Wolfgang Wünschheim, Thomas Miller, Dr. Dieter Rau, Dr. Peter Mayer, Christian Minke und Olga Lorenz für deren Hilfe bei diversen technischen und organisatorischen Fragen, sowie für zahlreiche analytische Messungen bedanken.

Darüber hinaus bedanke ich mich bei allen Mitglieder der Arbeitskreise Schnick, Hoch, Johrendt und Lotsch für die super Arbeitsatmosphäre, die schöne Zeit und die zahlreichen Schafkopf- und Filmabende im 2. Stock.

Meinen beiden Praktikanten Maximilian Benz und Thanh Giang Chau möchte ich recht herzlich für ihren hervorragenden Beitrag zu dieser Arbeit danken.

Des Weiteren möchte ich mich bei allen Mitgliedern der DFG-Forschergruppe Ammono-FOR für die überaus lehrreiche und erfolgreiche Zusammenarbeit und die schöne Zeit während unserer Meetings bedanken. Insbesondere möchte ich mich dabei bei Anna Kimmel, Dr. Thomas Steigerwald und Dr. Saskia Schimmel für deren Hilfsbereitschaft bei Problemen mit den Autoklaven, für die Durchführung von Löslichkeitsuntersuchungen und für die tolle Zeit während der Summerschool in Erlangen und Santa Barbara bedanken.

Meinen Freunden aus Hauzenberg Anna, Matthias, Florian, Jonas, Jonas, Severin und Sebastian sowie meinen Münchner Stammtischbrüdern den Simplern, mit denen ich zahlreiche unvergessene Momente erleben durfte, möchte ich hier ganz besonders danken. Ihr alle habt für die nötige Abwechslung zum Alltag in der Uni gesorgt.

Der größte Dank geht jedoch an meine Eltern und meine Schwester für ihre unendliche Unterstützung während meines Studiums und der Promotion. Ohne euch wäre ich nicht da wo ich jetzt bin.

Table of Contents

1	Introduction.....	1
1.1	Nitride Semiconductors.....	1
1.2	Ammonothermal Synthesis	5
1.3	Scope of this Thesis.....	8
1.4	References	10
2	Solid Solutions of Grimm-Sommerfeld Analogous Nitride Semiconductors <i>II-IV-N₂</i> (<i>II</i> = Mg, Mn, Zn; <i>IV</i> = Si, Ge): Ammonothermal Synthesis and DFT Calculations	17
2.1	Introduction	18
2.2	Results and Discussion.....	19
2.2.1	Synthesis	19
2.2.2	Crystal structure	20
2.2.3	Scanning electron microscopy	23
2.2.4	UV/Vis spectroscopy	24
2.2.5	DFT calculations	25
2.2.6	Magnetic measurements.....	30
2.3	Conclusion.....	31
2.4	Experimental Section	31
2.4.1	Ammonothermal synthesis of $Mg_{1-x}Mn_xGeN_2$, $Mg_{1-x}Zn_xGeN_2$, and $Mn_{1-x}Zn_xGeN_2$	32
2.4.2	Ammonothermal synthesis of $Mg_{1-x}Mn_xSiN_2$, $Mg_{1-x}Zn_xSiN_2$, and $Mn_{1-x}Zn_xSiN_2$	32
2.4.3	Digital microscopy	33
2.4.4	Powder XRD	33
2.4.5	Scanning electron microscopy	33
2.4.6	UV/Vis spectroscopy	34
2.4.7	Computational details	34
2.5	Acknowledgements	34
2.6	References	35

3	Ammonothermal Synthesis, Optical Properties and DFT Calculations of Mg_2PN_3 and Zn_2PN_3	41
3.1	Introduction	42
3.2	Results and Discussion	43
3.2.1	Synthesis	43
3.2.2	Crystal structure	45
3.2.3	Scanning electron microscopy	48
3.2.4	UV/Vis reflectance spectroscopy and DFT calculations	49
3.2.5	Dissolution experiment	50
3.3	Conclusion	51
3.4	Experimental Section	52
3.4.1	Synthesis of P_3N_5	52
3.4.2	Ammonothermal synthesis of Mg_2PN_3	52
3.4.3	Ammonothermal synthesis of Zn_2PN_3	53
3.4.4	Single-crystal X-ray diffraction	53
3.4.5	Powder X-ray diffraction	53
3.4.6	Scanning electron microscopy	54
3.4.7	UV/Vis spectroscopy	54
3.4.8	DFT calculations	54
3.4.9	Dissolution experiment	54
3.5	Acknowledgements	55
3.6	References	55
4	Crystalline Nitridophosphates by Ammonothermal Synthesis	59
4.1	Introduction	59
4.2	Results and Discussion	61
4.2.1	Ammonothermal synthesis	61
4.2.2	Crystallographic investigation	63
4.2.3	Crystal structures	65
4.3	Conclusions	67

4.4	Experimental Section	67
4.4.1	General	67
4.4.2	Synthesis of P_3N_5	68
4.4.3	Synthesis of $Sr(N_3)_2$	68
4.4.4	Ammonothermal synthesis of α - and β - $Li_{10}P_4N_{10}$	68
4.4.5	Ammonothermal synthesis of $Li_{18}P_6N_{16}$	69
4.4.6	Ammonothermal synthesis of Ca_2PN_3	69
4.4.7	Ammonothermal synthesis of SrP_8N_{14}	69
4.4.8	Ammonothermal synthesis of $LiPN_2$	69
4.4.9	Powder X-ray diffraction	70
4.4.10	Scanning electron microscopy	70
4.4.11	FTIR spectroscopy	70
4.5	Acknowledgments	70
4.6	References	71
5	$Sr_3P_3N_7$: Complementary Approach of Ammonothermal and High-Pressure Methods	75
5.1	Introduction	76
5.2	Results and Discussion	77
5.2.1	Synthesis	77
5.2.2	Crystal structure	78
5.2.3	Scanning electron microscopy	81
5.2.4	Fourier Transformed Infrared spectroscopy	82
5.2.5	UV/Vis spectroscopy	82
5.2.6	Luminescence	83
5.3	Conclusions	84
5.4	Experimental Section	84
5.4.1	Synthesis of $Eu(NH_2)_2$	85
5.4.2	Synthesis of P_3N_5	85
5.4.3	Synthesis of $Sr(N_3)_2$	85
5.4.4	Ammonothermal synthesis	85

5.4.5	High-pressure synthesis.....	86
5.4.6	Single-crystal X-ray diffraction	86
5.4.7	Powder X-ray diffraction	87
5.4.8	Scanning electron microscopy	87
5.4.9	Fourier Transformed Infrared (FTIR) spectroscopy	87
5.4.10	UV/Vis spectroscopy	87
5.4.11	Luminescence.....	88
5.5	Acknowledgements	88
5.6	References	88
6	Ammonothermal Synthesis of Ba ₂ PO ₃ N – An Oxonitridophosphate with Non-Condensed PO ₃ N Tetrahedra	93
6.1	Introduction	94
6.2	Results and Discussion.....	95
6.2.1	Synthesis	95
6.2.2	Crystal structure	96
6.2.3	Energy dispersive X-ray spectroscopy (EDX)	100
6.2.4	Fourier Transformed Infrared spectroscopy (FTIR)	100
6.2.5	UV/Vis spectroscopy	100
6.2.6	Luminescence.....	101
6.3	Conclusions	102
6.4	Experimental Section	103
6.4.1	Synthesis of Eu(NH ₂) ₂	103
6.4.2	Ammonothermal synthesis.....	103
6.4.3	Single-crystal X-ray diffraction	104
6.4.4	Powder X-ray diffraction	104
6.4.5	Scanning electron microscopy	105
6.4.6	Fourier Transformed Infrared spectroscopy.....	105
6.4.7	UV/Vis spectroscopy	105
6.4.8	Luminescence measurements.....	105

6.5	Acknowledgments	105
6.6	References	106
7	Ammonothermal Synthesis and Crystal Growth of the Chain-type Oxonitridosilicate $\text{Ca}_{1+x}\text{Y}_{1-x}\text{SiN}_{3-x}\text{O}_x$ ($x > 0$)	111
7.1	Introduction	112
7.2	Results and Discussion.....	113
7.2.1	Synthesis	113
7.2.2	Crystal structure	114
7.2.3	Scanning electron microscopy	117
7.3	Conclusions	118
7.4	Experimental Section	119
7.4.1	Preparation of starting materials	119
7.4.2	Ammonothermal synthesis of $\text{Ca}_{1+x}\text{Y}_{1-x}\text{SiN}_{3-x}\text{O}_x$	120
7.4.3	Single-crystal X-ray diffraction	120
7.4.4	Powder X-ray diffraction	120
7.4.5	Scanning electron microscopy	121
7.5	Acknowledgements	121
7.6	References	121
8	Summary	125
9	Conclusion and Outlook	131
9.1	Grimm-Sommerfeld Analogous Nitride Semiconductors	131
9.2	Extension of Ammonothermally Accessible (Oxide) Nitrides.....	134
9.3	Final Remarks	135
9.4	References	136
A	Supporting Information for Chapter 2	141
A.1	Additional crystallographic data	141
A.2	Details on scanning electron microscopy	146
A.3	Details on UV/Vis reflectance spectroscopy.....	148
A.4	Additional data of DFT calculations	150

A.5	Magnetic measurements	154
A.5.1	Experimental	154
A.5.2	Results and Discussion.....	154
A.6	References	158
B	Supporting Information for Chapter 3.....	161
B.1	Additional crystallographic data of Mg_2PN_3	161
B.2	Additional crystallographic data of Zn_2PN_3	163
B.3	Details on scanning electron microscopy	165
B.4	UV/Vis spectra	166
C	Supporting Information for Chapter 4.....	167
C.1	$\alpha\text{-Li}_{10}\text{P}_4\text{N}_{10}$, $\beta\text{-Li}_{10}\text{P}_4\text{N}_{10}$ and $\text{Li}_{18}\text{P}_6\text{N}_{16}$	167
C.2	Ca_2PN_3	174
C.3	$\text{SrP}_8\text{N}_{14}$	175
C.4	LiPN_2	176
C.5	References	179
D	Supporting Information for Chapter 5.....	181
D.1	Additional crystallographic data	181
D.2	Detailed Information on scanning electron microscopy.....	185
D.3	Detailed information on IR spectroscopy.....	185
D.4	Detailed information on UV/Vis spectroscopy	186
D.5	Luminescence properties.....	187
E	Supporting Information for Chapter 6.....	189
E.1	Additional crystallographic data	189
E.2	Detailed information on scanning electron microscopy.....	193
E.3	Detailed information on IR spectroscopy.....	194
E.4	Detailed information on UV/Vis spectroscopy	194
E.5	Luminescence properties.....	195
E.6	References	196
F	Supporting Information for Chapter 7.....	197

F.1	Additional crystallographic data	197
F.2	References	200
G	Miscellaneous	201
G.1	List of publications within this thesis.....	201
G.2	Other publications	203
G.3	Conference Contributions	204
G.4	Deposited Crystallographic Data	206

1 Introduction

Based on the steadily growing global population and the proceeding technologization, humanity's energy consumption has rapidly increased in the past years and will further grow in the future. So far, most of the required energy is obtained from fossil fuels (e.g. black coal, natural gas or mineral oil) and nuclear energy.^[1] The continuously progressing climate change and the unresolved problem of terminal storage, however, necessitate environmentally friendly and renewable energy sources, as well as energy efficient solutions for daily life.

Chemists and materials scientists, therefore, research innovative materials within industrial sectors such as lighting, photovoltaic, and mobility. Especially, highly developed functional solid-state materials with intriguing electronic and optical properties such as semiconductors, phosphor materials or ionic conductors are of essential importance for a variety of possible applications, such as data storage media, mobile phones, photovoltaics, solid-state batteries, and phosphor-converted light-emitting diodes (pc-LEDs), for instance. According to estimations of the United States Department of Energy (DOE), 75% of the energy consumption for illumination can be saved by 2035 by using solid-state lighting.^[2] Today's widespread optoelectronic semiconductors, however, are typically based on Ga and In^[3] that both are of rather low availability. Modern solid-state chemistry, therefore, researches for new functional materials that are composed of earth-abundant elements, prospectively providing indispensable substitutes for Ga/In-based materials.^[4]

As the ammonothermal method has been proven as a promising approach for the preparation and crystal growth of semiconducting materials (especially of GaN),^[5] this thesis deals with the synthesis of nitride semiconductors using the ammonothermal approach and the characterization of their optical and electronic properties. The ammonothermal technique is further advanced by accessing additional nitride compounds that had been scarcely investigated under ammonothermal conditions, prior to this thesis. Therefore, the following sections provide a brief overview on nitride semiconductors (Section 1.1) and the ammonothermal technique (Section 1.2), before the precise research objective of this thesis is deduced in Section 1.3.

1.1 Nitride Semiconductors

Semiconductors are key materials for energy efficient technologies and are characterized as solid-state materials with a moderate electrical conductivity, which increases with temperature. This behavior is attributable to their bandgap that can be overcome by thermal or optical excitation of electrons from the valence band to the conduction band. The electrical conductivity can originate

from both, excited electrons in the conduction band and corresponding holes in the valence band. In general, the bandgap of a semiconductor can be classified either as direct or indirect. In a direct semiconductor the energy of an electron changes upon excitation, whereas in an indirect semiconductor its momentum is changed additionally, causing a significantly lower transition efficiency.

The electronic properties can be modified by doping semiconductors with impurity atoms, creating additional localized energy levels in the band diagram that are typically located in the bandgap of the host material. The reduced energy difference between the valence and the conduction band causes a lower electron excitation energy and thus, a higher charge carrier concentration. In principal, two types of doping can be distinguished. In *n-doped* semiconductors, the electron concentration in the conduction band is increased by the introduction of electron donors, while in *p-doped* materials electron acceptors decrease the electron concentration in the valence band (Figure 1.1). By the formation of heterojunctions between p- and n-type doped materials, semiconductor devices such as light emitting diodes, solar cells or transistors can be manufactured.

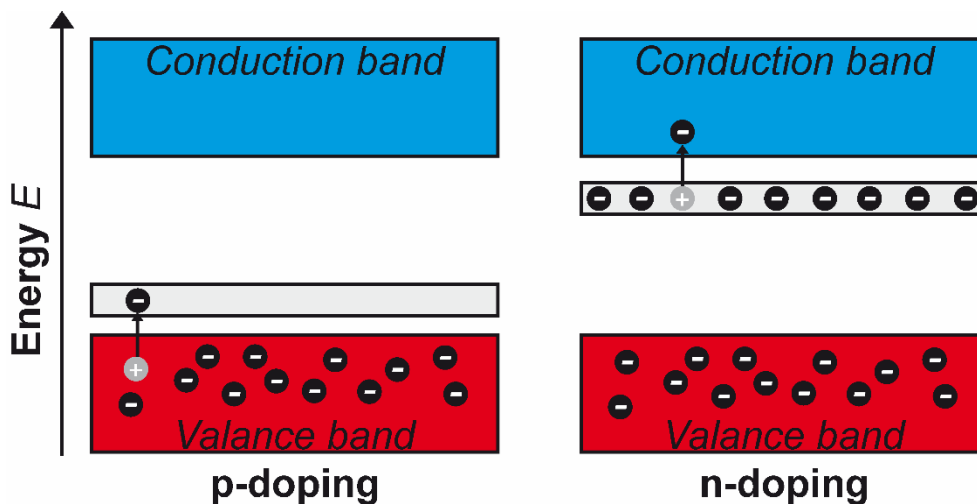


Figure 1.1. Band model of p- and n-type doped semiconductors. By introducing dopant atoms into the semiconductor, additional energy levels are formed in the bandgap (gray) that may either be filled with electrons from the valence band of the semiconductor (p-doping), or provide electrons for excitation into the conduction band of the semiconductor (n-doping).

Silicon is currently the most important semiconductor in diverse application fields such as photovoltaics and computer components. However, Grimm-Sommerfeld analogous compounds, which are structurally and electronically related to group 14 elements and exhibit a valence electron concentration of four,^[6] have gained great industrial interest.^[3] Most of these compounds crystallize in the sphalerite or wurtzite structure type and are predominately used in optoelectronic devices. The

most prominent representatives are the group 13 nitrides AlN, GaN, InN, and their solid solutions (Al,Ga,In)N. This compound class covers a direct bandgap range from approximately 0.7 to 6.2 eV and features a high chemical stability, as well as small electron and hole effective masses, which describe the apparent mass of a particle when responding to forces.^[4, 7] These so-called *III-N* semiconductors are applied in laser diodes and ultraviolet or blue light-emitting diodes (LEDs), and thus have paved the way to white light sources with high efficiency, as has been honored with the Nobel Prize in Physics to *Isamu Akasaki, Hiroshi Amano, and Shuji Nakamura* in 2014.^[8]

The limited abundance and the fact that Ga and In only occur as byproducts during the production of other metals, however, is a major drawback of the group 13 nitrides. In recent years, theoretical calculations suggested various ternary zinc nitrides (e.g. LiZnN, ZnTiN₂, ZnSnN₂, Zn₂PN₃) as promising alternatives.^[4] Especially, Zn-*IV*-N₂ compounds (*IV* = Si, Ge, Sn) have gained attention, as they crystallize in a wurtzite superstructure and are therefore structurally related to group 13 nitrides, as well. Furthermore, they are composed of earth-abundant elements and feature an appropriate bandgap tunability, small carrier effective masses, and high chemical and thermal stability.^[9–12] Despite their promising theoretical investigations, however, experimental data is still scarce and their bulk synthesis remains challenging. By substituting Zn by Mg or Mn in these Zn-*IV*-N₂ compounds, as well as by substituting the tetravalent cation by pentavalent ones, further promising semiconducting nitrides can be derived. The structural relation of these *II-IV*-N₂ (*II* = Mg, Mn, Zn; *IV* = Si, Ge, Sn) and *II₂-V*-N₃ (*II* = Mg, Zn; *V* = P) compounds to GaN is illustrated in Figure 1.2.

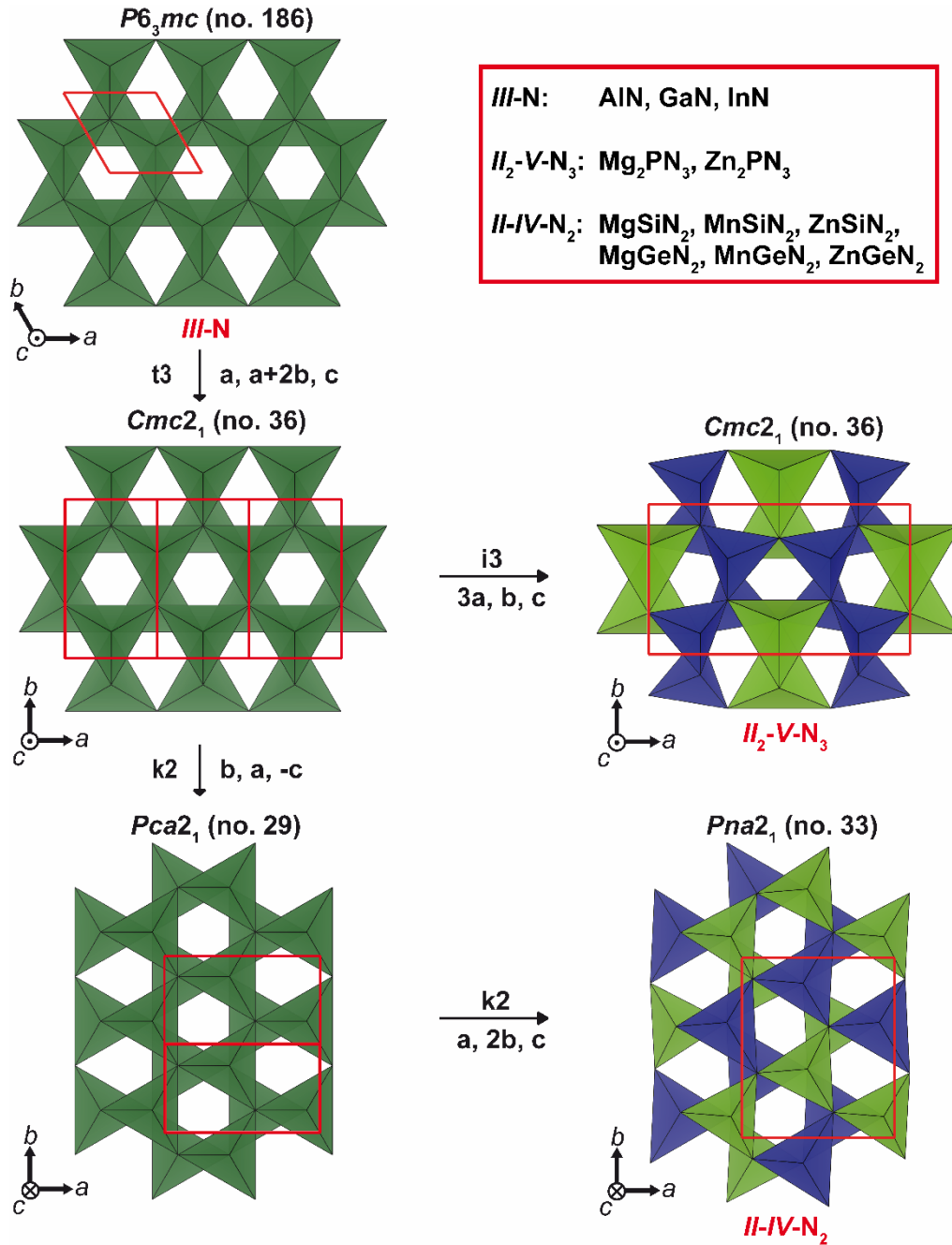
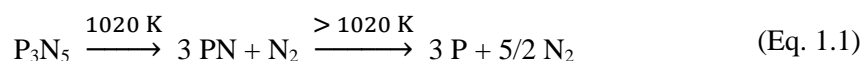


Figure 1.2. Group-subgroup relations of wurtzite-type $III-N$ ($P6_3mc$, no. 186, e.g. GaN)^[13] with II_2-V-N_3 ($Cmc2_1$, no. 36, e.g. Mg_2PN_3)^[14] and $II-IV-N_2$ compounds ($Pna2_1$, no. 33, e.g. $ZnGeN_2$)^[15] that crystallize in wurtzite superstructures. $III-N_4$ tetrahedra are depicted in dark green, $II-N_4$ tetrahedra in blue, $IV-N_4$ and $V-N_4$ tetrahedra in lime and unit cell edges in red. \odot indicates that the c -axis protrudes from the sheet level, \otimes indicates that the c -axis enters the sheet level.

1.2 Ammonothermal Synthesis

Nitride synthesis has ever been a challenging issue, considering the stability of the N₂ triple bond (941 kJ/mol) and the positive electron affinity of nitrogen (+ 0.07 eV).^[16, 17] Therefore, various synthetic methods have been developed, some of them customized to certain nitride classes.^[18] (Oxide) nitride materials are typically synthesized at high temperatures up to 2300 K by nitridation of metals, hydrides or alloys under nitrogen or ammonia atmosphere, by metathesis reactions, or carbothermal reduction. However, many (oxide) nitride compounds, especially (oxo)nitridophosphates, are prone to the thermally induced elimination of N₂ at elevated temperatures, as exemplary illustrated for P₃N₅ in Equation 1.1.^[19]



Following Le Chatelier's principle, high-pressure methods, such as the multianvil technique, can suppress this thermal decomposition enabling high reaction temperatures.^[20] Such high-pressure high-temperature techniques, however, usually imply small sample volumes, which may limit a detailed characterization of the as-synthesized material and narrow industrial applications. In contrast, the ammonothermal approach is an innovative technique that enables the synthesis of large-volume samples at moderate temperatures ($\leq 1070 \text{ K}$) and medium pressures ($\leq 300 \text{ MPa}$), employing supercritical ammonia as solvent.^[21, 22]

By analogy to the well-known hydrothermal method, the ammonothermal method is a solvothermal technique, in which a chemical reaction takes place in a closed system in the presence of a solvent at temperatures and pressures above ambient conditions.^[23] While water (H₂O) is mainly used as solvent for the synthesis and crystal growth of oxides and hydroxides, reactions in ammonia (NH₃) typically yield nitrides, amides, and imides. Although H₂O and NH₃ exhibit quite similar properties (e.g. autoprotolysis, polarity), the solubility of most inorganic compounds in NH₃ is considerably lower than in H₂O, which can be explained by a lower relative permittivity constant of NH₃.^[21] The solubility of certain compounds, however, may be increased when supercritical NH₃ is used ($T_{\text{crit}} = 405.2 \text{ K}$; $p_{\text{crit}} = 11.3 \text{ MPa}$),^[21] which raises the relative permittivity, leading to a better solubility. Furthermore, the addition of mineralizers can facilitate the formation of soluble intermediate species, which affects solubility in a similar manner. In principle, three different milieus can be adjusted by the use of mineralizers, as there are ammonobasic, ammononeutral, and ammonoacidic conditions. The use of alkali metal amides, for example, results in ammonobasic conditions, while ammonium halides are typically used to generate ammonoacidic conditions. Especially in the case of ammonothermal crystallization processes, the choice of suitable mineralizers is of significant importance.

Just as to the well-studied Chemical Vapor Transport, the ammonothermal crystal growth process is based on the reaction of the nutrient and the mineralizer forming an intermediate compound. This intermediate species can subsequently be transported along a temperature gradient to finally crystallize on seed crystals. GaN is probably the best investigated compound under ammonothermal conditions concerning its synthesis and crystal growth.^[21, 22] Here, different intermediate species are formed and varying transport behaviors are discussed, both depending on the choice of the mineralizer. Mixed amides such as $\text{Li}[\text{Ga}(\text{NH}_2)_4]$, $\text{Na}_2[\text{Ga}(\text{NH}_2)_4]\text{NH}_2$, and $\text{Ba}[\text{Ga}(\text{NH}_2)_4]_2$ have been discussed as intermediates under ammonobasic conditions,^[24, 25] which further results in a retrograde solubility of GaN (decreasing solubility with increasing temperature). In contrast, intermediates such as $\text{Ga}(\text{NH}_3)_3\text{F}_3$ or $[\text{Ga}(\text{NH}_3)_6]\text{X}_3\cdot\text{NH}_3$ ($X = \text{Br}, \text{I}$) are obtained using ammonoacidic mineralizers.^[26] The ammonothermal crystal growth of GaN has been continuously improved, concerning different mineralizers, concentration of starting materials, temperature and pressure, type of nutrient and seeds, fluid convection, impurities as well as scalability.^[22] Therefore, bulk crystals of high-purity GaN can be grown in rates of up to $300 \mu\text{m}$ per day, rendering the ammonothermal approach a promising technique for industrial application.^[5, 22, 27, 28]

Besides GaN, several other binary nitrides were obtained under ammonothermal conditions. The very first ammonothermally synthesized nitride was Be_3N_2 , which was obtained in 1966 from Juza and Jacobs.^[29] In the following years, Herbert Jacobs and co-workers synthesized numerous of other binary nitrides, amides, imides, and ammoniates, though only few ternary nitrides were obtained.^[21] These ternary nitrides include the alkali metal tantalum nitrides $M\text{TaN}_2$ ($M = \text{Na}, \text{K}, \text{Rb}, \text{Cs}$), $\text{Li}_2\text{Ta}_3\text{N}_5$, and NaSi_2N_3 , as well as the nitridophosphate $\text{K}_3\text{P}_6\text{N}_{11}$.^[30–33] Since the first ammonothermal synthesis of GaN in 1995,^[34] and after the retirement of Jacobs, however, ammonothermal research primarily focuses on the crystal growth of GaN rather than in the explorative ammonothermal synthesis of binary and multinary nitrides.^[35–37] However, many (oxide) nitride materials exhibit other interesting material properties that lead to a variety of possible applications such as ion conductors, catalysts for photocatalytical water splitting, ceramic materials or phosphor materials.^[38–45] Nevertheless, as mentioned above, their synthesis is still challenging. Here the ammonothermal method could serve as a promising alternative synthetic tool for an easier access to these compounds. In order to reinvigorate this approach, the DFG funded research group “*Ammono-FOR: Chemistry and technology of ammonothermal synthesis of nitrides*” was founded in 2011. The stated aim of this interdisciplinary research group was to gain a holistic picture of the ammonothermal technique, including

- autoclave design (Prof. Schlücker, University of Erlangen-Nürnberg),
- synthesis of ternary and multinary nitrides (Prof. Schnick, University of Munich),
- investigation of possible intermediate species (Prof. Niewa, University of Stuttgart),

- in situ X-ray imaging (Prof. Wellmann, University of Erlangen-Nürnberg),
- in situ Raman spectroscopy (Prof. Schlücker, University of Erlangen-Nürnberg),
- ultrasonic velocity measurements (Prof. Schwieger, University of Erlangen-Nürnberg), and
- examination of crystal growth processes (Dr. Meissner, University of Erlangen-Nürnberg).

Herein, the development of new high-pressure, high-temperature autoclaves (Figure 1.3) from nickel-based superalloys (Inconel® 718 and Haynes® 282®) that meet the special requirements of ammonothermal synthesis (chemical stability against supercritical NH₃) and exhibit high yield and tensile strengths at process conditions (up to 1100 K and 300 MPa), was of crucial importance.

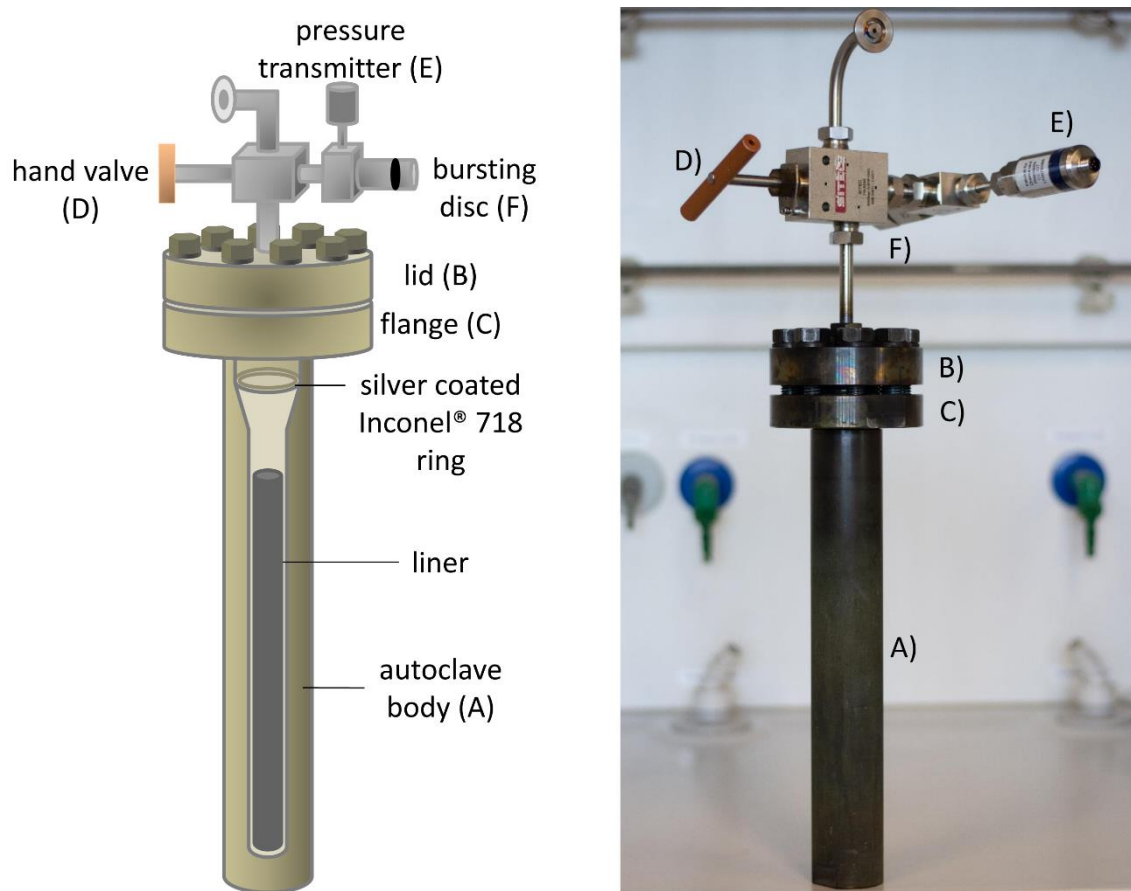


Figure 1.3. Scheme (left) and picture (right) of an autoclave, as typically used for ammonothermal reactions. The autoclave body (A) is sealed with the lid (B) via a flange construction (C) using a silver coated C-ring. A high-pressure tube connects the sealed autoclave body with the upper part, which is composed of a hand valve (D), a pressure transmitter (E), and a bursting disc (F).

Using these newly developed autoclaves as well as the above mentioned in situ techniques, numerous binary, ternary and multinary (oxide) nitrides were synthesized ammonothermally and information on in situ processes were obtained within the *Ammono-FOR* research group. Intriguing highlights are

the crystal growth of InN under ammononeutral conditions,^[46] the synthesis of various ternary Grimm-Sommerfeld analogous nitride semiconductors such as $I-IV_2-N_3$ and $II-IV-N_2$ compounds ($I = \text{Li}$; $II = \text{Mg, Mn, Zn}$; $IV = \text{Si, Ge}$),^[15, 47] the synthesis of the new multinary nitrides CaGaSiN_3 and $\text{Ca}_{1-x}\text{Li}_x\text{Al}_{1-x}\text{Ge}_{1+x}\text{N}_3$ ($x \approx 0.2$),^[48, 49] as well as the synthesis of numerous oxide nitride perovskites, and the Ruddlesden-Popper phase $\text{Eu}^{\text{II}}\text{Eu}^{\text{III}}_2\text{Ta}_2\text{N}_4\text{O}_3$.^[50-52] Figure 1.4 summarizes all (oxide) nitride materials that have been successfully synthesized under ammonothermal conditions and highlights the compounds that crystallize in prominent structure types. Apparently, the NaCl, the wurtzite, and the perovskite structure types are the most prominent.

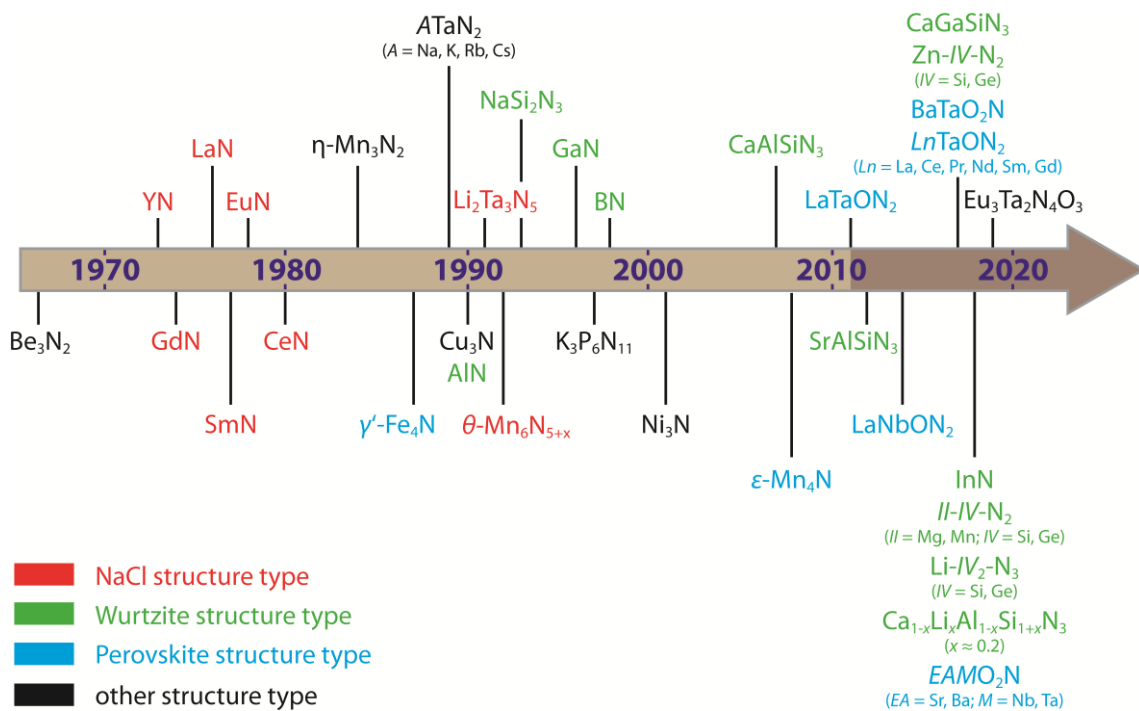


Figure 1.4. Timeline of ammonothermally synthesized (oxide) nitride materials.^[15, 21, 22, 29-35, 37, 46-70] Compounds crystallizing either in the NaCl (red), wurtzite (green), or perovskite structure type (blue) are highlighted. The color change of the timeline from beige to brown in 2011 illustrates the start of the *Ammono-FOR* research group.

1.3 Scope of this Thesis

The group 13 nitrides AlN, GaN, InN, and their solid solutions (Al,Ga,In)N are today's most important optoelectronic semiconductors for application in LEDs or laser diodes. Owing to low natural abundance of Ga and In, however, modern solid-state chemistry researches for sustainable, earth-abundant alternative nitride materials. Here, the ammonothermal approach has been claimed

as a promising tool for the synthesis and crystal growth of novel semiconducting nitrides. Fundamental research on these so-called Grimm-Sommerfeld analogous nitrides, however, is still in the early stage of development and the ammonothermal method itself is a rather scarcely studied technique with a limited number of accessible (oxide) nitrides covering a negligible structural diversity. Therefore, this thesis strives to investigate ammonothermally synthesized semiconducting nitride materials (solid solutions of $II-IV-N_2$, II_2-V-N_3) and to extend the quantity of ammonothermally accessible (oxide) nitrides by systematically investigate the ammonothermal synthesis of (oxo)nitridophosphates with their complete structural diversity as well as the characterization of their properties. For this purpose, custom-built high-temperature high-pressure autoclaves were used to screen suitable mineralizers and precursors and to examine reasonable reaction conditions, concerning temperature, pressure, and NH_3 concentration.

The first part of this thesis deals with the ammonothermal synthesis of semiconducting nitrides ($II-IV-N_2$ and II_2-V-N_3) and their detailed characterization in terms of optical and electronic properties. Due to the above mentioned structural analogy of Grimm-Sommerfeld analogous $II-IV-N_2$ semiconductors to group 13 nitrides (Figure 1.2), as well as their auspicious optical and electronic properties, these materials are currently highly relevant.^[4] Herein, Chapter 2 covers the ammonothermal synthesis of solid solutions of $II-IV-N_2$ compounds with the general formula ($II^a_{1-x}II^b_x$)- $IV-N_2$ ($II = Mg, Mn, Zn; IV = Si, Ge; x \approx 0.5$), as well as the investigation of their optical and electronic bandgap. The initial ammonothermal synthesis of the literature known semiconductors Mg_2PN_3 and Zn_2PN_3 is presented in Chapter 3. Furthermore, their optical properties were investigated for the first time and the initial growth of Mg_2PN_3 single crystals is reported, providing intriguing insights into the crystallization process under ammonothermal conditions.^[14, 71]

Based on these results, the second part of this thesis reports on the expansion of the ammonothermal method as a versatile synthetic tool for the synthesis of (oxo)nitridophosphates and -silicates with different degrees of condensation. Thus, Chapter 4 summarizes the synthesis of six nitridophosphates featuring diverse network types, namely α - $Li_{10}P_4N_{10}$, β - $Li_{10}P_4N_{10}$, $Li_{18}P_6N_{16}$, Ca_2PN_3 , SrP_8N_{14} , and $LiPN_2$.^[38, 72–76] Moreover, red phosphorus was established as a starting material, replacing commonly used but not readily available precursors such as P_3N_5 . Both, the use of simple starting materials and the synthesis of large-volume samples by the ammonothermal approach facilitate the detailed characterization of their materials properties. These fundamental new insights were further used to synthesize the previously unknown (oxo)nitridophosphates $Sr_3P_3N_7$ and Ba_2PO_3N , as is presented in Chapter 5 and 6. Both compounds are suitable host lattices for the activator ion Eu^{2+} and show deep red ($Sr_3P_3N_7:Eu^{2+}$) and green ($Ba_2PO_3N:Eu^{2+}$) luminescence when irradiated with UV to blue light. Moreover, the ammonothermal method was transferred to the (oxo)nitridosilicate class of compounds, as reported in Chapter 7. Herein, the synthesis and crystal growth of the

oxonitridosilicate $\text{Ca}_{1+x}\text{Y}_{1-x}\text{SiN}_{3-x}\text{O}_x$ ($x > 0$) is presented, serving as a case study for future expansions of the ammonothermal synthesis. Finally, the results of this thesis are summarized in Chapter 8 and discussed in their scientific context in Chapter 9.

1.4 References

- [1] Bundesanstalt für Geowissenschaften und Rohstoffe (BGR), "*BGR Energiestudie 2018 – Daten und Entwicklungen der deutschen und globalen Energieversorgung*", Hannover, Germany, **2019**.
- [2] Energy Efficiency and Renewable Energy, U.S. Department of Energy: Washington, D.C., "*Energy Savings Forecast of Solid-State Lighting in General Illumination Applications*", **2016**.
- [3] H. Morkoç, "*Handbook of Nitride Semiconductors and Devices, Materials Properties, Physics and Growth*", Wiley-VCH, Weinheim, Germany, **2009**.
- [4] Y. Hinuma, T. Hatakeyama, Y. Kumagai, L. A. Burton, H. Sato, Y. Muraba, S. Iimura, H. Hiramatsu, I. Tanaka, H. Hosono, F. Oba, "*Discovery of earth-abundant nitride semiconductors by computational screening and high-pressure synthesis*", *Nat. Commun.* **2016**, 7, 11962.
- [5] D. Ehretraut, E. Meissner, M. Bockowski, "*Technology of Gallium Nitride Crystal Growth*", Springer, Berlin, Heidelberg, **2010**.
- [6] H. G. Grimm, A. Sommerfeld, "*Über den Zusammenhang des Abschlusses der Elektronengruppen im Atom mit den chemischen Valenzzahlen*", *Z. Phys.* **1926**, 36, 36-59.
- [7] J. Wu, W. Walukiewicz, "*Band gaps of InN and group III nitride alloys*", *Superlattices Microstruct.* **2003**, 34, 63-75.
- [8] S. Nakamura, "*Background Story of the Invention of Efficient InGaN Blue-Light-Emitting Diodes (Nobel Lecture)*", *Angew. Chem.* **2015**, 127, 7880-7899; *Angew. Chem. Int. Ed.* **2015**, 54, 7770-7788.
- [9] V. L. Shaposhnikov, A. V. Krivosheeva, F. Arnaud D'Avitaya, J.-L. Lazzari, V. E. Borisenko, "*Structural, electronic and optical properties of II–IV–N₂ compounds (II = Be, Zn; IV = Si, Ge)*", *Phys. Status Solidi B* **2008**, 245, 142-148.
- [10] P. C. Quayle, K. He, J. Shan, K. Kash, "*Synthesis, lattice structure, and band gap of ZnSnN₂*", *MRS Commun.* **2013**, 3, 135-138.
- [11] P. Narang, S. Chen, N. C. Coronel, S. Gul, J. Yano, L. W. Wang, N. S. Lewis, H. A. Atwater, "*Bandgap Tunability in Zn(Sn,Ge)N₂ Semiconductor Alloys*", *Adv. Mater.* **2014**, 26, 1235-1241.
- [12] A. D. Martinez, A. N. Fioretti, E. S. Toberer, A. C. Tamboli, "*Synthesis, structure, and optoelectronic properties of II-IV-V₂ materials*", *J. Mater. Chem.* **2017**, 5, 11418-11435.

- [13] T. Pavloudis, J. Kioseoglou, T. Karakostas, P. Komninou, "Ordered structures in III-Nitride ternary alloys", *Comput. Mater. Sci.* **2016**, *118*, 22-31.
- [14] V. Schultz-Coulon, W. Schnick, " Mg_2PN_3 and Ca_2PN_3 – Phosphorus(V) Nitrides with Infinite Chains of Corner Sharing PN_4 Tetrahedra", *Z. Anorg. Allg. Chem.* **1997**, *623*, 69-74.
- [15] J. Häusler, S. Schimmel, P. Wellmann, W. Schnick, "Ammonothermal Synthesis of Earth-Abundant Nitride Semiconductors $ZnSiN_2$ and $ZnGeN_2$ and Dissolution Monitoring by In Situ X-ray Imaging", *Chem. Eur. J.* **2017**, *23*, 12275-12282.
- [16] E. Riedel, C. Janiak, "Anorganische Chemie", De Gruyter, Berlin, New York, 8th Ed., **2011**.
- [17] J. Mazeau, F. Greteau, R. I. Hall, A. Huetz, "Energy and width of $N(^3P)$ from observation of its formation by dissociative attachment to N_2 and NO ", *J. Phys. B: At. Mol. Phys.* **1978**, *11*, L557-L560.
- [18] M. Zeuner, S. Pagano, W. Schnick, "Nitridosilicates and Oxonitridosilicates: From Ceramic Materials to Structural and Functional Diversity", *Angew. Chem.* **2011**, *123*, 7898-7920; *Angew. Chem. Int. Ed.* **2011**, *50*, 7754-7775.
- [19] W. Schnick, J. Lücke, F. Krumeich, "Phosphorus Nitride P_3N_5 : Synthesis, Spectroscopic, and Electron Microscopic Investigations", *Chem. Mater.* **1996**, *8*, 281-286.
- [20] S. D. Kloß, W. Schnick, "Nitridophosphates – A Success Story of Nitride Synthesis", *Angew. Chem.* **2019**, *131*, 8015-8027; *Angew. Chem. Int. Ed.* **2019**, *58*, 7933-7944.
- [21] T. Richter, R. Niewa, "Chemistry of Ammonothermal Synthesis", *Inorganics* **2014**, *2*, 29-78.
- [22] J. Häusler, W. Schnick, "Ammonothermal Synthesis of Nitrides: Recent Developments and Future Perspectives", *Chem. Eur. J.* **2018**, *24*, 11864-11879.
- [23] K. Byrappa, M. Yoshimura, "Handbook of Hydrothermal Technology", William Andrew Publishing, Norwich, NY, USA, **2001**.
- [24] S. Zhang, N. S. A. Alt, E. Schlücker, R. Niewa, "Novel alkali metal amidogallates as intermediates in ammonothermal GaN crystal growth", *J. Cryst. Growth* **2014**, *403*, 22-28.
- [25] J. Hertrampf, N. S. A. Alt, E. Schlücker, R. Niewa, "Three Solid Modifications of $Ba[Ga(NH_2)_4]_2$: A Soluble Intermediate in Ammonothermal GaN Crystal Growth", *Eur. J. Inorg. Chem.* **2017**, 902-909.
- [26] S. Zhang, F. Hintze, W. Schnick, R. Niewa, "Intermediates in Ammonothermal GaN Crystal Growth under Ammonoacidic Conditions", *Eur. J. Inorg. Chem.* **2013**, 5387-5399.
- [27] D. Ehrentraut, R. T. Pakalapati, D. S. Kamber, W. Jiang, D. W. Pocius, B. C. Downey, M. McLaurin, M. P. D'Evelyn, "High Quality, Low Cost Ammonothermal Bulk GaN Substrates", *Jpn. J. Appl. Phys.* **2013**, *52*, 08JA01.
- [28] S. Pimputkar, S. Kawabata, J. S. Speck, S. Nakamura, "Improved growth rates and purity of basic ammonothermal GaN", *J. Cryst. Growth* **2014**, *403*, 7-17.

- [29] R. Juza, H. Jacobs, "Ammonothermal Synthesis of Magnesium and Beryllium Amides", *Angew. Chem.* **1966**, 78, 208; *Angew. Chem. Int. Ed. Engl.* **1966**, 5, 247.
- [30] H. Jacobs, E. von Pinkowski, "Synthese ternärer nitride von alkalimetallen: Verbindungen mit tantal, $MTaN_2$ mit $M = Na, K, Rb$ und Cs ", *J. Less Common Met.* **1989**, 146, 147-160.
- [31] T. Brokamp, H. Jacobs, "Synthese und Kristallstruktur eines gemischtvalenten Lithium-Tantalnitrids $Li_2Ta_3N_5$ ", *J. Alloys Compd.* **1991**, 176, 47-60.
- [32] H. Jacobs, H. Mengis, "Preparation and crystal structure of a sodium silicon nitride, $NaSi_2N_3$ ", *Eur. J. Solid State Inorg. Chem.* **1993**, 30, 45-53.
- [33] H. Jacobs, R. Nymwegen, "Synthesis and Crystal Structure of a Potassium Nitridophosphate, $K_3P_6N_{11}$ ", *Z. Anorg. Allg. Chem.* **1997**, 623, 429-433.
- [34] R. Dwilinski, A. Wysmolek, J. Baranowski, M. Kaminska, R. Doradziński, H. Jacobs, "GaN synthesis by ammonothermal method", *Acta Phys. Pol., A* **1995**, 88, 833-836.
- [35] J. Li, T. Watanabe, H. Wada, T. Setoyama, M. Yoshimura, "Low-Temperature Crystallization of Eu-Doped Red-Emitting $CaAlSiN_3$ from Alloy-Derived Ammonometallates", *Chem. Mater.* **2007**, 19, 3592-3594.
- [36] H. Watanabe, N. Kijima, "Crystal structure and luminescence properties of $Sr_xCa_{1-x}AlSiN_3:Eu^{2+}$ mixed nitride phosphors", *J. Alloys Compd.* **2009**, 475, 434-439.
- [37] T. Watanabe, K. Nonaka, J. Li, K. Kishida, M. Yoshimura, "Low temperature ammonothermal synthesis of europium-doped $SrAlSiN_3$ for a nitride red phosphor", *J. Ceram. Soc. Jpn.* **2012**, 120, 500-502.
- [38] E. M. Bertschler, C. Dietrich, T. Leichtweiß, J. Janek, W. Schnick, " Li^+ Ion Conductors with Adamantane-Type Nitridophosphate Anions $\beta-Li_{10}P_4N_{10}$ and $Li_{13}P_4N_{10}X_3$ with $X=Cl, Br$ ", *Chem. Eur. J.* **2018**, 24, 196-205.
- [39] S. G. Ebbinghaus, H.-P. Abicht, R. Dronskowski, T. Müller, A. Reller, A. Weidenkaff, "Perovskite-related oxynitrides – Recent developments in synthesis, characterisation and investigations of physical properties", *Prog. Solid State Chem.* **2009**, 37, 173-205.
- [40] A. Ziegler, J. C. Idrobo, M. K. Cinibulk, C. Kisielowski, N. D. Browning, R. O. Ritchie, "Interface Structure and Atomic Bonding Characteristics in Silicon Nitride Ceramics", *Science* **2004**, 306, 1768-1770.
- [41] P. Pust, P. J. Schmidt, W. Schnick, "A revolution in lighting", *Nat. Mater.* **2015**, 14, 454-458.
- [42] H. A. Höpfe, H. Lutz, P. Morys, W. Schnick, A. Seilmeier, "Luminescence in Eu^{2+} -doped $Ba_2Si_5N_8$: fluorescence, thermoluminescence, and upconversion", *J. Phys. Chem. Solids* **2000**, 61, 2001-2006.
- [43] K. Uheda, N. Hirotsaki, H. Yamamoto, "Host lattice materials in the system $Ca_3N_2-AlN-Si_3N_4$ for white light emitting diode", *Phys. Status Solidi A* **2006**, 203, 2712-2717.

- [44] K. Uheda, N. Hirosaki, Y. Yamamoto, A. Naito, T. Nakajima, H. Yamamoto, "Luminescence Properties of a Red Phosphor, $\text{CaAlSiN}_3:\text{Eu}^{2+}$, for White Light-Emitting Diodes", *Electrochem. Solid-State Lett.* **2006**, 9, H22-H25.
- [45] P. Pust, V. Weiler, C. Hecht, A. Tücks, A. S. Wochnik, A.-K. Henß, D. Wiechert, C. Scheu, P. J. Schmidt, W. Schnick, "Narrow-band red-emitting $\text{Sr}[\text{LiAl}_3\text{N}_4]:\text{Eu}^{2+}$ as a next-generation LED-phosphor material", *Nat. Mater.* **2014**, 13, 891-896.
- [46] J. Hertrampf, P. Becker, M. Widenmeyer, A. Weidenkaff, E. Schlücker, R. Niewa, "Ammonothermal Crystal Growth of Indium Nitride", *Cryst. Growth Des.* **2018**, 18, 2365-2369.
- [47] J. Häusler, R. Niklaus, J. Minár, W. Schnick, "Ammonothermal Synthesis and Optical Properties of Ternary Nitride Semiconductors Mg-IV-N_2 , Mn-IV-N_2 and $\text{Li-IV}_2\text{-N}_3$ ($\text{IV}=\text{Si, Ge}$)", *Chem. Eur. J.* **2018**, 24, 1686-1693.
- [48] J. Häusler, L. Neudert, M. Mallmann, R. Niklaus, A.-C. L. Kimmel, N. S. A. Alt, E. Schlücker, O. Oeckler, W. Schnick, "Ammonothermal Synthesis of Novel Nitrides: Case Study on CaGaSiN_3 ", *Chem. Eur. J.* **2017**, 23, 2583-2590.
- [49] J. Häusler, L. Eisenburger, O. Oeckler, W. Schnick, "Ammonothermal Synthesis and Crystal Structure of the Nitridoalumogermanate $\text{Ca}_{1-x}\text{Li}_x\text{Al}_{1-x}\text{Ge}_{1+x}\text{N}_3$ ($x \approx 0.2$)", *Eur. J. Inorg. Chem.* **2018**, 759-764.
- [50] N. Cordes, W. Schnick, "Ammonothermal Synthesis of Crystalline Oxonitride Perovskites LnTaON_2 ($\text{Ln}=\text{La, Ce, Pr, Nd, Sm, Gd}$)", *Chem. Eur. J.* **2017**, 23, 11410-11415.
- [51] N. Cordes, T. Bräuniger, W. Schnick, "Ammonothermal Synthesis of EAMO_2N ($\text{EA} = \text{Sr, Ba}$; $\text{M} = \text{Nb, Ta}$) Perovskites and ^{14}N Solid-State NMR Spectroscopic Investigations of $\text{AM}(\text{O,N})_3$ ($\text{A} = \text{Ca, Sr, Ba, La}$)", *Eur. J. Inorg. Chem.* **2018**, 5019-5026.
- [52] N. Cordes, M. Nentwig, L. Eisenburger, O. Oeckler, W. Schnick, "Ammonothermal Synthesis of the Mixed-Valence Nitrogen-Rich Europium Tantalum Ruddlesden-Popper Phase $\text{Eu}^{\text{II}}\text{Eu}^{\text{III}}_2\text{Ta}_2\text{N}_4\text{O}_3$ ", *Eur. J. Inorg. Chem.* **2019**, 2304-2311.
- [53] A. Stühr, H. Jacobs, R. Juza, "Amide of Yttrium", *Z. Anorg. Allg. Chem.* **1973**, 395, 291-300.
- [54] G. Linde, R. Juza, "Amidometallates of Lanthanum and Gadolinium and the Conversion of Lanthanum, Gadolinium, and Scandium with Ammonia", *Z. Anorg. Allg. Chem.* **1974**, 409, 191-198.
- [55] H. Jacobs, D. Schmidt, "High-pressure ammonolysis in solid-state chemistry", *Curr. Top. Mater. Sci.* **1982**, 8, 381-427.
- [56] H. Jacobs, H. Kistrup, "The System Potassium/Samarium/Ammonia", *Z. Anorg. Allg. Chem.* **1977**, 435, 127-136.
- [57] H. Jacobs, U. Fink, "Investigation of the System Potassium/Europium/Ammonia", *Z. Anorg. Allg. Chem.* **1978**, 438, 151-159.

- [58] H. Jacobs, D. Schmidt, "Struktur und Eigenschaften von perowskitartigen Cäsiumamidometallaten des Cers, Neodyms und Samariums $Cs_3Ln_2(NH_2)_9$ ", *J. Less Common Met.* **1980**, 76, 227-244.
- [59] H. Jacobs, C. Stüve, "Hochdrucksynthese der η -phase im System Mn-N: Mn_3N_2 ", *J. Less Common Met.* **1984**, 96, 323-329.
- [60] H. Jacobs, J. Bock, "Einkristallzüchtung von γ' - Fe_4N in überkritischem Ammoniak", *J. Less Common Met.* **1987**, 134, 215-220.
- [61] H. Jacobs, D. Rechenbach, U. Zachwieja, "Structure determination of γ' - Fe_4N and ϵ - Fe_3N ", *J. Alloys Compd.* **1995**, 227, 10-17.
- [62] U. Zachwieja, H. Jacobs, "Ammonothermal synthesis of Kupfernitrinid, Cu_3N ", *J. Less Common Met.* **1990**, 161, 175-184.
- [63] D. Peters, "Ammonothermal synthesis of aluminum nitride", *J. Cryst. Growth* **1990**, 104, 411-418.
- [64] G. Kreiner, H. Jacobs, "Magnetische Struktur von η - Mn_3N_2 ", *J. Alloys Compd.* **1992**, 183, 345-362.
- [65] R. Dwilinski, R. Doradzinski, J. Garczynski, L. Sierzputowski, M. Palczewska, A. Wysmolek, M. Kaminska, "AMMONO method of BN, AlN and GaN synthesis and crystal growth", *MRS Internet J. Nitride Semicond. Res.* **1998**, 3, e 25.
- [66] A. Leineweber, H. Jacobs, S. Hull, "Ordering of Nitrogen in Nickel Nitride Ni_3N Determined by Neutron Diffraction", *Inorg. Chem.* **2001**, 40, 5818-5822.
- [67] M. Zając, J. Gosk, E. Grzanka, S. Stelmakh, M. Palczewska, A. Wysmolek, K. Korona, M. Kamińska, A. Twardowski, "Ammonothermal synthesis of GaN doped with transition metal ions (Mn, Fe, Cr)", *J. Alloys Compd.* **2008**, 456, 324-338.
- [68] T. Watanabe, K. Tajima, J. Li, N. Matsushita, M. Yoshimura, "Low-temperature Ammonothermal Synthesis of $LaTaON_2$ ", *Chem. Lett.* **2011**, 40, 1101-1102.
- [69] C. Izawa, T. Kobayashi, K. Kishida, T. Watanabe, "Ammonothermal Synthesis and Photocatalytic Activity of Lower Valence Cation-Doped $LaNbON_2$ ", *Adv. Mater. Sci. Eng.* **2014**, 2014, 5.
- [70] T. Toshima, K. Kishida, Y. Maruyama, T. Watanabe, "Low-temperature synthesis of $BaTaO_2N$ by an ammonothermal method", *J. Ceram. Soc. Jpn.* **2017**, 125, 643-647.
- [71] S. J. Sedlmaier, M. Eberspächer, W. Schnick, "High-Pressure Synthesis, Crystal Structure, and Characterization of Zn_2PN_3 – A New catena-Polynitridophosphate", *Z. Anorg. Allg. Chem.* **2011**, 637, 362-367.
- [72] W. Schnick, U. Berger, " $Li_{10}P_4N_{10}$ - A Lithium Phosphorus(V) Nitride with the Novel Complex Anion $P_4N_{10}^{10-}$ ", *Angew. Chem.* **1991**, 103, 857-858; *Angew. Chem. Int. Ed. Engl.* **1992**, 31, 213-214.

- [73] E.-M. Bertschler, C. Dietrich, J. Janek, W. Schnick, "*Li₁₈P₆N₁₆ – A Lithium Nitridophosphate with Unprecedented Tricyclic [P₆N₁₆]¹⁸⁻ Ions*", *Chem. Eur. J.* **2017**, *23*, 2185-2191.
- [74] W. Schnick, V. Schultz-Coulon, "*Ca₂PN₃ - A Novel Phosphorus(V) Nitride with One-Dimensional Infinite Chains of Corner-Sharing PN₄ Tetrahedra*", *Angew. Chem.* **1993**, *105*, 308-309; *Angew. Chem. Int. Ed. Engl.* **1993**, *32*, 280-281.
- [75] S. Wendl, W. Schnick, "*SrH₄P₆N₁₂ and SrP₈N₁₄: Insights into the Condensation Mechanism of Nitridophosphates under High Pressure*", *Chem. Eur. J.* **2018**, *24*, 15889-15896.
- [76] W. Schnick, J. Lücke, "*On Lithium Phosphorus Nitride. Preparation and Refinement of the Crystal Structure of LiPN₂*", *Z. Anorg. Allg. Chem.* **1990**, *588*, 19-25.

2 Solid Solutions of Grimm-Sommerfeld Analogous Nitride Semiconductors $II-IV-N_2$ ($II = \text{Mg, Mn, Zn}$; $IV = \text{Si, Ge}$): Ammonothermal Synthesis and DFT Calculations

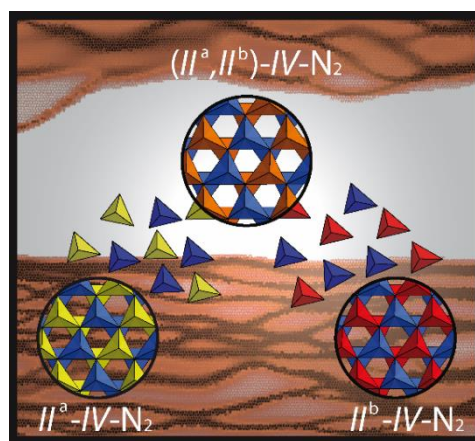
published in: *Chem. Eur. J.* **2019**, 25, 15887 - 15895.

authors: Mathias Mallmann, Robin Niklaus, Tobias Rackl, Maximilian Benz, Thanh G. Chau, Dirk Johrendt, Ján Minár, and Wolfgang Schnick

DOI: 10.1002/chem.201903897

Reprinted (adapted) with permission for non-commercial use from *Chemistry – A European Journal* (open access). Copyright 2019 John Wiley and Sons.

Abstract. Grimm–Sommerfeld analogous $II-IV-N_2$ nitrides such as ZnSiN_2 , ZnGeN_2 , and MgGeN_2 are promising semiconductor materials for substitution of commonly used $(\text{Al,Ga,In})\text{N}$. Herein, the ammonothermal synthesis of solid solutions of $II-IV-N_2$ compounds ($II = \text{Mg, Mn, Zn}$; $IV = \text{Si, Ge}$) having the general formula $(II^a_{1-x}II^b_x)-IV-N_2$ with $x \approx 0.5$ and ab initio DFT calculations of their electronic and optical properties are presented. The ammonothermal reactions



were conducted in custom-built, high-temperature, high-pressure autoclaves by using the corresponding elements as starting materials. NaNH_2 and KNH_2 act as ammonobasic mineralizers that increase the solubility of the reactants in supercritical ammonia. Temperatures between 870 and 1070 K and pressures up to 200 MPa were chosen as reaction conditions. All solid solutions crystallize in wurtzite-type superstructures with space group $Pna2_1$ (no. 33), confirmed by powder XRD. The chemical compositions were analyzed by energy-dispersive X-ray spectroscopy. Diffuse reflectance spectroscopy was used for estimation of optical bandgaps of all compounds, which ranged from 2.6 to 3.5 eV (Ge compounds) and from 3.6 to 4.4 eV (Si compounds), and thus demonstrated bandgap tunability between the respective boundary phases. Experimental findings

were corroborated by DFT calculations of the electronic structure of pseudorelaxed mixed-occupancy structures by using the KKR+CPA approach.

2.1 Introduction

The investigation of new semiconducting materials is of essential importance due to the increasing demand and the large number of possible applications. At present, GaN and solid solutions of group 13 nitrides (Al,Ga,In)N are the most important (opto)electronic semiconductors with different application fields in modern electronic technologies. These include areas such as light-emitting diodes, field-effect transistors, and laser diodes.^[1, 2] By using solid solutions of group 13 nitrides, a large bandgap range from around 0.7 to 6.2 eV can be covered.^[3] However, the major problem of these compounds arises from the limited availability of the constituent elements. Ga and In only arise as byproducts during the production of copper, aluminum, lead, and zinc and are therefore difficult to access. In contrast, the natural abundance of elements such as Zn or Si is considerably higher. Therefore, one goal of modern semiconductor research is to synthesize compounds composed of earth-abundant elements. Recently, DFT calculations indicated various zinc nitrides such as Grimm-Sommerfeld analogous Zn(Si,Ge,Sn)N₂ compounds as possible next-generation semiconductors.^[4] These materials exhibit similar electronic and optical properties to GaN, including high carrier mobility and small carrier effective masses, as well as high chemical stability and dopability. Additionally, such *II-IV-N₂* compounds show lattice parameters similar to those of (Al,Ga,In)N, which enable the formation of hybrid structures or epitaxial growth on group 13 nitrides. In the last few years, different studies examined the synthesis and properties of *II-IV-N₂* compounds.^[5-10] However, the bulk synthesis of these materials is still challenging. Recently, we employed the ammonothermal method as a suitable synthetic approach to Zn-*IV-N₂* compounds (*IV* = Si, Ge), as well as other Grimm-Sommerfeld analogous nitrides such as *II-IV-N₂* (*II* = Mg, Mn; *IV* = Si, Ge), *II₂-P-N₃* (*II* = Mg, Zn), CaGaSiN₃, and Ca_{1-x}Li_xAl_{1-x}Ge_{1+x}N₃ ($x \approx 0.2$).^[11-15] By employing this method, we were able to synthesize crystalline ZnSiN₂ and ZnGeN₂ with crystal sizes of several micrometers and, for the first time, single crystals of Mg₂PN₃ with lengths of up to 30 μm. Furthermore, well-defined crystallites of InN were obtained ammonothermally quite recently, indicating the ammonothermal process as an auspicious method for synthesis and crystal growth of semiconducting nitrides.^[16]

Herein, we present the synthesis of the solid solutions Mg_{1-x}Mn_xSiN₂, Mg_{1-x}Zn_xSiN₂, Mn_{1-x}Zn_xSiN₂, Mg_{1-x}Mn_xGeN₂, Mg_{1-x}Zn_xGeN₂, and Mn_{1-x}Zn_xGeN₂ ($x \approx 0.5$) under ammonothermal conditions. The Si compounds were synthesized at 1070 K and pressures up to 150 MPa, whereas the Ge compounds already decompose at such high temperatures and were therefore synthesized at 870 K and maximum

pressures of up to 200 MPa. The products were analyzed by powder X-ray diffraction (PXRD) and energy-dispersive X-ray spectroscopy (EDX). Diffuse reflectance spectroscopy and DFT calculations were used for evaluation of optical and electronic properties. Due to the mixed-occupancy sites in solid solutions, DFT calculations are challenging without relying on extensive supercell calculations. Previous works on mixed-occupancy CaMSiN_3 ($M = \text{Al, Ga}$) materials and fully ordered *II-IV-N₂* materials were successfully used to describe the electronic structure in the framework of the Korringa–Kohn–Rostoker (KKR) Green's function method together with bandgap corrections by the Engel–Vosko formalism.^[12, 17] Here we advance the described method to show successful application to solid solutions of these nitride materials. The presented results again demonstrate the great potential of the ammonothermal approach for synthesis of semiconducting materials and mark another step of *II-IV-N₂* compounds towards next-generation semiconductors as alternatives for commonly used group 13 nitrides.

2.2 Results and Discussion

2.2.1 Synthesis

The solid solutions of *II-IV-N₂* compounds $\text{Mg}_{1-x}\text{Mn}_x\text{SiN}_2$, $\text{Mg}_{1-x}\text{Zn}_x\text{SiN}_2$, $\text{Mn}_{1-x}\text{Zn}_x\text{SiN}_2$, $\text{Mg}_{1-x}\text{Mn}_x\text{GeN}_2$, $\text{Mg}_{1-x}\text{Zn}_x\text{GeN}_2$, and $\text{Mn}_{1-x}\text{Zn}_x\text{GeN}_2$ ($x \approx 0.5$) were synthesized by using supercritical ammonia as solvent in custom-built, high-pressure, high-temperature autoclaves. The respective elements (Mg, Mn, Zn, Ge, and Si) were used as starting materials. NaN_3 (Ge compounds) and KN_3 (Si compounds) were added to the reaction mixture. They decompose during the reaction and form the corresponding amides (NaNH_2 and KNH_2), which act as ammonobasic mineralizers. The azides were used instead of metals or amides because of their high purity and chemical stability towards hydrolysis. The mineralizers increase the solubility of the other starting materials in supercritical ammonia by formation of soluble intermediates (e.g., $\text{K}_2[\text{Zn}(\text{NH}_2)_4]$).^[18, 19] In the case of the Si compounds, the use of KNH_2 instead of NaNH_2 resulted in products with higher crystallinity. These findings are consistent with previous reports in which MgSiN_2 and MnSiN_2 were synthesized with KNH_2 , and MgGeN_2 and MnGeN_2 with NaNH_2 .^[12] Due to the preferred formation of intermediates around 700 K and the following transformation into the nitrides at higher temperatures, the syntheses were conducted in two temperature steps (see Experimental Section).

Whereas all Si compounds were synthesized at 1070 K with an autogenous pressure of around 150 MPa, Ge-containing compounds are thermally less stable and already decompose at these temperatures. Therefore, $\text{Mg}_{1-x}\text{Mn}_x\text{GeN}_2$, $\text{Mg}_{1-x}\text{Zn}_x\text{GeN}_2$ and $\text{Mn}_{1-x}\text{Zn}_x\text{GeN}_2$ ($x \approx 0.5$) were synthesized at 870 K and maximum pressures of about 200 MPa. To prevent uncontrolled diffusion

of the starting materials through the autoclave, the reaction mixtures were contained in closed Ta liners. The lids of the liners contain a small hole to ensure filling with ammonia. After reaction, residual amides and other impurity phases were removed as far as possible (see below) by washing the products with ethanol and acetic acid. Optical micrographs of the products are shown in Figure 2.1.

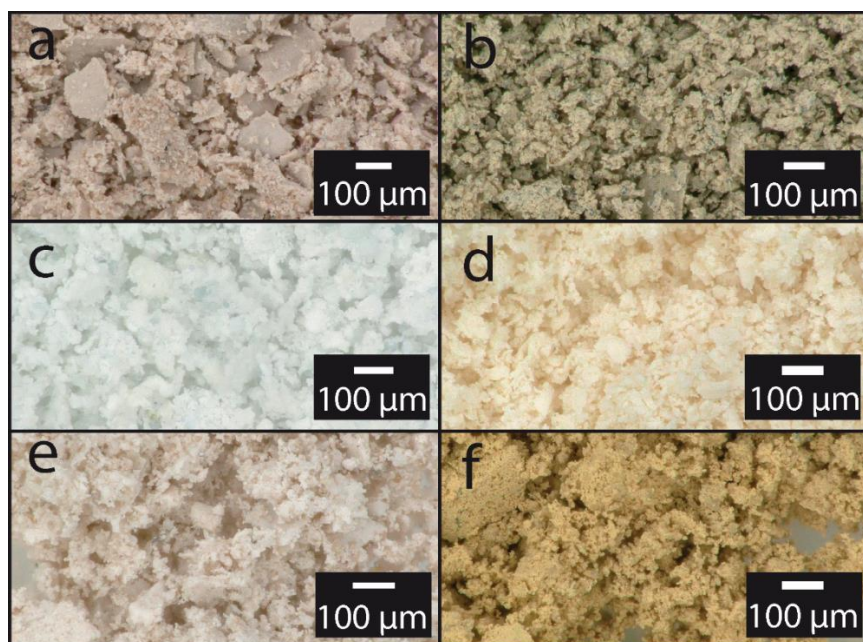


Figure 2.1. Optical micrographs of $\text{Mg}_{1-x}\text{Mn}_x\text{SiN}_2$ (a), $\text{Mg}_{1-x}\text{Mn}_x\text{GeN}_2$ (b), $\text{Mg}_{1-x}\text{Zn}_x\text{SiN}_2$ (c), $\text{Mg}_{1-x}\text{Zn}_x\text{GeN}_2$ (d), $\text{Mn}_{1-x}\text{Zn}_x\text{SiN}_2$ (e), and $\text{Mn}_{1-x}\text{Zn}_x\text{GeN}_2$ (f) with $x \approx 0.5$.

2.2.2 Crystal structure

The purified compounds were analyzed by PXRD. Rietveld plots of all products are shown in Figure 2.2. Wyckoff positions, atomic coordinates, and lattice parameters as starting values for the refinement were taken from ammonothermally synthesized *II-IV-N₂* phases in the literature.^[11, 12] Obtained crystallographic data are summarized in Table 2.1, and refined atomic coordinates and displacement parameters in Tables A.1–A.6 in the Supporting Information. All compounds crystallize in orthorhombic space group $Pna2_1$ (no. 33) and can be derived from the wurtzite structure type ($P6_3mc$, no. 186) by ordering of tetrahedrally coordinated divalent and tetravalent cations to form *sechser* rings along [001] (Figure 2.3).^[20] The ordering can be verified by the expected (011) and (110) superstructure reflections for the orthorhombic structure,^[21] which occur as the first two reflections of the target phases in the powder patterns. Further ordering of the different divalent cations in the solid solutions (e.g., Mg^{2+} and Zn^{2+} in $\text{Mg}_{1-x}\text{Zn}_x\text{GeN}_2$) could not be detected by PXRD. The occupation of the divalent cation positions were refined and slightly deviate from 0.5 for each

divalent cation (see Supporting Information Tables A.1–A.6). The largest deviation is found in $\text{Mg}_{0.375}\text{Mn}_{0.625}\text{GeN}_2$, whereas the deviations of all other compounds are in the range of ± 0.05 . The chemical compositions of the products were verified by elemental analysis (see below). Cell volumes of the solid solutions are within the range of those of the respective boundary phases reported in the literature.^[11, 12] However, the values of the solid solution deviate slightly from those expected from Vegard's rule (see Supporting Information Figure A.1).^[22] Possible explanations for this slight divergence could be a certain heterogeneous phase width of the solid solutions, which could also explain slight reflection broadening in the PXRD patterns of the solid solutions compared to the boundary phases, vacancies in the crystal structure, and measuring inaccuracies.

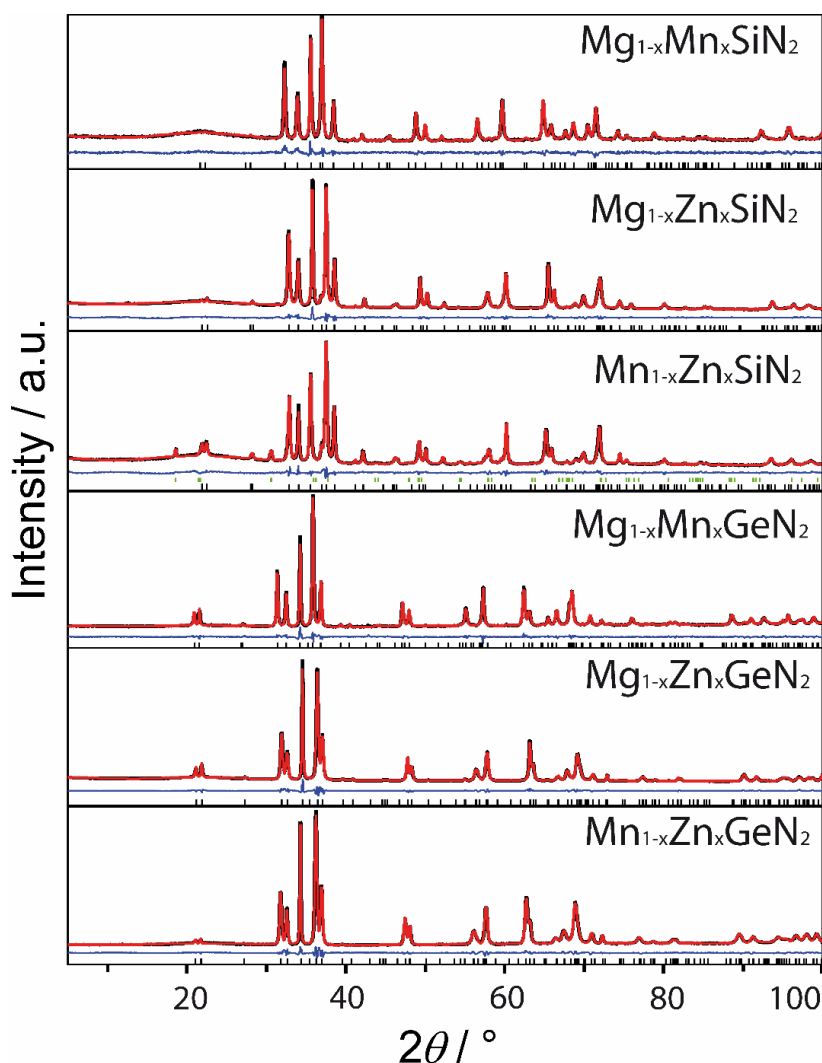


Figure 2.2. Rietveld refinement of PXRD patterns of solid solutions of *II-IV-N₂* compounds (*II* = Mg, Mn, Zn; *IV* = Si, Ge) with experimental data (black lines), calculated data (red lines), difference profiles (blue lines), and reflection positions (black bars). Green bars indicate reflection position of K_3MnO_4 side phase.

Table 2.1. Crystallographic data of $\text{Mg}_{1-x}\text{Mn}_x\text{SiN}_2$, $\text{Mg}_{1-x}\text{Mn}_x\text{GeN}_2$, $\text{Mg}_{1-x}\text{Zn}_x\text{SiN}_2$, $\text{Mg}_{1-x}\text{Zn}_x\text{GeN}_2$, $\text{Mn}_{1-x}\text{Zn}_x\text{SiN}_2$, and $\text{Mn}_{1-x}\text{Zn}_x\text{GeN}_2$ ($x \approx 0.5$) obtained by Rietveld refinement.

Formula	$\text{Mg}_{1-x}\text{Mn}_x\text{SiN}_2$ ($x = 0.543$)	$\text{Mg}_{1-x}\text{Mn}_x\text{GeN}_2$ ($x = 0.625$)	$\text{Mg}_{1-x}\text{Zn}_x\text{SiN}_2$ ($x = 0.515$)	$\text{Mg}_{1-x}\text{Zn}_x\text{GeN}_2$ ($x = 0.545$)	$\text{Mn}_{1-x}\text{Zn}_x\text{SiN}_2$ ($x = 0.53$)	$\text{Mn}_{1-x}\text{Zn}_x\text{GeN}_2$ ($x = 0.55$)
Crystal system	orthorhombic					
Space group	$Pna2_1$ (33)					
$a / \text{\AA}$	5.27579(12)	5.50086(8)	5.26264(8)	5.48149(8)	5.26071(10)	5.48798(9)
$b / \text{\AA}$	6.49871(17)	6.65560(11)	6.36667(11)	6.51446(11)	6.35726(15)	6.54510(13)
$c / \text{\AA}$	5.03780(13)	5.22654(8)	5.00805(7)	5.18384(7)	5.04257(11)	5.22186(9)
Cell volume / \AA^3	172.725(7)	191.352(5)	167.797(5)	185.110(5)	168.642(6)	187.566(6)
Density / $\text{g}\cdot\text{cm}^{-3}$	3.732	5.001	3.972	5.286	4.592	5.676
Formula units / cell	4					
T / K	293(2)					
Diffractometer	STOE STADI P					
Radiation	Cu- $K_{\alpha 1}$ ($\lambda = 1.5406 \text{\AA}$)					
2θ range / $^\circ$	$5.0 \leq 2\theta \leq 100$					
Profile function	fundamental parameters model					
Background function	Shifted Chebyshev					
Data points	6365					
Number of reflections	104	116	100	111	101	114
Refined parameters	56	51	50	56	64	52
R values	$R_p = 0.0266$	$R_p = 0.0342$	$R_p = 0.0395$	$R_p = 0.0413$	$R_p = 0.0339$	$R_p = 0.0368$
	$R_{wp} = 0.0340$	$R_{wp} = 0.0452$	$R_{wp} = 0.0490$	$R_{wp} = 0.0575$	$R_{wp} = 0.0419$	$R_{wp} = 0.0491$
	$R_{\text{Bragg}} = 0.0191$	$R_{\text{Bragg}} = 0.0134$	$R_{\text{Bragg}} = 0.0146$	$R_{\text{Bragg}} = 0.0158$	$R_{\text{Bragg}} = 0.0114$	$R_{\text{Bragg}} = 0.0105$
Goodness of fit	2.08	2.47	3.07	3.54	2.60	2.47

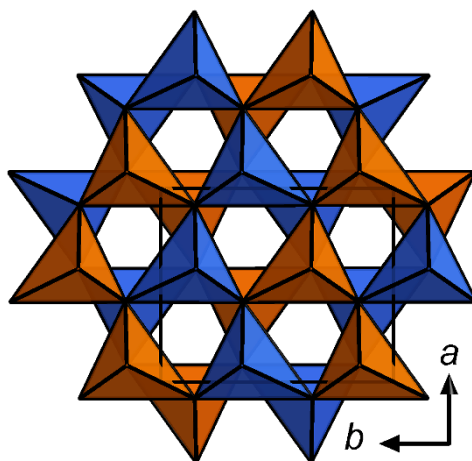


Figure 2.3. Crystal structure of solid solutions of *II-IV-N₂* compounds (*II* = Mg, Mn, Zn; *IV* = Si, Ge) along [001]. Mixed occupied *II-N₄* tetrahedra are depicted in blue and *IV-N₄* tetrahedra in orange.

To show that, in principle, solid solutions with other compositions are possible, $\text{Mg}_{1-x}\text{Zn}_x\text{GeN}_2$ with $x \approx 0.8$ was synthesized. The Rietveld plot, atomic coordinates, and crystallographic data are given in the Supporting Information (Figure A.2, Tables A.7 and A.8).

2.2.3 Scanning electron microscopy

SEM was conducted for verification of the chemical composition of the solid solutions as well as for examination of crystallite size and morphology. EDX values are summarized in Tables A.9 and A.10 in the Supporting Information. The slightly differing compositions measured at different measuring points suggest a phase width. A possible explanation could be the different solubilities of the starting materials (Mg, Mn, and Zn) in supercritical ammonia resulting in a varying transport through the autoclave, which could not be prevented completely by the use of Ta liners. Nevertheless, on the basis of the obtained values, it can be assumed that the solid solutions have an atomic ratio of the divalent cations close to 1:1, which is consistent with the findings obtained from Rietveld refinement. Exemplarily, SEM images of $\text{Mn}_{1-x}\text{Zn}_x\text{SiN}_2$ and $\text{Mn}_{1-x}\text{Zn}_x\text{GeN}_2$ (Figure A.3 in the Supporting Information) show crystallites with sizes up to several micrometers. The sizes and well-defined crystal faces suggest a solution-based growth mechanism, as already reported for ZnGeN_2 .^[11] SEM images of the Mg-containing compounds only show nanocrystalline products and were therefore not presented in the Supporting Information.

2.2.4 UV/Vis spectroscopy

The optical properties of the solid solutions were investigated by diffuse reflectance spectroscopy. Whereas the Si compounds show absorption bands in the region between 200 and 350 nm, the absorption bands of the Ge compounds are shifted to higher wavelengths between 300 and 500 nm (see Figure A.4 in the Supporting Information). In the case of Mn-containing compounds, sub-bandgap absorption was observed. These absorption bands can be attributed to the absorption of Mn²⁺ [transition of the ground state ⁶A₁(⁶S) to the excited states ⁴T₁(⁴G), ⁴T₂(⁴G), ⁴A₁, ⁴E(⁴G), ⁴T₂(⁴D) and ⁴E(⁴D)] according to the literature.^[18, 23] In the case of the germanium compounds, these absorption bands are partially overlaid by the bandgap absorption.

The Kubelka–Munk function $F(R) = (1-R)^2/2R$, where R is reflectance, was used to calculate pseudo-absorption spectra.^[24] Figure 2.4 shows Tauc plots, which were used for evaluation of the bandgaps E_g , whereby the energy $h\nu$ was plotted against $[F(R)h\nu]^{1/n}$ with $n = 1/2$ for direct bandgaps.^[25] Direct transitions were assumed according to DFT calculations (see below). Table 2.2 summarizes the measured bandgaps. The evaluated bandgaps are in similar ranges to those already described in the literature for the boundary phases.^[9, 11, 12, 26–31] Compared with the boundary phases prepared by ammonothermal syntheses (Figure A.5 in the Supporting Information), the measured E_g values of the mixed phases do not exactly match the mean values of their constituent boundary phases.

Table 2.2. Evaluated optical bandgaps E_g^{exp} of the mixed-occupancy ($II^{1-x}IV^x$)-*IV-N₂* ($x \approx 0.5$) compound series from Tauc plots at room temperature and optical bandgaps E_g^{JD} of the mixed-occupancy ($II^{0.5}IV^{0.5}$)-*IV-N₂* compound series from joint DOS calculations based on the EV-PBE functional within the Munich SPRKKR program package.

	Mg _{1-x} Mn _x SiN ₂	Mg _{1-x} Mn _x GeN ₂	Mg _{1-x} Zn _x SiN ₂	Mg _{1-x} Zn _x GeN ₂	Mn _{1-x} Zn _x SiN ₂	Mn _{1-x} Zn _x GeN ₂
E_g^{exp} ($x \approx 0.5$)	3.6 eV	2.7 eV	4.4 eV	3.5 eV	3.8 eV	2.6 eV
E_g^{JD} ($x = 0.5$)	3.4 eV	2.8 eV	4.9 eV	4.3 eV	3.4 eV	2.5 eV

This is in line with the aforementioned minor deviations and possible measuring inaccuracies of lattice parameters observed from structure refinement. Considering the extensive Urbach tailing observed in the diffuse reflectance spectra (see Figure A.4 in the Supporting Information), such deviations may well be explained by slight variations in the occupation of the divalent cation sites, possible defect sites, or resulting increased phonon-assisted absorption in the nanocrystallites obtained from ammonothermal synthesis.^[17, 32] In the case of Mg_{1-x}Zn_xGeN₂ the evaluated bandgap (3.5 eV) is larger than those of the corresponding boundary phases (both 3.2 eV). On the basis of

numerous theoretical calculations, it can be assumed that the bandgap of MgGeN₂ should actually be larger (around 4 eV) than previously estimated (3.2 eV).^[12, 33]

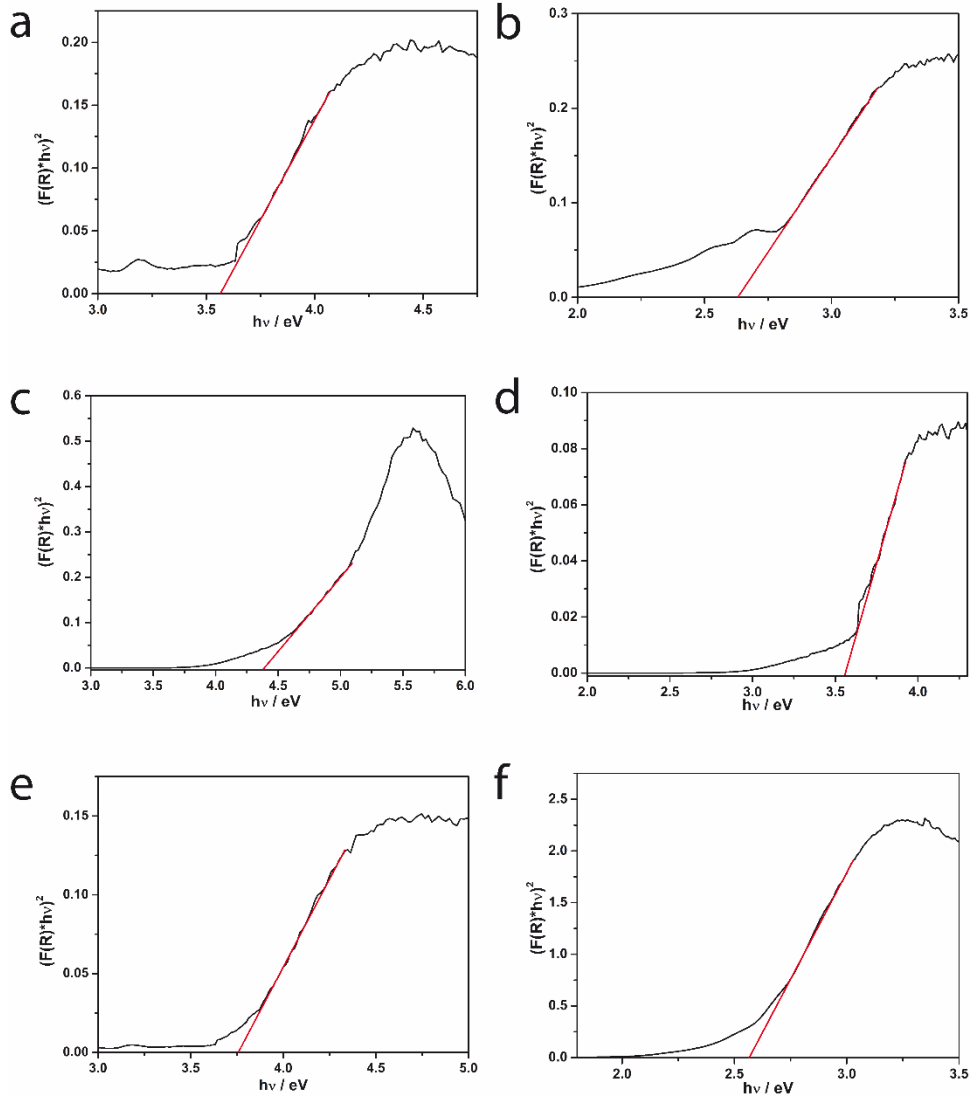


Figure 2.4. Tauc plots of Mg_{1-x}Mn_xSiN₂ (a), Mg_{1-x}Mn_xGeN₂ (b), Mg_{1-x}Zn_xSiN₂ (c), Mg_{1-x}Zn_xGeN₂ (d), Mn_{1-x}Zn_xSiN₂ (e), and Mn_{1-x}Zn_xGeN₂ (f) with $x \approx 0.5$. Red lines indicate tangents at the inflection points.

2.2.5 DFT calculations

To validate and investigate the observed trends of the experimentally deduced bandgaps of the examined solid solutions, DFT calculations were carried out for all boundary phases and the solid solutions Mg_{0.5}Mn_{0.5}SiN₂, Mg_{0.5}Zn_{0.5}SiN₂ and Mn_{0.5}Zn_{0.5}SiN₂, as well as the isotypical Ge series Mg_{0.5}Mn_{0.5}GeN₂, Mg_{0.5}Zn_{0.5}GeN₂, and Mn_{0.5}Zn_{0.5}GeN₂, in which the mixed occupancy was fixed at 0.5 for the sake of consistency. Each mixed-occupancy model was constructed from a symmetrized

average of three VASP-relaxed orderings with regard to atomic position and lattice parameters (for models, see Figure A.6 in the Supporting Information).

These pseudorelaxed models were used as starting points for electronic-structure calculations of the mixed-occupancy models ($II^{a_{0.5}}II^{b_{0.5}}-IV-N_2$) by means of the Munich SPRKKR package, which has been shown to be a sensible approach according to our previous work.^[17] Figure 2.5 depicts the calculated plots of the density of states (DOS) for each material. Excluding temperature effects, all ($\text{Mn}_{0.5}II_{0.5}$)- $IV-N_2$ ($II = \text{Mg, Zn}$ / $IV = \text{Si, Ge}$) compounds (Figure 2.5 a, b, e, f) exhibit spin polarization with total magnetic moments ranging between 4.17 and 4.23 μ_B . The obtained electronic bandgaps for the calculated solid solutions lie in between the calculated values of the respective boundary phases for all compounds calculated within the framework of the used code. These obtained E_g values for purely electronic transitions are estimated from the respective Bloch spectral functions (see Figures A.7 and A.8 in the Supporting Information) and are summarized in Figure 2.6. For spin-polarized Mn compounds E_g is given in terms of the respective spin-up and spin-down channels along values of magnetic moments. Owing to the underestimation of the exchange correlation by PBE we utilize the EV-PBE functional implemented in SPRKKR to correct the exchange-correlation and increase the bandgap accordingly. For a variety of materials including group 13 nitrides, EV-GGA has been shown to provide accurate band dispersion with gaps lying somewhere between those of LDA/GGA and those from the modified Becke–Johnson (mBJ) potential, the latter of which is widely considered to reproduce gaps with good accuracy.^[34–40] Due to the smearing of the bands introduced by the mixed-occupancy disorder and the induced smearing of the Bloch spectral functions, together with the relatively flat progression of the valence states, the assignment of the transition types for the solid solutions is not without ambiguity. For better analysis we performed subsequent calculations on the respective ordering models within VASP and the therein-available mBJ potential. For all ordered compounds $\text{Mg}_{0.5}\text{Zn}_{0.5}\text{SiN}_2$, $\text{Mn}_{0.5}\text{Zn}_{0.5}\text{SiN}_2$, and $\text{Mn}_{0.5}\text{Mg}_{0.5}\text{SiN}_2$, the ordered models suggest that indirect transitions are slightly favored over direct transitions, whereas for $\text{Mn}_{0.5}\text{Zn}_{0.5}\text{GeN}_2$ and $\text{Mn}_{0.5}\text{Mg}_{0.5}\text{GeN}_2$ direct and indirect transitions arise depending on the cation ordering with only $\text{Mg}_{0.5}\text{Zn}_{0.5}\text{GeN}_2$ showing consistent direct transitions. From the respective KKR calculations of the solid solutions indirect transitions are found for the ($II^{a_{0.5}}II^{b_{0.5}}$)- Si-N_2 compounds, albeit with only about 0.05 eV difference to direct transitions. For the ($II^{a_{0.5}}II^{b_{0.5}}$)- Ge-N_2 compound series, direct and indirect transitions were found to be energetically identical.

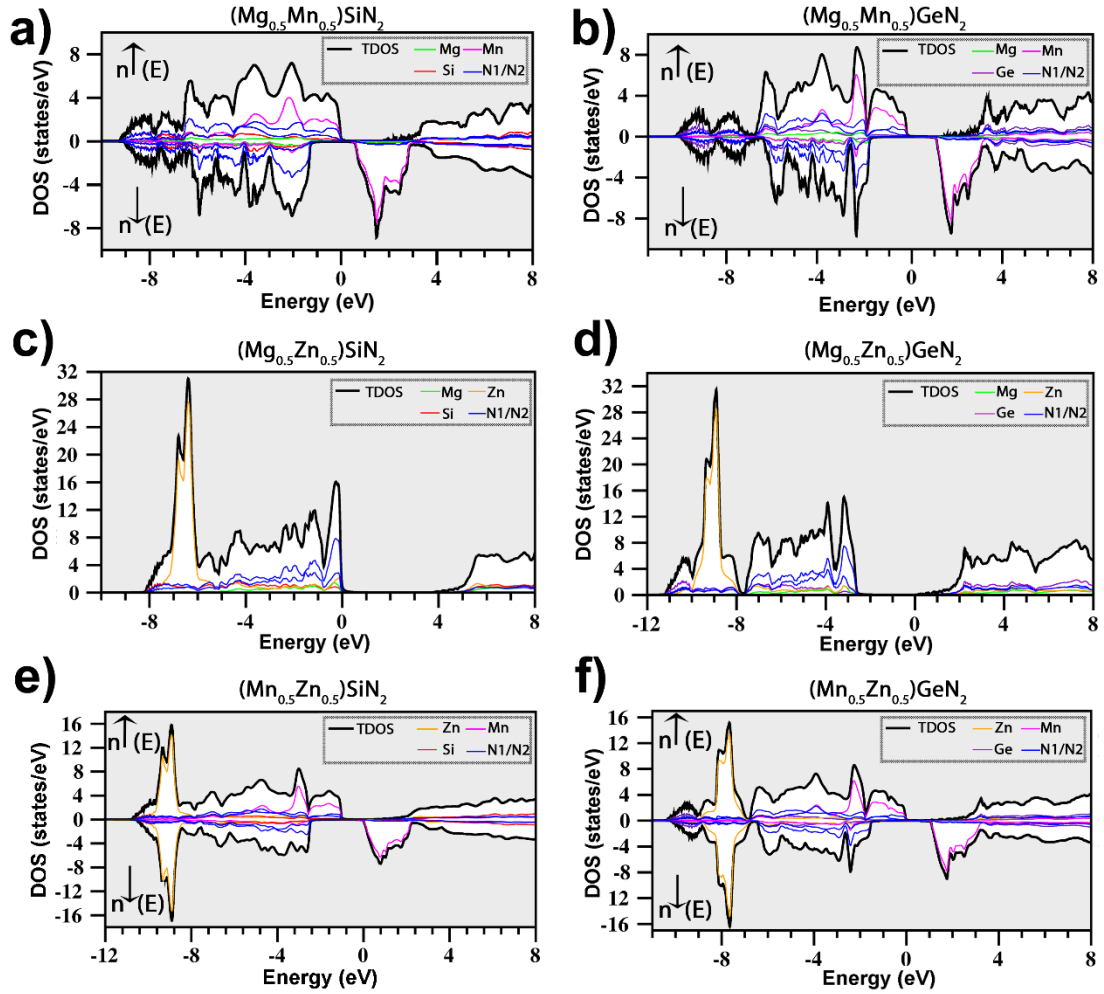


Figure 2.5. DOS as calculated by the KKR formalism with the coherent potential approximation and Engel–Vosko exchange correlation (EV-GGA) for the mixed-occupancy ($II^{P_{0.5}}/I^{P_{0.5}}$)- $IV-N_2$ compound series. $(\text{Mg}_{0.5}\text{Mn}_{0.5})\text{SiN}_2$ (a), $(\text{Mg}_{0.5}\text{Mn}_{0.5})\text{GeN}_2$ (b), $(\text{Mg}_{0.5}\text{Zn}_{0.5})\text{SiN}_2$ (c), $(\text{Mg}_{0.5}\text{Zn}_{0.5})\text{GeN}_2$ (d), $(\text{Mn}_{0.5}\text{Zn}_{0.5})\text{SiN}_2$ (e), and $(\text{Mn}_{0.5}\text{Zn}_{0.5})\text{GeN}_2$ (f).

As both types of transitions are found for the ordering models, KKR+CPA calculations appear to consistently describe the solid solution for statistical mixed occupancy. With regard to the minimal difference in direct and indirect transitions, we estimate that optically allowed direct transitions are more likely to occur and thus best described with the Kubelka–Munk formalism for direct transitions, as chosen accordingly for the experimental evaluation by UV/Vis spectroscopy.

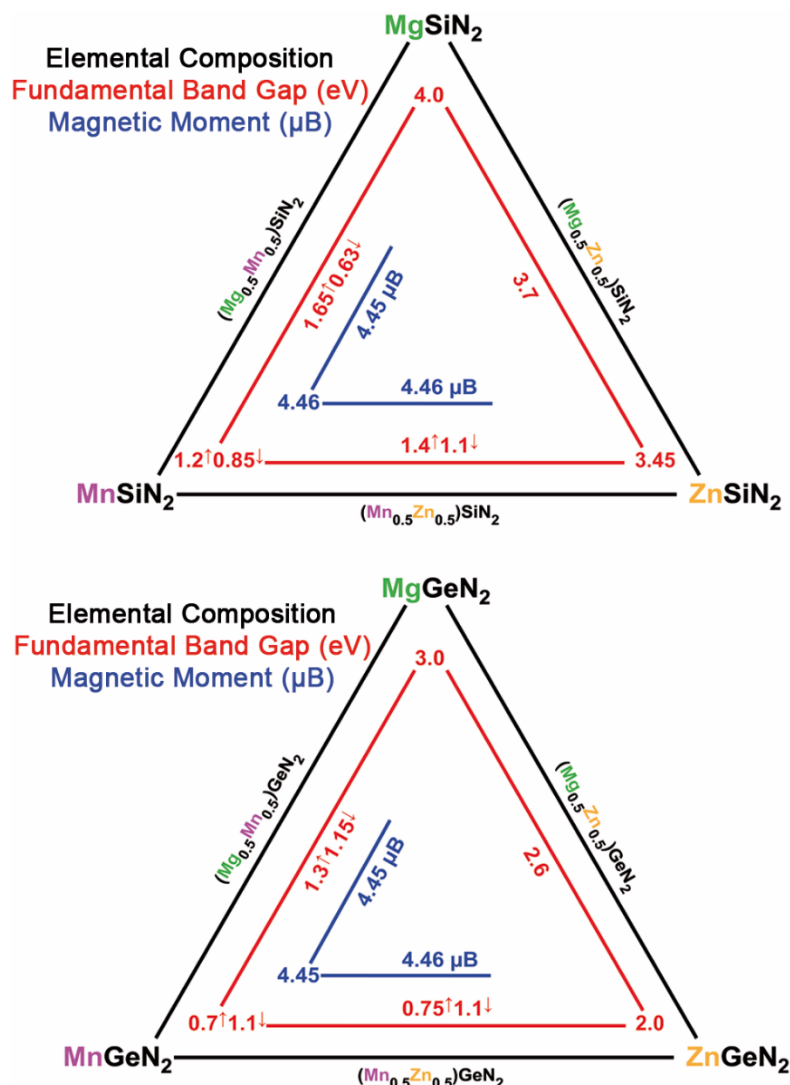


Figure 2.6. Electronic and magnetic properties as calculated by the KKR formalism with the coherent potential approximation and Engel–Vosko exchange correlation (EV-GGA) for the mixed-occupancy $(II_{0.5}IV_{0.5})-IV-N_2$ compound series. Top: Si series, bottom: Ge series. Arrows indicate direct electronic gaps for up and down spin channels.

With regard to the bandgap the ordered mBJ calculations on average further increase the bandgaps from EV-PBE by about 1 eV. Lambrecht et al. have further published a number of computationally dedicated bandgap estimates from QSGW calculations for MgSiN_2 , ZnSiN_2 , MgGeN_2 , and ZnGeN_2 . For MgSiN_2 and ZnSiN_2 indirect transitions of 5.84 and 5.44 eV are reported, whereas for MgGeN_2 and ZnGeN_2 direct transitions of 5.14 and 3.42 eV in magnitude were obtained from the QSGW calculations, respectively, while more recent calculations that explicitly correct the influence of semicore d states suggest a corrected bandgap of 4.11 eV for MgGeN_2 .^[33, 41, 42]

Although our bandgap determined for MgGeN_2 from EV-GGA appears to still underestimate E_g , it seems to be a reasonable cost-efficient correction for the exchange correlation compared to PBE while qualitatively describing the trend in bandgap progression between the $II-IV-N_2$ boundary phases correctly. Hence, we assume that the fundamental electronic bandgaps of both $(II^{a_{0.5}}II^{b_{0.5}})\text{-Si-N}_2$ and $(II^{a_{0.5}}II^{b_{0.5}})\text{-Ge-N}_2$ should be increased by approximately 1 eV, which would place them closer to the QSGW calculations.^[33, 41, 42] A summary of our bandgap determinations, along with experimental and QSGW evaluations from the literature where available, is given in Tables A.11 and A12 of the Supporting Information.

Figure 2.5 shows that the edges of the conduction bands (CBs) for the majority spin channels are characterized by a slow ascent for all $II-IV-N_2$ compounds. This is due to the limited number of states originating from a single band (conduction band minimum at the Γ point, see also Figure A.7 in the Supporting Information), which is mostly characterized by mixed N and M^{2+} states with s character. In turn this implies reduced optical transition probabilities for the optical absorption, as can be seen from calculations of the joint DOS shown in Figure 2.7. These calculations are in good agreement with the experimentally determined pseudo-absorption spectra from Kubelka–Munk theory, even in terms of analogous bandgap estimates, as shown in Table 2.2.

Whereas the experimentally determined bandgaps may be lowered due to defects during introduced synthesis and Urbach tail absorptions, the herein-estimated bandgaps from the JDOS are expected to overestimate the fundamental bandgap due to the decreased transition probability of the CB edges. This effect is, however, likely compensated by underestimations for E_g from DFT. The low-energy transitions to the CB at the Γ point seen from the JDOS may also further influence the broad absorption tails observed in the diffuse reflectance spectra. Accordingly, advanced experimental measurement techniques to determine the fundamental bandgaps with more accuracy, such as XAS-XES, may be promising for future investigations of this materials class, which are so far only available for MgSiN_2 (XANES-XES: 5.6 eV).^[31]

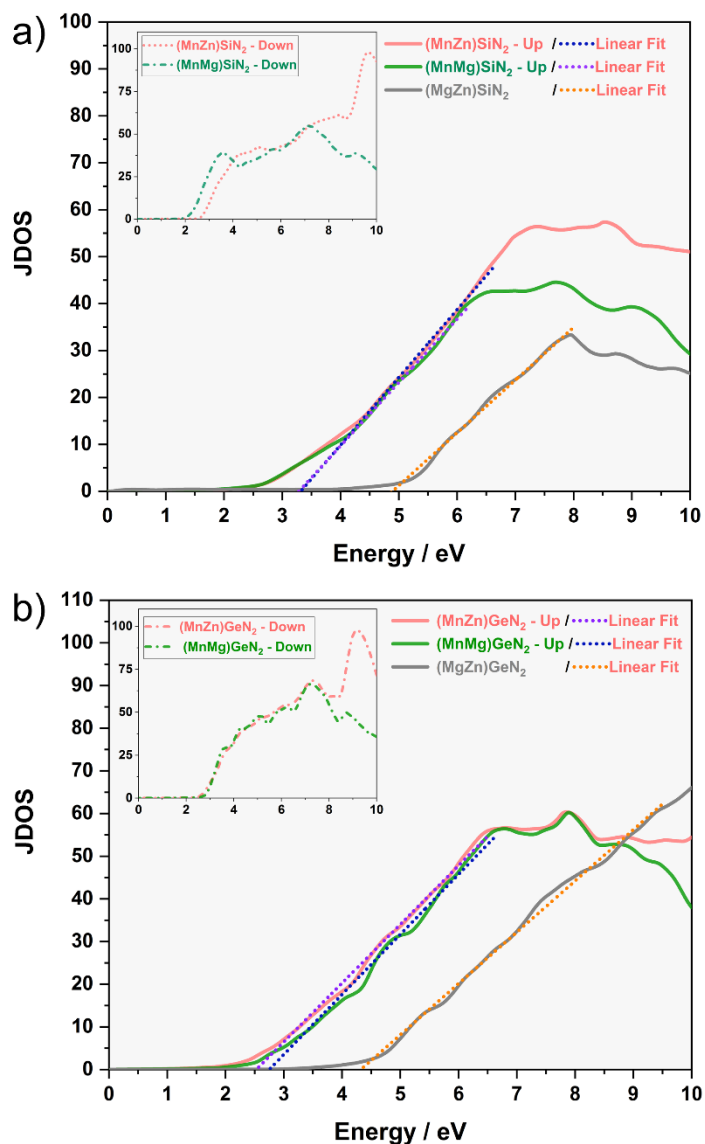


Figure 2.7. JDOS calculations for $(II^B_{0.5}/II^D_{0.5})-Si-N_2$ (a) and $(II^B_{0.5}/II^D_{0.5})-Ge-N_2$ -compounds (b) within the KKR formalism. Extrapolated linear fits (dotted lines) were used for the estimation of optical bandgaps. Inset: JDOS of spin down channels.

2.2.6 Magnetic measurements

Magnetic measurements were performed to investigate the magnetic behavior of the Mn-containing solid solutions. However, due to paramagnetic impurities, a precise statement on the magnetic properties is difficult. A corresponding discussion together with detailed information on the magnetic measurements is presented in the Supporting Information.

2.3 Conclusion

We have reported the synthesis of the solid solutions $\text{Mg}_{1-x}\text{Mn}_x\text{SiN}_2$, $\text{Mg}_{1-x}\text{Zn}_x\text{SiN}_2$, $\text{Mn}_{1-x}\text{Zn}_x\text{SiN}_2$, $\text{Mg}_{1-x}\text{Mn}_x\text{GeN}_2$, $\text{Mg}_{1-x}\text{Zn}_x\text{GeN}_2$, and $\text{Mn}_{1-x}\text{Zn}_x\text{GeN}_2$ ($x \approx 0.5$) using supercritical ammonia ($T_{\text{crit}} = 405.5$ K, $p_{\text{crit}} = 11.3$ MPa) as reaction medium and alkali metal amides as mineralizers.^[19] Special autoclaves constructed of nickel-based superalloys (Inconel 718 and Haynes 282) were used for the syntheses. All six compounds crystallize in a wurtzite-type superstructure in space group $Pna2_1$. The measured optical bandgaps range from 2.6 to 3.5 eV (Ge compounds) and 3.6 to 4.4 eV (Si compounds). Additionally, DFT calculations of ($II^{a_{0.5}}IV^{b_{0.5}}$)-*IV-N₂* (*II* = Mg, Mn, Zn; *IV* = Si, Ge) provided detailed insights into the electronic structures, electronic and optical bandgaps, and type of band transitions. The resulting values for the electronic bandgaps and the values for the optical transitions obtained by JDOS calculations are of the same order of magnitude as the measured ones and thus corroborate the validity of our approach to calculate both solid solutions and boundary phases of *II-IV-N₂* semiconductors.

Although the ammonothermal synthesis of ternary and higher (oxide) nitrides is still challenging and only a small number of synthesized compounds are known in the literature, these studies once again demonstrate the great potential of this method.^[11–15, 43–46] Furthermore, it could be shown within the scope of this work that bandgap tunability is possible in this system, paving the way for possible future applications of bandgap engineering. With regard to the semiconducting properties of *II-IV-N₂* and their potential as alternatives to commonly used group 13 nitride semiconductors, the crystal growth and further characterization of materials properties of these solid solutions, for example, electronic band structure measurements by means of XES-XAS measurements, is the next step in the exploration and contribution to a better understanding of *II-IV-N₂* compounds.

2.4 Experimental Section

The autoclaves were loaded in an Ar-filled glovebox (Unilab, MBraun, Garching, $\text{O}_2 < 1$ ppm, $\text{H}_2\text{O} < 1$ ppm) to prevent contamination with oxygen or moisture. Ammonia was condensed into the autoclaves by using a vacuum line (≤ 0.1 Pa) with argon and ammonia (both: Air Liquide, 99.999%) supply. Gas-purification cartridges (Micro torr FT400-902 (for Ar) and MC400-702FV (for NH_3), SAES Pure Gas Inc., San Luis Obispo, CA, USA) were used for further purification, providing a purity level of < 1 ppbV H_2O , O_2 , and CO_2 .

2.4.1 Ammonothermal synthesis of $\text{Mg}_{1-x}\text{Mn}_x\text{GeN}_2$, $\text{Mg}_{1-x}\text{Zn}_x\text{GeN}_2$, and $\text{Mn}_{1-x}\text{Zn}_x\text{GeN}_2$

$\text{Mg}_{1-x}\text{Mn}_x\text{GeN}_2$, $\text{Mg}_{1-x}\text{Zn}_x\text{GeN}_2$, and $\text{Mn}_{1-x}\text{Zn}_x\text{GeN}_2$ ($x \approx 0.5$) as well as $\text{Mg}_{1-x}\text{Zn}_x\text{GeN}_2$ ($x \approx 0.8$) were synthesized under ammonothermal conditions starting from the corresponding metals [Mg (1.5 mmol, 36.5 mg, Alfa Aesar, 99.8 %), Mn (1.5 mmol, 82.4 mg, Alfa Aesar, 99.95 %), and Zn (1.5 mmol, 98.1 mg, Alfa Aesar, 99.9 %)], Ge (3 mmol, 217.9 mg, smart-elements, 99.99 %), and NaN_3 (7.5 mmol, 487.5 mg, Sigma-Aldrich, 99.5 %) as mineralizer for $x \approx 0.5$ and Mg (0.75 mmol, 18.2 mg, Alfa Aesar, 99.8 %), Zn (2.25 mmol, 147.2 mg, Alfa Aesar, 99.9 %), Ge (3 mmol, 217.9 mg, smart-elements, 99.99 %), and NaN_3 (7.5 mmol, 487.5 mg, Sigma-Aldrich, 99.5 %) for $x \approx 0.8$. The starting materials were mixed and transferred to a Ta liner, to protect the mixture against contamination by the autoclave material. The liners were closed by means of a Ta lid with a small hole. Afterwards, the liner was placed in the autoclave (Inconel 718, max. 900 K, 300 MPa, 10 mL), which was sealed with a lid by means of flange joints with a sealing gasket (silver-coated Inconel 718 ring, GFD seals). The autoclave body is connected via an Inconel 718 high-pressure tube to the upper part, consisting of a hand valve (SITEC), a pressure transmitter (HBM P2VA1/5000 bar), and a bursting disk (SITEC). After closing under argon, the autoclave was evacuated and cooled with an ethanol/liquid nitrogen mixture to 198 K. Subsequently, ammonia (≈ 7 mL) was directly condensed into the autoclave via a pressure regulating valve. The amount of NH_3 was determined by means of a mass flow meter (D-6320-DR, Bronkhorst, Ruurlo, Netherlands). The autoclave was heated to 670 K within 2 h, held at this temperature for 16 h, heated to 870 K within 2 h, and kept at this temperature for 96 h, reaching pressures around 200 MPa. After cooling, residual ammonia was removed and the products were separated in air, washed with EtOH and acetic acid, and dried at 350 K. $\text{Mg}_{1-x}\text{Mn}_x\text{GeN}_2$, $\text{Mg}_{1-x}\text{Zn}_x\text{GeN}_2$ and $\text{Mn}_{1-x}\text{Zn}_x\text{GeN}_2$ ($x \approx 0.5$) were obtained as light brown, beige, and ocher powders, respectively.

2.4.2 Ammonothermal synthesis of $\text{Mg}_{1-x}\text{Mn}_x\text{SiN}_2$, $\text{Mg}_{1-x}\text{Zn}_x\text{SiN}_2$, and $\text{Mn}_{1-x}\text{Zn}_x\text{SiN}_2$

The ammonothermal method was used for synthesis of the solid solutions $\text{Mg}_{1-x}\text{Mn}_x\text{SiN}_2$, $\text{Mg}_{1-x}\text{Zn}_x\text{SiN}_2$, and $\text{Mn}_{1-x}\text{Zn}_x\text{SiN}_2$ ($x \approx 0.5$). The corresponding metals [Mg (1.5 mmol, 36.5 mg, Alfa Aesar, 99.8 %), Mn (1.5 mmol, 82.4 mg, Alfa Aesar, 99.95 %), and Zn (1.5 mmol, 98.1 mg, Alfa Aesar, 99.9 %)], Si (3 mmol, 84.3 mg, Alfa Aesar, 99.9 %), and KN_3 (7.5 mmol, 608.4 mg, Sigma-Aldrich, 99.9 %) as mineralizer were used as starting materials. Si was ball-milled under argon for 10 h in a planetary ball mill (Retsch PM 400) to support reaction in supercritical ammonia. The reactants were mixed and placed in a Ta liner. The liner was closed by means of a Ta lid with a small hole. Subsequently, the liner was transferred into the autoclave (Haynes 282, max. 1100 K, 170 MPa,

10 mL), which was closed under argon. The autoclave setup was similar to that described above. After evacuating and cooling the reactor to 198 K, NH₃ (\approx 4.5 mL) was condensed into the autoclave. The amount of NH₃ was determined by means of a mass flow meter (D-6320-DR, Bronkhorst, Ruurlo, Netherlands). The autoclave was heated to 670 K over 2 h, held for at that temperature for 16 h, heated to 1070 K within 3 h, and kept at this temperature for 96 h, resulting in maximum pressures of up to 150 MPa. After cooling to room temperature and removing residual ammonia, the samples were extracted from the liners and washed with ethanol and acetic acid. Mg_{1-x}Mn_xSiN₂ ($x \approx$ 0.5) was obtained as a white powder, and Mg_{1-x}Zn_xSiN₂ and Mn_{1-x}Zn_xSiN₂ ($x \approx$ 0.5) were obtained as brown powders.

2.4.3 Digital microscopy

Optical micrographs of the obtained powders were recorded with a digital microscope (VHX-5000, Keyence) under white-light illumination. All images were collected with a magnification of 200.

2.4.4 Powder XRD

The products were ground and filled in glass capillaries (0.3 mm diameter, 0.01 mm wall thickness, Hilgenberg GmbH). The data were collected with a Stoe STADI P diffractometer with Cu-K _{α} 1 radiation ($\lambda = 1.5406 \text{ \AA}$), Ge(111) monochromator, and Mythen 1K detector in Debye–Scherrer geometry. TOPAS was used for Rietveld refinement.^[47]

CCDC 1903084, 1903085, 1903088, 1903087, 1903086, 1903089 (Mg_{0.375}Mn_{0.625}GeN₂, Mg_{0.455}Zn_{0.545}GeN₂, Mn_{0.55}Zn_{0.45}GeN₂, Mg_{0.457}Mn_{0.543}SiN₂, Mg_{0.515}Zn_{0.485}SiN₂, Mn_{0.47}Zn_{0.53}SiN₂) contain the supplementary crystallographic data for this paper. These data are provided free of charge by The Cambridge Crystallographic Data Centre.

2.4.5 Scanning electron microscopy

A Dualbeam Helios Nanolab G3 UC (FEI) scanning electron microscope, equipped with an EDX detector (X-Max 80 SDD, Oxford instruments), was used for determination of crystal morphology and chemical composition. The samples were placed on an adhesive carbon pad and coated with a conductive carbon film by using a high-vacuum sputter coater (BAL-TEC MED 020, Bal Tec A).

2.4.6 UV/Vis spectroscopy

For determination of the optical bandgaps, diffuse reflectance measurements on samples at room temperature were performed with a Jasco V-650 UV/Vis spectrophotometer equipped with Czerny-Turner mount, photomultiplier tube detector, and deuterium (190–350 nm)/halogen (330–900 nm) lamps as light sources.

2.4.7 Computational details

Initial structural relaxations for the ordered models for all $(II^a_{0.5}II^b_{0.5})-IV-N_2$ compounds were performed by means of the VASP program package with the implemented projector augmented wave (PAW) method.^[48–52] The generalized gradient approximation (GGA) functional of Perdew, Burke, and Ernzerhof (PBE) was used to model the exchange correlation.^[53, 54] A plane-wave cutoff energy of 535 eV was used for all calculations together with Brillouin zone sampling on dense gamma-centered Monkhorst–Pack meshes of $10 \times 8 \times 10$. Electronic and structural convergence criteria of 10^{-8} and 10^{-7} eV were set in order to ensure precision of total energies. For the respective ordering models the exchange-correlation was further corrected with the modified Becke–Johnson formalism (mBJ-GGA) to estimate the bandgaps more accurately.^[40, 55, 56] Subsequently, to accurately estimate the electronic properties of the experimental solid solution the relaxed structures were averaged, symmetrized, and converted with the CIF2Cell program^[57] to formats compatible with the Munich SPRKKR program package.^[58, 59] The electronic structure was further converged to values of 10^{-5} eV utilizing the implemented fully relativistic Korringa–Kohn–Rostoker (KKR) Green's function method with the PBE functional.^[53, 54] Owing to the currently missing implementation of the mBJ-GGA potential the EV-GGA (Engel Vosko) formalism was used to obtain more reliable bandgaps by calculating the respective Bloch spectral functions and DOS.^[60] The chemical disorder was treated by the coherent potential approximation (CPA) self consistently and fully relativistic within the four-component Dirac formalism. For all calculations an angular momentum expansion of $l = 3$ was used.

2.5 Acknowledgements

The project was funded by the Deutsche Forschungsgemeinschaft (DFG, German Research Foundation) under Germany's Excellence Strategy—EXC 2089/1-390776260 and within the research group “Chemistry and Technology of the Ammonothermal Synthesis of Nitrides” (FOR 1600), project SCHN377/16-2, by the European Regional Development Fund (ERDF), project CEDAMNF, reg. no. CZ.02.1.01/0.0/0.0/15_003/0000358 and the Czech Science Foundation (GACR), Proj. 17-14840S. The authors gratefully acknowledge the group of Prof. Dr. E. Schlücker

(Anna Kimmel and Thomas Steigerwald) for fabrication and maintenance of the autoclaves (FAU Erlangen-Nürnberg). In addition, we want to thank Lisa Gamperl for SEM/EDX measurements and Dr. C. Hoch for digital microscopy pictures (both at Department of Chemistry, LMU Munich).

2.6 References

- [1] S. P. DenBaars, D. Feezell, K. Kelchner, S. Pimputkar, C.-C. Pan, C.-C. Yen, S. Tanaka, Y. Zhao, N. Pfaff, R. Farrell, M. Iza, S. Keller, U. Mishra, J. S. Speck, S. Nakamura, "Development of gallium-nitride-based light-emitting diodes (LEDs) and laser diodes for energy-efficient lighting and displays", *Acta Mater.* **2013**, *61*, 945-951.
- [2] K. Shinohara, D. C. Regan, Y. Tang, A. L. Corrión, D. F. Brown, J. C. Wong, J. F. Robinson, H. H. Fung, A. Schmitz, T. C. Oh, S. J. Kim, P. S. Chen, R. G. Nagele, A. D. Margomenos, M. Micovic, "Scaling of GaN HEMTs and Schottky Diodes for Submillimeter-Wave MMIC Applications", *IEEE Trans. Electron Devices* **2013**, *60*, 2982-2996.
- [3] J. Wu, W. Walukiewicz, "Band gaps of InN and group III nitride alloys", *Superlattices Microstruct.* **2003**, *34*, 63-75.
- [4] Y. Hinuma, T. Hatakeyama, Y. Kumagai, L. A. Burton, H. Sato, Y. Muraba, S. Iimura, H. Hiramatsu, I. Tanaka, H. Hosono, F. Oba, "Discovery of earth-abundant nitride semiconductors by computational screening and high-pressure synthesis", *Nat. Commun.* **2016**, *7*, 11962.
- [5] P. C. Quayle, K. He, J. Shan, K. Kash, "Synthesis, lattice structure, and band gap of ZnSnN₂", *MRS Commun.* **2013**, *3*, 135-138.
- [6] A. D. Martinez, A. N. Fioretti, E. S. Toberer, A. C. Tamboli, "Synthesis, structure, and optoelectronic properties of II-IV-V₂ materials", *J. Mater. Chem.* **2017**, *5*, 11418-11435.
- [7] P. Narang, S. Chen, N. C. Coronel, S. Gul, J. Yano, L. W. Wang, N. S. Lewis, H. A. Atwater, "Bandgap Tunability in Zn(Sn,Ge)N₂ Semiconductor Alloys", *Adv. Mater.* **2014**, *26*, 1235-1241.
- [8] S. Esmailzadeh, U. Hålenius, M. Valldor, "Crystal Growth, Magnetic, and Optical Properties of the Ternary Nitride MnSiN₂", *Chem. Mater.* **2006**, *18*, 2713-2718.
- [9] C. J. Duan, A. C. A. Delsing, H. T. Hintzen, "Red emission from Mn²⁺ on a tetrahedral site in MgSiN₂", *J. Lumin.* **2009**, *129*, 645-649.
- [10] M. Råsaender, J. B. Quirk, T. Wang, S. Mathew, R. Davies, R. G. Palgrave, M. A. Moram, "Structure and lattice dynamics of the wide band gap semiconductors MgSiN₂ and MgGeN₂", *J. Appl. Phys.* **2017**, *122*, 085705.

- [11] J. Häusler, S. Schimmel, P. Wellmann, W. Schnick, "Ammonothermal Synthesis of Earth Abundant Nitride Semiconductors ZnSiN₂ and ZnGeN₂ and Dissolution Monitoring by In Situ X-ray Imaging", *Chem. Eur. J.* **2017**, *23*, 12275-12282.
- [12] J. Häusler, R. Niklaus, J. Minár, W. Schnick, "Ammonothermal Synthesis and Optical Properties of Ternary Nitride Semiconductors Mg-IV-N₂, Mn-IV-N₂ and Li-IV₂-N₃ (IV = Si, Ge)", *Chem. Eur. J.* **2018**, *24*, 1686-1693.
- [13] M. Mallmann, C. Maak, R. Niklaus, W. Schnick, "Ammonothermal Synthesis, Optical Properties, and DFT Calculations of Mg₂PN₃ and Zn₂PN₃", *Chem. Eur. J.* **2018**, *24*, 13963-13970.
- [14] J. Häusler, L. Neudert, M. Mallmann, R. Niklaus, A.-C. L. Kimmel, N. S. A. Alt, E. Schlücker, O. Oeckler, W. Schnick, "Ammonothermal Synthesis of Novel Nitrides: Case Study on CaGaSiN₃", *Chem. Eur. J.* **2017**, *23*, 2583-2590.
- [15] J. Häusler, L. Eisenburger, O. Oeckler, W. Schnick, "Ammonothermal Synthesis and Crystal Structure of the Nitridoalumogermanate Ca_{1-x}Li_xAl_{1-x}Ge_{1+x}N₃ (x ≈ 0.2)", *Eur. J. Inorg. Chem.* **2018**, 759-764.
- [16] J. Hertrampf, P. Becker, M. Widenmeyer, A. Weidenkaff, E. Schlücker, R. Niewa, "Ammonothermal Crystal Growth of Indium Nitride", *Cryst. Growth Des.* **2018**, *18*, 2365-2369.
- [17] R. Niklaus, J. Minár, J. Häusler, W. Schnick, "First-principles and experimental characterization of the electronic properties of CaGaSiN₃ and CaAlSiN₃: the impact of chemical disorder", *Phys. Chem. Chem. Phys.* **2017**, *19*, 9292-9299.
- [18] J. Häusler, W. Schnick, "Ammonothermal Synthesis of Nitrides: Recent Developments and Future Perspectives", *Chem. Eur. J.* **2018**, *24*, 11864-11879.
- [19] T. Richter, R. Niewa, "Chemistry of Ammonothermal Synthesis", *Inorganics* **2014**, *2*, 29-78.
- [20] The term *sechser* ring was coined by Liebau and is derived from the German word "sechser"; a *sechser* ring comprises six tetrahedra centers.
- [21] E. W. Blanton, K. He, J. Shan, K. Kash, "Characterization and control of ZnGeN₂ cation lattice ordering", *J. Cryst. Growth* **2017**, *461*, 38-45.
- [22] A. R. Denton, N. W. Ashcroft, "Vegard's law", *Phys. Rev. A* **1991**, *43*, 3161-3164.
- [23] Y. Tanabe, S. Sugano, "On the Absorption Spectra of Complex Ions. I", *J. Phys. Soc. Jpn.* **1954**, *9*, 753-766.
- [24] R. López, R. Gómez, "Band-gap energy estimation from diffuse reflectance measurements on sol-gel and commercial TiO₂: a comparative study", *J. Sol-Gel Sci. Technol.* **2012**, *61*, 1-7.
- [25] J. Tauc, R. Grigorovici, A. Vancu, "Optical Properties and Electronic Structure of Amorphous Germanium", *Phys. Status Solidi B* **1966**, *15*, 627-637.

- [26] C. M. Fang, R. A. d. Groot, R. J. Bruls, H. T. Hintzen, G. d. With, "Ab initio band structure calculations of Mg₃N₂ and MgSiN₂", *J. Phys.: Condens. Matter* **1999**, *11*, 4833-4842.
- [27] T. Endo, Y. Sato, H. Takizawa, M. Shimada, "High-pressure synthesis of new compounds, ZnSiN₂ and ZnGeN₂ with distorted wurtzite structure", *J. Mater. Sci. Lett.* **1992**, *11*, 424-426.
- [28] W. L. Larson, H. P. Maruska, D. A. Stevenson, "Synthesis and Properties of ZnGeN₂", *J. Electrochem. Soc.* **1974**, *121*, 1673-1674.
- [29] T. Misaki, A. Wakahara, H. Okada, A. Yoshida, "Optical properties of ZnGeN₂ epitaxial layer", *Phys. Status Solidi C* **2003**, *0*, 2890-2893.
- [30] M. Shang, J. Wang, J. Fan, H. Lian, Y. Zhang, J. Lin, "ZnGeN₂ and ZnGeN₂:Mn²⁺ phosphors: hydrothermal-ammonolysis synthesis, structure and luminescence properties", *J. Mater. Chem. C* **2015**, *3*, 9306-9317.
- [31] T. de Boer, T. D. Boyko, C. Braun, W. Schnick, A. Moewes, "Band gap and electronic structure of MgSiN₂ determined using soft X-ray spectroscopy and density functional theory", *Phys. Status Solidi RRL* **2015**, *9*, 250-254.
- [32] E. F. Schubert, *Light-Emitting Diodes*, Cambridge University Press 2006.
- [33] S. Lyu, W. R. L. Lambrecht, "Quasiparticle self-consistent GW band structures of Mg-IV-N₂ compounds: The role of semicore d states", *Solid State Commun.* **2019**, 113664.
- [34] M. Bilal, I. Ahmad, H. A. Rahnamaye Aliabad, S. J. Asadabadi, "Detailed DFT studies of the band profiles and optical properties of antiperovskites SbNCa₃ and BiNCa₃", *Comput. Mater. Sci.* **2014**, *85*, 310-315.
- [35] R. Ali, S. Mohammad, H. Ullah, S. A. Khan, H. Uddin, M. Khan, N. U. Khan, "The structural, electronic and optical response of IIA–VIA compounds through the modified Becke–Johnson potential", *Physica B* **2013**, *410*, 93-98.
- [36] A. Reshak, "First Principle Calculations of Transition Metal Oxide, AgAlO₂, as Active Photocatalyst: Sustainable Alternative Sources of Energy", *Int. J. Electrochem. Sci.* **2013**, *8*, 9371-9383.
- [37] R. Ahmed, S. J. Hashemifar, H. Akbarzadeh, M. Ahmed, Fazal-e-Aleem, "Ab initio study of structural and electronic properties of III-arsenide binary compounds", *Comput. Mater. Sci.* **2007**, *39*, 580-586.
- [38] R. Ahmed, H. Akbarzadeh, Fazal-e-Aleem, "A first principle study of band structure of III-nitride compounds", *Physica B* **2005**, *370*, 52-60.
- [39] M. I. Ziane, Z. Bensaad, T. Ouahrani, B. Labdelli, H. B. Nacer, H. Abid, "First-principles prediction of the structural and electronic properties of zinc blende GaN_xAs_{1-x} alloys", *Mater. Sci. Semicond. Process.* **2013**, *16*, 1138-1147.
- [40] J. A. Camargo-Martínez, R. Baquero, "Performance of the modified Becke-Johnson potential for semiconductors", *Phys. Rev. B* **2012**, *86*, 195106.

- [41] A. Punya, W. R. L. Lambrecht, M. van Schilfgaarde, "Quasiparticle band structure of Zn-IV-N₂ compounds", *Phys. Rev. B* **2011**, *84*, 165204.
- [42] A. P. Jaroenjittichai, W. R. L. Lambrecht, "Electronic band structure of Mg-IV-N₂ compounds in the quasiparticle-self-consistent GW approximation", *Phys. Rev. B* **2016**, *94*, 125201.
- [43] N. Cordes, W. Schnick, "Ammonothermal Synthesis of Crystalline Oxonitride Perovskites LnTaON₂ (Ln = La, Ce, Pr, Nd, Sm, Gd)", *Chem. Eur. J.* **2017**, *23*, 11410-11415.
- [44] J. Li, T. Watanabe, H. Wada, T. Setoyama, M. Yoshimura, "Low-Temperature Crystallization of Eu-Doped Red-Emitting CaAlSiN₃ from Alloy-Derived Ammonometallates", *Chem. Mater.* **2007**, *19*, 3592-3594.
- [45] T. Watanabe, K. Nonaka, J. Li, K. Kishida, M. Yoshimura, "Low temperature ammonothermal synthesis of europium-doped SrAlSiN₃ for a nitride red phosphor", *J. Ceram. Soc. Jpn.* **2012**, *120*, 500-502.
- [46] T. Toshima, K. Kishida, Y. Maruyama, T. Watanabe, "Low-temperature synthesis of BaTaO₂N by an ammonothermal method", *J. Ceram. Soc. Jpn.* **2017**, *125*, 643-647.
- [47] A. Coelho, *TOPAS Academic, Version 6*, Coelho Software, Brisbane (Australia), **2016**.
- [48] G. Kresse, J. Hafner, "Ab initio molecular dynamics for liquid metals", *Phys. Rev. B* **1993**, *47*, 558-561.
- [49] G. Kresse, J. Hafner, "Ab initio molecular-dynamics simulation of the liquid-metal-amorphous-semiconductor transition in germanium", *Phys. Rev. B* **1994**, *49*, 14251-14269.
- [50] G. Kresse, J. Furthmüller, "Efficiency of ab-initio total energy calculations for metals and semiconductors using a plane-wave basis set", *Comput. Mater. Sci.* **1996**, *6*, 15-50.
- [51] G. Kresse, D. Joubert, "From ultrasoft pseudopotentials to the projector augmented-wave method", *Phys. Rev. B* **1999**, *59*, 1758-1775.
- [52] P. E. Blöchl, "Projector augmented-wave method", *Phys. Rev. B* **1994**, *50*, 17953-17979.
- [53] J. P. Perdew, K. Burke, M. Ernzerhof, "Generalized Gradient Approximation Made Simple", *Phys. Rev. Lett.* **1996**, *77*, 3865-3868.
- [54] J. P. Perdew, K. Burke, M. Ernzerhof, "Generalized Gradient Approximation Made Simple", *Phys. Rev. Lett.* **1997**, *78*, 1396-1396.
- [55] A. D. Becke, E. R. Johnson, "A simple effective potential for exchange", *J. Chem. Phys.* **2006**, *124*, 221101.
- [56] F. Tran, P. Blaha, "Accurate Band Gaps of Semiconductors and Insulators with a Semilocal Exchange-Correlation Potential", *Phys. Rev. Lett.* **2009**, *102*, 226401.
- [57] T. Björkman, "CIF2Cell: Generating geometries for electronic structure programs", *Comput. Phys. Commun.* **2011**, *182*, 1183-1186.
- [58] H. Ebert et al., The Munich SPR-KKR Package, Version 7.7, <http://olymp.cup.uni-muenchen.de/ak/ebert/SPRKKR>, 2012.

- [59] H. Ebert, D. Ködderitzsch, J. Minár, "*Calculating condensed matter properties using the KKR-Green's function method—recent developments and applications*", *Rep. Prog. Phys.* **2011**, 74, 096501.
- [60] E. Engel, S. H. Vosko, "*Exact exchange-only potentials and the virial relation as microscopic criteria for generalized gradient approximations*", *Phys. Rev. B* **1993**, 47, 13164-13174.

3 Ammonothermal Synthesis, Optical Properties and DFT Calculations of Mg_2PN_3 and Zn_2PN_3

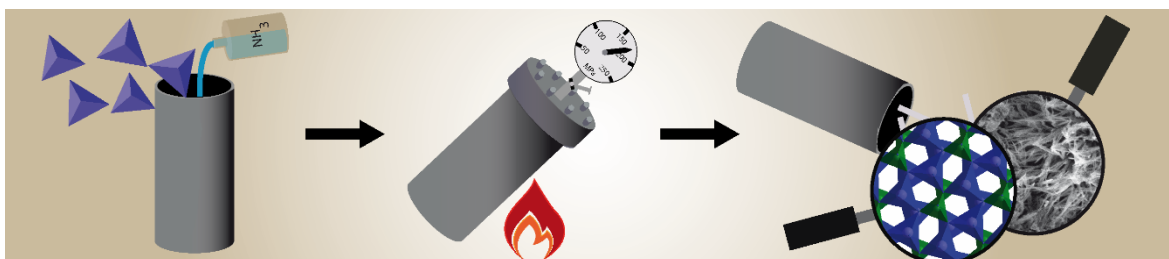
published in: *Chem. Eur. J.* **2018**, *24*, 13963 - 13970.

authors: Mathias Mallmann, Christian Maak, Robin Niklaus, and Wolfgang Schnick

DOI: 10.1002/chem.201803293

Reprinted (adapted) with permission from *Chemistry – A European Journal*.

Copyright 2018 John Wiley and Sons.



Abstract. The phosphorus nitrides, Mg_2PN_3 and Zn_2PN_3 , are wide bandgap semiconductor materials with potential for application in (opto)electronics or photovoltaics. For the first time, both compounds were synthesized ammonothermally in custom-built high-temperature, high-pressure autoclaves starting from P_3N_5 and the corresponding metals (Mg or Zn). Alkali amides (NaNH_2 , KNH_2) were employed as ammonobasic mineralizers to increase solubility of the starting materials in supercritical ammonia through formation of reactive intermediates. Single crystals of Mg_2PN_3 , with length up to $30\ \mu\text{m}$, were synthesized at 1070 K and 140 MPa. Zn_2PN_3 already decomposes at these conditions and was obtained as submicron-sized crystallites at 800 K and 200 MPa. Both compounds crystallize in a wurtzite-type superstructure in orthorhombic space group $Cmc2_1$, which was confirmed by powder X-ray diffraction. In addition, single-crystal X-ray diffraction measurements of Mg_2PN_3 were carried out for the first time. To our knowledge, this is the first single-crystal X-ray study of ternary nitrides synthesized by the ammonothermal method. The bandgaps of both nitrides were estimated to be 5.0 eV for Mg_2PN_3 and 3.8 eV for Zn_2PN_3 by diffuse reflectance spectroscopy. DFT calculations were carried out to verify the experimental values. Furthermore, a dissolution experiment was conducted to obtain insights into the crystallization behavior of Mg_2PN_3 .

3.1 Introduction

Optoelectronic semiconductors in the system Al/Ga/In/N are important materials for different application fields in electronic technologies (e.g., light emitting diodes or field effective transistors).^[1, 2] However, a drawback of these compounds is the low elemental abundance of Ga and In. Therefore, the quest for new semiconducting compounds with properties comparable to group 13 nitrides is an important task of modern materials research. Recently, first principle calculations showed that various ternary zinc nitrides exhibit electronic and optical properties, as well as stability and dopability comparable to GaN.^[3] The significant advantage of these nitrides is their composition containing earth-abundant elements like Zn, Si, P, and N. In particular, Grimm–Sommerfeld analogous Zn-IV-N₂ compounds, with IV = Si, Ge, and Sn, represent promising new semiconductor materials.^[4–6] Zn_2PN_3 was also predicted to be a semiconductor with a bandgap around 4 eV. However, until now there are no experimental data of the optical bandgap or other semiconductor properties of Zn_2PN_3 .^[3]

The main problem of these compounds is their challenging bulk synthesis. For example, bulk $ZnSnN_2$ could so far only be synthesized by high-pressure synthesis at pressures above 5.5 GPa in microcrystalline form.^[7] However, applications in semiconductor technologies require synthesis of single crystals with acceptable sizes and high quality. In particular, the ammonothermal process has been identified as a suitable method for both synthesis and crystal growth of binary nitrides like high-quality GaN.^[8] Quite recently, Niewa and co-workers succeeded in preparation of InN single crystals with well-developed crystal faces by employing the ammonothermal method.^[9] In addition, it was possible to obtain crystals of $ZnSiN_2$ and $ZnGeN_2$ in the μm range with this method.^[10] Furthermore, the ammonothermal method was used for synthesis of other nitrides, oxonitrides, and other compounds with crystallites in the μm range.^[11–13] Accordingly, the ammonothermal method could be applicable for synthesis and crystal growth of other nitrides, like phosphorus nitrides and nitridophosphates, where single crystals are often hard to access.^[14]

A major challenge regarding the synthesis of phosphorus nitrides and nitridophosphates is the limited thermal stability and the low decomposition temperature of P_3N_5 (1070 K). Consequently, only a few phosphorus nitrides, for example, Ca_2PN_3 or $Li_{10}P_4N_{10}$, were synthesized at ambient pressure.^[15–17] To prevent decomposition of P_3N_5 , high-pressure synthesis techniques in the 10–20 GPa range, such as the multi-anvil approach, have been used. Thereby, numerous P-N-compounds like SrP_2N_4 or $LiNdP_4N_8$ became accessible.^[18, 19] With the synthesis of $K_3P_6N_{11}$ and HPN_2 in 1997, Jacobs and Nymwegen demonstrated that the ammonothermal method can also be used for the synthesis of nitridophosphates.^[20, 21] So far, these are the only known nitridophosphates synthesized under ammonothermal conditions.

Herein, we report on the synthesis of Zn_2PN_3 , as well as the synthesis and crystal growth of Mg_2PN_3 , in supercritical ammonia at moderate temperatures and pressures. Initially, Mg_2PN_3 was synthesized at 1070 K in nitrogen atmosphere at standard pressure, whereas Zn_2PN_3 could only be obtained under high-pressure conditions (1470 K and 8 GPa) starting from the binary nitrides.^[22, 23] The products were analyzed by powder X-ray diffraction (PXRD) and single-crystal X-ray diffraction in the case of Mg_2PN_3 . The optical bandgaps of both compounds were determined by diffuse reflectance spectroscopy. DFT calculations, with the modified Becke–Johnson formalism (GGA-mbj), were conducted to determine the band structures of both materials. Furthermore, the dissolution behavior of Mg_2PN_3 was investigated in supercritical ammonia at 670 K with NaN_3 as mineralizer. Our results demonstrate that the ammonothermal method is a promising alternative for the synthesis of P-N compounds. Furthermore, the determined bandgaps and the observed crystal quality make these ammonothermally synthesized nitridophosphates auspicious candidates for application in optoelectronics or photovoltaics.

3.2 Results and Discussion

3.2.1 Synthesis

Colorless transparent single crystals of Mg_2PN_3 , as well as submicron-sized crystallites of Zn_2PN_3 , were synthesized ammonothermally, using custom-built high-temperature, high-pressure autoclaves. The pure metals (Mg and Zn), P_3N_5 , and alkali metal azides (NaN_3 for Mg_2PN_3 , KN_3 for Zn_2PN_3) were used as starting materials. The azides react in supercritical ammonia in situ to the corresponding amides ANH_2 ($A = \text{Na}, \text{K}$), which act as ammonobasic mineralizers.^[11] The azides were used because of their high purity and their chemical stability in air, compared to the alkali metals or amides. After formation of the amides, the latter react with the other starting materials, increasing their solubility by forming intermediates like $\text{K}_2[\text{Zn}(\text{NH}_2)_4]$.^[24] In contrast to alkaline earth or transition metals which form amides, there are only very few investigations in the literature concerning the behavior of phosphorus nitrides or nitridophosphates under ammonothermal conditions. At much lower pressure (ca. 3 MPa), polymeric phosphorus nitride imide HPN_2 is formed by ammonolysis of P_3N_5 .^[25] Under supercritical conditions soluble intermediates like hexaaminocyclotriphosphazene $(\text{PN}(\text{NH}_2)_2)_3$ ^[26] or $\text{Na}_{10}[\text{P}_4(\text{NH})_6\text{N}_4](\text{NH}_2)_6(\text{NH}_3)_{0.5}$ ^[27] could be formed. The latter compound was already synthesized in supercritical ammonia.^[27] After the reaction, remaining amides or side phases were washed out with ethanol or 1 M HCl (see Experimental section), resulting in phase-pure products. Mg_2PN_3 was synthesized at 1070 K and an autogenous pressure of 140 MPa. Under these conditions, colorless single crystals of Mg_2PN_3 were obtained for the first time, with sizes up to

30 μm . It is noteworthy that these are the first crystals of ternary or higher nitrides suitable for single-crystal X-ray diffraction experiments that have been obtained by the ammonothermal method. Single-crystal formation was only observed at temperatures of 1070 K, whereas reactions at 870 K only yielded microcrystalline products. Furthermore, the selection of the liner material was essential to obtain phase-pure samples. While the reaction with molybdenum liner resulted in phase-pure products after washing, the reaction in tantalum and niobium liners promoted the formation of Ta or Nb containing side phases (e.g., $\text{Mg}_{2.6-x}\text{Ta}_{1.3+x}\text{N}_4$)^[28] at reaction temperatures of 1070 K. This observation can be explained by the inertness of Mo in supercritical ammonia, and the reaction of Ta and Nb with hydrogen, which is formed in situ due to decomposition of ammonia.^[29, 30] The shape and size of the obtained crystals suggest a solution growth mechanism. To underline this assumption, a dissolution experiment was conducted (see Dissolution experiment section). In contrast, submicron-sized Zn_2PN_3 could only be synthesized at temperatures between 800 and 870 K and pressures up to 200 MPa. A second temperature step at 630 K was added, since the mentioned intermediates are primarily formed at lower temperatures. At higher temperatures and with NaN_3 as mineralizer, the product decomposes to Zn and NaN_3P ,^[31] which is the first known phosphide obtained by ammonothermal synthesis. This temperature limitation results in a relatively low crystallinity of the product, as higher temperatures are probably needed to improve crystal growth. To overcome decomposition at higher temperatures, higher pressures seem to be required, which cannot be achieved with the current setup. This assumption is supported by the fact that previously, Zn_2PN_3 was only synthesized under high-pressure conditions (8 GPa).^[23] However, crystal growth can occur in particular areas of the autoclave and very thin filaments are accessible at the selected reaction conditions (see Scanning electron microscopy section).

Besides $\text{K}_3\text{P}_6\text{N}_{11}$,^[20] Mg_2PN_3 and Zn_2PN_3 represent the first nitridophosphates which have been synthesized in supercritical ammonia. Nitridophosphates with a low degree of condensation (i.e., the atomic ratio $\text{P} : \text{N} < 0.5$) have been typically synthesized in thick-walled silica ampoules and pressures up to 3 MPa. In contrast, synthesis of highly condensed nitridophosphates ($\text{P} : \text{N} > 0.5$) usually requires high-pressure conditions (several GPa) which can be provided by the multi-anvil technique.^[32] High nitrogen pressure prevents the thermal decomposition of P_3N_5 , and therefore has a decisive influence on the synthesis of nitridophosphates. With the ammonothermal approach, a powerful synthetic tool can be used for synthesis of nitridophosphates, which offers significant advantages in crystal growth and scalability compared to high-pressure methods employing the multi-anvil technique.

3.2.2 Crystal structure

The crystal structure of Mg_2PN_3 was solved and refined from single-crystal X-ray diffraction data in the orthorhombic space group $Cmc2_1$ (no. 36). Structure determination details, as well as crystallographic data, are summarized in Table 3.1. Mg and P atom positions were refined anisotropically. Atomic coordinates and anisotropic displacement parameters are given in Table B.1 and B.2 in the Supporting Information. Interatomic distances are summarized in Table B.3. The crystal structure can be derived from the wurtzite structure type (*translationengleiche* subgroup of $P6_3mc$) by ordering of the tetrahedrally coordinated sites of Mg and P cations (see Figure 3.1) and is isotopic to that of Li_2SiO_3 .^[33] The relation of both crystal structures was illustrated recently by Häusler et al.^[34]

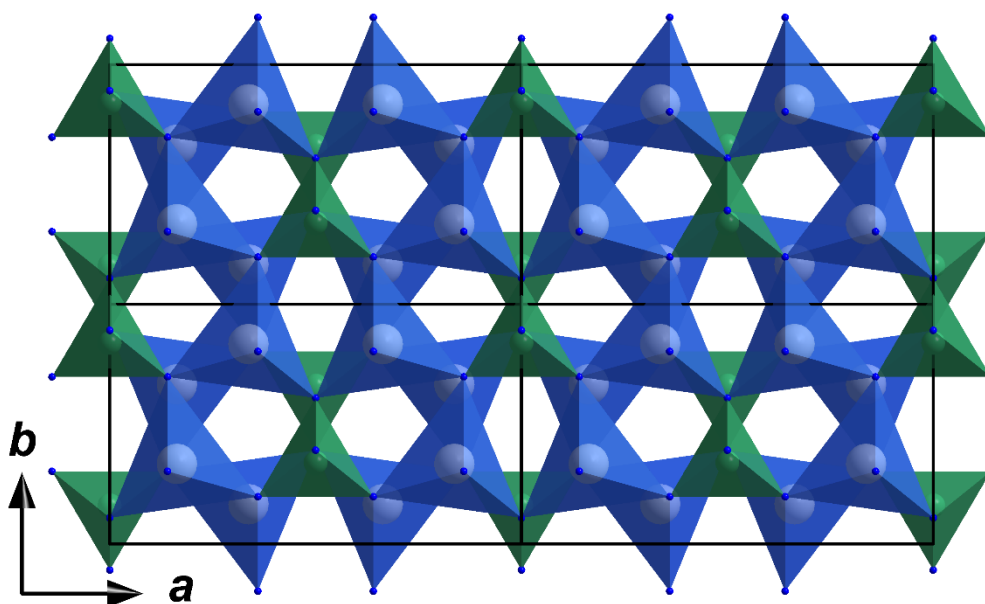


Figure 3.1. Crystal Structure of M_2PN_3 ($M = \text{Mg}, \text{Zn}$). MN_4 -tetrahedra are depicted in blue, PN_4 -tetrahedra in green.

Along the c -axis, the structure has infinite chains of corner sharing PN_4 -tetrahedra with a periodicity of $P = 2$ (*zweier* single chain, see Figure 3.2). The stretching factor is $f_s = 0.89$.^[35] These chains, and the fact that c is the shortest lattice parameter, may explain the growth direction of the single crystals along $[001]$, and therefore the needle-shaped habitus of the crystallites. As mentioned above, both cations are coordinated tetrahedrally by N. Therefore, both compounds can be described as double nitrides of the constituting binary nitrides. The interatomic distances P–N range from 1.616(3) to 1.693(4) Å. As expected, the P–N distances to nitrogen atoms, which are involved in the P–N chain (bridging two PN_4 -tetrahedra) are shorter (1.616(3) Å) than to the nitrogen atoms linking a PN_4 - and a MgN_4 -tetrahedron (1.676(4) and 1.693(4) Å). The Mg–N distances range from 2.075(2) to

2.149(4) Å agreeing well with the sum of the ionic radii.^[36] All distances are in good agreement with values reported earlier for Mg₂PN₃ on the basis of PXRD data.^[22]

Table 3.1. Crystallographic data of Mg₂PN₃ from single crystal X-ray diffraction, standard deviations in parentheses.

Formula	Mg ₂ PN ₃
Crystal system	orthorhombic
Space group	<i>Cmc</i> 2 ₁ (no. 36)
<i>a</i> / Å	9.7234(16)
<i>b</i> / Å	5.6562(9)
<i>c</i> / Å	4.7083(7)
Cell volume / Å ³	258.94(7)
Formula units per cell	4
Density / g·cm ⁻³	3.120
Crystal size / mm	0.02×0.004×0.004
μ / mm ⁻¹	1.234
<i>T</i> / K	293(2)
Diffractometer	Bruker D8 Venture
Radiation / Å	Mo- <i>K</i> _α (0.71073)
<i>F</i> (000)	240
2 θ range / °	8.383–47.68
Total no. of reflections	3693
Independent reflections	307
Refined parameters	23
Flack parameter	0.14(9)
GooF	1.184
<i>R</i> indices (all data)	<i>R</i> 1 = 0.0205, <i>wR</i> 2 = 0.0432
<i>R</i> indices [<i>F</i> ² ≥ 2σ(<i>F</i> ²)]	<i>R</i> 1 = 0.0203, <i>wR</i> 2 = 0.0431
$\Delta\rho_{\max}$, $\Delta\rho_{\min}$ / e Å ⁻³	0.43, -0.36
<i>R</i> _{int} , <i>R</i> _σ	0.0219, 0.0268

Figure 3.3 shows the Rietveld plot of a Mg_2PN_3 powder sample. The refinement is based on the structure model obtained from single-crystal X-ray data. Cell parameters are given in Table 3.2, details on crystallographic data are listed in the Supporting Information (Table B.4).

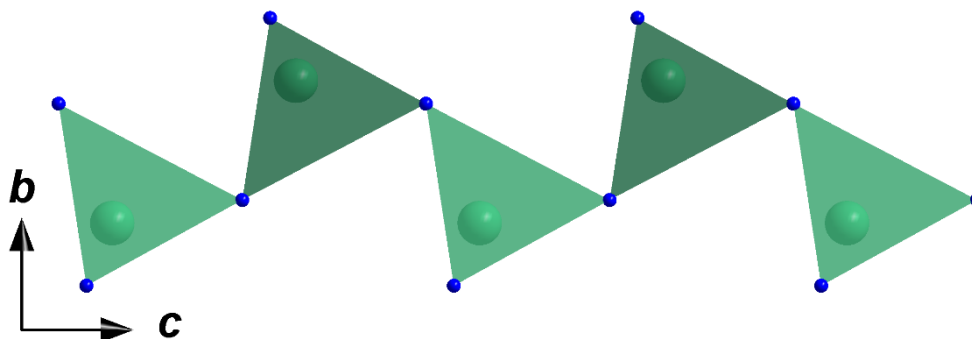


Figure 3.2. Infinite chains of PN_4 -tetrahedra running along the c -axis.

Isotypic Zn_2PN_3 was also analyzed by PXRD (see Figure 3.4). Atomic coordinates were taken from literature.^[23] The lattice parameters are given in Table 3.2. Further crystallographic details, as well as atomic coordinates and intermolecular distances, are presented in the Supporting Information (Table B.5, B.6, and B.7). Because of the poor crystallinity of the product and the resulting overlap of the reflections in the PXRD, distance restraints were applied during the refinement, (see Supporting Information). On the basis of the PXRD data it can be concluded that, analogous to Mg_2PN_3 , a preferred growth direction (along c) occurs in Zn_2PN_3 . This conjecture is illustrated by the 002 reflection (36.3°), which has a narrower shape and is therefore fitted less accurately than the other reflections. This assumption can also be confirmed by SEM images (see below). The stretching factor f_s of PN_4 -tetrahedron chains is 0.89, analogous to Mg_2PN_3 .

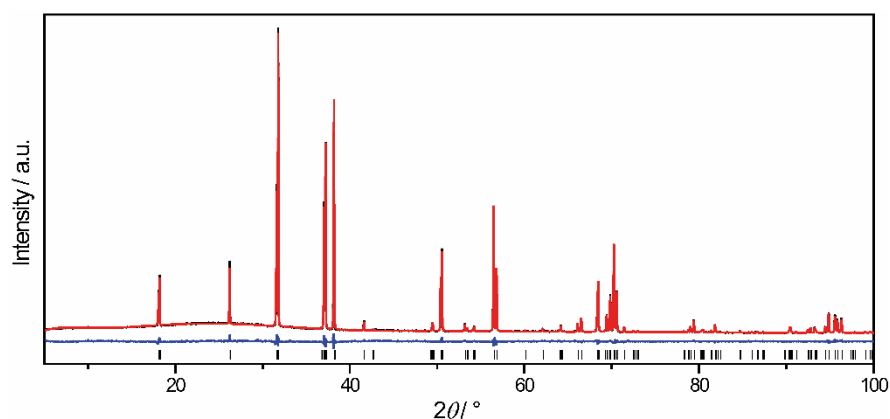


Figure 3.3. Rietveld refinement of powder X-ray diffraction pattern of Mg_2PN_3 with experimental data (black line), calculated data (red line), difference profile (blue line), and reflection positions (black bars).

Table 3.2. Cell parameters of Mg_2PN_3 and Zn_2PN_3 obtained by Rietveld refinement, standard deviations in parentheses.

Formula	Mg_2PN_3	Zn_2PN_3
Crystal system	orthorhombic	
Space group	$Cmc2_1$ (no. 36)	
$a / \text{\AA}$	9.70545(4)	9.4177(4)
$b / \text{\AA}$	5.64482(2)	5.4399(3)
$c / \text{\AA}$	4.70160(2)	4.9477(2)
Cell volume / \AA^3	257.58(2)	253.48(2)
Formula units per cell	4	

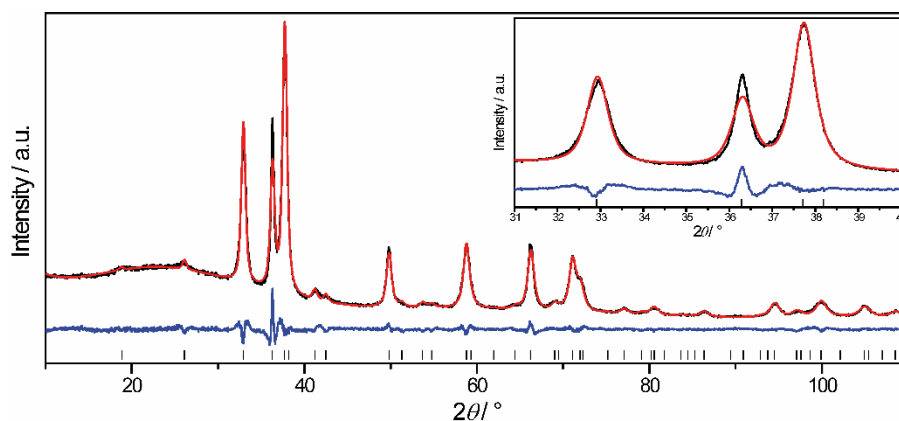


Figure 3.4. Rietveld refinement of powder X-ray diffraction pattern of Zn_2PN_3 with experimental data (black line), calculated data (red line), difference profile (blue line), and reflection positions (black bars). Enlarged part shows the narrower shape of the 002 reflection.

3.2.3 Scanning electron microscopy

Scanning electron microscopy (SEM) images show needle-shaped single crystals of Mg_2PN_3 with sizes up to $30 \mu\text{m}$ (see Figure 3.5 a). In Zn_2PN_3 , acicular crystallites are recognizable as well (Figure 3.5 b). In contrast to Mg_2PN_3 , the crystallites are in the nm range. With regard to PXRD data, it can be assumed that these needles also grow along the c -axis. Needle-shaped crystals of Zn_2PN_3 were only observed with NaN_3 as mineralizer.

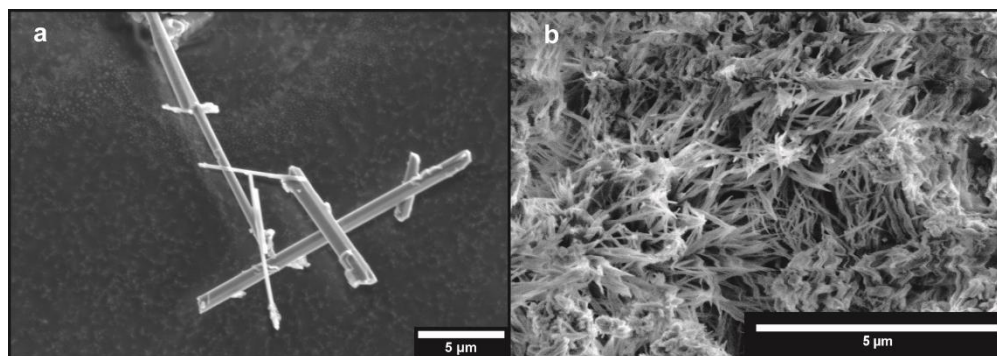


Figure 3.5. SEM images of (a) Mg_2PN_3 and (b) Zn_2PN_3 .

Energy-dispersive X-ray spectroscopy (EDX) values for both compounds are summarized in the Supporting Information (Table B.8 and B.9). The values are consistent with the composition of the products. K and Na impurities can be explained with residual mineralizer, oxygen, and chlorine by washing treatment.

3.2.4 UV/Vis reflectance spectroscopy and DFT calculations

To investigate the optical properties of both compounds, diffuse reflectance measurements were conducted. The spectra show absorption bands around 250 nm for Mg_2PN_3 and 350 nm for Zn_2PN_3 (see Figure B.1 and B.2 in the Supporting Information). To estimate the optical bandgaps, pseudo-absorption spectra were calculated using the Kubelka–Munk function $F(R) = (1-R)^2/2R$, where R represents the reflectance.^[37] Subsequently, the bandgap was determined using Tauc plots, where $h\nu$ is plotted versus $(F(R) \cdot h\nu)^{1/n}$ with $n = 1/2$ for direct and $n = 2$ for indirect bandgap, by drawing tangents at the inflection points (see Figure 3.6).^[38] The absorption band of Mg_2PN_3 was attributed to an indirect bandgap ($Z_c-\Gamma_v$) according to DFT calculations (see Figure 3.7), whereas the absorption band of Zn_2PN_3 was attributed to a direct transition, due to the small difference (0.1 eV) between direct ($\Gamma_c-\Gamma_v$) and indirect ($Z_c-\Gamma_v$) bandgap in the DFT calculations (see Figure 3.7).

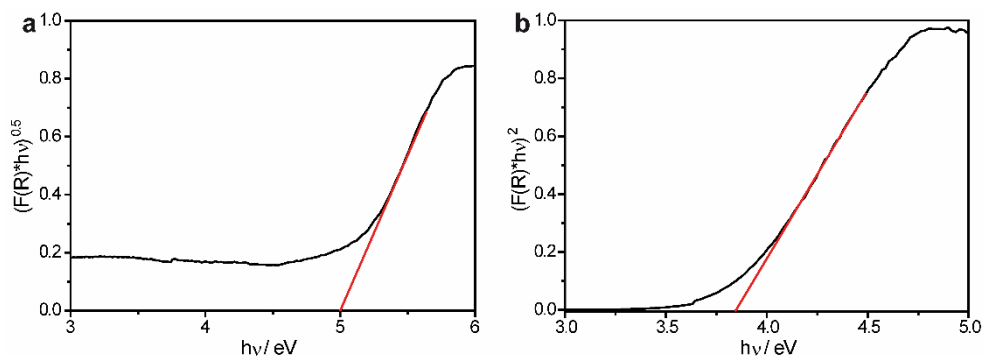


Figure 3.6. Tauc plots of (a) Mg_2PN_3 and (b) Zn_2PN_3 . Red lines are tangents at the inflection points.

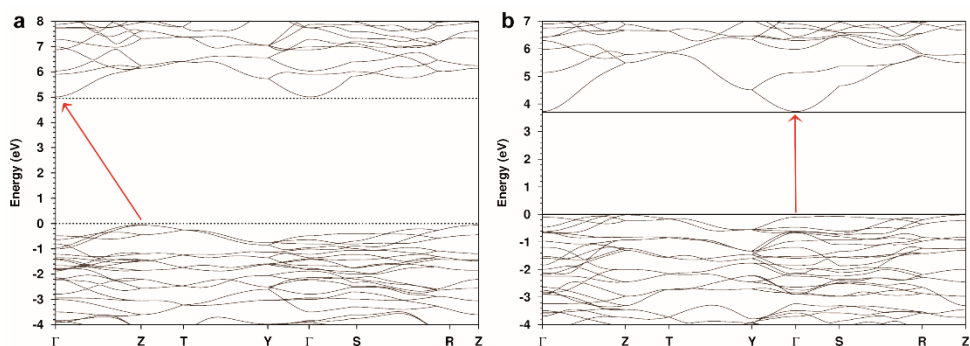


Figure 3.7. Calculated band structures of (a) Mg_2PN_3 and (b) Zn_2PN_3 . Red arrows indicate the transitions.

Experimental bandgaps were determined to 5.0 and 3.8 eV for Mg_2PN_3 and Zn_2PN_3 , respectively. Both values are in good agreement with the electronic bandgaps determined from DFT. With a value of 3.8 eV, especially Zn_2PN_3 is a promising candidate as an earth-abundant semiconductor, similar to ZnGeN_2 and ZnSiN_2 .^[10] In addition, recent calculations indicated high charge carrier mobility and small effective masses for Zn_2PN_3 .^[3]

3.2.5 Dissolution experiment

Ammonothermal crystal growth can be achieved by solution (dissolution and recrystallization of already formed crystallites), or by growth from an amide melt at the bottom of the autoclave. A dissolution experiment was conducted to illuminate which growth process is the most probable one for Mg_2PN_3 . Based on this experiment we observed that Mg_2PN_3 was partially dissolved, using NaNH_2 in ammonia at 670 K and 110 MPa. PXRD data show reflections of NaNH_2 , Mg_2PN_3 , $\text{Na}_2\text{Mg}(\text{NH}_2)_4$, and an unknown species. In particular, the formation of $\text{Na}_2\text{Mg}(\text{NH}_2)_4$ suggests a slow dissolution of Mg_2PN_3 , nonetheless further experiments have to be made to clarify the growth

mechanism and possible phosphorus containing intermediates during synthesis of nitridophosphates under ammonothermal conditions.

In addition, we attempted an in situ X-ray absorption monitoring experiment to capture the dissolution behavior similar to ZnGeN_2 .^[10] However, the results have not proven to be reasonable, because both the mineralizer cation Na^+ and the constituting cations within the nitride-Mg and P have similar atomic numbers, resulting in very similar X-ray absorption contrast. As a result of this and the large excess of used azide, no statement could be made about the decrease in the transmitted X-ray intensity due to dissolving Mg_2PN_3 .

3.3 Conclusion

Herein we present the ammonothermal syntheses of the two phosphorus nitrides Mg_2PN_3 and Zn_2PN_3 . Both compounds crystallize in a wurtzite-superstructure with space group $Cmc2_1$ (no. 36). Custom-built autoclaves made of nickel-based super alloys (Inconel 718 and Haynes alloy 282) were used to achieve supercritical conditions of ammonia ($T_{\text{crit}} = 405.5 \text{ K}$, $p_{\text{crit}} = 11.3 \text{ MPa}$). Besides $\text{K}_3\text{P}_6\text{N}_{11}$, Mg_2PN_3 and Zn_2PN_3 are the first ternary P-N compounds (nitridophosphates, phosphorus nitrides) synthesized under ammonothermal conditions, illustrating the great potential of the ammonothermal method for the synthesis of nitride materials. Furthermore, we were able to grow single crystals of Mg_2PN_3 for the first time. In addition, this is the first ammonothermally-synthesized ternary nitride, which is suitable for single-crystal X-ray diffraction measurements. Diffuse reflectance spectra were collected to determine the bandgaps of Mg_2PN_3 (5.0 eV) and Zn_2PN_3 (3.8 eV). The measurements were confirmed by band structure calculations using DFT. Especially, Zn_2PN_3 shows a bandgap suitable for semiconductor applications. In addition, theoretical calculations have already shown that other properties, such as carrier mobility, are in favorable ranges.^[3] Further materials property measurements are now planned for better understanding of such nitrides. A dissolution experiment of Mg_2PN_3 was conducted to obtain insights into the crystallization process and suggests a solution growth mechanism. Together with previous studies in our group, this work demonstrates the great potential of the ammonothermal method in the synthesis and crystal growth of nitrides as well as possible semiconducting materials.

3.4 Experimental Section

3.4.1 Synthesis of P_3N_5

P_3N_5 was synthesized according to Stock et al.^[39] by reaction of P_4S_{10} (Sigma Aldrich, 99 %) in a continuous flow of NH_3 (Air Liquid, 99.999 %). After saturation for 4 h with NH_3 , the silica tube was heated to 1125 K with a heating rate of 5 K min^{-1} and held at this temperature for 4 h. The reaction product was then cooled down to room temperature with 5 K min^{-1} . The orange product was washed with concentrated HCl, water, and ethanol and then dried in vacuum. Powder X-ray diffraction was used to confirm phase purity.

All further operations were performed in argon filled glove boxes (Unilab, MBraun, Garching, $\text{O}_2 < 1 \text{ ppm}$, $\text{H}_2\text{O} < 1 \text{ ppm}$) or in dried Schlenk-type glassware connected to a vacuum line ($\leq 0.1 \text{ Pa}$) with argon or ammonia supply, to prevent oxygen or moisture contamination. Ammonia and argon (Air Liquid, 99.999 %) were further purified through gas purification cartridges (Micro torr MC400-702FV (for NH_3) and FT400-902 (for Ar), SAES Pure Gas Inc., San Luis Obispo, CA, USA).

3.4.2 Ammonothermal synthesis of Mg_2PN_3

Mg_2PN_3 was synthesized under ammonothermal conditions using a custom-built nickel-based superalloy autoclave (Haynes[®] 282[®]) reaching a maximum temperature of 1100 K and a maximum pressure of 170 MPa. Mg (3 mmol, 72.9 mg, Alfa Aesar, 99.8 %), P_3N_5 (0.5 mmol, 81.5 mg), and NaN_3 (7.5 mmol, 487.5 mg, Sigma Aldrich, $\geq 99.5 \%$) were mixed and transferred to a Mo-liner, to prevent contamination of the reaction mixture by the autoclave. Subsequently, the liner was placed in the autoclave body which is sealed with a sealing gasket (silver coated Inconel[®] 718 ring, GFD seals). An Inconel[®] 718 high-pressure tube connects the vessel (10 mL internal volume) with the upper part, which is composed of a hand valve (SITEC), a pressure transmitter (HBM P2VA1/5000 bar), and a bursting disc (SITEC). After closing under argon, the autoclave was evacuated and cooled with an ethanol/liquid nitrogen mixture to 198 K. Subsequently, liquid ammonia ($\approx 4 \text{ mL}$) was condensed directly into the reaction vessel via a pressure regulating valve. The autoclave was heated in a vertical tube furnace (Loba, HTM Reetz) to 1070 K within 5 h, and kept at this temperature for 96 h reaching a maximum pressure of 140 MPa. After cooling to room temperature, the white product was separated, washed with 100 % ethanol, and dried at 350 K in air. Transparent, needle-shaped crystals of Mg_2PN_3 were obtained.

3.4.3 Ammonothermal synthesis of Zn₂PN₃

For synthesis of Zn₂PN₃, Zn (3 mmol, Alfa Aesar, 99.9 %), P₃N₅ (0.5 mmol, 81.5 mg), and KN₃ (6 mmol, 486.7 mg, Sigma Aldrich, ≥99.5 %) or NaN₃ (6 mmol, 390.0 Sigma Aldrich, ≥99.5 %) were mixed and transferred in an Nb-liner. The filled liner was placed in the autoclave (Inconel[®] 718, $T_{\max} = 870$ K $p_{\max} = 300$ MPa, internal volume: 10 mL) and closed under argon. The setup of the autoclave is similar to the previous one. After evacuating and cooling to 198 K with an ethanol/liquid nitrogen mixture, liquid ammonia (≈ 7 mL) was directly condensed into the high-pressure reactor via a pressure regulating valve. Subsequently, the autoclave was heated to 630 K within 2 h, held for 16 h, heated to 800 K within 2 h, and kept at this temperature for 96 h. The autoclave reached a maximum pressure of 200 MPa. After cooling down, the white product was washed with 1 M HCl and dried at 350 K in air.

3.4.4 Single-crystal X-ray diffraction

For the single-crystal XRD measurement, a Mg₂PN₃ crystal was purified with deionized water and placed on a MicroMount[™] (MiTeGen) with an aperture size of 20 μm . The diffraction data was recorded with a D8 Venture single-crystal X-ray diffractometer (Bruker) with Mo- K_{α} radiation ($\lambda = 0.71073$ Å). The program SADABS was used for absorption correction.^[40] The crystal structure was solved by direct methods (SHELXS)^[41] and refined by full-matrix least-squares methods (SHELXL).^[42]

Further details of the crystal structure investigations of Mg₂PN₃ may be obtained from Fachinformationszentrum Karlsruhe, 76344 Eggenstein-Leopoldshafen, Germany (fax: (+49)7247-808-666; e-mail: crysdata@fiz-karlsruhe.de) on quoting the deposition number CSD-434689.

3.4.5 Powder X-ray diffraction

A Stoe STADI P diffractometer with Cu- $K_{\alpha 1}$ radiation ($\lambda = 1.5406$ Å), Ge(1 1 1) monochromator, and Mythen 1 K detector, in modified Debye–Scherrer geometry was used to collect PXRD data of Mg₂PN₃ and Zn₂PN₃. For this purpose, the products were filled and sealed in glass capillaries with a diameter of 0.3 mm (Hilgenberg GmbH). The program TOPAS was used for Rietveld refinement of the received data.^[43]

Further details of the crystal structure investigations of Zn₂PN₃ may be obtained from the Fachinformationszentrum Karlsruhe, 76344 Eggenstein-Leopoldshafen, Germany (fax: (+49)7247-808-666; e-mail: crysdata@fiz-karlsruhe.de) on quoting the deposition number CSD-434690.

3.4.6 Scanning electron microscopy

The chemical compositions, as well as the crystal morphologies, of the samples were recorded using a Dualbeam Helios Nanolab G3 UC (FEI) scanning electron microscope, equipped with an EDX detector (X-Max 80 SDD, Oxford instruments). Therefore, the products were placed on an adhesive carbon pad and coated with a conductive carbon film using a high-vacuum sputter coater (BAL-TEC MED 020, Bal Tec A).

3.4.7 UV/Vis spectroscopy

A Jasco V-650 UV/VIS spectrophotometer equipped with Czerny-Turner mount, photomultiplier tube detector, and deuterium (190–350 nm)/ halogen (330–900 nm) lamps as light sources was used for diffuse reflectance measurements at room temperature for determination of the optical bandgaps of both samples.

3.4.8 DFT calculations

Structure relaxations were performed with VASP.^[44–46] Exchange correlation was treated with generalized gradient approximation (GGA) of Perdew, Burke, and Ernzerhof (PBE)^[47, 48] and the projector-augmented-wave (PAW) method.^[49, 50] A plane-wave cut-off of 535 eV was used while the Brillouin zone was sampled on a Γ -centered k -mesh ($6\times 9\times 9$ for Zn_2PN_3 and $6\times 9\times 11$ for Mg_2PN_3) produced from the method of Monkhorst and Pack.^[51] Total energies of the unit cells were converged to 10^{-7} eV $\cdot\text{atom}^{-1}$ with residual atomic forces below 4×10^{-3} eV $\cdot\text{\AA}^{-1}$. Bandgap evaluation was based on additional calculations with the modified Becke–Johnson formalism (GGA-mbj).^[52, 53]

3.4.9 Dissolution experiment

For the dissolution experiment, ammonothermally synthesized Mg_2PN_3 (2 mmol) and NaN_3 (15 mmol) were mixed and transferred to an Inconel 600-liner. The liner was placed in the autoclave (Haynes[®] 282[®], $T_{\text{max}} = 1073$ °C $p_{\text{max}} = 170$ MPa, internal volume: 10 mL) and closed under argon. Ammonia (≈ 7 mL) was directly condensed into the autoclave. The autoclave was heated to 670 K and kept at this temperature for 96 h reaching a maximum pressure of 110 MPa. After cooling down, the received colorless product was analyzed by PXRD to verify the dissolution of Mg_2PN_3 .

3.5 Acknowledgements

The authors gratefully thank the group of Prof. Dr. E. Schlücker, especially Anna Kimmel and Thomas Steigerwald, for development and fabrication of the autoclaves and Saskia Schimmel for in situ X-ray measurements (FAU Erlangen-Nürnberg). Furthermore, we want to thank the Deutsche Forschungsgemeinschaft (DFG) for financial support within the research group “Chemistry and Technology of the Ammonothermal Synthesis of Nitrides” (FOR 1600), project SCHN377/16-2. In addition, we want to thank Dr. Peter Mayer for single crystal X-ray measurements, as well as Maximilian Benz for preliminary work (all at Department of Chemistry of LMU Munich).

3.6 References

- [1] S. P. DenBaars, D. Feezell, K. Kelchner, S. Pimputkar, C.-C. Pan, C.-C. Yen, S. Tanaka, Y. Zhao, N. Pfaff, R. Farrell, M. Iza, S. Keller, U. Mishra, J. S. Speck, S. Nakamura, "Development of gallium-nitride-based light-emitting diodes (LEDs) and laser diodes for energy-efficient lighting and displays", *Acta Mater.* **2013**, *61*, 945-951.
- [2] K. Shinohara, D. C. Regan, Y. Tang, A. L. Corrion, D. F. Brown, J. C. Wong, J. F. Robinson, H. H. Fung, A. Schmitz, T. C. Oh, S. J. Kim, P. S. Chen, R. G. Nagele, A. D. Margomenos, M. Micovic, "Scaling of GaN HEMTs and Schottky Diodes for Submillimeter-Wave MMIC Applications", *IEEE Trans. Electron Devices* **2013**, *60*, 2982-2996.
- [3] Y. Hinuma, T. Hatakeyama, Y. Kumagai, L. A. Burton, H. Sato, Y. Muraba, S. Iimura, H. Hiramatsu, I. Tanaka, H. Hosono, F. Oba, "Discovery of earth-abundant nitride semiconductors by computational screening and high-pressure synthesis", *Nat. Commun.* **2016**, *7*, 11962.
- [4] P. Narang, S. Chen, N. C. Coronel, S. Gul, J. Yano, L. W. Wang, N. S. Lewis, H. A. Atwater, "Bandgap Tunability in $Zn(Sn,Ge)N_2$ Semiconductor Alloys", *Adv. Mater.* **2014**, *26*, 1235-1241.
- [5] P. C. Quayle, K. He, J. Shan, K. Kash, "Synthesis, lattice structure, and band gap of $ZnSnN_2$ ", *MRS Commun.* **2013**, *3*, 135-138.
- [6] A. D. Martinez, A. N. Fioretti, E. S. Toberer, A. C. Tamboli, "Synthesis, structure, and optoelectronic properties of II-IV- V_2 materials", *J. Mater. Chem.* **2017**, *5*, 11418-11435.
- [7] F. Kawamura, N. Yamada, M. Imai, T. Taniguchi, "Synthesis of $ZnSnN_2$ crystals via a high-pressure metathesis reaction", *Cryst. Res. Technol.* **2016**, *51*, 220-224.
- [8] D. Ehretraut, E. Meissner, M. Bockowski, *Technology of Gallium Nitride Crystal Growth*, Springer, Berlin, Heidelberg, **2010**, 137-202.

- [9] J. Hertrampf, P. Becker, M. Widenmeyer, A. Weidenkaff, E. Schlücker, R. Niewa, "Ammonothermal Crystal Growth of Indium Nitride", *Cryst. Growth Des.* **2018**, *18*, 2365-2369.
- [10] J. Häusler, S. Schimmel, P. Wellmann, W. Schnick, "Ammonothermal Synthesis of Earth Abundant Nitride Semiconductors ZnSiN₂ and ZnGeN₂ and Dissolution Monitoring by In Situ X-ray Imaging", *Chem. Eur. J.* **2017**, *23*, 12275-12282.
- [11] J. Häusler, W. Schnick, "Ammonothermal Synthesis of Nitrides: Recent Developments and Future Perspectives", *Chem. Eur. J.* **2018**, *24*, 11864-11879.
- [12] N. Cordes, W. Schnick, "Ammonothermal Synthesis of Crystalline Oxonitride Perovskites LnTaON₂ (Ln = La, Ce, Pr, Nd, Sm, Gd)", *Chem. Eur. J.* **2017**, *23*, 11410-11415.
- [13] M. Mallmann, J. Häusler, N. Cordes, W. Schnick, "Ammonothermal Synthesis of Alkali-Alkaline Earth Metal and Alkali-Rare Earth Metal Carbodiimides: K_{5-x}M_x(CN₂)_{2+x}(HCN)_{1-x} (M = Sr, Eu) and Na_{4.32}Sr_{0.68}(CN₂)_{2.68}(HCN₂)_{0.32}", *Z. Anorg. Allg. Chem.* **2017**, *643*, 1956-1961.
- [14] W. Schnick, "Solid State Chemistry with Nonmetal Nitrides", *Angew. Chem.* **1993**, *105*, 846-858; *Angew. Chem. Int. Ed. Engl.* **1993**, *32*, 806-818.
- [15] W. Schnick, V. Schultz-Coulon, "Ca₂PN₃ – A Novel Phosphorus(V) Nitride with One-Dimensional Infinite Chains of Corner-Sharing PN₄ Tetrahedra", *Angew. Chem.* **1993**, *105*, 308-309; *Angew. Chem. Int. Ed. Engl.* **1993**, *32*, 280-281.
- [16] W. Schnick, U. Berger, "Li₁₀P₄N₁₀ – A Lithium Phosphorus(V) Nitride with the Novel Complex Anion P₄N₁₀¹⁰⁻", *Angew. Chem.* **1991**, *103*, 857-858; *Angew. Chem. Int. Ed. Engl.* **1992**, *31*, 213-214.
- [17] E. M. Bertschler, C. Dietricj, T. Leichtweiß, J. Janek, W. Schnick, "Li⁺ Ion Conductors with Adamantane-type Nitridophosphate Anions – β-Li₁₀P₄N₁₀ and Li₃P₄N₁₀X₃ with X = Cl, Br", *Chem. Eur. J.* **2018**, *24*, 196-205.
- [18] F. W. Karau, L. Seyfarth, O. Oeckler, J. Senker, K. Landskron, W. Schnick, "The Stuffed Framework Structure of SrP₂N₄: Challenges to Synthesis and Crystal Structure Determination", *Chem. Eur. J.* **2007**, *13*, 6841-6852.
- [19] S. D. Kloß, W. Schnick, "Rare-Earth-Metal Nitridophosphates through High-Pressure Metathesis", *Angew. Chem.* **2015**, *127*, 11402-11405; *Angew. Chem. Int. Ed.* **2015**, *54*, 11250-11253.
- [20] H. Jacobs, R. Nymwegen, "Synthesis and Crystal Structure of a Potassium Nitridophosphate, K₃P₆N₁₁", *Z. Anorg. Allg. Chem.* **1997**, *623*, 429-433.
- [21] H. Jacobs, R. Nymwegen, S. Doyle, T. Wroblewski, W. Kockelmann, "Crystalline Phosphorus(V) Nitride Imide, HPN₂ and DPN₂, respectively, - Structure Determination with X-Ray, Synchrotron, and Neutron Radiation", *Z. Anorg. Allg. Chem.* **1997**, *623*, 1467-1474.

- [22] V. Schultz-Coulon, W. Schnick, "*Mg₂PN₃ and Ca₂PN₃ – Phosphorus(V) Nitrides with Infinite Chains of Corner Sharing PN₄ Tetrahedra*", *Z. Anorg. Allg. Chem.* **1997**, 623, 69-74.
- [23] S. J. Sedlmaier, M. Eberspächer, W. Schnick, "*High-Pressure Synthesis, Crystal Structure, and Characterization of Zn₂PN₃ – A New catena-Polynitridophosphate*", *Z. Anorg. Allg. Chem.* **2011**, 637, 362-367.
- [24] T. Richter, R. Niewa, "*Chemistry of Ammonothermal Synthesis*", *Inorganics* **2014**, 2, 29-78.
- [25] W. Schnick, J. Lücke, "*Preparation, Crystal Structure, and IR-spectroscopic Investigation of Phosphorus Nitride Imide, HPN₂*", *Z. Anorg. Allg. Chem.* **1992**, 610, 121-126.
- [26] F. Golinski, H. Jacobs, "*Crystal Structure of Hexamine Cyclotriphosphazene, P₃N₃(NH₂)₆*", *Z. Anorg. Allg. Chem.* **1994**, 620, 965-968.
- [27] H. Jacobs, S. Pollok, F. Golinski, "*Synthesis and Crystal Structure of Na₁₀[P₄(NH)₆N₄](NH₂)₆(NH₃)_{0.5} with an Adamantane-like Anion [P₄(NH)₆N₄]⁴⁻*", *Z. Anorg. Allg. Chem.* **1994**, 620, 1213-1218.
- [28] T. Brokamp, H. Jacobs, "*Darstellung und Struktur einiger Gemischtvalenter ternärer Tantalnitride mit Lithium und Magnesium*", *J. Alloys Compd.* **1992**, 183, 325-344.
- [29] S. Pimputkar, T. F. Malkowski, S. Griffiths, A. Espenlaub, S. Suihkonen, J. S. Speck, S. Nakamura, "*Stability of materials in supercritical ammonia solutions*", *J. Supercrit. Fluids* **2016**, 110, 193-229.
- [30] T. G. Steigerwald, J. Balouschek, B. Hertweck, A.-C. L. Kimmel, N. S. A. Alt, E. Schlücker, "*In situ investigation of decomposing ammonia and ammonobasic solutions under supercritical conditions via UV/vis and Raman Spectroscopy*", *J. Supercrit. Fluids* **2018**, 134, 96-105.
- [31] B. Eisenmann, M. Somer, "*On New Ternary Alkali Metal Phosphides: K₂CuP, NaZnP and K₄CdP₂*", *Z. Naturforsch., B: Chem. Sci.* **1985**, 40, 1419-1423.
- [32] H. Huppertz, "*Multianvil high-pressure / high-temperature synthesis in solid state chemistry*", *Z. Kristallogr.* **2004**, 219, 330-338.
- [33] K.-F. Hesse, "*Refinement of the crystal structure of lithium polysilicate*", *Acta Crystallogr. Sect. B* **1977**, 33, 901-902.
- [34] J. Häusler, R. Niklaus, J. Minár, W. Schnick, "*Ammonothermal Synthesis and Optical Properties of Ternary Nitride Semiconductors Mg-IV-N₂, Mn-IV-N₂ and Li-IV₂-N₃ (IV = Si, Ge)*", *Chem. Eur. J.* **2018**, 24, 1686-1693.
- [35] F. Liebau, *Structural Chemistry of Silicates*, Springer, Berlin, **1985**, 80.
- [36] W. H. Baur, "*Effective Ionic Radii in Nitrides*", *Cryst. Rev.* **1987**, 1, 59-83.
- [37] A. Stock, B. Hoffmann, "*Die Einwirkung von Ammoniak auf Phosphorpentasulfid und der Phosphorstickstoff, P₃N₅*", *Ber. Dtsch. Chem. Ges.* **1903**, 36, 314-319.

- [38] R. López, R. Gómez, "Band-gap energy estimation from diffuse reflectance measurements on sol-gel and commercial TiO_2 : a comparative study", *J. Sol-Gel Sci. Technol.* **2012**, 61, 1-7.
- [39] J. Tauc, R. Grigorovici, A. Vancu, "Optical Properties and Electronic Structure of Amorphous Germanium", *Phys. Status Solidi B* **1966**, 15, 627-637.
- [40] G. M. Sheldrick, *SADABS, Multi-Scan Absorption Correction*, v.2, Bruker-AXS, Madison, WI, USA, **2012**.
- [41] G. M. Sheldrick, *SHELXS-97: A program for crystal structure solution*, University of Göttingen, Germany, **1997**.
- [42] G. M. Sheldrick, *SHELXL-97: A program for crystal structure refinement*, University of Göttingen, Germany, **1997**.
- [43] A. Coelho, *TOPAS Academic, Version 4.1*, Coelho Software, Brisbane (Australia), **2007**.
- [44] G. Kresse, J. Furthmüller, "Efficiency of ab-initio total energy calculations for metals and semiconductors using a plane-wave basis set", *Comput. Mater. Sci.* **1996**, 6, 15-50.
- [45] G. Kresse, J. Hafner, "Ab initio molecular dynamics for liquid metals", *Phys. Rev. B* **1993**, 47, 558-561.
- [46] G. Kresse, J. Hafner, "Ab initio molecular-dynamics simulation of the liquid-metal-amorphous-semiconductor transition in germanium", *Phys. Rev. B* **1994**, 49, 14251-14269.
- [47] J. P. Perdew, K. Burke, M. Ernzerhof, "Generalized Gradient Approximation Made Simple", *Phys. Rev. Lett.* **1996**, 77, 3865-3868.
- [48] J. P. Perdew, K. Burke, M. Ernzerhof, "Generalized Gradient Approximation Made Simple", *Phys. Rev. Lett.* **1997**, 78, 1396-1396.
- [49] P. E. Blöchl, "Projector augmented-wave method", *Phys. Rev. B* **1994**, 50, 17953-17979.
- [50] G. Kresse, D. Joubert, "From ultrasoft pseudopotentials to the projector augmented-wave method", *Phys. Rev. B* **1999**, 59, 1758-1775.
- [51] H. J. Monkhorst, J. D. Pack, "Special points for Brillouin-zone integrations", *Phys. Rev. B* **1976**, 13, 5188-5192.
- [52] F. Tran, P. Blaha, "Accurate Band Gaps of Semiconductors and Insulators with a Semilocal Exchange-Correlation Potential", *Phys. Rev. Lett.* **2009**, 102, 226401.
- [53] J. A. Camargo-Martínez, R. Baquero, "Performance of the modified Becke-Johnson potential for semiconductors", *Phys. Rev. B* **2012**, 86, 195106.

4 Crystalline Nitridophosphates by Ammonothermal Synthesis

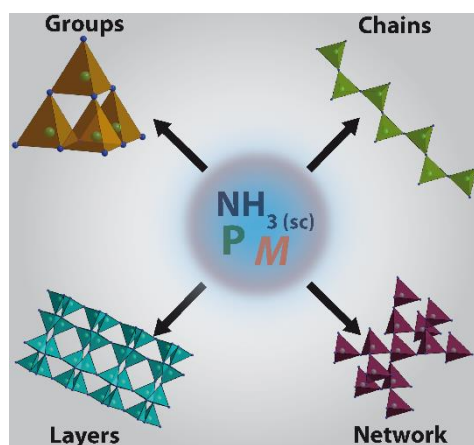
published in: *Chem. Eur. J.* **2020**, *26*, 2067 - 2072.

authors: Mathias Mallmann, Sebastian Wendl, and Wolfgang Schnick

DOI: 10.1002/chem.201905227

Reprinted (adapted) with permission for non-commercial use from *Chemistry – A European Journal* (open access). Copyright 2020 John Wiley and Sons.

Abstract. Nitridophosphates are a well-studied class of compounds with high structural diversity. However, their synthesis is quite challenging, particularly due to the limited thermal stability of starting materials like P_3N_5 . Typically, it requires even high-pressure techniques (e.g. multianvil) in most cases. Herein, we establish the ammonothermal method as a versatile synthetic tool to access nitridophosphates with different degrees of condensation. α - $Li_{10}P_4N_{10}$, β - $Li_{10}P_4N_{10}$, $Li_{18}P_6N_{16}$, Ca_2PN_3 , SrP_8N_{14} , and $LiPN_2$ were synthesized in supercritical NH_3 at temperatures and pressures up to 1070 K and 200 MPa employing ammonobasic conditions. The products were analyzed by powder X-ray diffraction, energy dispersive X-ray spectroscopy, and FTIR spectroscopy. Moreover, we established red phosphorus as a starting material for nitridophosphate synthesis instead of commonly used and not readily available precursors, such as P_3N_5 . This opens a promising preparative access to the emerging compound class of nitridophosphates.



4.1 Introduction

By analogy with well-known hydrothermal syntheses, the ammonothermal method was developed by Jacobs and co-workers and was established as an innovative synthetic approach for amides, imides and nitrides.^[1–5] The ammonothermal technique gained fundamental interest in materials science as

it facilitates the growth of high-quality GaN single crystals up to 50 mm in diameter with growth rates of several hundred μm per day.^[6–9]

Recent explorative syntheses under ammonothermal conditions made crystalline wurtzite-type Grimm–Sommerfeld analogous nitrides available, such as InN, *II-IV-N*₂ compounds (*II* = Mg, Mn, Zn; *IV* = Si, Ge) and CaGaSiN₃, as well as oxide nitride perovskites such as *LnTaON*₂ (*Ln* = La, Ce, Pr, Nd, Sm, Gd).^[10–15] Applying the ammonothermal technique, even the challenging preparation of a few nitridophosphates has been accomplished successfully as reported for K₃P₆N₁₁ and the double nitrides Mg₂PN₃ and Zn₂PN₃.^[16–18] Furthermore, various phosphorus-containing imidonitrides were synthesized in supercritical ammonia and thus, the ammonothermal method appears as a promising general synthetic approach for nitridophosphate synthesis.^[19–22]

Nitridophosphates are built up from PN₄ tetrahedra and their tetrahedra-based networks can be characterized by the degree of condensation $\kappa = n(T)/n(X)$, which represents the atomic ratio of tetrahedral centers (*T* = P) and coordinating atoms (*X* = N). Accordingly, compounds that are built up from non-condensed PN₄ tetrahedra (e.g. Li₇PN₄)^[23] possess a degree of condensation of $\kappa = 1/4$, whereas highly condensed frameworks feature $\kappa \geq 1/2$ (e.g. LiPN₂).^[24] For $1/4 < \kappa < 1/2$, partially condensed PN₄ tetrahedra may form complex anions, such as adamantane-like groups (α -Li₁₀P₄N₁₀, β -Li₁₀P₄N₁₀),^[25, 26] chain structures (e.g. Ca₂PN₃),^[27] or layers (e.g. Ho₂P₃N₇).^[28] The degree of condensation may further be correlated with materials properties, such as chemical inertness and rigidity of the network as well as physical properties like ion conductivity.^[18] Nitridophosphate synthesis, however, is a challenging issue, as these compounds are prone to thermal decomposition starting at 1020 K and the elimination of N₂ at elevated temperatures [Eq. 4.1]:



Consequently, the number of nitridophosphates synthesized at ambient pressure so far is limited (e.g. Ca₂PN₃, α -Li₁₀P₄N₁₀, β -Li₁₀P₄N₁₀, LiPN₂ or Mg₂PN₃).^[24–27, 29] Following Le Chatelier's principle, thermal decomposition, however, can be suppressed by applying pressure. In this context, especially the multianvil technique ($p \leq 25$ GPa) turned out to be a powerful synthetic tool.^[18] This high-pressure high-temperature method revealed numerous nitridophosphates with different types of anionic tetrahedra-based networks (e.g. SrP₈N₁₄, Li₁₈P₆N₁₆ or LiNdP₄N₈).^[30–32] Nevertheless, utilizing high-pressure techniques implicates small sample volumes, which limits detailed characterization of materials properties as well as practical applications. Furthermore, precursors like P₃N₅ are typically used,^[18] requiring a multistep synthesis procedure. Thus, the ammonothermal method is a promising and innovative alternative, as it enables the preparation of large-volume samples, while suppressing thermal decomposition by medium pressures ($p \leq 300$ MPa). However,

there has been no systematic investigation on the ammonothermal synthesis of nitridophosphates that covers their broad structural diversity.

In this contribution, we exemplarily present the ammonothermal synthesis ($T \leq 1070$ K, $p \leq 200$ MPa) of six nitridophosphates that feature non-condensed PN_4 tetrahedra groups, infinite PN_4 tetrahedra chains, layered substructures, and highly condensed frameworks, namely $\alpha\text{-Li}_{10}\text{P}_4\text{N}_{10}$, $\beta\text{-Li}_{10}\text{P}_4\text{N}_{10}$, $\text{Li}_{18}\text{P}_6\text{N}_{16}$, Ca_2PN_3 , $\text{SrP}_8\text{N}_{14}$, and LiPN_2 . This is a major extension of the structural diversity of ammonothermally accessible ternary and multinary compounds, which have hitherto been limited mainly to wurtzite-type derivatives and oxide nitride perovskites. In addition, red phosphorus (P_{red}), which was up to now only used for the synthesis of HPN_2 in ammonia,^[33] is employed as a starting material for nitridophosphates. This makes highly reactive and chlorine-containing precursors (e.g. PCl_5 , $(\text{PNCl}_2)_3$) dispensable, which can produce toxic and corrosive byproducts, emphasizing the innovative character of the ammonothermal approach.

4.2 Results and Discussion

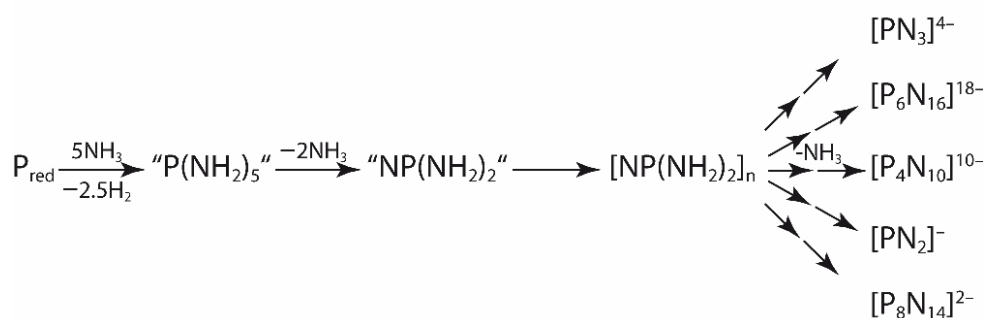
4.2.1 Ammonothermal synthesis

Nitridophosphates $\alpha\text{-Li}_{10}\text{P}_4\text{N}_{10}$, $\beta\text{-Li}_{10}\text{P}_4\text{N}_{10}$, $\text{Li}_{18}\text{P}_6\text{N}_{16}$, Ca_2PN_3 , $\text{SrP}_8\text{N}_{14}$, and LiPN_2 were synthesized ammonothermally using custom-built high-pressure, high-temperature autoclaves. P_3N_5 or P_{red} were used as phosphorus source during syntheses. The other starting materials as well as the corresponding reaction conditions (maximum reaction temperature T_{max} , maximum pressure p_{max} , reaction time at maximum temperature t) are summarized in Table 4.1. Ammonobasic mineralizers, such as alkali metals, alkali metal nitrides, alkali metal azides or alkaline earth metal azides, which react in situ to the corresponding metal amides, were added to increase the solubility of the starting materials by forming soluble intermediate species. Since such intermediates are preferentially formed at lower temperatures, an additional temperature step at 670 K (holding time: 16 h) was conducted for all reactions before heating to T_{max} .^[5] The addition of these mineralizers can also dissolve compounds such as P_{red} , which are actually insoluble in NH_3 even at temperatures above the critical point.^[34] Therefore, in the case of the synthesized lithium nitridophosphates ($\alpha\text{-Li}_{10}\text{P}_4\text{N}_{10}$, $\beta\text{-Li}_{10}\text{P}_4\text{N}_{10}$, $\text{Li}_{18}\text{P}_6\text{N}_{16}$ and LiPN_2), Li_3N or Li was added, respectively, in excess to increase the solubility of P_{red} . While NaN_3 was added for the synthesis of Ca_2PN_3 , to increase both, the solubility of Ca and P_{red} , no additional mineralizer was added for the synthesis of $\text{SrP}_8\text{N}_{14}$. Instead, $\text{Sr}(\text{N}_3)_2$ acts as an ammonobasic mineralizer itself by forming $\text{Sr}(\text{NH}_2)_2$, as the heavier alkaline earth metals have been discussed as ammonobasic mineralizers as well.^[35] Possible intermediates are mixed-metal amides, such as $\text{NaCa}(\text{NH}_2)_3$, and reactive P/N compounds, for example, hexaaminocyclotriphosphazene

(PN(NH₂)₂)₃, the corresponding ammoniate (PN(NH₂)₂)₃·0.5 NH₃ or imidonitrides in analogy to Na₁₀[P₄(NH)₆N₄](NH₂)₆(NH₃)_{0.5}, which have already been synthesized using the ammonothermal method.^[20, 36–38] A possible condensation mechanism of phosphorus containing intermediates is illustrated in Scheme 4.1. When starting from P_{red}, the element has to be oxidized in a first step to an oxidation state of +V forming an intermediate species like hypothetical „P(NH₂)₅“, in which two possible mechanisms are conceivable. On the one hand, N₂, which originates from the decomposition of NH₃, could act as oxidizing agent, on the other hand, NH₃ could directly react with P_{red} under elimination of H₂. „P(NH₂)₅“ could immediately form „NP(NH₂)₂“ by elimination of ammonia, which can react to reactive P/N compounds such as (PN(NH₂)₂)₃.^[37] However, for a precise statement on possible reaction mechanisms or phosphorus containing intermediates, in situ measurements like Raman or NMR spectroscopy could be helpful.

Table 4.1. Starting materials, mineralizers and reaction conditions of the ammonothermal synthesis of α-Li₁₀P₄N₁₀, β-Li₁₀P₄N₁₀, Li₁₈P₆N₁₆, Ca₂PN₃, SrP₈N₁₄, and LiPN₂.

Compd.	Starting material	Mineralizer	T _{max} [K]	p _{max} [MPa]	t [h]
α-Li ₁₀ P ₄ N ₁₀	Li ₃ N + P _{red}	Li ₃ N	920	100	72
β-Li ₁₀ P ₄ N ₁₀	Li ₃ N + P _{red}	Li ₃ N	1070	135	72
Li ₁₈ P ₆ N ₁₆	Li ₃ N + P ₃ N ₅	Li ₃ N	970	165	50
Ca ₂ PN ₃	CaH ₂ + P _{red}	NaN ₃	870	200	96
SrP ₈ N ₁₄	Sr(N ₃) ₂ + P ₃ N ₅	Sr(N ₃) ₂	1070	170	96
LiPN ₂	Li + P _{red}	Li	1070	135	96



Scheme 4.1. Simplified condensation sequence of nitridophosphates during ammonothermal synthesis, starting from P_{red}.

Subsequent heating from 670 K to the maximum temperature T_{\max} (see Table 4.1) leads to decomposition of the discussed intermediates and formation of the corresponding nitridophosphates under elimination of NH_3 (see Scheme 4.1). After reaction, residual mineralizers and intermediate species were removed by washing of the products with dry ethanol ($\alpha\text{-Li}_{10}\text{P}_4\text{N}_{10}$, $\beta\text{-Li}_{10}\text{P}_4\text{N}_{10}$, $\text{Li}_{18}\text{P}_6\text{N}_{16}$, and Ca_2PN_3) or 1 M HCl ($\text{SrP}_8\text{N}_{14}$ and LiPN_2). SEM images of octahedrally shaped $\beta\text{-Li}_{10}\text{P}_4\text{N}_{10}$ and needle-shaped $\text{SrP}_8\text{N}_{14}$ crystallites are illustrated in Figure 4.1, while the other compounds were obtained as microcrystalline powders.

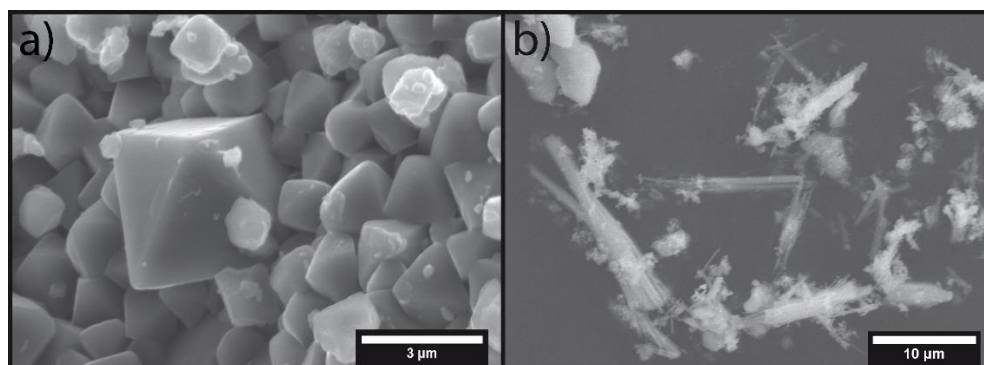


Figure 4.1. SEM images of octahedrally shaped crystals of $\beta\text{-Li}_{10}\text{P}_4\text{N}_{10}$ (a) and crystalline needles of $\text{SrP}_8\text{N}_{14}$ (b).

As mentioned above, both P_3N_5 and P_{red} were used as starting materials. While $\alpha\text{-Li}_{10}\text{P}_4\text{N}_{10}$, $\beta\text{-Li}_{10}\text{P}_4\text{N}_{10}$, Ca_2PN_3 , and LiPN_2 were synthesized starting from P_{red} , $\text{Li}_{18}\text{P}_6\text{N}_{16}$ and $\text{SrP}_8\text{N}_{14}$ could only be obtained starting from P_3N_5 . A possible explanation could be the higher reactivity of P_3N_5 compared to P_{red} , which is needed for the synthesis of $\text{Li}_{18}\text{P}_6\text{N}_{16}$ and $\text{SrP}_8\text{N}_{14}$.^[24–27, 30, 31] Probably, higher synthesis temperatures and pressures would lead to successful synthesis of these two compounds starting from P_{red} as well.

The introduction of P_{red} as a starting material for nitridophosphate synthesis as well as the use of simple starting materials like pure elements, lower reaction temperatures, pressures and larger sample volumes compared to other synthesis methods, indicates the high potential of the ammonothermal approach as an alternative synthetic tool for a systematic access to nitridophosphates.

4.2.2 Crystallographic investigation

The purified products were analyzed by PXRD. Rietveld refinements of $\alpha\text{-Li}_{10}\text{P}_4\text{N}_{10}$, $\beta\text{-Li}_{10}\text{P}_4\text{N}_{10}$, $\text{Li}_{18}\text{P}_6\text{N}_{16}$, Ca_2PN_3 , and LiPN_2 were conducted starting from atomic coordinates and Wyckoff positions known from the literature.^[24–27, 31] An exemplary Rietveld plot of Ca_2PN_3 is illustrated in Figure 4.2. The Rietveld plots of $\alpha\text{-Li}_{10}\text{P}_4\text{N}_{10}$, $\beta\text{-Li}_{10}\text{P}_4\text{N}_{10}$, $\text{Li}_{18}\text{P}_6\text{N}_{16}$, and LiPN_2 can be found in the

Supporting Information (Figures C.1 and C.6, Supporting Information). The crystallographic data as well as atomic coordinates are summarized in Tables C.1–C.4, C.6–C.7 and C.10–C.11 in the Supporting Information. In the case of $\text{Li}_{18}\text{P}_6\text{N}_{16}$ additional reflections could be observed, which can be attributed to $\alpha\text{-Li}_{10}\text{P}_4\text{N}_{10}$ and LiPN_2 . Due to the fact that $\text{Li}_{18}\text{P}_6\text{N}_{16}$ is so far only reported using high-pressure conditions (1270 K, 5.5 GPa), a possible explanation for these side phases could be that higher reaction pressures would be necessary to achieve phase purity.^[31] In analogy, higher pressures as well as temperatures would be necessary for the synthesis of $\text{SrP}_8\text{N}_{14}$, as the synthesis at 1070 K and 170 MPa resulted in broad reflections in the measured PXRD pattern (see Figure C.5 in the Supporting Information), suggesting a nanocrystalline sample morphology. However, further increases of temperature or pressure are challenging and not possible with the current high-pressure equipment. Therefore, the measured PXRD was only compared with a simulated pattern from literature data (see Figure C.5, Supporting Information)^[30] and may most likely be characterized as $\text{SrP}_8\text{N}_{14}$.

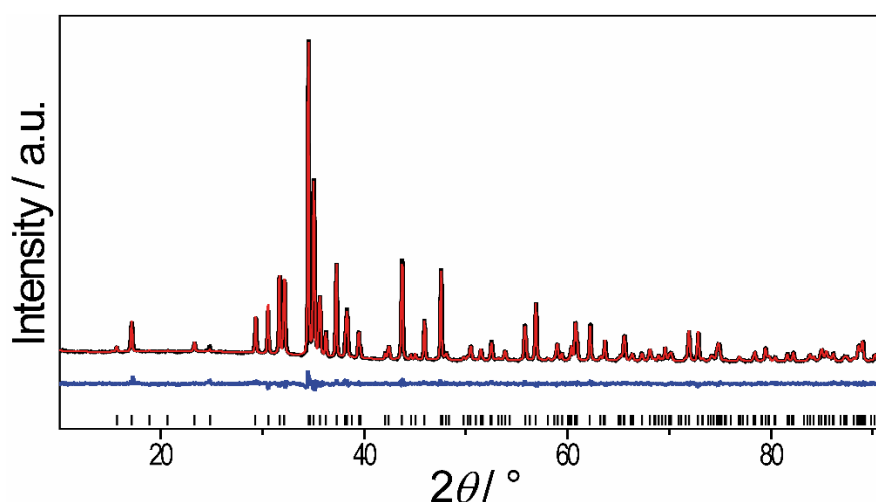


Figure 4.2. Rietveld refinement of PXRD pattern ($\lambda = 1.5406 \text{ \AA}$) of Ca_2PN_3 with experimental data (black line), calculated data (red line), difference profile (blue line) and reflection positions (black bars). Start values for Rietveld refinement were taken from literature.^[27] Unknown reflections between 6 and 10° only occur after washing treatment and were, therefore, not taken into account during the refinement.

EDX measurements of all compounds are summarized in Tables C.5, C.8, C.9, and C.12 in the Supporting Information. Deviations from the theoretical values can be explained by surface hydrolysis during sample preparation, washing treatment or by crystalline and amorphous side phases. The absence of any NH_x functionality in the Li containing nitridophosphates was confirmed by FTIR spectroscopy (Figures C.2–C.4 and C.7 in the Supporting Information).

4.2.3 Crystal structures

α -Li₁₀P₄N₁₀, β -Li₁₀P₄N₁₀, and Li₁₈P₆N₁₆ are built up from corner sharing PN₄ tetrahedra. While α -Li₁₀P₄N₁₀ and β -Li₁₀P₄N₁₀ contain adamantane-like T2 supertetrahedra ([P₄N₁₀]¹⁰⁻) with a degree of condensation of $\kappa = 2/5$, Li₁₈P₆N₁₆ is built up from [P₆N₁₆]¹⁸⁻ anions corresponding to a degree of condensation of $\kappa = 3/8$ (see Figure 4.3). These [P₆N₁₆]¹⁸⁻ units consist of four PN₄ tetrahedra forming a *vierer*-ring, which is connected to two further PN₄ tetrahedra forming two *dreier*-rings.^[39, 40] In contrast to these non-condensed tetrahedra groups, the anionic P/N-structure of Ca₂PN₃ is composed of *zwei*er single chains running along [100] made up of corner sharing PN₄ tetrahedra (see Figure 4.3).^[39, 40] The chains exhibit a stretching factor of $f_s = 1.0$ and a degree of condensation of $\kappa = 1/3$. The crystal structure of SrP₈N₁₄ is composed of PN₄ tetrahedra forming a layered structure (see Figure 4.3) and can be described as a highly condensed nitridophosphate with a degree of condensation of $\kappa = 4/7$. This is the highest degree of condensation observed in nitridophosphates so far. LiPN₂ is composed of all-side vertex-sharing PN₄ tetrahedra, which are connected via common corners forming a 3D anionic network with a degree of condensation of $\kappa = 1/2$ (see Figure 4.3) isoelectronic and homeotypic to β -cristobalite (SiO₂). Detailed crystal structure descriptions of all six compounds are given in the literature.^[24-27, 30, 31] As shown in Figure 4.3, the above described nitridophosphates can be divided into different groups regarding their anionic P/N-substructures (non-condensed tetrahedra groups, tetrahedra chains, tetrahedra layers, and tetrahedra networks). This is a major extension of the structural diversity of ammonothermally accessible ternary and multinary nitrides, which have hitherto been limited mainly to wurtzite-type derivatives and oxide nitride perovskites. Furthermore, the degree of condensation of ammonothermally accessible nitridophosphates is widely extended and ranges now from $\kappa = 1/3$ to $4/7$ (see Figure 4.4), covering almost the entirely accessible range. These results show the great potential of the ammonothermal method and can pave the way for synthesis of hitherto unknown nitridophosphates using the ammonothermal approach.

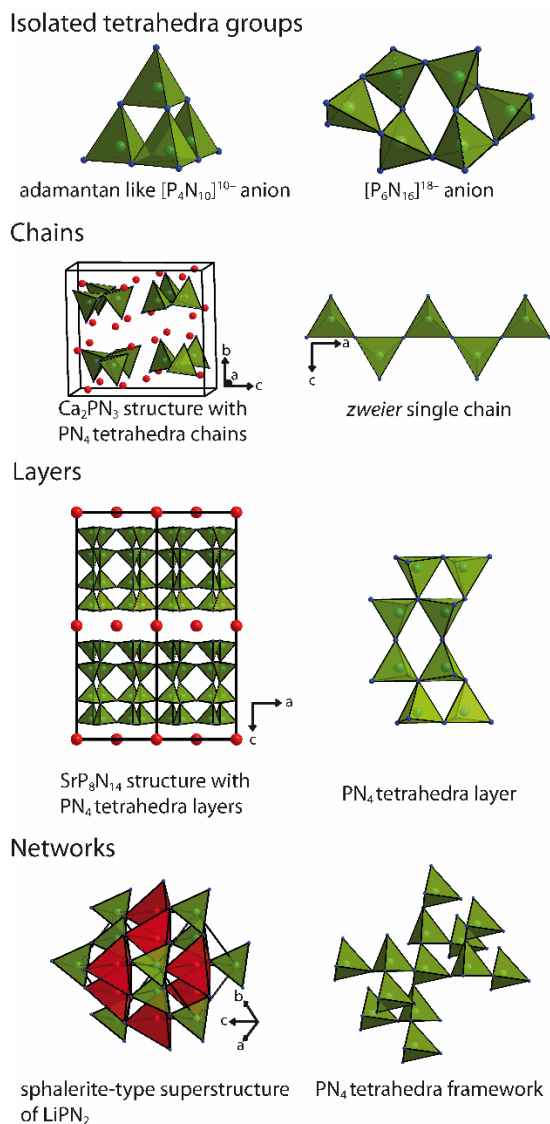


Figure 4.3. Crystal structures and/or constituting PN_4 tetrahedra units (green) occurring in α - $Li_{10}P_4N_{10}$, β - $Li_{10}P_4N_{10}$, $Li_{18}P_6N_{16}$, Ca_2PN_3 , SrP_8N_{14} , and $LiPN_2$. Ca^{2+} and Sr^{2+} cations as well as LiN_4 tetrahedra are depicted in red.

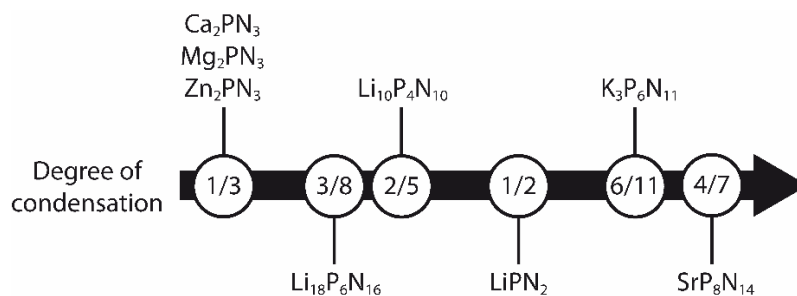


Figure 4.4. Ammonothermally synthesized nitridophosphates, arranged in order of their degree of condensation.

4.3 Conclusions

Recently, we reported on the synthesis and crystal growth of wurtzite-type Mg_2PN_3 and Zn_2PN_3 under ammonothermal conditions, raising the question of a systematic access to nitridophosphates using supercritical NH_3 .^[17] In this contribution we report on the ammonothermal syntheses of $\alpha\text{-Li}_{10}\text{P}_4\text{N}_{10}$, $\beta\text{-Li}_{10}\text{P}_4\text{N}_{10}$, $\text{Li}_{18}\text{P}_6\text{N}_{16}$, Ca_2PN_3 , $\text{SrP}_8\text{N}_{14}$, and LiPN_2 . Those compounds feature a degree of condensation in the range $1/3 \leq \kappa \leq 4/7$ (Figure 4.4), corresponding to different types of anionic tetrahedra-based substructures, such as non-condensed tetrahedra groups, chains, layers and 3D-networks. In contrast to established high-pressure techniques, the ammonothermal method requires only moderate pressures and temperatures, exemplifying the high potential of this preparative approach. Furthermore, readily available red phosphorus was introduced as a starting material in nitridophosphate syntheses, avoiding the usage of halide or sulfur-containing precursors (e.g. $(\text{PNCl}_2)_3$, P_4S_{10}). Using simple starting materials and yielding large sample volumes, the ammonothermal method enables more detailed characterization of material properties of nitridophosphates. Supporting fundamental research on the reaction mechanisms, intermediate species and dissolution/crystallization processes, however, might be necessary. Therefore, in situ measurements such as X-ray, NMR, or Raman techniques may provide important insights into these processes.^[41, 42]

4.4 Experimental Section

4.4.1 General

Loading of the autoclaves with solid starting materials (see below) were conducted under exclusion of oxygen and moisture in an argon-filled glovebox (Unilab, MBraun, Garching, $\text{O}_2 < 1$ ppm, $\text{H}_2\text{O} < 1$ ppm). The condensation of ammonia into the autoclaves was performed using a vacuum line (≤ 0.1 Pa) with argon and ammonia (both: Air Liquide, 99.999 %) supply. The gases were further purified by gas cartridges (Micro torr FT400-902 (for Ar) and MC400-702FV (for NH_3), SAES Pure Gas Inc., San Luis Obispo, CA, USA), providing a purity level of < 1 ppbV H_2O , O_2 and CO_2 . The amount of condensed ammonia was detected using a mass flow meter (d-6320-DR, Bronkhorst, Ruurlo, Netherlands).

4.4.2 Synthesis of P_3N_5

P_3N_5 was synthesized by reaction of P_4S_{10} (Sigma Aldrich, 99 %) in a continuous flow of NH_3 (Air Liquid, 99.999 %).^[43] After saturation with NH_3 (4 h), the silica tube was heated with a rate of 5 K min^{-1} to 1125 K and held for 4 h. After cooling to room temperature (5 K min^{-1}), the orange product was washed with ethanol, water and acetone and dried under vacuum. Powder X-ray diffraction was used to confirm phase purity.

4.4.3 Synthesis of $Sr(N_3)_2$

Based on the work of Suhrmann and Karau,^[44, 45] $Sr(N_3)_2$ was synthesized by reaction of in situ formed diluted HN_3 (by passing aqueous NaN_3 (Acros Organics, 99 %) through a cation exchanger (Amberlyst 15)) with $SrCO_3$ (Sigma Aldrich, 99.995 %). The HN_3 -solution was dropped slowly into an aqueous suspension of $SrCO_3$ and stirred until the liquid phase turned completely clear. Residual $SrCO_3$ was removed by filtration and the clear filtrate was evaporated under reduced pressure (50 mbar, $40\text{ }^\circ\text{C}$). After evaporation, the product was recrystallized from acetone and dried in vacuo. PXRD and FTIR measurements were used to confirm phase purity.

Caution! Since HN_3 solutions are potentially explosive and the vapor is highly poisonous, special care issues are necessary.

4.4.4 Ammonothermal synthesis of α - and β - $Li_{10}P_4N_{10}$

For ammonothermal synthesis of α - and β - $Li_{10}P_4N_{10}$, Li_3N (3 mmol, 104.5 mg, Sigma–Aldrich, 99.99 %) and red P (3 mmol, 92.9 mg, Merck, 99 %) were ground and transferred to Ta-liners, for protection of the samples against autoclave impurities. The liners were then placed in high-temperature autoclaves (Haynes® 282®, max. 1100 K, 170 MPa, 10 mL) and sealed with a lid via flange joints using a sealing gasket (silver coated Inconel® 718 ring, GFD seals). The autoclave body and the upper part, consisting of a hand valve (SITEC) with integrated bursting disc (SITEC) and pressure transmitter (HBM P2VA1/5000 bar), are connected by an Inconel® 718 high-pressure tube.^[12] The closed autoclave was evacuated and cooled to 198 K using an ethanol/liquid nitrogen mixture. Afterwards, NH_3 ($\approx 4\text{ mL}$) was directly condensed into the autoclaves via a pressure regulating valve. For both reactions, the autoclaves were primarily heated to 670 K within 2 h, kept at this temperature for 16 h and subsequently heated to 920 K (α - $Li_{10}P_4N_{10}$) or 1070 K (β - $Li_{10}P_4N_{10}$) within 3 h and held at this temperature for 72 h, reaching maximum pressures of 100 (α - $Li_{10}P_4N_{10}$) and 135 MPa (β - $Li_{10}P_4N_{10}$), respectively. After cooling and removal of NH_3 , the colorless products were separated under argon, washed with EtOH and dried in vacuo.

4.4.5 Ammonothermal synthesis of $\text{Li}_{18}\text{P}_6\text{N}_{16}$

$\text{Li}_{18}\text{P}_6\text{N}_{16}$ was synthesized ammonothermally starting from Li_3N (3.75 mmol, 130.6 mg, Sigma–Aldrich, 99.99 %), P_3N_5 (1.5 mmol, 244.4 mg) and NH_3 (≈ 5 mL) in a Ta-liner. Following the autoclave preparation (as described for $\text{Li}_{10}\text{P}_4\text{N}_{10}$), the vessel was heated to 670 K within 2 h, kept at this temperature for 16 h, heated to 970 K within 3 h and held at this temperature for 50 h reaching a maximum pressure of 165 MPa. After cooling and removing of NH_3 , the colorless product was separated under argon, washed with EtOH and dried in vacuo.

4.4.6 Ammonothermal synthesis of Ca_2PN_3

Ca_2PN_3 was synthesized under ammonothermal conditions using an Inconel[®] 718 autoclave (max. 870 K, 300 MPa, 10 mL). The setup and preparation of the autoclave is analogous to the autoclaves described above. CaH_2 (3 mmol, 126.3 mg, Sigma–Aldrich, 99.99 %), red P (1.5 mmol, 46.5 mg, Merck, 99 %), NaN_3 (7.5 mmol, 487.5 mg, Sigma–Aldrich, 99.5 %) as mineralizer and NH_3 (≈ 6.5 mL) were used as starting materials in a Ta-liner. After autoclave preparation (as described above), the reaction mixture was heated to 670 K within 2 h, held for 16 h, heated to 870 K within 2 h and kept at this temperature for 96 h, resulting in a maximum pressure of 200 MPa. The beige product was separated after cooling and ammonia removed under argon, washed with EtOH and dried in vacuo.

4.4.7 Ammonothermal synthesis of $\text{SrP}_8\text{N}_{14}$

$\text{Sr}(\text{N}_3)_2$ (0.375 mmol, 64.4 mg), P_3N_5 (1 mmol, 163 mg) were ground, transferred to a Ta-liner, which was placed in a Haynes[®] 282[®] autoclave. After preparation of the autoclave as described above, NH_3 (≈ 5 mL) was condensed into the autoclave. Subsequently, the autoclave was heated to 670 K within 2 h, held at this temperature for 16 h, heated to 1070 K within 3 h, and kept at this temperature for 96 h, reaching a maximum pressure of 170 MPa. After cooling and removal of NH_3 , the colorless product was isolated in air, washed with 1 M HCl and dried at 370 K.

4.4.8 Ammonothermal synthesis of LiPN_2

For the synthesis of LiPN_2 in supercritical ammonia, Li (10 mmol, 69.4 mg, Alfa Aesar, 99 %) and red P (7.5 mmol, 232.3 mg, Merck, 99 %) were transferred in a Ta-liner and placed in a Haynes[®] 282[®] autoclave. After preparation of the autoclave as described above, approximately 4 mL NH_3 were added. The reaction mixture was heated to 670 K within 2 h, held for 16 h, heated to

1070 K within 3 h and kept at this temperature for 96 h, resulting in maximum pressures of 135 MPa. After cooling and elimination of NH_3 , the isolated colorless product was washed with 1 M HCl and dried at 370 K.

4.4.9 Powder X-ray diffraction

The purified products were filled and sealed in glass capillaries (0.3–0.5 mm diameter, 0.01 mm wall thickness, Hilgenberg GmbH). A Stoe STADI P diffractometer with $\text{Cu-K}_{\alpha 1}$ radiation ($\lambda = 1.5406 \text{ \AA}$), Ge(111) monochromator and Mythen 1 K detector in Debye–Scherrer geometry was used for data collection. TOPAS was used for Rietveld refinement.^[46]

4.4.10 Scanning electron microscopy

A Dualbeam Helios Nanolab G3 UC (FEI) scanning electron microscope, equipped with an EDX detector (X-Max 80 SDD, Oxford instruments) was used for EDX measurements. For this purpose, the samples were placed on adhesive carbon pads and coated with a conductive carbon film using a high-vacuum sputter coater (BAL-TEC MED 020, Bal Tec A).

4.4.11 FTIR spectroscopy

A FTIR-IFS 66 v/S spectrometer (Bruker) was used for recording of IR spectra of air-sensitive samples. The samples were mixed with KBr (Acros Organics, 99 %) under argon and pressed into a pellet. The spectra were measured in the range of $400\text{--}4000 \text{ cm}^{-1}$ and evaluated by OPUS.^[47]

A FTIR spectrum of LiPN_2 was recorded on a Perkin–Elmer BX II FTIR spectrometer equipped with a DuraSampler Diamond ATR (attenuated total reflection) unit under exposure to air.

4.5 Acknowledgments

The authors gratefully acknowledge financial support by the Deutsche Forschungsgemeinschaft (DFG) within the research group “Chemistry and Technology of the Ammonothermal Synthesis of Nitrides” (FOR 1600), project SCHN377/16-2 and the project SCHN377/18-1 “Neue Wege zu nitridischen Phosphat-Netzwerken”. Furthermore, we want to thank the group of Prof. Dr. E. Schlücker for fabrication of the autoclaves (FAU Erlangen-Nürnberg), Marion Sokoll for IR measurements and Christian Minke for EDX measurements (both at Department of Chemistry, LMU Munich).

4.6 References

- [1] H. Jacobs, R. Juza, "Darstellung und Eigenschaften von Magnesiumamid und -imid", *Z. Anorg. Allg. Chem.* **1969**, 370, 254-261.
- [2] R. Juza, H. Jacobs, "Ammonothermal Synthesis of Magnesium and Beryllium Amides", *Angew. Chem.* **1966**, 78, 208; *Angew. Chem. Int. Ed. Engl.* **1966**, 5, 247.
- [3] H. Jacobs, E. von Pinkowski, "Synthese ternärer nitride von alkalimetallen: Verbindungen mit tantal, $MTaN_2$ mit $M = Na, K, Rb$ und Cs ", *J. Less Common Met.* **1989**, 146, 147-160.
- [4] J. Häusler, W. Schnick, "Ammonothermal Synthesis of Nitrides: Recent Developments and Future Perspectives", *Chem. Eur. J.* **2018**, 24, 11864-11879.
- [5] T. Richter, R. Niewa, "Chemistry of Ammonothermal Synthesis", *Inorganics* **2014**, 2, 29-78.
- [6] R. Dwiliński, R. Doradziński, J. Garczyński, L. Sierzputowski, R. Kucharski, M. Zając, M. Rudziński, R. Kudrawiec, W. Strupiński, J. Misiewicz, "Ammonothermal GaN substrates: Growth accomplishments and applications", *Phys. Status Solidi A* **2011**, 208, 1489-1493.
- [7] S. Pimputkar, S. Kawabata, J. S. Speck, S. Nakamura, "Improved growth rates and purity of basic ammonothermal GaN", *J. Cryst. Growth* **2014**, 403, 7-17.
- [8] W. Jiang, D. Ehretraut, J. Cook, D. S. Kamber, R. T. Pakalapati, M. P. D'Evelyn, "Transparent, conductive bulk GaN by high temperature ammonothermal growth", *Phys. Status Solidi B* **2015**, 252, 1069-1074.
- [9] J. B. Shim, G. H. Kim, Y. K. Lee, "Basic ammonothermal growth of bulk GaN single crystal using sodium mineralizers", *J. Cryst. Growth* **2017**, 478, 85-88.
- [10] J. Hertrampf, P. Becker, M. Widenmeyer, A. Weidenkaff, E. Schlücker, R. Niewa, "Ammonothermal Crystal Growth of Indium Nitride", *Cryst. Growth Des.* **2018**, 18, 2365-2369.
- [11] J. Häusler, R. Niklaus, J. Minár, W. Schnick, "Ammonothermal Synthesis and Optical Properties of Ternary Nitride Semiconductors $Mg-IV-N_2$, $Mn-IV-N_2$ and $Li-IV_2-N_3$ ($IV=Si, Ge$)", *Chem. Eur. J.* **2018**, 24, 1686-1693.
- [12] J. Häusler, S. Schimmel, P. Wellmann, W. Schnick, "Ammonothermal Synthesis of Earth-Abundant Nitride Semiconductors $ZnSiN_2$ and $ZnGeN_2$ and Dissolution Monitoring by In Situ X-ray Imaging", *Chem. Eur. J.* **2017**, 23, 12275-12282.
- [13] J. Häusler, L. Neudert, M. Mallmann, R. Niklaus, A.-C. L. Kimmel, N. S. A. Alt, E. Schlücker, O. Oeckler, W. Schnick, "Ammonothermal Synthesis of Novel Nitrides: Case Study on $CaGaSiN_3$ ", *Chem. Eur. J.* **2017**, 23, 2583-2590.
- [14] M. Mallmann, R. Niklaus, T. Rackl, M. Benz, T. G. Chau, D. Johrendt, J. Minár, W. Schnick, "Solid Solutions of Grimm-Sommerfeld Analogous Nitride Semiconductors $II-IV-N_2$ ($II = Mg,$

- Mn, Zn; IV = Si, Ge): Ammonothermal Synthesis and DFT Calculations*", *Chem. Eur. J.* **2019**, *25*, 15887-15895.
- [15] N. Cordes, W. Schnick, "Ammonothermal Synthesis of Crystalline Oxonitride Perovskites $LnTaON_2$ ($Ln=La, Ce, Pr, Nd, Sm, Gd$)", *Chem. Eur. J.* **2017**, *23*, 11410-11415.
- [16] H. Jacobs, R. Nymwegen, "Synthesis and Crystal Structure of a Potassium Nitridophosphate, $K_3P_6N_{11}$ ", *Z. Anorg. Allg. Chem.* **1997**, *623*, 429-433.
- [17] M. Mallmann, C. Maak, R. Niklaus, W. Schnick, "Ammonothermal Synthesis, Optical Properties, and DFT Calculations of Mg_2PN_3 and Zn_2PN_3 ", *Chem. Eur. J.* **2018**, *24*, 13963-13970.
- [18] S. D. Kloß, W. Schnick, "Nitridophosphates – A Success Story of Nitride Synthesis", *Angew. Chem.* **2019**, *131*, 8015-8027; *Angew. Chem. Int. Ed.* **2019**, *58*, 7933-7944.
- [19] H. Jacobs, R. Nymwegen, S. Doyle, T. Wroblewski, W. Kockelmann, "Crystalline Phosphorus(V) Nitride Imide, HPN_2 and DPN_2 , respectively, – Structure Determination with X-Ray, Synchrotron, and Neutron Radiation", *Z. Anorg. Allg. Chem.* **1997**, *623*, 1467-1474.
- [20] H. Jacobs, S. Pollok, F. Golinski, "Synthesis and Crystal Structure of $Na_{10}[P_4(NH)_6N_4](NH_2)_6(NH_3)_{0.5}$ with an Adamantane-like Anion $[P_4(NH)_6N_4]^{4-}$ ", *Z. Anorg. Allg. Chem.* **1994**, *620*, 1213-1218.
- [21] H. Jacobs, F. Golinski, "Synthesis and Crystal Structure of a Cesium-tetraimidophosphate-diamid, $Cs_5[P(NH)_4](NH_2)_2 = Cs_3[P(NH)_4] \cdot 2 CsNH_2$ ", *Z. Anorg. Allg. Chem.* **1994**, *620*, 531-534.
- [22] F. Golinski, H. Jacobs, "Synthesis and Crystal Structure of $Rb_8[P_4N_6(NH)_4](NH_2)_2$, with the Adamantane-like Anion $[P_4N_6(NH)_4]^{6-}$ ", *Z. Anorg. Allg. Chem.* **1995**, *621*, 29-33.
- [23] W. Schnick, J. Luecke, "Synthesis and Crystal Structure of Lithium Phosphorus Nitride Li_7PN_4 : The First Compound Containing Isolated PN_4 -Tetrahedra", *J. Solid State Chem.* **1990**, *87*, 101-106.
- [24] W. Schnick, J. Lücke, "On Lithium Phosphorus Nitride. Preparation and Refinement of the Crystal Structure of $LiPN_2$ ", *Z. Anorg. Allg. Chem.* **1990**, *588*, 19-25.
- [25] W. Schnick, U. Berger, " $Li_{10}P_4N_{10}$ - A Lithium Phosphorus(V) Nitride with the Novel Complex Anion $P_4N_{10}^{10-}$ ", *Angew. Chem.* **1991**, *103*, 857-858; *Angew. Chem. Int. Ed. Engl.* **1992**, *31*, 213-214.
- [26] E. M. Bertschler, C. Dietrich, T. Leichtweiß, J. Janek, W. Schnick, " Li^+ Ion Conductors with Adamantane-Type Nitridophosphate Anions β - $Li_{10}P_4N_{10}$ and $Li_{13}P_4N_{10}X_3$ with $X=Cl, Br$ ", *Chem. Eur. J.* **2018**, *24*, 196-205.
- [27] W. Schnick, V. Schultz-Coulon, " Ca_2PN_3 - A Novel Phosphorus(V) Nitride with One-Dimensional Infinite Chains of Corner-Sharing PN_4 Tetrahedra", *Angew. Chem.* **1993**, *105*, 308-309; *Angew. Chem. Int. Ed. Engl.* **1993**, *32*, 280-281.

- [28] S. D. Kloß, N. Weidmann, R. Niklaus, W. Schnick, "High-Pressure Synthesis of Melilite-type Rare-Earth Nitridophosphates $RE_2P_3N_7$ and a $Ba_2Cu[Si_2O_7]$ -type Polymorph", *Inorg. Chem.* **2016**, *55*, 9400-9409.
- [29] V. Schultz-Coulon, W. Schnick, " Mg_2PN_3 and Ca_2PN_3 – Phosphorus(V) Nitrides with Infinite Chains of Corner Sharing PN_4 Tetrahedra", *Z. Anorg. Allg. Chem.* **1997**, *623*, 69-74.
- [30] S. Wendl, W. Schnick, " $SrH_4P_6N_{12}$ and SrP_8N_{14} : Insights into the Condensation Mechanism of Nitridophosphates under High Pressure", *Chem. Eur. J.* **2018**, *24*, 15889-15896.
- [31] E.-M. Bertschler, C. Dietrich, J. Janek, W. Schnick, " $Li_{18}P_6N_{16}$ – A Lithium Nitridophosphate with Unprecedented Tricyclic $[P_6N_{16}]^{18-}$ Ions", *Chem. Eur. J.* **2017**, *23*, 2185-2191.
- [32] S. D. Kloß, W. Schnick, "Rare-Earth-Metal Nitridophosphates through High-Pressure Metathesis", *Angew. Chem.* **2015**, *127*, 11402-11405; *Angew. Chem. Int. Ed.* **2015**, *54*, 11250-11253.
- [33] J. M. Sullivan, "Ammoniated phosphonitrilic amides, imides, and nitrides. I. The equilibrium $4NH_3(g) + 2P(r) = 2PN_2H(s) + 5H_2(g)$ ", *Inorg. Chem.* **1976**, *15*, 1055-1059.
- [34] F. Friedrichs, "Critical Phenomena in Binary Systems", *J. Am. Chem. Soc.* **1913**, *35*, 1866-1883.
- [35] J. Hertrampf, N. S. A. Alt, E. Schlücker, R. Niewa, "Three Solid Modifications of $Ba[Ga(NH_2)_4]_2$: A Soluble Intermediate in Ammonothermal GaN Crystal Growth", *Eur. J. Inorg. Chem.* **2017**, 902-909.
- [36] H. Jacobs, U. Fink, "Über natrium- und kaliumamidometallate des calciums, strontiums und europiums", *J. Less Common Met.* **1979**, *63*, 273-286.
- [37] F. Golinski, H. Jacobs, "Crystal Structure of Hexamine Cyclotriphosphazene, $P_3N_3(NH_2)_6$ ", *Z. Anorg. Allg. Chem.* **1994**, *620*, 965-968.
- [38] H. Jacobs, R. Kirchgässner, "Hexaminecyclotriphosphazenehemiammoniat, $P_3N_3(NH_2)_6 \cdot 0.5 NH_3$, a Product of High Pressure Ammonolysis of White Phosphorus", *Z. Anorg. Allg. Chem.* **1990**, *581*, 125-134.
- [39] The terms *dreier* rings, *vierer* rings and *zweier* single chain were coined by Liebau and are derived from the German words "dreier, vierer and zweier"; a *dreier* ring comprises three tetrahedra centers, a *vierer* ring four tetrahedra centers, a *zweier* chain can be described as two polyhedra within one repeating unit of the linear part of the chain.
- [40] F. Liebau, "Structural Chemistry of Silicates", Springer, Berlin, **1985**.
- [41] S. Schimmel, M. Lindner, T. G. Steigerwald, B. Hertweck, T. M. M. Richter, U. Künecke, N. S. A. Alt, R. Niewa, E. Schlücker, P. J. Wellmann, "Determination of GaN solubility in supercritical ammonia with NH_4F and NH_4Cl mineralizer by in situ x-ray imaging of crystal dissolution", *J. Cryst. Growth* **2015**, *418*, 64-69.

- [42] T. G. Steigerwald, J. Balouschek, B. Hertweck, A.-C. L. Kimmel, N. S. A. Alt, E. Schlücker, "In situ investigation of decomposing ammonia and ammonobasic solutions under supercritical conditions via UV/vis and Raman Spectroscopy", *J. Supercrit. Fluids* **2018**, *134*, 96-105.
- [43] A. Stock, B. Hoffmann, "Die Einwirkung von Ammoniak auf Phosphorpentasulfid und der Phosphorstickstoff, P_3N_5 ", *Ber. Dtsch. Chem. Ges.* **1903**, *36*, 314-319.
- [44] R. Suhrmann, K. Clusius, "Über die Reindarstellung der Alkalimetalle", *Z. Anorg. Allg. Chem.* **1926**, *152*, 52-58.
- [45] F. W. Karau, *Dissertation*, Ludwig-Maximilians-Universität München (Germany) **2007**.
- [46] A. Coelho, *TOPAS Academic, Version 6*, Coelho Software, Brisbane (Australia), **2016**.
- [47] *OPUS/IR*, Bruker Analytik GmbH, Karlsruhe, **2000**.

5 Sr₃P₃N₇: Complementary Approach of Ammonothermal and High-Pressure Methods

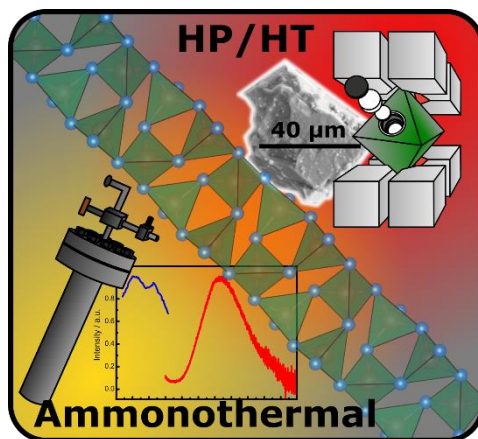
published in: *Chem. Eur. J.* **2020**, *26*, 6257 - 6263.

authors: Mathias Mallmann, Sebastian Wendl, Philipp Strobel, Peter J. Schmidt, and Wolfgang Schnick

DOI: 10.1002/chem.202000297

Reprinted (adapted) with permission for non-commercial use from *Chemistry – A European Journal* (open access). Copyright 2020 John Wiley and Sons.

Abstract. Nitridophosphates exhibit an intriguing structural diversity with different structural motifs, for example, chains, layers or frameworks. In this contribution the novel nitridophosphate Sr₃P₃N₇ with unprecedented *dreier* double chains is presented. Crystalline powders were synthesized using the ammonothermal method, while single crystals were obtained by high-pressure multianvil technique. The crystal structure of Sr₃P₃N₇ was solved and refined from single-crystal X-ray diffraction and confirmed by powder X-ray methods. Sr₃P₃N₇ crystallizes in monoclinic space group *P2/c*. Energy-dispersive X-ray and Fourier-transformed infrared spectroscopy were conducted to confirm the chemical composition, as well as the absence of NH_x functionality. The optical bandgap was estimated to be 4.4 eV using diffuse reflectance UV/Vis spectroscopy. Upon doping with Eu²⁺, Sr₃P₃N₇ shows a broad deep-red to infrared emission ($\lambda_{em} = 681$ nm, $fwhm \approx 3402$ cm⁻¹) with an internal quantum efficiency of 42 %.



5.1 Introduction

Due to the fact that the element combination P/N is isoelectronic to Si/O, nitridophosphates exhibit structural analogies to silicates and are built up from condensed or non-condensed PN₄ tetrahedra. In recent years, numerous nitridophosphates have been synthesized with a high structural diversity with different degrees of condensation κ (ratio of tetrahedra centers to ligands) ranging from 1/4 to 4/7.^[1] Thereby, different structural motifs like non-condensed tetrahedra, chains, layers or frameworks can occur.^[2–5] Particularly due to their structural diversity, these compounds exhibit diverse, interesting physical properties, for example luminescence upon doping with Eu²⁺. So far, P/N-network and -layer compounds such as MP₂N₄ ($M = \text{Ca, Sr, Ba}$), Ba₃P₅N₁₀X ($X = \text{Cl, Br, I}$) or BaP₆N₁₀NH were used as host lattices, almost covering emission in the entire visible spectrum.^[6–9] Especially, Ba₃P₅N₁₀Br, crystallizing in a zeolite-like structure, exhibits intriguing luminescence properties and is discussed as natural-white-light single emitter, demonstrating nicely the potential of nitridophosphate materials.^[7]

But in contrast to silicates, only a few nitridophosphates could be synthesized under ambient pressure conditions (e.g., Ca₂PN₃, Li₁₀P₄N₁₀).^[3, 10, 11] This is due to the fact that the appropriate temperature range for crystallization of nitridophosphates is significantly beyond the decomposition temperature of the most important starting material P₃N₅, which can be circumvented by applying high-pressure methods.

Among these, the multianvil approach is the most frequently employed method, following Le Chatelier's principle in order to compensate thermal decomposition. Over the years, different synthesis strategies using the multianvil approach were developed, including the azide route, high-pressure metathesis or the synthesis with ammonium chloride as mineralizer.^[5, 6, 12] The most valuable advantage of this technique is that the enormous pressure allows for sufficient temperatures for the reconstructive cleavage of P–N bonds. Furthermore, in many cases these high temperatures enable the formation of single crystals, facilitating structure elucidation significantly. However, a drawback of such high-pressure methods is the low sample volume, especially in the context of materials characterization and application.

Therefore, a promising alternative for nitridophosphate synthesis is the ammonothermal approach as a medium pressure method. Herein, the reduced pressure, compared to the multianvil technique, is compensated by the usage of a highly reactive supercritical ammonia atmosphere. In 1997 Jacobs and coworkers used this approach to synthesize K₃P₆N₁₁.^[13] In the meantime, the ammonothermal method enabled synthesis of nitridophosphates with isolated tetrahedra units, chains, layers and frameworks.^[14, 15] Even nitridophosphates like SrP₈N₁₄ or Li₁₈P₆N₁₆, which were so far only accessible by the high-pressure multianvil approach, could be synthesized under ammonothermal

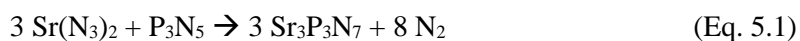
conditions in high yield, simplifying the investigation of their physical properties significantly. Although, the ammonothermal method was already used for synthesis of numerous nitride materials,^[16–22] the crystal growth of ternary or quaternary nitrides during ammonothermal synthesis, except for a few examples like Mg₂PN₃ or MTaN₂ (*M* = Na, K, Rb, Cs), is still challenging.^[15, 23]

In this contribution, we present a combination of medium- and high-pressure methods with their respective advantages for the investigation of unknown nitridophosphates. Herein, we report on Sr₃P₃N₇ as a case study for a complementary approach of ammonothermal and multianvil syntheses. Sr₃P₃N₇ extends the class of ternary alkaline earth nitridophosphates by the degree of condensation of $\kappa = 3/7$. Structure elucidation was based on single-crystal X-ray diffraction data, enabled by high-pressure synthesis, while ammonothermal methods facilitated bulk synthesis targeting for further analysis as well as studies on the luminescence properties of Sr₃P₃N₇:Eu²⁺.

5.2 Results and Discussion

5.2.1 Synthesis

The title compound initially has been observed in heterogeneous products obtained by ammonothermal as well as high-pressure methods, targeting new nitridophosphates with a low degree of condensation. While high-pressure high-temperature synthesis leads to suitable single crystals for structure elucidation, ammonothermal synthesis provided the highest yield of bulk samples, expressing the complementary approach. The synthesis of single crystals was started from stoichiometric amounts of Sr(N₃)₂ and P₃N₅ according to Equation 5.1 together with small amounts of EuCl₂. The starting mixture was treated by high-pressure high-temperature reaction at 5 GPa and 1270 K. These reaction conditions were achieved by using a hydraulic 1000 t press and a modified Walker-type multianvil apparatus.^[24, 25]



Analogously, translucent orange Sr₃P₃N₇:Eu²⁺ crystals of up to 40 μm in length were isolated (see Scanning electron microscopy section). After optimizing the synthesis based on the results of single-crystal X-ray diffraction and energy dispersive X-ray spectroscopy, bulk samples of Sr₃P₃N₇ were prepared under ammonothermal conditions in custom-built high-temperature autoclaves using SrH₂, P₃N₅ and the ammonobasic mineralizer NaN₃. NaN₃ decomposes at elevated temperatures and forms NaNH₂ in situ, which increases the solubility of the other starting materials by formation of

intermediate species (e.g. Na₂Sr₃(NH₂)₈, Na₁₀[P₄(NH)₆N₄](NH₂)₆(NH₃)_{0.5} or P₃N₃(NH₂)₆) which have already been observed under ammonothermal conditions at temperatures around 670 K.^[26–28] Subsequent heating to 1070 K, reaching a maximum pressure of 140 MPa in the autoclave, resulted in synthesis of Sr₃P₃N₇ as a crystalline white powder, which hydrolyses slowly on exposure to moist air. The product was therefore washed with dry ethanol to remove residual mineralizer and intermediate species. Analogous syntheses with red phosphorus instead of P₃N₅ also resulted in the desired product. Doping with Eu²⁺ (nominal concentration of 2 mole% regarding to Sr) in the form of Eu(NH₂)₂ resulted in deep red luminescence of Sr₃P₃N₇:Eu²⁺ when irradiated with UV light (see Luminescence section).

5.2.2 Crystal structure

The crystal structure of Sr₃P₃N₇ was solved and refined from single-crystal X-ray diffraction data in monoclinic space group *P2/c* (no. 13). Details on the structure determination are summarized in Table 5.1. Atomic coordinates and anisotropic displacement parameters are given in Table D1 and D2 in the Supporting Information. Selected interatomic distances and bond angles are summarized in the Supporting Information (Table D3). With $\kappa = n(\text{P})/n(\text{N}) = 3/7$, Sr₃P₃N₇ has a hitherto unknown degree of condensation of an alkaline earth nitridophosphate and is composed of infinite PN₄-tetrahedra *dreier* double chains. A degree of condensation of $\kappa = 3/7$ is already known for rare earth nitridophosphates (RE₂P₃N₇ with RE = La, Ce, Pr, Nd, Sm, Eu, Ho, Yb), however, there is no structural correlation between these compounds.^[29] Apart from Ca₂PN₃, Sr₃P₃N₇ is the only known alkaline earth nitridophosphate with a chain structure, while Mg₂PN₃ crystallizes strictly speaking in a wurtzite-type superstructure and can be interpreted as a double nitride.^[3, 30] The chains in Sr₃P₃N₇ show a periodicity of P = 3 and a stretching factor of $f_s = 0.90$ (see Figure 5.1) and are built up from *dreier*-rings according to Liebau.^[31, 32] Two of these *dreier*-rings, which are structurally related to each other by a rotating mirror axis (*2/m*), are connected via two common corners forming an additional *vierer*-ring. The resulting [P₆N₁₆]-units were already found in Li₁₈P₆N₁₆ as non-condensed [P₆N₁₆]¹⁸⁻ anion.^[14, 33] In the title compound these subunits are connected via two common corners on each side, forming infinite chains. The P–N distances vary from 1.575 to 1.683 Å. As expected, the shortest distances belong to the terminal P(2)–N(2) atoms. The corresponding N–P–N bond angles are between 103.3(5) and 115.0(4)°. Angles as well as distances are in good agreement with values observed in other nitridophosphates described in literature.^[3, 4, 13, 29]

Table 5.1. Crystallographic data of Sr₃P₃N₇ (synthesized by the multianvil approach) obtained from single-crystal X-ray diffraction.

Formula	Sr ₃ P ₃ N ₇
Crystal system	monoclinic
Space group	<i>P2/c</i> (no. 13)
<i>a</i> / Å	6.882(8)
<i>b</i> / Å	7.416(9)
<i>c</i> / Å	7.036(8)
β / °	104.96(3)
Cell volume / Å ³	346.9(7)
Formula units/cell	2
Density / g·cm ⁻³	4.345
Crystal size / mm	0.02x0.02x0.03
μ / mm ⁻¹	23.617
<i>T</i> / K	298(2)
Diffractometer	Bruker D8 Quest
Radiation / Å	Mo- <i>K</i> _{α} (0.71073)
<i>F</i> (000)	416
θ range / °	2.7 - 30.5
Total no. of reflections	3621
No. of independent reflections	1064
Observed reflections ($F^2 > 2\sigma(F^2)$)	728
<i>R</i> _{int} ; <i>R</i> _{σ}	0.0858; 0.0970
Structure solution	SHELXT
Structure refinement	SHELXL
Refined parameters	61
Goodness of fit (χ^2)	1.044
<i>R</i> 1 (all data); <i>R</i> 1 ($F^2 > 2\sigma(F^2)$)	0.100; 0.059
<i>wR</i> 2 (all data); <i>wR</i> 2 ($F^2 > 2\sigma(F^2)$)	0.131; 0.117
$\Delta\rho_{\max}$; $\Delta\rho_{\min}$ [e·Å ⁻³]	1.892, -1.790

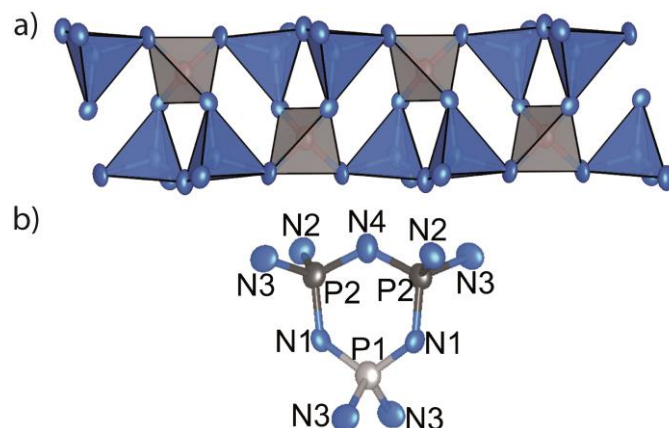


Figure 5.1. Infinite dreier double chain (a) and dreier-ring subunit (b). Thermal ellipsoids are depicted at 90% probability.

The infinite chains are oriented along $[001]$ and are stacked congruently in a and b (see Figure 5.2). The crystal structure contains two crystallographically different Sr sites. The Sr1 site is located between two chains stacked along $[100]$ and is coordinated by 10 N atoms with distances between 2.740(9) and 3.068(10) Å. In contrast, the second Sr site (Sr2) is located between two chains stacked along $[010]$ and is coordinated by 9 N atoms with distances ranging from 2.504(10) to 3.283(10) Å. The coordination polyhedra of both sites are illustrated in Figure D1 in the Supporting Information. All Sr–N distances are in good agreement with values from other Sr (oxo)nitridophosphates known from literature (e.g. SrP_2N_4 , $\text{SrP}_3\text{N}_5\text{O}$, $\text{Sr}_3\text{P}_6\text{O}_6\text{N}_8$).^[34–36]

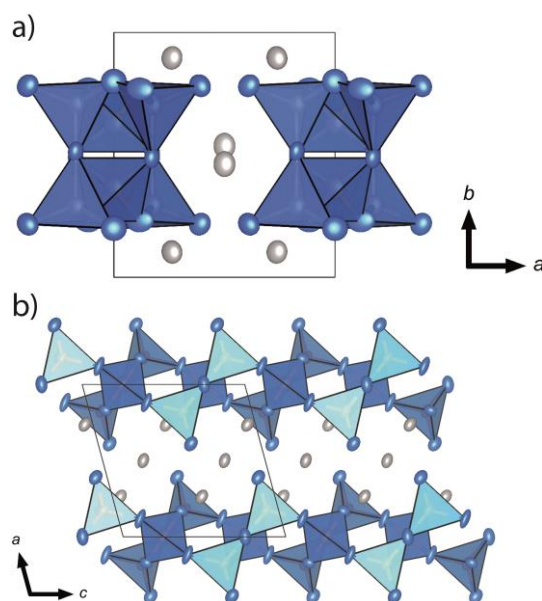


Figure 5.2. Crystal structure of $\text{Sr}_3\text{P}_3\text{N}_7$ viewed along $[001]$ (a) and $[010]$ (b). PN_4 tetrahedra and N atoms are depicted in blue, Sr atoms in gray. Thermal ellipsoids are depicted at 90% probability.

To confirm the structure model obtained from single-crystal X-ray data, a PXRD measurement and subsequent Rietveld refinement were conducted (Figure 5.3). The refined crystallographic data as well as Wyckoff positions are summarized in Table D4 and D5 in the Supporting Information. As described above (Synthesis section), residual mineralizer (NaNH_2) can be removed by washing with dry ethanol. However, the sample partially decomposes during the washing process, resulting in the formation of an amorphous side-phase. Due to this fact, the unwashed sample was used for Rietveld refinement. A comparison of washed and unwashed samples is illustrated in Figure D2 in the Supporting Information.

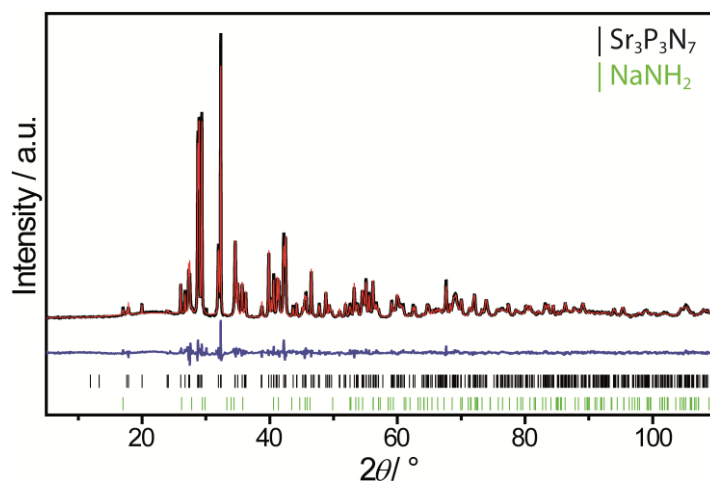


Figure 5.3. Rietveld refinement of PXRD measurements of ammonothermally synthesized $\text{Sr}_3\text{P}_3\text{N}_7$ with experimental data (black line), calculated data (red line), difference profile (blue line) and reflection positions ($\text{Sr}_3\text{P}_3\text{N}_7$: black bars, NaNH_2 : green bars).

5.2.3 Scanning electron microscopy

Energy dispersive X-ray (EDX) spectroscopy was used for determination of the chemical composition. The determined atomic ratios are in good agreement with the expected chemical formulas (see Table D5 in the Supporting Information). Traces of europium can be attributed to doping of the sample and oxygen impurities to surface hydrolysis of the products. Furthermore, a scanning electron micrograph of the product was collected and is illustrated in Figure 5.4.

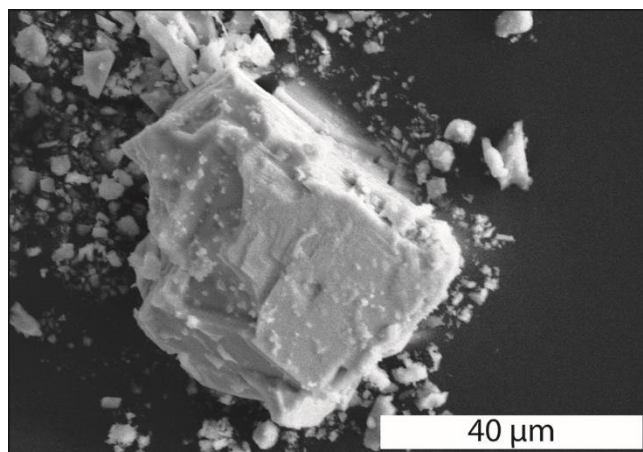


Figure 5.4. SEM image of a Sr₃P₃N₇ single crystal obtained from high-pressure synthesis.

5.2.4 Fourier Transformed Infrared spectroscopy

A FTIR spectrum was recorded in order to prove the absence of any NH_x functionality in Sr₃P₃N₇. The spectrum (see Figure D3 in the Supporting Information) shows no significant absorption bands around 3000 cm⁻¹, indicating the absence of N–H groups in accordance to the crystal structure obtained from single-crystal X-ray diffraction, since the presence of imide or amide groups would lead to strong absorption bands.^[4] Weak signals could be attributed to partial surface hydrolysis of the product. The absorption bands between 500 and 1300 cm⁻¹ can be attributed to symmetric and asymmetric stretching modes of the P–N-framework and are characteristic for nitridophosphates.

5.2.5 UV/Vis spectroscopy

Diffuse reflectance UV/Vis spectroscopy was conducted to estimate the optical bandgap of the undoped sample. Therefore, the Kubelka-Munk function $F(R) = (1-R)^2/2R$ was used to convert the measured diffuse reflectance spectrum to a pseudoabsorption spectrum.^[37] A Tauc plot (see Figure 5.5) was then used to estimate the optical bandgap by plotting $(F(R) \cdot h\nu)^{1/n}$ versus $h\nu$ (with $n = 1/2$, assuming direct transition) and drawing of a tangent at the inflection point.^[38] The diffuse reflectance spectrum shows an absorption band around 250 nm (see Figure D4 in the Supporting Information). The determined bandgap is approximately 4.4 eV.

A diffuse reflectance spectrum of the Eu²⁺ doped sample is illustrated in Figure D5 in the Supporting Information. It shows an additional broad absorption band between 400 and 550 nm, which can be attributed to dopant absorption and is in good agreement with the corresponding excitation spectrum (see Luminescence section).

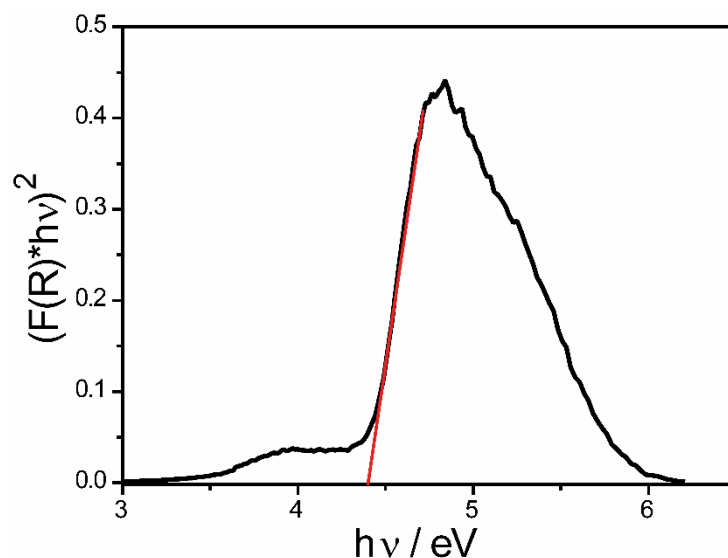


Figure 5.5. Tauc plot (black line) of ammonothermally synthesized Sr₃P₃N₇. Red line as a tangent at the inflection point.

5.2.6 Luminescence

Luminescence properties of Sr₃P₃N₇:Eu²⁺ were measured from crystalline powder samples. Sr₃P₃N₇:Eu²⁺ shows deep-red luminescence when irradiated with UV to blue light (see Figure D6 in the Supporting Information). The emission spectrum ($\lambda_{\text{exc}} = 450$ nm) and the excitation spectrum are illustrated in Figure 5.6. The excitation spectrum has two maxima at around 405 and 465 nm, while the emission spectrum (2 mol-% Eu regarding to Sr) shows one broad band in the deep red to infrared region ($\lambda_{\text{em}} = 681$ nm) with a full width at half maximum (fwhm) of 162 nm/3402 cm⁻¹.

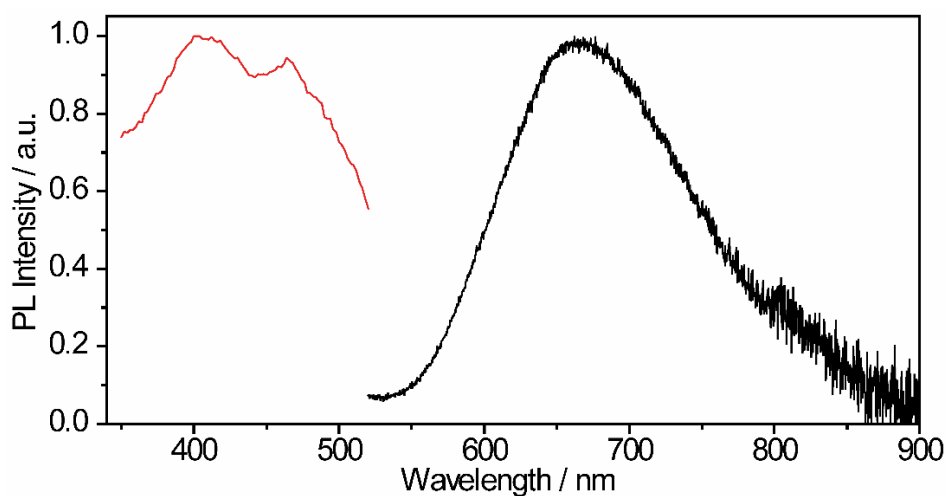


Figure 5.6. Excitation (red line) and emission (black line) spectra of ammonothermally synthesized Sr₃P₃N₇:Eu²⁺.

The broad emission band probably results from the different coordination of the cations (see Crystal structure section). In order to capture the complete emission spectrum, a second spectrometer was used for the measurement ($\lambda_{\text{exc}} = 410 \text{ nm}$) of the emission in the IR region beyond 800 nm. This leads to the higher background level above 800 nm. The internal quantum efficiency (IQE) was determined with an excitation wavelength of 438 nm to be 42% in the range up to 800 nm. These luminescent properties make Sr₃P₃N₇:Eu²⁺ interesting, as such materials may be applied in horticultural lighting, as they can convert green light into the red to IR spectral range with increased photosynthesis quantum efficiency. A further possible application field is, for example, hyper- or multispectral imaging, with diverse applications in e.g. agriculture, automated driving or molecular biology.^[39, 40]

5.3 Conclusions

In this contribution we present a complementary approach of ammonothermal and multianvil techniques as a powerful combination for a simplified and much faster access to a detailed structural and physical analysis of nitridophosphates. Exploitation of the advantages of each method leads to the discovery of the new nitridophosphate Sr₃P₃N₇. Thereby, the best crystallization conditions were realized via a high-pressure approach using the azide route, allowing higher temperatures during syntheses compared to the ammonothermal approach. The structure model was solved and refined from single-crystal X-ray diffraction data. Sr₃P₃N₇ is composed of unprecedented *dreier* double chains made up of PN₄ tetrahedra with a degree of condensation $\kappa = 3/7$, which is hitherto unknown for alkaline earth nitridophosphates. Due to larger sample volumes, studies on the physical properties of the title compound were carried out with bulk samples obtained from ammonothermal synthesis. The bandgap (4.4 eV) was determined using diffuse reflectance spectroscopy. Upon doping with Eu²⁺, Sr₃P₃N₇ exhibits a broad emission band in the deep-red to infrared region ($\lambda_{\text{em}} = 681 \text{ nm}$, $\text{fwhm} \approx 3402 \text{ cm}^{-1}$) with an internal quantum efficiency of 42%, making it practically interesting for commercial applications (e.g. horticultural lighting). For this purpose, stoichiometry and doping concentration optimization as major parts of an industrial process development will further improve the luminescence efficiency.

5.4 Experimental Section

All manipulations were conducted in argon-filled gloveboxes (Unilab, MBraun, Garching, O₂ < 1 ppm, H₂O < 1 ppm) under exclusion from oxygen and moisture because of the air-sensitivity of starting materials and products. A vacuum line ($\leq 0.1 \text{ Pa}$) with argon and ammonia (both: Air Liquide, 99.999%) supply was used for filling of the autoclaves with NH₃. The gases were further

purified by gas cartridges (Micro Torr FT400-902 (for Ar) and MC400-702FV (for NH₃), SAES Pure Gas Inc., San Luis Obispo, CA, USA), providing a purity level of < 1 ppbV H₂O, O₂ and CO₂.

5.4.1 Synthesis of Eu(NH₂)₂

Eu(NH₂)₂ was synthesized ammonothermally starting from Eu metal (99.99 %, smart elements). The experiment was carried out analogously to the synthesis described in literature.^[41]

5.4.2 Synthesis of P₃N₅

P₃N₅ was synthesized following Stock et al.^[42] by ammonolysis of P₄S₁₀ (Sigma Aldrich, 99%) at 1125 K for 4 h (heating rate: 5 K/min). Before reaction, the silica tube was saturated with NH₃ for 4 h. After cooling down to room temperature (5 K/min), the received product was washed in multiple steps with ethanol, water and acetone and dried under vacuum. Powder X-ray diffraction was conducted to confirm phase purity.

5.4.3 Synthesis of Sr(N₃)₂

Sr(N₃)₂ was synthesized starting from SrCO₃ (Sigma Aldrich, 99.995%) and *in situ* formed HN₃ (using aqueous NaN₃ (Acros Organics, 99%) and a cation exchanger (Amberlyst 15)) following the syntheses of Suhrmann and Karau.^[43, 44] HN₃ was slowly added to an aqueous suspension of SrCO₃ until the liquid turned clear. After filtration, the solution was evaporated under reduced pressure (50 mbar, 40 °C), recrystallized from acetone and dried under vacuum. FTIR and PXRD measurements were conducted to confirm phase purity.

Caution: Since HN₃ solutions are potentially explosive and the vapor is highly poisonous, special care issues are necessary.

5.4.4 Ammonothermal synthesis

Sr₃P₃N₇ was synthesized under ammonothermal conditions starting from 0.5 mmol P₃N₅ (81.5 mg), 1.5 mmol SrH₂ (134.4 mg, Materion, 99.5%) and 5 mmol NaN₃ (325.0 mg, Sigma-Aldrich, 99.5%) as ammonobasic mineralizer. For the synthesis of Eu²⁺-doped product 0.03 mmol Eu(NH₂)₂ (5.5 mg) was added to the reaction mixture. The starting materials were ground using an agate mortar and transferred into a Ta-liner, which protects the reaction mixture against autoclave impurities. The liner was placed in a high-temperature autoclave constructed of a nickel based super-alloy (Haynes® 282®),

max. 1100 K, 170 MPa, 10 mL). The autoclave is sealed with a lid via flange joints using a silver coated Inconel[®] 718 ring (GFD seals). An Inconel[®] 718 high-pressure tube connects the lid with a hand valve (SITEC), which is equipped with a pressure transmitter (HBM P2VA1/5000 bar) and a bursting disc (SITEC). After evacuation, the sealed autoclave was cooled to 198 K using an ethanol/liquid nitrogen mixture and filled with NH₃ (≈ 3.7 mL). A mass flow meter (D-6320-DR, Bronkhorst, Ruurlo, Netherlands) was used for detection of the amount of inserted ammonia. The filled autoclave was heated in two steps (heated to 670 K within 2 h, held at this temperature for 16 h, heated to 1070 K within 3 h and held at this temperature for 96 h) to 1070 K reaching a maximum pressure of 140 MPa. After cooling to room temperature and removal of NH₃, the reaction products were separated under argon, washed with ethanol and dried under vacuum. While the undoped product exhibit a white color, the Eu²⁺-doped sample is orange.

5.4.5 High-pressure synthesis

Single crystals of Sr₃P₃N₇:Eu²⁺ were synthesized starting from stoichiometric amounts of Sr(N₃)₂ and P₃N₅ as well as small amounts of EuCl₂ (Strem Chemicals, 99.9%) as dopant using a modified Walker-type multianvil press.^[24, 25] The reactants were mixed and grounded in an agate mortar and packed in a capsule of hexagonal boron nitride (Henze, Kempten). After sealing with a BN-cap the sample was placed in the middle of a MgO octahedron (doped with 5 % Cr₂O₃, edge length 18 mm, Ceramic Substrates & Components Ltd, Isle of Wight) using two MgO spacers (Cesima Ceramics, Wust-Fischbach). To ensure heating of the sample, the octahedron was further equipped with two graphite furnaces (Schunk Kohlenstofftechnik GmbH, Zolling), a ZrO₂ tube (Cesima Ceramics, Wust-Fischbach) for thermal insulation and two Mo plates for electrical contact between the graphite furnaces and the anvils of the multianvil press. The assembled octahedron was placed between eight WC cubes (doped with 7% Co, Hawedia, Marklkofen, Germany) with truncated edges (edge length 11 mm), which were separated with pyrophyllite gaskets (Ceramic Substrates & Components, Isle of Wight, UK). Further details on the experimental setup and the multianvil apparatus are given in literature.^[25] The sample was slowly compressed to 5 GPa and subsequently heated to 1270 K within 30 min. After 30 min at 1270 K the sample was allowed to cool down to room temperature within 30 minutes and slowly decompressed. The crystalline orange product was isolated and stored under argon.

5.4.6 Single-crystal X-ray diffraction

Single crystals of Sr₃P₃N₇:Eu²⁺ were placed and sealed in glass capillaries (Hilgenberg GmbH) in argon atmosphere for single-crystal XRD measurements. The data were collected using a Bruker D8

Quest diffractometer with Mo- K_{α} radiation ($\lambda = 0.71073 \text{ \AA}$). The measured data were indexed and integrated with the software package APEX3.^[45, 46] APEX3 was also used for semi-empirical absorption corrections (SADABS) and the determination of the space group.^[46–48] The crystal structure was solved using the SHELXT algorithm and refined by full-matrix least-squares methods using WinGX with implemented SHELXL.^[49–51]

CCDC 1975990 contains the supplementary crystallographic data for this paper. These data are provided free of charge by The Cambridge Crystallographic Data Centre through the CCDC/FIZ Karlsruhe deposition service.

5.4.7 Powder X-ray diffraction

For powder XRD measurements, the grounded product was filled and sealed in a glass capillary ($d = 0.3 \text{ mm}$, Hilgenberg GmbH). A Stoe STADI P diffractometer with Cu- $K_{\alpha 1}$ ($\lambda = 1.5406 \text{ \AA}$) radiation, Ge(111) monochromator and Mythen 1K detector in modified Debye-Scherrer geometry was used for the measurements. TOPAS was used for Rietveld refinement of the data.^[52]

5.4.8 Scanning electron microscopy

A scanning electron microscope (Dualbeam Helios Nanolab G3 UC (FEI), equipped with an EDX detector (X-Max 80 SDD, Oxford instruments)) was used for imaging of the crystals and for EDX measurements. Thereto, the crystallites were placed on adhesive carbon pads. A high-vacuum sputter coater (BAL-TEC MED 020, Bal Tec A) was used for coating of the samples with a conductive carbon film.

5.4.9 Fourier Transformed Infrared (FTIR) spectroscopy

An IR spectrum (range between 400 and 4000 cm^{-1}) were collected using a FTIR-IFS 66 v/S spectrometer (Bruker). The samples were mixed with KBr (Acros Organics, 99%) and pressed into pellets under argon. OPUS was used for evaluation of the measurements.^[53]

5.4.10 UV/Vis spectroscopy

The optical bandgaps were estimated using UV/Vis spectroscopy. For this purpose, diffuse reflectance measurements of the samples at room temperature were performed using a Jasco V-650

UV/Vis spectrophotometer equipped with Czerny-Turner mount, photomultiplier tube detector and deuterium (190 - 350 nm) / halogen (330 - 900 nm) lamps as light sources.

5.4.11 Luminescence

A microcrystalline powder of Sr₃P₃N₇:Eu²⁺ was used to determine luminescence properties. The measurement was conducted on a PTFE sample holder using an in-house built system based on a 5.3" integration sphere and a spectrofluorimeter equipped with a 150 W Xe lamp, two 500 mm Czerny–Turner monochromators, 1800 1/mm lattices, and 250/500 nm lamps, with a spectral range from 230 to 820 nm ($\lambda_{\text{exc}} = 450$ nm). Additional data from a spectrometer sensitive in the 600–1100 nm wavelength range (Avantes) ($\lambda_{\text{exc}} = 410$ nm) were used to obtain the complete emission band by merging data of both measurements. A comparison of integrated emission intensities and absorption at excitation wavelength ($\lambda_{\text{exc}} = 438$ nm) of the sample with reference materials (BaSO₄, Merck for white standard DIN 5033 commercial (Sr,Ca)AlSiN₃:Eu²⁺, Mitsubishi Chemical, and Y₃Al₅O₁₂:Ce³⁺, Philips) were conducted to determine the internal quantum efficiency (IQE).

5.5 Acknowledgements

We acknowledge the Deutsche Forschungsgemeinschaft (DFG) for financial support within the research group “Chemistry and Technology of the Ammonothermal Synthesis of Nitrides” (FOR 1600), project SCHN377/16-2. We also want to thank Arthur Haffner for single-crystal measurements, Marion Sokoll for FTIR measurements and Lisa Gamperl for EDX measurements (all at Department of Chemistry, LMU Munich) as well as the group of Prof. Dr. E. Schlücker for fabrication of the autoclaves (FAU Erlangen-Nürnberg).

5.6 References

- [1] S. D. Kloß, W. Schnick, "Nitridophosphates – A Success Story of Nitride Synthesis", *Angew. Chem.* **2019**, *131*, 8015-8027; *Angew. Chem. Int. Ed.* **2019**, *58*, 7933-7944.
- [2] W. Schnick, J. Luecke, "Synthesis and Crystal Structure of Lithium Phosphorus Nitride Li₇PN₄: The First Compound Containing Isolated PN₄-Tetrahedra", *J. Solid State Chem.* **1990**, *87*, 101-106.
- [3] W. Schnick, V. Schultz-Coulon, "Ca₂PN₃ - A Novel Phosphorus(V) Nitride with One-Dimensional Infinite Chains of Corner-Sharing PN₄ Tetrahedra", *Angew. Chem.* **1993**, *105*, 308-309; *Angew. Chem. Int. Ed. Engl.* **1993**, *32*, 280-281.

- [4] S. Wendl, W. Schnick, "*SrH₄P₆N₁₂ and SrP₈N₁₄: Insights into the Condensation Mechanism of Nitridophosphates under High Pressure*", *Chem. Eur. J.* **2018**, *24*, 15889-15896.
- [5] S. D. Kloß, W. Schnick, "*Rare-Earth-Metal Nitridophosphates through High-Pressure Metathesis*", *Angew. Chem.* **2015**, *127*, 11402-11405; *Angew. Chem. Int. Ed.* **2015**, *54*, 11250-11253.
- [6] F. J. Pucher, A. Marchuk, P. J. Schmidt, D. Wiechert, W. Schnick, "*Luminescent Nitridophosphates CaP₂N₄:Eu²⁺, SrP₂N₄:Eu²⁺, BaP₂N₄:Eu²⁺, and BaSr₂P₆N₁₂:Eu²⁺*", *Chem. Eur. J.* **2015**, *21*, 6443-6448.
- [7] A. Marchuk, W. Schnick, "*Ba₃P₅N₁₀Br:Eu²⁺: A Natural-White-Light Single Emitter with a Zeolite Structure Type*", *Angew. Chem.* **2015**, *127*, 2413-2417; *Angew. Chem. Int. Ed.* **2015**, *54*, 2383-2387.
- [8] A. Marchuk, S. Wendl, N. Imamovic, F. Tambornino, D. Wiechert, P. J. Schmidt, W. Schnick, "*Nontypical Luminescence Properties and Structural Relation of Ba₃P₅N₁₀X:Eu²⁺ (X = Cl, I): Nitridophosphate Halides with Zeolite-like Structure*", *Chem. Mater.* **2015**, *27*, 6432-6441.
- [9] S. Wendl, L. Eisenburger, M. Zipkat, D. Günther, J. P. Wright, P. J. Schmidt, O. Oeckler, W. Schnick, "*BaP₆N₁₀NH:Eu²⁺ as a Case Study – An Imidonitridophosphate Showing Luminescence*", *Chem. Eur. J.*; DOI: 10.1002/chem.201905082.
- [10] E. M. Bertschler, C. Dietrich, T. Leichtweiß, J. Janek, W. Schnick, "*Li⁺ Ion Conductors with Adamantane-Type Nitridophosphate Anions β-Li₁₀P₄N₁₀ and Li₁₃P₄N₁₀X₃ with X=Cl, Br*", *Chem. Eur. J.* **2018**, *24*, 196-205.
- [11] W. Schnick, U. Berger, "*Li₁₀P₄N₁₀ - A Lithium Phosphorus(V) Nitride with the Novel Complex Anion P₄N₁₀¹⁰⁻*", *Angew. Chem.* **1991**, *103*, 857-858; *Angew. Chem. Int. Ed. Engl.* **1992**, *31*, 213-214.
- [12] A. Marchuk, F. J. Pucher, F. W. Karau, W. Schnick, "*A High-Pressure Polymorph of Phosphorus Nitride Imide*", *Angew. Chem.* **2014**, *126*, 2501-2504; *Angew. Chem. Int. Ed.* **2014**, *53*, 2469-2472.
- [13] H. Jacobs, R. Nymwegen, "*Synthesis and Crystal Structure of a Potassium Nitridophosphate, K₃P₆N₁₁*", *Z. Anorg. Allg. Chem.* **1997**, *623*, 429-433.
- [14] M. Mallmann, S. Wendl, W. Schnick, "*Crystalline Nitridophosphates by Ammonothermal Synthesis*", *Chem. Eur. J.* **2020**, *26*, 2067-2072.
- [15] M. Mallmann, C. Maak, R. Niklaus, W. Schnick, "*Ammonothermal Synthesis, Optical Properties, and DFT Calculations of Mg₂PN₃ and Zn₂PN₃*", *Chem. Eur. J.* **2018**, *24*, 13963-13970.
- [16] R. Dwilinski, A. Wyszomolek, J. Baranowski, M. Kaminska, R. Doradziński, H. Jacobs, "*GaN synthesis by ammonothermal method*", *Acta Phys. Pol., A* **1995**, *88*, 833-836.

- [17] J. Hertrampf, P. Becker, M. Widenmeyer, A. Weidenkaff, E. Schlücker, R. Niewa, "Ammonothermal Crystal Growth of Indium Nitride", *Cryst. Growth Des.* **2018**, *18*, 2365-2369.
- [18] J. Li, T. Watanabe, H. Wada, T. Setoyama, M. Yoshimura, "Low-Temperature Crystallization of Eu-Doped Red-Emitting CaAlSiN₃ from Alloy-Derived Ammonometallates", *Chem. Mater.* **2007**, *19*, 3592-3594.
- [19] T. Watanabe, K. Nonaka, J. Li, K. Kishida, M. Yoshimura, "Low temperature ammonothermal synthesis of europium-doped SrAlSiN₃ for a nitride red phosphor", *J. Ceram. Soc. Jpn.* **2012**, *120*, 500-502.
- [20] J. Häusler, L. Neudert, M. Mallmann, R. Niklaus, A.-C. L. Kimmel, N. S. A. Alt, E. Schlücker, O. Oeckler, W. Schnick, "Ammonothermal Synthesis of Novel Nitrides: Case Study on CaGaSiN₃", *Chem. Eur. J.* **2017**, *23*, 2583-2590.
- [21] J. Häusler, S. Schimmel, P. Wellmann, W. Schnick, "Ammonothermal Synthesis of Earth-Abundant Nitride Semiconductors ZnSiN₂ and ZnGeN₂ and Dissolution Monitoring by In Situ X-ray Imaging", *Chem. Eur. J.* **2017**, *23*, 12275-12282.
- [22] M. Mallmann, R. Niklaus, T. Rackl, M. Benz, T. G. Chau, D. Johrendt, J. Minár, W. Schnick, "Solid Solutions of Grimm-Sommerfeld Analogous Nitride Semiconductors II-IV-N₂ (II = Mg, Mn, Zn; IV = Si, Ge): Ammonothermal Synthesis and DFT Calculations", *Chem. Eur. J.* **2019**, *25*, 15887-15895.
- [23] N. Cordes, R. Niklaus, W. Schnick, "Ammonothermal Crystal Growth of ATaN₂ with A = Na, K, Rb, and Cs and Their Optical and Electronic Properties", *Cryst. Growth Des.* **2019**, *19*, 3484-3490.
- [24] D. Walker, "Lubrication, gasketing, and precision in multianvil experiments", *Am. Mineral.* **1991**, *76*, 1092-1100.
- [25] H. Huppertz, "Multianvil high-pressure / high-temperature synthesis in solid state chemistry", *Z. Kristallogr.* **2004**, *219*, 330-338.
- [26] H. Jacobs, U. Fink, "Über natrium- und kaliumamidometallate des calciums, strontiums und europiums", *J. Less Common Met.* **1979**, *63*, 273-286.
- [27] H. Jacobs, S. Pollok, F. Golinski, "Synthesis and Crystal Structure of Na₁₀[P₄(NH)₆N₄](NH₂)₆(NH₃)_{0.5} with an Adamantane-like Anion [P₄(NH)₆N₄]⁴⁻", *Z. Anorg. Allg. Chem.* **1994**, *620*, 1213-1218.
- [28] F. Golinski, H. Jacobs, "Crystal Structure of Hexamine Cyclotriphosphazene, P₃N₃(NH₂)₆", *Z. Anorg. Allg. Chem.* **1994**, *620*, 965-968.
- [29] S. D. Klob, N. Weidmann, R. Niklaus, W. Schnick, "High-Pressure Synthesis of Melilite-type Rare-Earth Nitridophosphates RE₂P₃N₇ and a Ba₂Cu[Si₂O₇]-type Polymorph", *Inorg. Chem.* **2016**, *55*, 9400-9409.

- [30] V. Schultz-Coulon, W. Schnick, "*Mg₂PN₃ and Ca₂PN₃ – Phosphorus(V) Nitrides with Infinite Chains of Corner Sharing PN₄ Tetrahedra*", *Z. Anorg. Allg. Chem.* **1997**, 623, 69-74.
- [31] F. Liebau, "*Structural Chemistry of Silicates*", Springer, Berlin, **1985**.
- [32] The terms *dreier* rings, *vierer* rings and *zweier* single chain were coined by Liebau and are derived from the German words "dreier, vierer and zweier"; a *dreier* ring comprises three tetrahedra centers, a *vierer* ring four tetrahedra centers, a *zweier* chain can be described as two polyhedra within one repeating unit of the linear part of the chain.
- [33] E.-M. Bertschler, C. Dietrich, J. Janek, W. Schnick, "*Li₁₈P₆N₁₆ – A Lithium Nitridophosphate with Unprecedented Tricyclic [P₆N₁₆]¹⁸⁻ Ions*", *Chem. Eur. J.* **2017**, 23, 2185-2191.
- [34] F. W. Karau, L. Seyfarth, O. Oeckler, J. Senker, K. Landskron, W. Schnick, "*The Stuffed Framework Structure of SrP₂N₄: Challenges to Synthesis and Crystal Structure Determination*", *Chem. Eur. J.* **2007**, 13, 6841-6852.
- [35] S. J. Sedlmaier, E. Mugnaioli, O. Oeckler, U. Kolb, W. Schnick, "*SrP₃N₅O: A Highly Condensed Layer Phosphate Structure Solved from a Nanocrystal by Automated Electron Diffraction Tomography*", *Chem. Eur. J.* **2011**, 17, 11258-11265.
- [36] S. J. Sedlmaier, J. Schmedt auf der Günne, W. Schnick, "*Sr₃P₆O₆N₈—a highly condensed layered phosphate*", *Dalton Trans.* **2009**, 4081-4084.
- [37] R. López, R. Gómez, "*Band-gap energy estimation from diffuse reflectance measurements on sol-gel and commercial TiO₂: a comparative study*", *J. Sol-Gel Sci. Technol.* **2012**, 61, 1-7.
- [38] J. Tauc, R. Grigorovici, A. Vancu, "*Optical Properties and Electronic Structure of Amorphous Germanium*", *Phys. Status Solidi B* **1966**, 15, 627-637.
- [39] L. M. Dale, A. Thewis, C. Boudry, I. Rotar, P. Dardenne, V. Baeten, J. A. F. Pierna, "*Hyperspectral Imaging Applications in Agriculture and Agro-Food Product Quality and Safety Control: A Review*", *Appl. Spectrosc. Rev.* **2013**, 48, 142-159.
- [40] A. A. Gowen, Y. Feng, E. Gaston, V. Valdramidis, "*Recent applications of hyperspectral imaging in microbiology*", *Talanta* **2015**, 137, 43-54.
- [41] M. Mallmann, J. Häusler, N. Cordes, W. Schnick, "*Ammonothermal Synthesis of Alkali-Alkaline Earth Metal and Alkali-Rare Earth Metal Carbodiimides: K_{5-x}M_x(CN₂)_{2+x}(HCN₂)_{1-x} (M = Sr, Eu) and Na_{4.32}Sr_{0.68}(CN₂)_{2.68}(HCN₂)_{0.32}*", *Z. Anorg. Allg. Chem.* **2017**, 643, 1956-1961.
- [42] A. Stock, B. Hoffmann, "*Die Einwirkung von Ammoniak auf Phosphorpentasulfid und der Phosphorstickstoff, P₃N₅*", *Ber. Dtsch. Chem. Ges.* **1903**, 36, 314-319.
- [43] R. Suhrmann, K. Clusius, "*Über die Reindarstellung der Alkalimetalle*", *Z. Anorg. Allg. Chem.* **1926**, 152, 52-58.
- [44] F. W. Karau, *Dissertation*, Ludwig-Maximilians-Universität München (Germany) **2007**.
- [45] *SAINT*, Data Integration Software, Madison, Wisconsin, USA, **1997**.
- [46] *APEX 3*, Vers. 2016.2015-2010, Bruker-AXS, Karlsruhe, **2016**.

- [47] G. M. Sheldrick, *SADABS, Multi-Scan Absorption Correction*, v.2, Bruker-AXS, Madison, WI, USA, **2012**.
- [48] *XPREP Reciprocal Space Exploration*, Vers. 6.12, Bruker-AXS, Karlsruhe, **2001**.
- [49] G. M. Sheldrick, "*SHELXT - Integrated space-group and crystal-structure determination*", *Acta Crystallogr. Sect. A* **2015**, 71, 3-8.
- [50] G. M. Sheldrick, *SHELXL-97: A program for crystal structure refinement*, University of Göttingen, Germany, **1997**.
- [51] G. M. Sheldrick, "*Crystal structure refinement with SHELXL*", *Acta Crystallogr. Sect. C* **2015**, 71, 3-8.
- [52] A. Coelho, *TOPAS Academic, Version 6*, Coelho Software, Brisbane (Australia), **2016**.
- [53] *OPUS/IR*, Bruker Analytik GmbH, Karlsruhe, **2000**.

6 Ammonothermal Synthesis of Ba₂PO₃N – An Oxonitridophosphate with Non-Condensed PO₃N Tetrahedra

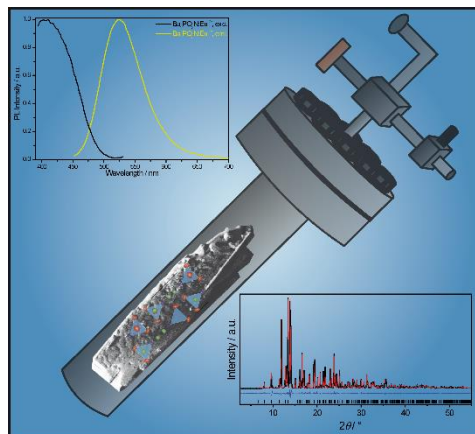
published in: *Eur. J. Inorg. Chem.* **2020**, 2020, 841 - 846.

authors: Sebastian Wendl, Mathias Mallmann, Philipp Strobel, Peter J. Schmidt, and Wolfgang Schnick

DOI: 10.1002/ejic.202000041

Reprinted (adapted) with permission for non-commercial use from *European Journal of Inorganic Chemistry* (open access). Copyright 2020 John Wiley and Sons.

Abstract. The *ortho*-oxonitridophosphate Ba₂PO₃N was synthesized under ammonobasic conditions ($T = 1070$ K, $p = 120$ MPa) in custom-built high-temperature autoclaves, starting from red phosphorus, BaO, NaN₃ and KOH. Thus, single crystals of up to several hundred μm were obtained, which were used for singlecrystal X-ray diffraction. Ba₂PO₃N [$Pnma$ (no. 62), $a = 7.596(2)$, $b = 5.796(1)$, $c = 10.212(3)$ Å, $Z = 4$] crystallizes in the β -K₂SO₄ structure type with non-condensed [PO₃N]⁴⁻ ions and isotypic to its lighter homologues EA₂PO₃N ($EA = \text{Ca, Sr}$). Powder X-ray diffraction, energy dispersive X-ray and Fourier Transformed Infrared spectroscopy corroborate the crystal structure. The optical bandgap was determined by means of diffuse reflectance UV/Vis spectroscopy to be 4.3 eV. Eu²⁺ doped samples show green luminescence ($\lambda_{\text{em}} = 534$ nm, $\text{fwhm} = 85$ nm/2961 cm⁻¹) when irradiated with UV light ($\lambda_{\text{exc}} = 420$ nm). However, Ba₂PO₃N:Eu²⁺ shows strong thermal quenching, even at room temperature.



6.1 Introduction

During the 1960s, Jacobs and co-workers developed the ammonothermal method, in which supercritical ammonia is used as solvent and nitrogen source for the synthesis of various imides, amides and nitrides.^[1–6] Thereby, supercritical ammonia facilitates the crystallization process, as it increases the solubility of the inorganic starting materials, which are quite insoluble in liquid ammonia.^[7, 8] With the first synthesis of GaN in supercritical ammonia in 1995, the ammonothermal approach was established as important method for synthesis and crystal growth of high-quality GaN crystals.^[9–11] Subsequently, the ammonothermal approach turned out as a promising route for explorative synthesis of different (oxide) nitrides such as wurtzite-type Grimm–Sommerfeld analogous nitrides [e.g. InN, II-IV-N₂ (II = Mg, Mn, Zn; IV = Si, Ge), CaGaSiN₃ or Ca_{1-x}Li_xAl_{1-x}Ge_{1+x}N₃ ($x \approx 0.2$)] and oxide nitride perovskites [e.g. *EAMO*₂N (*EA* = Sr, Ba; *M* = Nb, Ta)] as well.^[12–18] Most recently, the syntheses of numerous nitridophosphates with different degrees of condensations κ (i.e. atomic ratio of tetrahedra centers to ligand) could be realized. Here, a great structural diversity ranging from non-condensed tetrahedra groups up to network structure types, exhibiting values for κ from 1/3 to 4/7, was observed.^[19–21] Compared to other synthetic methods towards nitridophosphates, such as condensation reactions, synthesis in pressure ampoules or high-pressure synthesis using the multianvil technique, the ammonothermal method exhibits significant advantages.^[22] This includes the prevention of thermal decomposition of the target compounds, the use of simple starting materials including red phosphorus (P_{red}) as well as large sample volumes for a detailed characterization of their materials properties.^[21]

However, there is no ammonothermally synthesized *ortho*-(oxo)nitridophosphate showing non-condensed [PO_{4-x}N_x]^{(3+x)-} tetrahedra, up to now. Such structural features were only observed in Li₇PN₄, Li₁₄[PON₃]₂O, *EA*₂PO₃N (*EA* = Ca, Sr) and Ho₃[PN₄]O, which were synthesized in ampoules or via high-pressure synthesis, respectively.^[23–26] Especially, the *EA*₂PO₃N compounds are of special interest, as they crystallize isotypically to β -K₂SO₄. Accompanied with a plethora of compounds crystallizing in this structure type, a great diversity of materials properties is observed. Especially, the potential as host lattices for luminescent materials is impressive, covering the whole visible spectrum from red (La*EASiO*₃N:Eu²⁺ with *EA* = Sr, Ba) over green (Ca₂PO₃N:Eu²⁺) to blue (KSrPO₄:Eu²⁺) emission.^[25, 27, 28]

In this contribution, we present the ammonothermal synthesis of the *ortho*-oxonitridophosphate Ba₂PO₃N containing discrete [PO₃N]⁴⁻ ions, extending the degree of condensation range of ammonothermally accessible nitridophosphates to $1/4 \leq \kappa \leq 4/7$. The structure was elucidated using single-crystal X-ray diffraction on ammonothermally grown crystallites with sizes up to several hundreds of μm . Bulk samples were used for further analysis as well as for examination of luminescence properties of Eu²⁺ doped Ba₂PO₃N. Together with earlier reported investigations on

the ammonothermal approach, this work demonstrates once again the high potential of this method regarding synthesis and crystal growth of (oxide) nitride materials.

6.2 Results and Discussion

6.2.1 Synthesis

The oxonitridophosphate Ba₂PO₃N was synthesized ammonothermally using custom-built high-temperature autoclaves made of the nickel-based super-alloy Haynes® 282®. Stoichiometric amounts of P_{red} and BaO were used as starting materials. KOH and NaN₃ were added as additional oxygen and nitrogen sources as well as ammonobasic mineralizers. They form in situ NaNH₂ and KNH₂, which increase the solubility of the other starting materials by the formation of soluble intermediate species, such as mixed amides [e.g. KBa(NH₂)₃] and phosphorus containing compounds like hexaaminocyclotriphosphazene [PN(NH₂)₂]₃, the corresponding ammoniate [PN(NH₂)₂]₃·0.5NH₃ or the imidonitride Na₁₀[P₄(NH)₆N₄](NH₂)₆(NH₃)_{0.5}.^[3, 7, 21, 29–31] When using NaOH instead of KOH, Ba₂PO₃N appears only as side-phase without any single crystals of significant size. The remaining PXRD reflections could not be assigned to any known compound. A possible explanation could be the non-existence of a Na analog to KBa(NH₂)₃, resulting in a lower solubility.

Based on the observation that such intermediates are preferably formed at low temperatures, the reaction mixture was heated in a first step to a temperature of 670 K. After 16 h the autoclave was subsequently heated to 1070 K, reaching a pressure of 120 MPa, in order to transform the intermediate species into the oxonitridophosphate Ba₂PO₃N. Upon adding Eu(NH₂)₂ to the starting materials, the product exhibits green luminescence (see Luminescence section). To prevent the product from autoclave impurities, the reaction mixture was filled into a Ta-liner. In addition, the liner wall acted as a substrate for single-crystal growth of the product. Thereby, single crystals with sizes up to ≈ 600 μm were accessible. Figure 6.1 illustrates ammonothermally grown crystals of Ba₂PO₃N:Eu²⁺. The size of the crystals, which are up to several hundred μm, as well as the fact that the crystals grew on the wall at the upper part of the liner, which is supposed to be the colder zone, suggest a solution based transport and growth mechanism via intermediate species.

The obtained white (Ba₂PO₃N) and yellow (Ba₂PO₃N:Eu²⁺) products are slightly sensitive towards moisture and were therefore washed with dry ethanol to eliminate hygroscopic residual mineralizer and intermediate species.

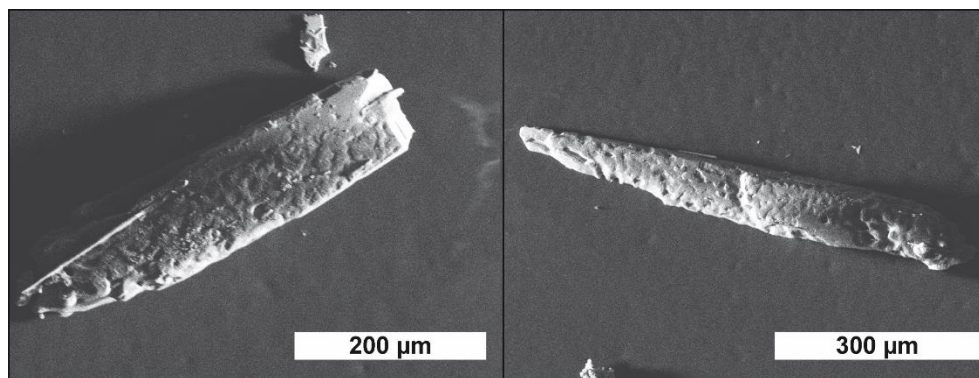


Figure 6.1. SEM images of $\text{Ba}_2\text{PO}_3\text{N}:\text{Eu}^{2+}$ crystals.

6.2.2 Crystal structure

The crystal structure of $\text{Ba}_2\text{PO}_3\text{N}$ was solved and refined from single-crystal X-ray diffraction data in the orthorhombic space group $Pnma$ (no. 62) with lattice parameters $a = 7.596(2)$, $b = 5.796(1)$ and $c = 10.212(3)$ Å. The crystallographic data are summarized in Table 6.1. Wyckoff positions and atomic coordinates, anisotropic displacement parameters, as well as interatomic distances and angles are given in Tables E.1–E.3 (Supporting Information). $\text{Ba}_2\text{PO}_3\text{N}$ crystallizes in the $\beta\text{-K}_2\text{SO}_4$ structure type and is isotypic to its lighter homologues $\text{Ca}_2\text{PO}_3\text{N}$ and $\text{Sr}_2\text{PO}_3\text{N}$.^[25] As expected, the lattice parameters of the three $\text{EA}_2\text{PO}_3\text{N}$ compounds increase linearly with increasing size of the alkaline earth ions (see Figure E.1, Supporting Information). The crystal structure is built up from non-condensed $[\text{PO}_3\text{N}]^{4-}$ tetrahedra (see Figure 6.2) and therefore exhibits a degree of condensation of $\kappa = n(\text{P})/n(\text{O},\text{N}) = 1/4$, which expands the range of ammonothermally accessible degrees of condensation for (oxo)nitridophosphates to $1/4 \leq \kappa \leq 4/7$. The assignment of O and N atoms was carried out in accordance with the structure model of $\text{EA}_2\text{PO}_3\text{N}$ ($\text{EA} = \text{Ca}, \text{Sr}$).^[25] Lattice energy calculations (MAPLE),^[32–35] bond-valance sums (BVS)^[36,37] as well as charge distribution (CHARDI)^[38] calculations support the ordering and show only slight deviations from expected values (see Tables E.4–E.6, Supporting Information). The P–O [1.573(2)–1.602(2) Å] and P–N distances [1.578(2) Å] are in good agreement with bond lengths of other alkaline earth oxonitridophosphates known from literature (e.g. $\text{Ca}_2\text{PO}_3\text{N}$, $\text{Sr}_2\text{PO}_3\text{N}$, $\text{SrP}_3\text{N}_5\text{O}$, $\text{Sr}_3\text{P}_6\text{O}_6\text{N}_8$, $\text{Ba}_3\text{P}_6\text{O}_6\text{N}_8$).^[25, 39–41] The corresponding O/N–P–O/N angles vary between 107.81(9) and 112.6(2)° and deviate only slightly from the regular tetrahedron angle and are also in good agreement with values known from literature. The crystal structure contains two crystallographically different Ba positions.

Table 6.1. Crystallographic data of Ba₂PO₃N obtained from single-crystal X-ray diffraction.

Formula	Ba ₂ PO ₃ N
Crystal system	orthorhombic
Space group	<i>Pnma</i> (no. 62)
<i>a</i> / Å	7.596(2)
<i>b</i> / Å	5.796(1)
<i>c</i> / Å	10.212(3)
Cell volume / Å ³	449.6(2)
Formula units/cell	4
Density / g·cm ⁻³	5.4325
Crystal size / mm	0.01×0.03×0.04
μ / mm ⁻¹	17.640
<i>T</i> / K	296(2)
Diffractometer	Bruker D8 Quest
Radiation / Å	Mo- <i>K</i> _α (0.71073)
<i>F</i> (000)	632
2 θ range / °	3.343 - 35.687
Total no. of reflections	15148
No. of independent reflections	1121
Observed reflections ($F^2 > 2\sigma(F^2)$)	1029
<i>R</i> _{int} ; <i>R</i> _σ	0.0432; 0.0182
Structure solution	SHELXT
Structure refinement	SHELXL
Refined parameters	40
Goodness of fit (χ^2)	1.197
<i>R</i> 1 (all data); <i>R</i> 1 ($F^2 > 2\sigma(F^2)$)	0.0210; 0.0177
<i>wR</i> 2 (all data); <i>wR</i> 2 ($F^2 > 2\sigma(F^2)$)	0.0344; 0.0335
$\Delta\rho_{\max}$; $\Delta\rho_{\min}$ [e·Å ⁻³]	1.050, -1.327

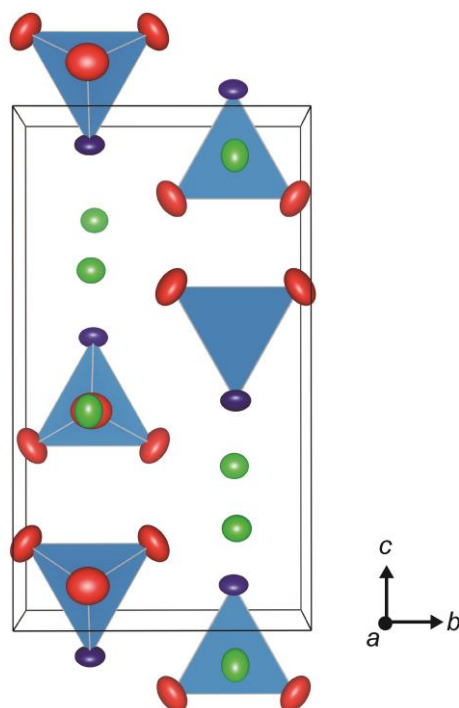


Figure 6.2. Crystal structure of $\text{Ba}_2\text{PO}_3\text{N}$ along $[001]$ with Ba atoms in green, O atoms in red, N atoms in blue and PO_3N tetrahedra in blue (displacement parameters with 90% probability, drawings generated with VESTA).^[42]

While Ba1 is coordinated by three N and seven O atoms, Ba2 is only surrounded by two N and seven O atoms (see Figure 6.3). The Ba–O [2.764(2)–3.131(2) Å] and Ba–N [2.731(3)–3.043(3) Å] are in the same range as already reported for other barium (oxo)nitridophosphates (e.g. $\text{Ba}_3\text{P}_6\text{O}_6\text{N}_8$, BaP_2N_4 , $\text{Ba}_3\text{P}_5\text{N}_{10}\text{X}$).^[41, 43, 44] Based on the obtained structure model from single-crystal X-ray diffraction, a Rietveld refinement of powder X-ray diffraction data was conducted in order to check phase purity. Thereby, a small amount of an unknown side phase, which is marked with asterisks in Figure 6.4, was observed. The washed product shows no evidence of residual mineralizers such as NaNH_2 or KNH_2 . Table E.7 and E.8 in the Supporting Information summarize the crystallographic data.

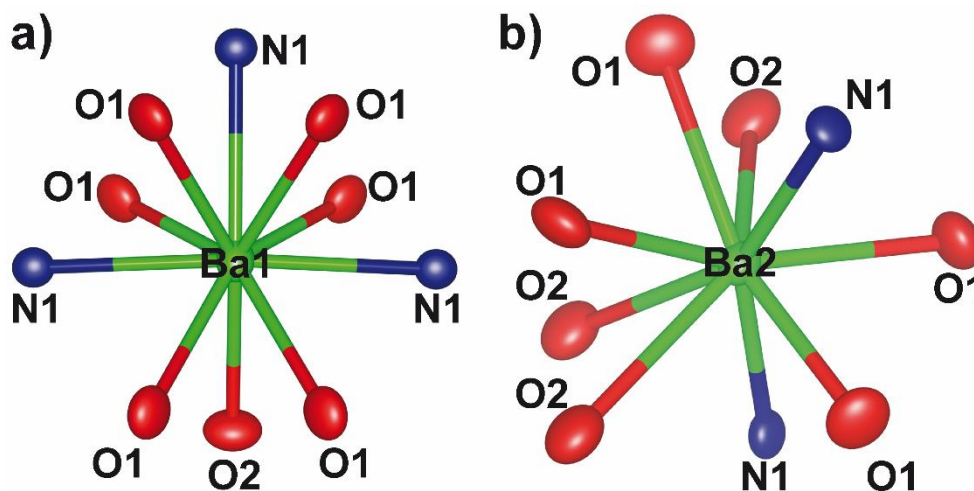


Figure 6.3. Coordination of Ba1 (a) and Ba2 (b) atoms in $\text{Ba}_2\text{PO}_3\text{N}$. Ba atoms are illustrated in green, O atoms in red and N atoms in blue (displacement parameters with 90% probability, drawings generated with VESTA).^[42]

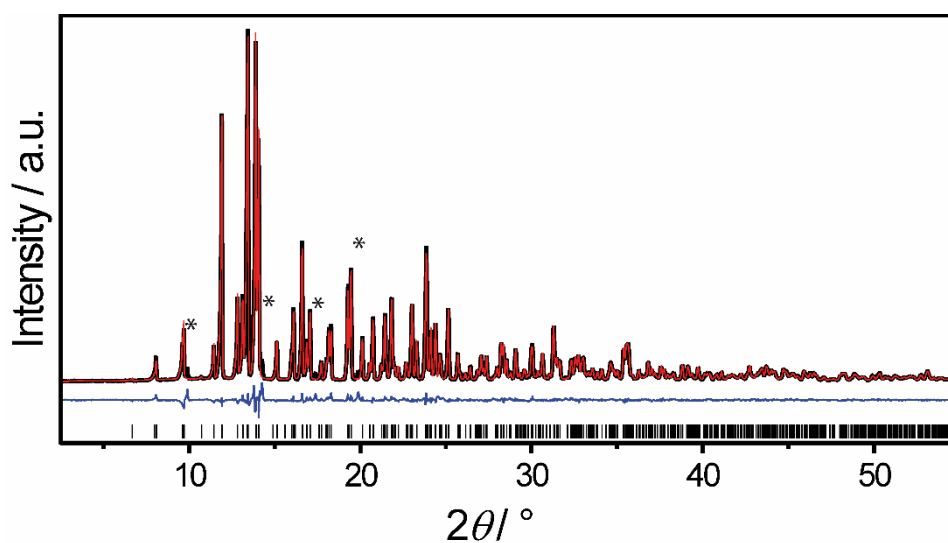


Figure 6.4. Rietveld refinement of PXRD data of $\text{Ba}_2\text{PO}_3\text{N}$ with experimental data (black line), calculated diffraction pattern (red line), difference profile (blue line) and reflection positions of $\text{Ba}_2\text{PO}_3\text{N}$ (black bars). Reflections of unknown side phases are marked with asterisks.

6.2.3 Energy dispersive X-ray spectroscopy (EDX)

EDX measurements on Eu²⁺ doped Ba₂PO₃N samples (nominal concentration of \approx 1 mol-% regarding to Ba) were carried out for chemical analysis and no elements other than the expected (Ba, P, O, and N) and trace amounts of Eu were detected. The obtained atomic ratio of Ba/P/O/N \approx 2.1:1.0:2.5:0.9 is in good agreement with the sum formula of the title compound (Table E.9, Supporting Information).

6.2.4 Fourier Transformed Infrared spectroscopy (FTIR)

The exclusion of any NH_x functionality in Ba₂PO₃N was performed by FTIR spectroscopy. As no significant absorption bands appear in the region around 3000 cm⁻¹ (Figure E.2, Supporting Information), the absence of N-H groups in the crystal structure can be confirmed.^[45] However, the broad and weak band between 2400 and 3400 cm⁻¹ can be explained by partial surface hydrolysis of the sample, owed to the measuring method. The strong absorption bands in the region between 600 and 1400 cm⁻¹ can be attributed to symmetric and asymmetric stretching modes of the P–N-framework and are similar to the absorption bands of Ca₂PO₃N and Sr₂PO₃N, indicating the structural similarity of these three compounds.^[25]

6.2.5 UV/Vis spectroscopy

In order to investigate the optical properties of Ba₂PO₃N, diffuse reflectance spectroscopy was conducted. The spectrum shows an absorption band around 250 nm (Figure E.3, Supporting Information), which is in agreement with the white color of the sample. The Kubelka–Munk function $F(R) = (1-R)^2/2R$, where R represents the reflectance, was used to calculate a pseudo-absorption spectrum.^[46] The bandgap was determined subsequently by drawing a tangent at the inflection point of the Tauc plot (see Figure 6.5), where $[F(R) \cdot h\nu]^{1/n}$ is plotted vs. $h\nu$, with $n = 1/2$ assuming a direct transition.^[47] The determined bandgap is approximately 4.3 eV.

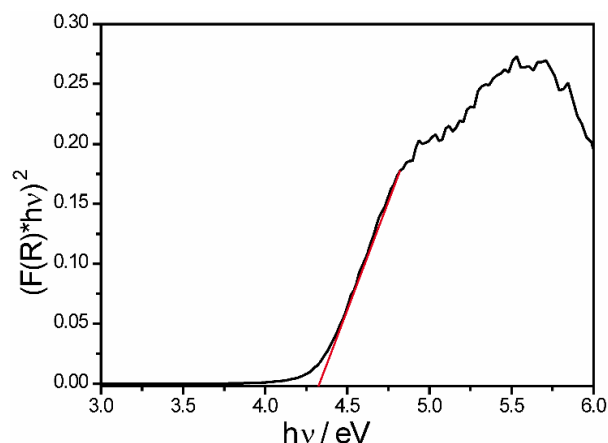


Figure 6.5. Tauc plot of Ba₂PO₃N (black line) with a tangent at the inflection point (red line).

6.2.6 Luminescence

Ba₂PO₃N:Eu²⁺ shows strong green emission upon irradiation with UV light (see Figure E.4 in the Supporting Information). The excitation spectrum (see Figure 6.6) of a Ba₂PO₃N:Eu²⁺ (≈ 1 at.-% Eu²⁺) single crystal shows a maximum at 410 nm. Upon excitation ($\lambda_{\text{exc}} = 420$ nm), the title compound shows broad emission at $\lambda_{\text{em}} = 534$ nm with a full width at half-maximum (fwhm) of 85 nm/2961 cm⁻¹. The broad emission arises most likely from the two emission bands, due to two different Ba positions, which can be substituted by Eu²⁺. The luminescence behavior is similar to that of isotopic Ca₂PO₃N:Eu²⁺ and the oxosilicates $M_2\text{SiO}_4\text{:Eu}^{2+}$ ($M = \text{Ca}, \text{Sr}, \text{Ba}$) crystallizing in the β -K₂SO₄ structure type as well.^[25, 48] Furthermore, the emission wavelength of Ba₂PO₃N:Eu²⁺ is similar to that of SrP₂N₄:Eu²⁺ ($\lambda_{\text{em}} = 529$ nm), however, the emission is broader (fwhm = 2432 cm⁻¹).^[43]

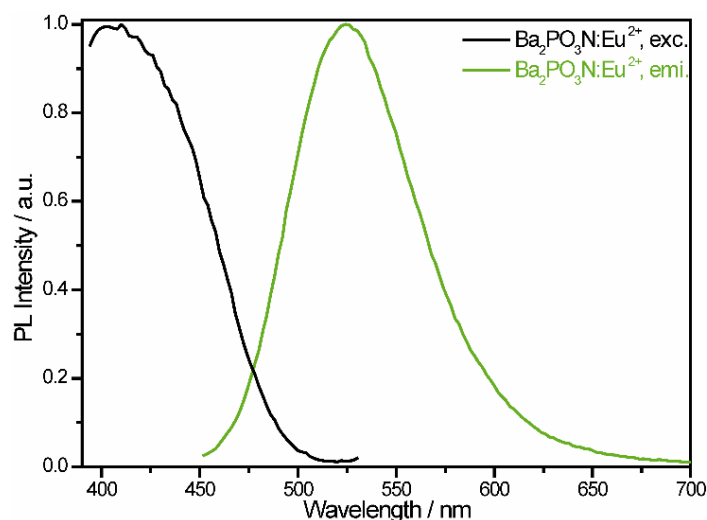


Figure 6.6. Excitation (black line) and emission (green line) spectra of Ba₂PO₃N:Eu²⁺.

Low temperature measurements ($\lambda_{\text{exc}} = 390$ nm) between 6 and 300 K were conducted on thick-bed powder samples in order to investigate thermal quenching of Ba₂PO₃N:Eu²⁺. For this purpose, the luminescence intensities were measured and integrated at different temperatures (Figure E.5 in the Supporting Information). Figure 6.7 illustrates the thermal quenching of Ba₂PO₃N:Eu²⁺, by decreasing the initial intensity (6 K) down to $\approx 40\%$ at room temperature. For this reason, no further measurements such as internal quantum efficiency or high-temperature measurements were conducted. The stronger thermal quenching of the title compound compared to the isotypic orthosilicates (Ba,Sr)₂SiO₄:Eu²⁺ ($\lambda_{\text{em}} \approx 525$ nm, $\text{fwhm} \approx 2420$ cm⁻¹)^[48] that found practical application in solid-state lighting can be explained by the smaller optical bandgap of the title compound (Ba₂SiO₄: $E_{\text{g}} = 6.81$ eV) that results in more pronounced non-radiative de-excitation of the activator ion via a photoionization process.^[49] Additionally, the low temperature measurements reveal a second emission band, which is in accordance with the former mentioned presence of two substantially different Ba²⁺ sites. The observation of this second band, which is not obvious in the emission spectrum of the single crystal, might be traced back to the different excitation wavelengths or different activation energies of the two different excited Eu states towards photoionization.

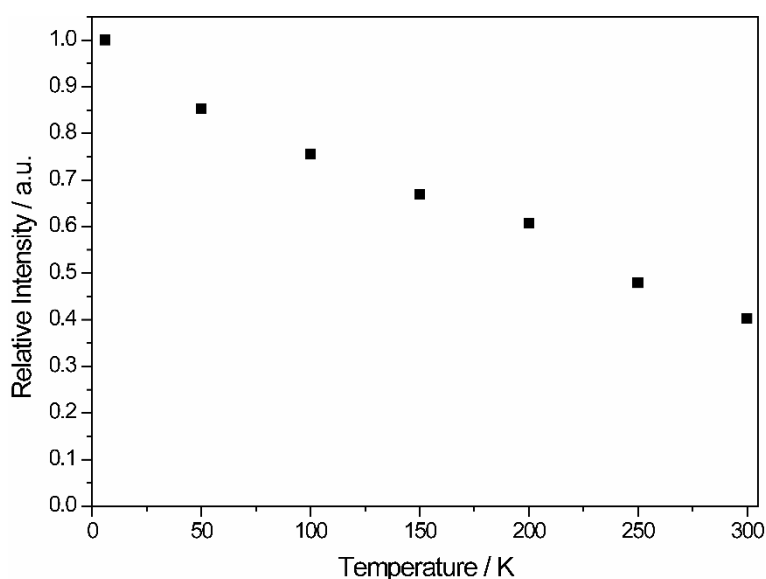


Figure 6.7. Thermal quenching data for Ba₂PO₃N:Eu²⁺ at low temperatures (6-300 K).

6.3 Conclusions

The *ortho*-oxonitridophosphate Ba₂PO₃N was synthesized in supercritical ammonia starting from BaO, red phosphorus, KOH and NaN₃ at a temperature of 1070 K and a maximum pressure of 120 MPa using custom-built high-temperature autoclaves. KOH and NaN₃ act as ammonobasic

mineralizers to increase the solubility of the other starting materials. In doing so, crystallites with sizes up to $\approx 600 \mu\text{m}$ grew on the wall at the upper part of the liner, which suggest a solution-based crystallization process via soluble intermediate species. The crystal structure was solved and refined from single-crystal X-ray diffraction. Ba₂PO₃N crystallizes in the β -K₂SO₄ structure type and is the first representative of an ammonothermally synthesized oxonitridophosphate with non-condensed PO₃N tetrahedra, expanding the degree of condensation range of ammonothermally accessible nitridophosphates to $1/4 \leq \kappa \leq 4/7$. The bandgap was determined with diffuse reflectance spectroscopy to be 4.3 eV. Eu²⁺ doped samples show luminescence in the green region of the visible spectrum ($\lambda_{\text{em}} = 534 \text{ nm}$, $\text{fwhm} = 85 \text{ nm}/2961 \text{ cm}^{-1}$) when excited with UV light ($\lambda_{\text{exc}} = 420 \text{ nm}$). Low temperature measurements indicated strong thermal quenching even at room temperature, as only 40% intensity remains compared to the intensity at 6 K. For future investigations, it would be interesting, if the ammonothermal method is applicable for synthesis of further *ortho*-(oxo)nitridophosphates and if the findings on ammonothermal (oxo)nitridophosphates in general could be transferred to other oxide or nitride systems such as (oxo)nitridosilicates.

6.4 Experimental Section

Due to moisture-sensitivity of the product, all manipulations were conducted under exclusion of oxygen and moisture in argon filled gloveboxes (Unilab, MBraun, Garching, O₂ < 1 ppm, H₂O < 1 ppm). The filling of the autoclaves with ammonia was performed on a vacuum line ($\leq 0.1 \text{ Pa}$) with argon and ammonia (both: Air Liquide, 99.999%) supply. Washing treatments of the products were carried out in flame-dried Schlenk-type glassware connected to a vacuum line ($\leq 0.1 \text{ Pa}$). All gases were further purified using gas purification cartridges [Micro Torr FT400–902 (for Ar) and MC400–702FV (for NH₃), SAES Pure Gas Inc., San Luis Obispo, CA, USA], providing a purity level of < 1 ppbV H₂O, O₂ and CO₂ (manufacturer's data).

6.4.1 Synthesis of Eu(NH₂)₂

Eu(NH₂)₂ was synthesized starting from Eu metal (99.99%, smart elements) in supercritical ammonia according to the synthesis described in literature.^[50]

6.4.2 Ammonothermal synthesis

Ba₂PO₃N was synthesized ammonothermally starting from 0.75 mmol red P (23.2 mg, Merck, 99%), 1.5 mmol BaO (230 mg, Alfa Aesar, 99.5%), 0.75 mmol KOH (42.1 mg, Merck, 90%) and

0.75 mmol NaN₃ (48.8 mg, Sigma-Aldrich, 99.5%). In order to obtain Eu²⁺ doped samples, 0.015 mmol Eu(NH₂)₂ (3 mg) were added to the reaction mixture. All starting materials were ground in an agate mortar and transferred into a tantalum liner to protect the sample from autoclave impurities. After placing the liner in a Haynes[®] 282[®] autoclave (nickel based super-alloy, max. 1100 K, 170 MPa, 10 mL), the later was sealed via flange joints using a silver coated Inconel[®] 718 ring (GFD seals). The autoclave body is connected to a hand valve (SITEC) by an Inconel[®] 718 high-pressure tube. The hand valve contains a pressure transmitter (HBM P2VA1/5000 bar) and a bursting disk (SITEC). The assembled autoclave was evacuated, cooled to 198 K using an ethanol/liquid nitrogen mixture and filled with NH₃ (≈ 3.0 mL). The amount of NH₃ was determined using a mass flow meter (D-6320-DR, Bronkhorst, Ruurlo, Netherlands). After filling, the autoclave was heated within 2 h to 670 K and held at this temperature for 16 h, then heated to 1070 K within 3 h and held for 72 h reaching a maximum pressure of 120 MPa. Subsequently, the autoclave was cooled down and residual NH₃ was removed. The white (Ba₂PO₃N) and yellow (Ba₂PO₃N:Eu²⁺) products were removed and washed with dry ethanol and dried under vacuum. Irregularly shaped single crystals of the product with sizes up to several hundred of μm grew on the wall of the liner.

6.4.3 Single-crystal X-ray diffraction

For single-crystal XRD measurements, Ba₂PO₃N:Eu²⁺ single crystals were placed and sealed in glass capillaries (Hilgenberg GmbH) under argon atmosphere. A Bruker D8 Quest diffractometer with Mo-K_α radiation ($\lambda = 0.71073 \text{ \AA}$) was used for data collection. The software package APEX3 was used for indexing and integration.^[51, 52] Furthermore, APEX3 was used for semiempirical absorption corrections (SADABS) and space group determination.^[52–54] The crystal structure was solved using the SHELXT algorithm and refined by full-matrix least-squares methods using WinGX with implemented SHELXL.^[55, 56]

CSD 1975933 (for Ba₂PO₃N) contains the supplementary crystallographic data for this paper. These data can be obtained free of charge from FIZ Karlsruhe.

6.4.4 Powder X-ray diffraction

The ground product was placed and sealed in a glass capillary ($d = 0.3 \text{ mm}$, Hilgenberg GmbH) in argon atmosphere for PXRD measurement. The measurement was conducted using a Stoe STADI P diffractometer with Mo-K_{α1} ($\lambda = 0.71073 \text{ \AA}$) radiation, Ge(111) monochromator and Mythen 1K detector in modified Debye–Scherrer geometry. The program TOPAS was used for Rietveld refinement of the measured data.^[57]

6.4.5 Scanning electron microscopy

Single-crystal images as well as EDX measurements were conducted on a scanning electron microscope [Dualbeam Helios Nanolab G3 UC (FEI), equipped with an EDX detector (X-Max 80 SDD, Oxford instruments)]. For this purpose, the samples were placed on adhesive carbon pads. Coating of the samples with a conductive carbon film was performed with a high-vacuum sputter coater (BAL-TEC MED 020, Bal Tec A).

6.4.6 Fourier Transformed Infrared spectroscopy

A Perkin Elmer BX II FTIR spectrometer equipped with a DuraSampler Diamond ATR (attenuated total reflection) unit under exposure to air was used for collection of a FTIR spectrum of Ba₂PO₃N.

6.4.7 UV/Vis spectroscopy

UV/Vis measurements were conducted using a Jasco V-650 UV/Vis spectrophotometer equipped with Czerny-Turner mount, photomultiplier tube detector and deuterium (190–350 nm)/halogen (330–900 nm) lamps as light sources to estimate the optical bandgap of Ba₂PO₃N. For this purpose, a diffuse reflectance measurement of the sample at room temperature was performed.

6.4.8 Luminescence measurements

Single crystals sealed in silica glass capillaries were used for investigation of the luminescence properties of Ba₂PO₃N:Eu²⁺. A HORIBA Fluoromax4 spectrofluorimeter system, attached via optical fibers to an Olympus BX51 microscope was used for data collection ($\lambda_{exc} = 420$ nm).

Low-temperature measurements were conducted in the range from 300 to 6 K performed on a thick-bed powder layer using a fiber-coupled spectroscopy system containing a thermally stabilized LED light source and a fiber-optic spectrometer from Ocean Optics (HR2000+ES) in an evacuated cooling chamber ($\lambda_{exc} = 390$ nm). The samples was cooled via a liquid-He compressor system from Advance Research System Inc. (ARS4HW).

6.5 Acknowledgments

The authors want to thank Lisa Gamperl for EDX measurements and Arthur Haffner for single-crystal X-ray measurements (all at Department of Chemistry, LMU Munich) as well as the group of Prof. Dr. E. Schlücker (especially Anna Kimmel and Dr. Thomas Steigerwald) for fabrication of the

autoclaves (FAU Erlangen-Nürnberg). Financial support by the Deutsche Forschungsgemeinschaft (DFG) within the research group “Chemistry and Technology of the Ammonothermal Synthesis of Nitrides” (FOR 1600), project SCHN377/16-2, is gratefully acknowledged.

6.6 References

- [1] R. Juza, H. Jacobs, "Ammonothermal Synthesis of Magnesium and Beryllium Amides", *Angew. Chem.* **1966**, 78, 208; *Angew. Chem. Int. Ed. Engl.* **1966**, 5, 247.
- [2] H. Jacobs, U. Fink, "Über natrium- und kaliumamidometallate des calciums, strontiums und europiums", *J. Less Common Met.* **1979**, 63, 273-286.
- [3] H. Jacobs, J. Kockelkorn, J. Birkenbeul, "Struktur und eigenschaften der ternären metallamide NaCa(NH₂)₃, KBa(NH₂)₃, RbBa(NH₂)₃, RbEu(NH₂)₃ und RbSr(NH₂)₃", *J. Less Common Met.* **1982**, 87, 215-224.
- [4] D. Peters, H. Jacobs, "Ammonothermalsynthese von kristallinem siliciumnitridimid, Si₂N₂NH", *J. Less Common Met.* **1989**, 146, 241-249.
- [5] T. Brokamp, H. Jacobs, "Darstellung und Struktur einiger Gemischtvalenter ternärer Tantalnitride mit Lithium und Magnesium", *J. Alloys Compd.* **1992**, 183, 325-344.
- [6] H. Jacobs, E. von Pinkowski, "Synthese ternärer nitride von alkalimetallen: Verbindungen mit tantal, MTaN₂ mit M = Na, K, Rb und Cs", *J. Less Common Met.* **1989**, 146, 147-160.
- [7] T. Richter, R. Niewa, "Chemistry of Ammonothermal Synthesis", *Inorganics* **2014**, 2, 29-78.
- [8] J. Häusler, W. Schnick, "Ammonothermal Synthesis of Nitrides: Recent Developments and Future Perspectives", *Chem. Eur. J.* **2018**, 24, 11864-11879.
- [9] R. Dwilinski, A. Wyszomolek, J. Baranowski, M. Kaminska, R. Doradziński, H. Jacobs, "GaN synthesis by ammonothermal method", *Acta Phys. Pol., A* **1995**, 88, 833-836.
- [10] R. Dwiliński, R. Doradziński, J. Garczyński, L. Sierzputowski, R. Kucharski, M. Zajac, M. Rudziński, R. Kudrawiec, W. Strupiński, J. Misiewicz, "Ammonothermal GaN substrates: Growth accomplishments and applications", *Phys. Status Solidi A* **2011**, 208, 1489-1493.
- [11] S. Pimputkar, S. Kawabata, J. S. Speck, S. Nakamura, "Improved growth rates and purity of basic ammonothermal GaN", *J. Cryst. Growth* **2014**, 403, 7-17.
- [12] J. Hertrampf, P. Becker, M. Widenmeyer, A. Weidenkaff, E. Schlücker, R. Niewa, "Ammonothermal Crystal Growth of Indium Nitride", *Cryst. Growth Des.* **2018**, 18, 2365-2369.
- [13] J. Häusler, S. Schimmel, P. Wellmann, W. Schnick, "Ammonothermal Synthesis of Earth-Abundant Nitride Semiconductors ZnSiN₂ and ZnGeN₂ and Dissolution Monitoring by In Situ X-ray Imaging", *Chem. Eur. J.* **2017**, 23, 12275-12282.

- [14] J. Häusler, R. Niklaus, J. Minár, W. Schnick, "Ammonothermal Synthesis and Optical Properties of Ternary Nitride Semiconductors Mg-IV-N₂, Mn-IV-N₂ and Li-IV₂-N₃ (IV=Si, Ge)", *Chem. Eur. J.* **2018**, 24, 1686-1693.
- [15] M. Mallmann, R. Niklaus, T. Rackl, M. Benz, T. G. Chau, D. Johrendt, J. Minár, W. Schnick, "Solid Solutions of Grimm-Sommerfeld Analogous Nitride Semiconductors II-IV-N₂ (II = Mg, Mn, Zn; IV = Si, Ge): Ammonothermal Synthesis and DFT Calculations", *Chem. Eur. J.* **2019**, 25, 15887-15895.
- [16] J. Häusler, L. Neudert, M. Mallmann, R. Niklaus, A.-C. L. Kimmel, N. S. A. Alt, E. Schlücker, O. Oeckler, W. Schnick, "Ammonothermal Synthesis of Novel Nitrides: Case Study on CaGaSiN₃", *Chem. Eur. J.* **2017**, 23, 2583-2590.
- [17] J. Häusler, L. Eisenburger, O. Oeckler, W. Schnick, "Ammonothermal Synthesis and Crystal Structure of the Nitridoalumogermanate Ca_{1-x}Li_xAl_{1-x}Ge_{1+x}N₃ (x ≈ 0.2)", *Eur. J. Inorg. Chem.* **2018**, 759-764.
- [18] N. Cordes, T. Bräuniger, W. Schnick, "Ammonothermal Synthesis of EAMO₂N (EA = Sr, Ba; M = Nb, Ta) Perovskites and ¹⁴N Solid-State NMR Spectroscopic Investigations of AM(O,N)₃ (A = Ca, Sr, Ba, La)", *Eur. J. Inorg. Chem.* **2018**, 5019-5026.
- [19] H. Jacobs, R. Nymwegen, "Synthesis and Crystal Structure of a Potassium Nitridophosphate, K₃P₆N₁₁", *Z. Anorg. Allg. Chem.* **1997**, 623, 429-433.
- [20] M. Mallmann, C. Maak, R. Niklaus, W. Schnick, "Ammonothermal Synthesis, Optical Properties, and DFT Calculations of Mg₂PN₃ and Zn₂PN₃", *Chem. Eur. J.* **2018**, 24, 13963-13970.
- [21] M. Mallmann, S. Wendl, W. Schnick, "Crystalline Nitridophosphates by Ammonothermal Synthesis", *Chem. Eur. J.* **2020**, 26, 2067-2072.
- [22] S. D. Kloß, W. Schnick, "Nitridophosphates – A Success Story of Nitride Synthesis", *Angew. Chem.* **2019**, 131, 8015-8027; *Angew. Chem. Int. Ed.* **2019**, 58, 7933-7944.
- [23] W. Schnick, J. Luecke, "Synthesis and Crystal Structure of Lithium Phosphorus Nitride Li₇PN₄: The First Compound Containing Isolated PN₄-Tetrahedra", *J. Solid State Chem.* **1990**, 87, 101-106.
- [24] D. Baumann, W. Schnick, "Li₁₄(PON₃)₂O – A Non-Condensed Oxonitridophosphate Oxide", *Eur. J. Inorg. Chem.* **2015**, 617-621.
- [25] A. Marchuk, P. Schultz, C. Hoch, O. Oeckler, W. Schnick, "M₂PO₃N (M = Ca, Sr): ortho-Oxonitridophosphates with β-K₂SO₄ Structure Type", *Inorg. Chem.* **2016**, 55, 974-982.
- [26] S. D. Kloß, N. Weidmann, W. Schnick, "Antiperovskite Nitridophosphate Oxide Ho₃[PN₄]O by High-Pressure Metathesis", *Eur. J. Inorg. Chem.* **2017**, 1930-1937.

- [27] A. P. Black, K. A. Denault, J. Oró-Solé, A. R. Goñi, A. Fuertes, "Red luminescence and ferromagnetism in europium oxynitridosilicates with a β -K₂SO₄ structure", *Chem. Commun.* **2015**, 51, 2166-2169.
- [28] Y.-S. Tang, S.-F. Hu, C. C. Lin, N. C. Bagkar, R.-S. Liu, "Thermally stable luminescence of K₂SrPO₄:Eu²⁺ + phosphor for white light UV light-emitting diodes", *Appl. Phys. Lett.* **2007**, 90, 151108.
- [29] F. Golinski, H. Jacobs, "Crystal Structure of Hexamine Cyclotriphosphazene, P₃N₃(NH₂)₆", *Z. Anorg. Allg. Chem.* **1994**, 620, 965-968.
- [30] H. Jacobs, R. Kirchgässner, "Hexaminecyclotriphosphazenehemiammoniat, P₃N₃(NH₂)₆ · 0,5 NH₃, a Product of High Pressure Ammonolysis of White Phosphorus", *Z. Anorg. Allg. Chem.* **1990**, 581, 125-134.
- [31] H. Jacobs, S. Pollok, F. Golinski, "Synthesis and Crystal Structure of Na₁₀[P₄(NH)₆N₄](NH₂)₆(NH₃)_{0,5} with an Adamantane-like Anion [P₄(NH)₆N₄]⁴⁻", *Z. Anorg. Allg. Chem.* **1994**, 620, 1213-1218.
- [32] R. Hoppe, "Madelung Constants", *Angew. Chem.* **1966**, 78, 52-63; *Angew. Chem. Int. Ed. Engl.* **1966**, 5, 95-106.
- [33] R. Hoppe, "The Coordination Number – an "Inorganic Chameleon"", *Angew. Chem.* **1970**, 82, 7-16; *Angew. Chem. Int. Ed. Engl.* **1970**, 9, 25-34.
- [34] R. Hübenthal, *Maple, Program for the Calculation of MAPLE values, version 4*; University of Gießen, Germany, 1993.
- [35] W. H. Baur, "Effective Ionic Radii in Nitrides", *Crystallogr. Rev.* **1987**, 1, 59-83.
- [36] I. D. Brown, D. Altermatt, "Bond-valence parameters obtained from a systematic analysis of the Inorganic Crystal Structure Database", *Acta Crystallogr. Sect. B* **1985**, 41, 244-247.
- [37] N. E. Brese, M. O'Keeffe, "Bond-valence parameters for solids", *Acta Crystallogr. Sect. B* **1991**, 47, 192-197.
- [38] R. Hoppe, S. Voigt, H. Glaum, J. Kissel, H. P. Müller, K. Bernet, "A new route to charge distributions in ionic solids", *J. Less Common Met.* **1989**, 156, 105-122.
- [39] S. J. Sedlmaier, E. Mugnaioli, O. Oeckler, U. Kolb, W. Schnick, "SrP₃N₅O: A Highly Condensed Layer Phosphate Structure Solved from a Nanocrystal by Automated Electron Diffraction Tomography", *Chem. Eur. J.* **2011**, 17, 11258-11265.
- [40] S. J. Sedlmaier, J. Schmedt auf der Günne, W. Schnick, "Sr₃P₆O₆N₈—a highly condensed layered phosphate", *Dalton Trans.* **2009**, 4081-4084.
- [41] S. J. Sedlmaier, D. Weber, W. Schnick, "Crystal structure of barium oxonitridophosphate, Ba₃P₆O₆N₈", *Z. Kristallogr. - New Cryst. Struct.* **2012**, 227, 1-2.
- [42] K. Momma, F. Izumi, "VESTA 3 for three-dimensional visualization of crystal, volumetric and morphology data", *J. Appl. Crystallogr.* **2011**, 44, 1272-1276.

- [43] F. J. Pucher, A. Marchuk, P. J. Schmidt, D. Wiechert, W. Schnick, "Luminescent Nitridophosphates CaP₂N₄:Eu²⁺, SrP₂N₄:Eu²⁺, BaP₂N₄:Eu²⁺, and BaSr₂P₆N₁₂:Eu²⁺", *Chem. Eur. J.* **2015**, *21*, 6443-6448.
- [44] A. Marchuk, S. Wendl, N. Imamovic, F. Tambornino, D. Wiechert, P. J. Schmidt, W. Schnick, "Nontypical Luminescence Properties and Structural Relation of Ba₃P₅N₁₀X:Eu²⁺ (X = Cl, I): Nitridophosphate Halides with Zeolite-like Structure", *Chem. Mater.* **2015**, *27*, 6432-6441.
- [45] S. Wendl, W. Schnick, "SrH₄P₆N₁₂ and SrP₈N₁₄: Insights into the Condensation Mechanism of Nitridophosphates under High Pressure", *Chem. Eur. J.* **2018**, *24*, 15889-15896.
- [46] R. López, R. Gómez, "Band-gap energy estimation from diffuse reflectance measurements on sol-gel and commercial TiO₂: a comparative study", *J. Sol-Gel Sci. Technol.* **2012**, *61*, 1-7.
- [47] J. Tauc, R. Grigorovici, A. Vancu, "Optical Properties and Electronic Structure of Amorphous Germanium", *Phys. Status Solidi B* **1966**, *15*, 627-637.
- [48] T. L. Barry, "Fluorescence of Eu²⁺-Activated Phases in Binary Alkaline Earth Orthosilicate Systems", *J. Electrochem. Soc.* **1968**, *115*, 1181-1184.
- [49] P. Dorenbos, "Thermal quenching of Eu²⁺ luminescence in inorganic compounds", *J. Phys.: Condens. Matter* **2005**, *17*, 8103-8111.
- [50] M. Mallmann, J. Häusler, N. Cordes, W. Schnick, "Ammonothermal Synthesis of Alkali-Alkaline Earth Metal and Alkali-Rare Earth Metal Carbodiimides: K_{5-x}M_x(CN₂)_{2+x}(HCN₂)_{1-x} (M = Sr, Eu) and Na_{4.32}Sr_{0.68}(CN₂)_{2.68}(HCN₂)_{0.32}", *Z. Anorg. Allg. Chem.* **2017**, *643*, 1956-1961.
- [51] SAINT, Data Integration Software, Madison, Wisconsin, USA, **1997**.
- [52] APEX 3, Vers. 2016.2015-2010, Bruker-AXS, Karlsruhe, **2016**.
- [53] G. M. Sheldrick, *SADABS, Multi-Scan Absorption Correction*, v.2, Bruker-AXS, Madison, WI, USA, **2012**.
- [54] *XPREP Reciprocal Space Exploration*, Vers. 6.12, Bruker-AXS, Karlsruhe, **2001**.
- [55] G. M. Sheldrick, "SHELXT - Integrated space-group and crystal-structure determination", *Acta Crystallogr. Sect. A* **2015**, *71*, 3-8.
- [56] G. M. Sheldrick, "Crystal structure refinement with SHELXL", *Acta Crystallogr. Sect. C* **2015**, *71*, 3-8.
- [57] A. Coelho, *TOPAS Academic, Version 6*, Coelho Software, Brisbane (Australia), **2016**.

7 Ammonothermal Synthesis and Crystal Growth of the Chain-type Oxonitridosilicate $\text{Ca}_{1+x}\text{Y}_{1-x}\text{SiN}_{3-x}\text{O}_x$ ($x > 0$)

published in: *Z. Anorg. Allg. Chem.* **2020**, DOI: 10.1002/zaac.202000018.

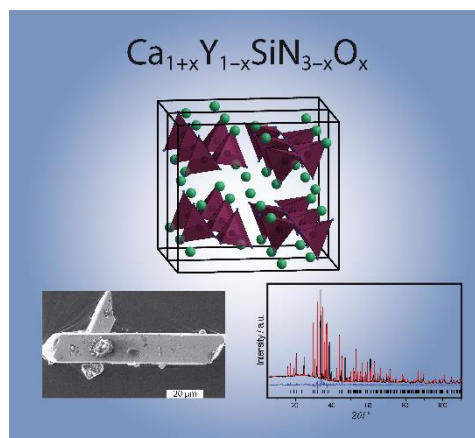
authors: Mathias Mallmann, Christian Maak, and Wolfgang Schnick

DOI: 10.1002/zaac.202000018

Reprinted (adapted) with permission for non-commercial use from *Zeitschrift für anorganische und allgemeine Chemie* (open access). Copyright 2020 John Wiley and Sons.

Abstract. The oxonitridosilicate $\text{Ca}_{1+x}\text{Y}_{1-x}\text{SiN}_{3-x}\text{O}_x$ ($x > 0$) was synthesized in custom-built high-temperature autoclaves starting from CaH_2 , intermetallic YSi and NaN_3 using supercritical ammonia as solvent at a maximum pressure of 140 MPa and temperature of 1070 K. In situ formed NaNH_2 acts as ammonobasic mineralizer and increases the solubility of the other starting materials. Air and moisture sensitive rod-shaped single crystals of the title compound with length of up to

200 μm were obtained. The crystal structure was solved and refined by single-crystal X-ray diffraction. The results are supported by powder X-ray diffraction, energy dispersive X-ray spectroscopy and lattice energy (MAPLE) calculations. $\text{Ca}_{1+x}\text{Y}_{1-x}\text{SiN}_{3-x}\text{O}_x$ ($x > 0$) is isostructural to Ca_2PN_3 and Eu_2SiN_3 and crystallizes in the orthorhombic space group *Cmce* (no. 64) with $a = 5.331(2)$, $b = 10.341(4)$, $c = 11.248(4)$ Å and $Z = 8$ ($R_1 = 0.0257$, $wR_2 = 0.0447$) and contains infinite *zweier* single chains running along [100] which are built up from corner sharing $\text{Si}(\text{N},\text{O})_4$ tetrahedra.



7.1 Introduction

Due to their intriguing structural diversity as well as their auspicious chemical and physical properties, (oxo)nitridosilicates gained increased attention in the last decades.^[1] These properties open the way for different applications such as lithium ion conductors, thermal conductors and nonlinear optical (NLO) materials.^[1] One of the most important application fields of (oxo)nitridosilicates is their usage as host materials (e.g. $(\text{Sr},\text{Ba})_2\text{Si}_5\text{N}_8$, $(\text{Ca},\text{Sr})\text{AlSiN}_3$) for activator ions like Eu^{2+} and the associated application in phosphor-converted light-emitting diodes.^[2, 3] Typically, these materials are synthesized via high-temperature reactions in radio-frequency furnaces, tantalum ampules or tube furnaces.^[1] In doing so, various synthesis routes like metathesis reactions or the carbothermal approach were employed accessing new compounds like $\text{RE}_4\text{Ba}_2[\text{Si}_9\text{ON}_{16}]\text{O}:\text{Eu}^{2+}$, $\text{La}_3\text{BaSi}_5\text{N}_9\text{O}_2:\text{Ce}^{3+}$ or $\text{RE}_4\text{Ba}_2[\text{Si}_{12}\text{O}_2\text{N}_{16}\text{C}_3]:\text{Eu}^{2+}$ ($\text{RE} = \text{Lu}, \text{Y}$).^[4-6] However, the growth of large single crystals of (oxo)nitridosilicates, which is inevitable for numerous applications, is quite challenging.

In contrast to above mentioned high-temperature routes, the ammonothermal method is a solution-based process, which could be crucial for synthesis and crystal growth of (oxo)nitridosilicates and other nitride materials in general at relatively low temperatures ($T \leq 1070$ K). This might open the way to hitherto hardly accessible (oxo)nitridosilicates, as already demonstrated for CaGaSiN_3 .^[7] An essential aspect of ammonothermal synthesis is the solubility of the starting materials in ammonia. The rather low solubility of most inorganic compounds in liquid NH_3 is circumvented by using high-pressurized NH_3 in the supercritical state, due to the fact that the relative permittivity is increased with increasing density.^[8] A further increase of the solubility can be accomplished by adding ammonobasic mineralizers like alkali metal amides during synthesis, which form soluble intermediate species (e.g. amides, imides, ammoniates) with the other starting materials.^[8] GaN for example shows how well the ammonothermal method is suitable for crystal growth of a nitride. Continuous developments make it possible to obtain high-purity bulk GaN crystals with growth rates of up to $300 \mu\text{m}$ per day by using the ammonothermal approach.^[9-11] In recent years, further ternary and multinary (oxide) nitrides such as CaAlSiN_3 , CaGaSiN_3 , $\text{Ca}_{1-x}\text{Li}_x\text{Al}_{1-x}\text{Ge}_{1+x}\text{N}_3$ ($x \approx 0.2$), II-IV- N_2 (II = Mg, Mn, Zn; IV = Si, Ge), LnTaON_2 ($\text{Ln} = \text{La}, \text{Ce}, \text{Pr}, \text{Nd}, \text{Sm}, \text{Gd}$) and various nitridophosphates were synthesized ammonothermally.^[7, 12-20]

In 2014, *Hintzen et al.* calculated the stability of several $\text{EA}^{2+}\text{RE}^{3+}\text{SiN}_3$ compounds ($\text{EA} =$ alkaline earth metal, $\text{RE} =$ rare earth metal), assuming structures isotypic to Eu_2SiN_3 and Ca_2PN_3 .^[21-23] Using density functional theory (DFT) calculations they showed that various combinations of alkaline earth and/or rare earth metals such as CaYSiN_3 , CaLaSiN_3 or SrLaSiN_3 are energetically favorable over the respective binary (REN) and ternary nitrides (MSiN_2).

In this contribution we report on the ammonothermal synthesis and crystal growth of the oxonitridosilicate $\text{Ca}_{1+x}\text{Y}_{1-x}\text{SiN}_{3-x}\text{O}_x$ ($x > 0$) under ammonobasic conditions using custom-built high-temperature autoclaves. Especially, the fact that single crystals with sizes up to several hundreds of μm can be obtained, makes the ammonothermal method interesting for synthesis of further (oxo)nitridosilicates.

7.2 Results and Discussion

7.2.1 Synthesis

$\text{Ca}_{1+x}\text{Y}_{1-x}\text{SiN}_{3-x}\text{O}_x$ ($x > 0$) was synthesized in supercritical NH_3 using custom-built high-temperature autoclaves. CaH_2 and YSi as an intermetallic precursor in a molar ratio of 1:1, as well as NaN_3 were used as starting materials. Intermetallic YSi was used in order to achieve a better mixing of Y and Si on an atomic level, as reactions with elemental Y and Si instead of YSi resulted in significantly smaller amounts and poorer crystallinity of the target phase. NaN_3 , which decomposes to Na and N_2 during reaction, forms in situ the respective amide NaNH_2 and acts as ammonobasic mineralizer. Presumably, the mineralizer increases the solubility of the other starting materials through the formation of soluble intermediate species such as $\text{NaCa}(\text{NH}_2)_3$, $\text{NaY}(\text{NH}_2)_4$, $\text{Na}_3[\text{Y}(\text{NH}_2)_6]$ or $\text{Si}_2\text{N}_2\text{NH}$.^[24–26] NaN_3 was used instead of Na or NaNH_2 due to its high purity and insensitivity towards hydrolysis. As such intermediates are preferably formed at lower temperatures, a first heating step to 670 K was conducted. During subsequent heating to 1070 K ($p_{\text{max}} = 140$ MPa), the intermediates decompose and form the air and moisture sensitive product $\text{Ca}_{1+x}\text{Y}_{1-x}\text{SiN}_{3-x}\text{O}_x$ ($x > 0$) as well as YN as a side phase. Transparent red rod-shaped single-crystals with sizes up to 200 μm in length were obtained (see scanning electron microscopy section). These represent the first ammonothermally grown crystallites of oxonitridosilicates, which are suitable for single-crystal X-ray measurements. Presumably, there are several reasons why it is not possible to form the desired pure nitride CaYSiN_3 . On the one hand, the formation of YN as side phase could implicate an excess of Ca in the crystal structure, which has to be compensated by incorporation of oxygen to achieve charge neutrality. Furthermore, a partial hydrolysis of CaYSiN_3 during reaction could also result in an incorporation of oxygen, which has to be compensated by an excess of Ca . These small amounts of oxygen may originate from oxide layers of the autoclave and liner wall or from oxygen impurities of the starting materials. Nevertheless, an excess of Y did not result in the synthesis of the pure nitride CaYSiN_3 with an atomic ratio Ca to Y of 1:1.

Analogous reactions at lower temperatures (870 K) also resulted in formation of the product. However, the crystallinity as well as the yield of the target phase improved with increasing

temperature. With respect to air and moisture sensitivity of $\text{Ca}_{1+x}\text{Y}_{1-x}\text{SiN}_{3-x}\text{O}_x$ ($x > 0$), residual mineralizer and intermediates were removed by washing the product with dry ethanol.

7.2.2 Crystal structure

The crystal structure of $\text{Ca}_{1+x}\text{Y}_{1-x}\text{SiN}_{3-x}\text{O}_x$ ($x > 0$) was solved and refined from single-crystal X-ray diffraction data. The compound crystallizes in orthorhombic space group *Cmce* (no. 64). Crystallographic data and details on the structure determination are summarized in Table 7.1. Atomic coordinates and Wyckoff positions are listed in Table 7.2. Anisotropic displacement parameters as well as interatomic distances are given in Tables F.1 and F.2 (Supporting Information). The crystal structure of $\text{Ca}_{1+x}\text{Y}_{1-x}\text{SiN}_{3-x}\text{O}_x$ ($x > 0$) (see Figure 7.1) is isostructural to Ca_2PN_3 and Eu_2SiN_3 and contains infinite *zweier* single chains^[27] built up from corner-sharing $\text{Si}(\text{N},\text{O})_4$ tetrahedra.^[22, 23, 28] These chains (see Figure 7.2 a) run along [100] and exhibit a periodicity of $P = 2$ and the maximum possible stretching factor of $f_s = 1.0$.^[28] The $\text{Si}(\text{N},\text{O})_4$ tetrahedra contain three crystallographically independent anion sites. While two of them (N1/O1 and N2/O2) are terminal, the third position (N3) is bridging two tetrahedra centers. The corresponding Si–(N,O) distances vary between 1.714(1) Å for the bridging nitrogen atom to 1.736(4) Å for the terminal N2/O2 atoms and are in the same range as reported for other oxonitridosilicates in literature.^[6, 22, 29]

The crystal structure contains two crystallographically different Ca/Y sites, which are both mixed occupied by Ca and Y, according to single-crystal XRD analysis (see Table F.3, Supporting Information). Both sites are coordinated in a distorted pentagonal bipyramidal way by N and O atoms (see Figure 7.2 b). The corresponding distances vary between 2.321(4) and 2.7086(11) Å for Y1/Ca1 and 2.396(4) to 3.036(4) Å for Y2/Ca2, which is in accordance with values known from literature.^[6, 30–32] Corresponding to the different bond lengths, the smaller Y^{3+} ion preferably occupies the atom site with the shorter *M*-N/O distances (Y1($\approx 79\%$) / Ca1($\approx 21\%$)), whereas Ca^{2+} preferably occupies the second cation position (Ca2($\approx 95\%$) / Y2($\approx 5\%$)) (see Table 7.2).^[33] This results in an atomic ratio of Ca:Y of approximately 1.16(2):0.84(2). If the positions (Ca1/Y1 and Ca2/Y2) are not refined under the assumption of a mixed occupation, the *R* values of the refinement increase significantly (see Table F.3 in the Supporting Information). Therefore, a value of *x* of 0.16 was assumed during single-crystal refinement.

To obtain charge neutrality, mixed occupation of N and O was assumed for the two terminal anion positions (N1/O1 and N2/O2) and constrained to 92.1% N and 7.9% O for both sites. To verify the crystal structure, lattice energy calculations (MAPLE) were performed.^[33–36] Detailed information on the MAPLE calculations are given in Table F.4 in the Supporting Information. All partial MAPLE values for the cations and anions are in the expected ranges. The total MAPLE value of

$\text{Ca}_{1+x}\text{Y}_{1-x}\text{SiN}_{3-x}\text{O}_x$ ($x > 0$) agrees within a deviation of 0.34% with the MAPLE value calculated from a hypothetical reaction of the binary nitrides and oxides.

Table 7.1. Crystallographic data of $\text{Ca}_{1+x}\text{Y}_{1-x}\text{SiN}_{3-x}\text{O}_x$ ($x > 0$) from single-crystal X-ray diffraction, standard deviations in parentheses.

Formula	$\text{Ca}_{1+x}\text{Y}_{1-x}\text{SiN}_{3-x}\text{O}_x$ ($x > 0$)
Crystal system	orthorhombic
Space group	<i>Cmce</i> (no. 64)
$a / \text{\AA}$	5.331(2)
$b / \text{\AA}$	10.341(4)
$c / \text{\AA}$	11.248(4)
Cell volume / \AA^3	620.1(4)
Formula units/cell	8
Density / $\text{g}\cdot\text{cm}^{-3}$	4.107
Crystal size / mm	0.05×0.02×0.01
μ / mm^{-1}	17.948
T / K	293(2)
Diffractometer	Bruker D8 Venture
Monochromator	Göbel mirror optics
Radiation / \AA	Mo- K_α (0.71073)
$F(000)$	729
θ range / $^\circ$	3.623 - 30.484
Total no. of reflections	3205
No. of independent reflections	522
R_{int} ; R_σ	0.0568, 0.0404
Refined parameters	38
Goodness of fit (χ^2)	1.063
$R1$ (all data); $R1$ ($F^2 > 2\sigma(F^2)$)	0.0373; 0.0257
$wR2$ (all data); $wR2$ ($F^2 > 2\sigma(F^2)$)	0.0465; 0.0447
$\Delta\rho_{\text{max}}$; $\Delta\rho_{\text{min}}$ [$\text{e}\cdot\text{\AA}^{-3}$]	0.588, -0.827

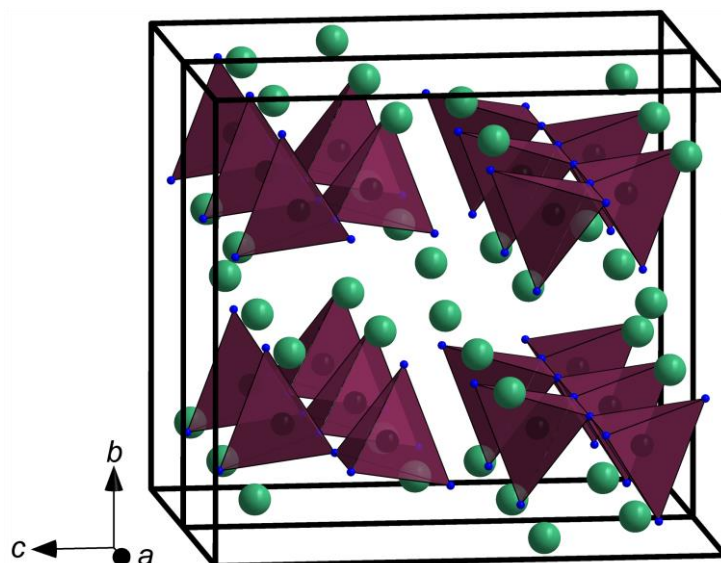


Figure 7.1. Crystal structure of $\text{Ca}_{1+x}\text{Y}_{1-x}\text{SiN}_{3-x}\text{O}_x$ ($x > 0$) viewed along [100]. Ca/Y atoms are depicted in green, Si atoms in black, N/O atoms in blue and $\text{Si}(\text{N},\text{O})_4$ tetrahedra in purple.

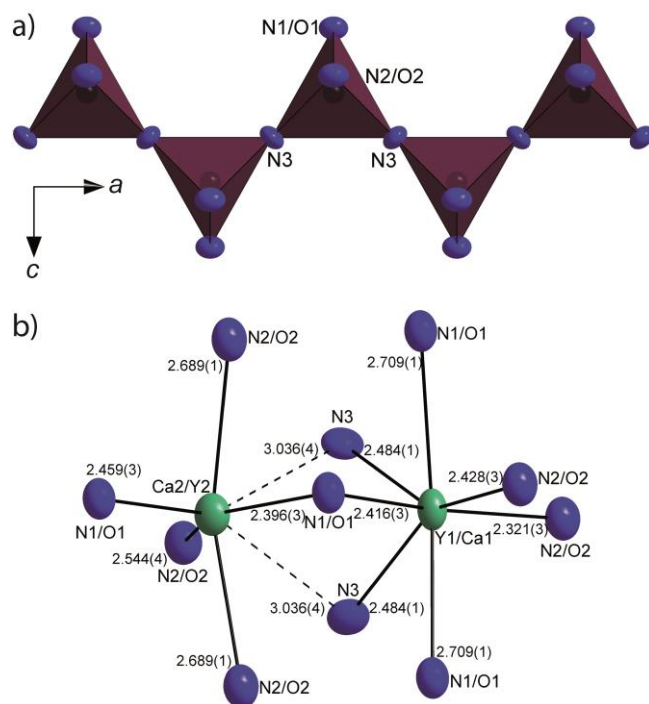


Figure 7.2. Infinite chains of $\text{Si}(\text{N},\text{O})_4$ tetrahedra viewed along [010] (a) and coordination of the two different cation sites with bond lengths [Å] of the Ca/Y-N/O bonds (b) in $\text{Ca}_{1+x}\text{Y}_{1-x}\text{SiN}_{3-x}\text{O}_x$ ($x > 0$). Ellipsoids are displayed at 90% probability level.

Figure 7.3 illustrates the result of the Rietveld refinement of the product in order to check phase purity. Starting values for the refinement were taken from the structure model obtained from single-crystal X-ray data. Details on the refinement as well as Wyckoff positions are summarized in Table F.5 and F.6 in the Supporting Information. The occupation of Ca and Y changes only marginally during refinement and were therefore fixed on the values of the single-crystal analysis. In addition to the target phase $\text{Ca}_{1+x}\text{Y}_{1-x}\text{SiN}_{3-x}\text{O}_x$, YN and an unidentified side phase occur (see Figure 7.3) in the PXRD. Starting values for the side phase (YN) were taken from literature.^[37] In particular, as already mentioned above, the formation of YN (11 weight-%) might explain the excess of Ca incorporated into $\text{Ca}_{1+x}\text{Y}_{1-x}\text{SiN}_{3-x}\text{O}_x$ ($x > 0$).

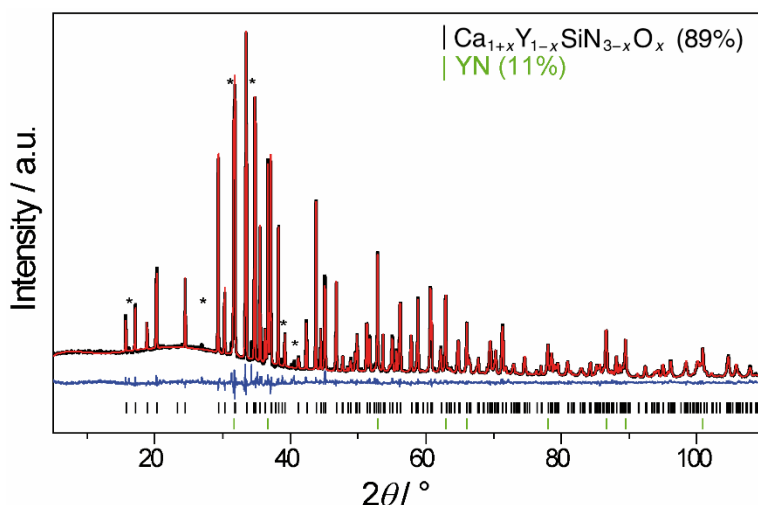


Figure 7.3. Rietveld refinement of powder X-ray diffraction pattern of $\text{Ca}_{1+x}\text{Y}_{1-x}\text{SiN}_{3-x}\text{O}_x$ ($x > 0$) with experimental data (black line), calculated data (red line), difference profile (blue line) and reflection positions ($\text{Ca}_{1+x}\text{Y}_{1-x}\text{SiN}_{3-x}\text{O}_x$ ($x > 0$): black bars, YN: green bars). Reflections of unknown side phases are marked with asterisks

7.2.3 Scanning electron microscopy

In order to confirm the chemical composition of the compound, energy dispersive X-ray spectroscopy (EDX) measurements were conducted on $\text{Ca}_{1+x}\text{Y}_{1-x}\text{SiN}_{3-x}\text{O}_x$ ($x > 0$) crystallites. The obtained data is summarized in Table 7.3. The determined atomic ratio of Ca and Y with approximately 1.10(6) : 0.90(3) agrees with the determined Ca:Y ratio obtained from single-crystal XRD measurements within one standard deviation. The fact that the ratio of anions (O and N) to cations (Ca, Y and Si) does not lead to charge neutrality can be explained by the uncertainty of EDX measurements on light elements. However, EDX measurements also show charge neutrality within two standard deviations. Despite the agreement of the EDX values with single-crystal XRD data, a determination of an exact value of x is only possible to a limited extent with these methods. The

excess of detected oxygen can be attributed to partial surface hydrolysis of the crystallites during sample preparation.

Table 7.3. SEM EDX measurements in atom-% of $\text{Ca}_{1+x}\text{Y}_{1-x}\text{SiN}_{3-x}\text{O}_x$ ($x > 0$) crystallites, standard deviations in parentheses.

	Ca	Y	Si	N	O
measurement 1:	19.2	15.6	16.9	38.6	9.7
measurement 2:	19.1	15.7	17.4	39.1	8.7
measurement 3:	18.3	15.6	17.6	40.3	8.2
measurement 4:	18.4	15.8	17.4	40.1	8.3
measurement 5:	20.4	15.5	17.9	36.9	9.3
$\bar{\emptyset}$	19.1(7)	15.6(1)	17.4(4)	39(2)	8.8(7)
calculated	19.3	14.0	16.7	47.3	2.7

Figure 7.4 shows SEM images of $\text{Ca}_{1+x}\text{Y}_{1-x}\text{SiN}_{3-x}\text{O}_x$ ($x > 0$) crystals. The size as well as the shape of the crystals suggest a solution based growth mechanism of the compound, as already reported in literature for ZnGeN_2 and Mg_2PN_3 .^[15, 18]

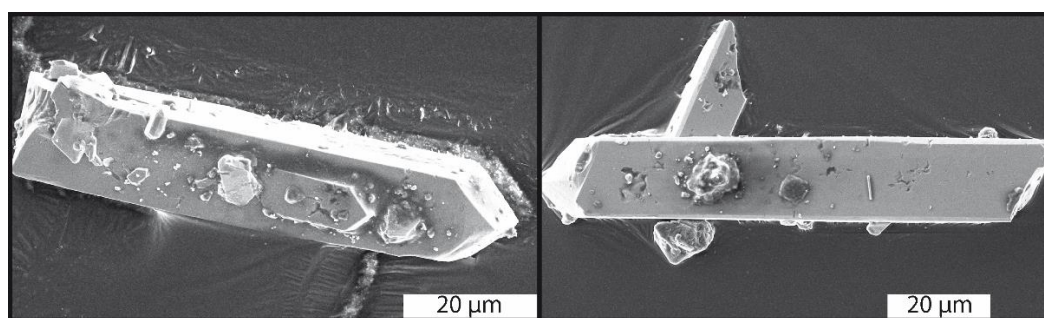


Figure 7.4. SEM images of two different crystals of $\text{Ca}_{1+x}\text{Y}_{1-x}\text{SiN}_{3-x}\text{O}_x$ ($x > 0$).

7.3 Conclusions

The oxonitridosilicate $\text{Ca}_{1+x}\text{Y}_{1-x}\text{SiN}_{3-x}\text{O}_x$ ($x > 0$) was synthesized under ammonothermal conditions using custom-built high-temperature autoclaves, starting from CaH_2 , intermetallic YSi and NaN_3 . In situ formed NaNH_2 acts as ammonobasic mineralizer to increase the solubility of the starting

materials, facilitating crystal growth of the product. In doing so, rod-shaped crystallites with sizes up to 200 μm were obtained, representing the first single crystals of oxonitridosilicates from ammonothermal synthesis, which are suitable for single-crystal X-ray diffraction measurements. The shape as well as the size of the crystallites suggest a solution based growth process. $\text{Ca}_{1+x}\text{Y}_{1-x}\text{SiN}_{3-x}\text{O}_x$ ($x > 0$) is built up from corner-sharing $\text{Si}(\text{N},\text{O})_4$ tetrahedra forming *zweier* single chains running along [100] and is isostructural to Ca_2PN_3 and Eu_2SiN_3 .^[22, 23] Based on these results as well as on earlier calculations,^[21] it can be assumed that further substitutions in this structure type should be possible. Not only the substitution of the divalent and trivalent cations seems possible, but also the substitution of tetrahedra centers, as already demonstrated in Ca_2PN_3 .^[23] Furthermore, we recently reported on the ammonothermal synthesis of nitridophosphates with different anionic frameworks including non-condensed tetrahedra groups, chains, layers and networks, indicating that the ammonothermal method can provide access to a wide variety of structurally diverse nitrides.^[20] In future work, the acquired knowledge should be applied to ammonothermal syntheses of further (oxo)nitridosilicates, to get access to hitherto unknown compounds with new structure types.

7.4 Experimental Section

All manipulations were conducted in argon filled gloveboxes (Unilab, MBraun, Garching, $\text{O}_2 < 1$ ppm, $\text{H}_2\text{O} < 1$ ppm) or in dried Schlenk-type glassware connected to a vacuum line (≤ 0.1 Pa) with argon or ammonia supply. Argon and ammonia (both Air Liquide, 99.999%) were further purified by gas cartridges (Micro Torr FT400-902 (for Ar) and MC400-702FV (for NH_3), SAES Pure Gas Inc., San Luis Obispo, CA, USA), providing a purity level of < 1 ppbV H_2O , O_2 and CO_2 . A mass flow meter (D-6320-DR, Bronkhorst, Ruurlo, Netherlands) was used for determination of the amount of inserted ammonia.

7.4.1 Preparation of starting materials

YSi was synthesized according to Parthé^[38] by mixing 5 mmol Y (444.5 mg, smart-elements 99.99%) and 5 mmol Si (140.4 mg, Alfa Aesar, 99.9%) and transferring the mixture into a Ta ampule. The ampule was weld shut and placed in a silica tube. The evacuated tube was placed in a tube furnace, heated to 1220 K with a heating rate of 5 K/min and held at this temperature for 24 h. After cooling to room temperature, the product was ground in an agate mortar and stored under argon.

7.4.2 Ammonothermal synthesis of $\text{Ca}_{1+x}\text{Y}_{1-x}\text{SiN}_{3-x}\text{O}_x$

$\text{Ca}_{1+x}\text{Y}_{1-x}\text{SiN}_{3-x}\text{O}_x$ ($x > 0$) was synthesized ammonothermally in custom-built high-temperature autoclaves (Haynes[®] 282[®], max. 1100 K, 170 MPa, 10 mL), starting from CaH_2 (1.5 mmol, 67.4 mg, Sigma-Aldrich, 99.99%), YSi (1.5 mmol, 185.9 mg) and NaN_3 (4.5 mmol, 292.5 mg, Sigma-Aldrich, 99.5%). The starting materials were ground and filled into a Nb-liner. After placing the liner in the autoclave, the reactor was sealed using flange joints and a silver coated Inconel[®] 718 ring (GFD seals). An Inconel[®] 718 tube connects the autoclave body with the upper part, which is constructed of a hand valve (SITEC), a pressure transmitter (HBM P2VA1/5000 bar) and a bursting disc (SITEC). After cooling the autoclave to 198 K using an ethanol/liquid nitrogen mixture, ammonia ($\approx 4\text{mL}$) was directly condensed into the vessel via a pressure regulating valve. The reaction mixture was heated to 670 K within 2 h, held at this temperature for 16 h and subsequently heated to 1070 K within 3 h. The temperature was held for 90 h reaching a maximum pressure of 140 MPa. After cooling to room temperature, the product was separated, washed with dry ethanol and dried under vacuum. A reddish powder with red, transparent rod-shaped crystals, which are sensitive towards air and moisture, were obtained. The red color may result from point defects in the compound.

7.4.3 Single-crystal X-ray diffraction

For single-crystal X-ray diffraction measurements, rod-shaped crystallites were placed and sealed in glass capillaries (0.2 mm, Hilgenberg GmbH) in argon atmosphere. Diffraction data were collected with a Bruker D8 Venture single-crystal X-ray diffractometer with Mo-K_α radiation ($\lambda = 0.71073 \text{ \AA}$). SADABS was used for absorption correction.^[39] The crystal structure was solved using direct methods (SHELXS)^[40] and refined by full-matrix least-squares methods (SHELXL).^[41]

Crystallographic data (excluding structure factors) for the structure in this paper have been deposited with the Cambridge Crystallographic Data Centre, CCDC, 12 Union Road, Cambridge CB21EZ, UK. Copies of the data can be obtained free of charge on quoting the depository number CCDC-1975994 (Fax: +44-1223-336-033; E-Mail: deposit@ccdc.cam.ac.uk, <http://www.ccdc.cam.ac.uk>).

7.4.4 Powder X-ray diffraction

Powder X-ray measurements were conducted on a STOE STADI P diffractometer with Cu-K_α ($\lambda = 1.5406 \text{ \AA}$) radiation, Ge(111) monochromator and Mythen 1K detector in modified Debye-Scherrer geometry. The samples were sealed in a glass capillary (0.3 mm, Hilgenberg GmbH). TOPAS was used for Rietveld refinement of the data.^[42]

7.4.5 Scanning electron microscopy

EDX measurements and images of the crystals were collected on a scanning electron microscope (Dualbeam Helios Nanolab G3 UC, FEI), equipped with an EDX detector (X-Max 80 SDD, Oxford instruments)). Therefore, the crystals were placed on adhesive carbon pads and coated with a conductive carbon film using a high-vacuum sputter coater (BAL-TEC MED 020, Bal Tec A).

7.5 Acknowledgements

The authors want to thank the group of Prof. Dr. E. Schlücker for fabrication of the autoclaves (FAU Erlangen-Nürnberg) and the Deutsche Forschungsgemeinschaft (DFG) for financial support within the research group "Chemistry and Technology of the Ammonothermal Synthesis of Nitrides" (FOR 1600), project SCHN377/16-2. We also want to thank Dr. Peter Mayer for single-crystal X-ray diffraction measurements (Department of Chemistry, LMU Munich).

7.6 References

- [1] M. Zeuner, S. Pagano, W. Schnick, "Nitridosilicates and Oxonitridosilicates: From Ceramic Materials to Structural and Functional Diversity", *Angew. Chem.* **2011**, 123, 7898-7920; *Angew. Chem. Int. Ed.* **2011**, 50, 7754-7775.
- [2] H. A. Höpfe, H. Lutz, P. Morys, W. Schnick, A. Seilmeier, "Luminescence in Eu^{2+} -doped $\text{Ba}_2\text{Si}_5\text{N}_8$: fluorescence, thermoluminescence, and upconversion", *J. Phys. Chem. Solids* **2000**, 61, 2001-2006.
- [3] H. Watanabe, N. Kijima, "Crystal structure and luminescence properties of $\text{Sr}_x\text{Ca}_{1-x}\text{AlSiN}_3:\text{Eu}^{2+}$ mixed nitride phosphors", *J. Alloys Compd.* **2009**, 475, 434-439.
- [4] C. Maak, L. Eisenburger, J. P. Wright, M. Nentwig, P. J. Schmidt, O. Oeckler, W. Schnick, " $\text{RE}_4\text{Ba}_2[\text{Si}_{12}\text{O}_2\text{N}_{16}\text{C}_3]:\text{Eu}^{2+}$ (RE = Lu, Y): Green-Yellow Emitting Oxonitridocarbidosilicates with a Highly Condensed Network Structure Unraveled through Synchrotron Microdiffraction", *Inorg. Chem.* **2018**, 57, 13840-13846.
- [5] D. Durach, L. Neudert, P. J. Schmidt, O. Oeckler, W. Schnick, " $\text{La}_3\text{BaSi}_5\text{N}_9\text{O}_2:\text{Ce}^{3+}$ – A Yellow Phosphor with an Unprecedented Tetrahedra Network Structure Investigated by Combination of Electron Microscopy and Synchrotron X-ray Diffraction", *Chem. Mater.* **2015**, 27, 4832-4838.
- [6] C. Maak, R. Niklaus, F. Friedrich, A. Mähringer, P. J. Schmidt, W. Schnick, "Efficient Yellow-Orange Phosphor $\text{Lu}_4\text{Ba}_2[\text{Si}_9\text{ON}_{16}]\text{O}:\text{Eu}^{2+}$ and Orange-Red Emitting $\text{Y}_4\text{Ba}_2[\text{Si}_9\text{ON}_{16}]\text{O}:\text{Eu}^{2+}$:

- Two Oxonitridosilicate Oxides with Outstanding Structural Variety*", *Chem. Mater.* **2017**, *29*, 8377-8384.
- [7] J. Häusler, L. Neudert, M. Mallmann, R. Niklaus, A.-C. L. Kimmel, N. S. A. Alt, E. Schlücker, O. Oeckler, W. Schnick, "Ammonothermal Synthesis of Novel Nitrides: Case Study on CaGaSiN_3 ", *Chem. Eur. J.* **2017**, *23*, 2583-2590.
- [8] T. Richter, R. Niewa, "Chemistry of Ammonothermal Synthesis", *Inorganics* **2014**, *2*, 29-78.
- [9] S. Pimputkar, S. Kawabata, J. S. Speck, S. Nakamura, "Improved growth rates and purity of basic ammonothermal GaN", *J. Cryst. Growth* **2014**, *403*, 7-17.
- [10] D. Ehretraut, R. T. Pakalapati, D. S. Kamber, W. Jiang, D. W. Pocius, B. C. Downey, M. McLaurin, M. P. D'Evelyn, "High Quality, Low Cost Ammonothermal Bulk GaN Substrates", *Jpn. J. Appl. Phys.* **2013**, *52*, 08JA01.
- [11] J. Häusler, W. Schnick, "Ammonothermal Synthesis of Nitrides: Recent Developments and Future Perspectives", *Chem. Eur. J.* **2018**, *24*, 11864-11879.
- [12] J. Li, T. Watanabe, H. Wada, T. Setoyama, M. Yoshimura, "Low-Temperature Crystallization of Eu-Doped Red-Emitting CaAlSiN_3 from Alloy-Derived Ammonometallates", *Chem. Mater.* **2007**, *19*, 3592-3594.
- [13] J. Häusler, L. Eisenburger, O. Oeckler, W. Schnick, "Ammonothermal Synthesis and Crystal Structure of the Nitridoalumogermanate $\text{Ca}_{1-x}\text{Li}_x\text{Al}_{1-x}\text{Ge}_{1+x}\text{N}_3$ ($x \approx 0.2$)", *Eur. J. Inorg. Chem.* **2018**, 759-764.
- [14] J. Häusler, R. Niklaus, J. Minár, W. Schnick, "Ammonothermal Synthesis and Optical Properties of Ternary Nitride Semiconductors Mg-IV-N_2 , Mn-IV-N_2 and $\text{Li-IV}_2\text{-N}_3$ (IV=Si, Ge)", *Chem. Eur. J.* **2018**, *24*, 1686-1693.
- [15] J. Häusler, S. Schimmel, P. Wellmann, W. Schnick, "Ammonothermal Synthesis of Earth-Abundant Nitride Semiconductors ZnSiN_2 and ZnGeN_2 and Dissolution Monitoring by In Situ X-ray Imaging", *Chem. Eur. J.* **2017**, *23*, 12275-12282.
- [16] M. Mallmann, R. Niklaus, T. Rackl, M. Benz, T. G. Chau, D. Johrendt, J. Minár, W. Schnick, "Solid Solutions of Grimm-Sommerfeld Analogous Nitride Semiconductors II-IV-N_2 (II = Mg, Mn, Zn; IV = Si, Ge): Ammonothermal Synthesis and DFT Calculations", *Chem. Eur. J.* **2019**, *25*, 15887-15895.
- [17] N. Cordes, W. Schnick, "Ammonothermal Synthesis of Crystalline Oxonitride Perovskites LnTaON_2 (Ln=La, Ce, Pr, Nd, Sm, Gd)", *Chem. Eur. J.* **2017**, *23*, 11410-11415.
- [18] M. Mallmann, C. Maak, R. Niklaus, W. Schnick, "Ammonothermal Synthesis, Optical Properties, and DFT Calculations of Mg_2PN_3 and Zn_2PN_3 ", *Chem. Eur. J.* **2018**, *24*, 13963-13970.
- [19] H. Jacobs, R. Nymwegen, "Synthesis and Crystal Structure of a Potassium Nitridophosphate, $\text{K}_3\text{P}_6\text{N}_{11}$ ", *Z. Anorg. Allg. Chem.* **1997**, *623*, 429-433.

- [20] M. Mallmann, S. Wendl, W. Schnick, "Crystalline Nitridophosphates by Ammonothermal Synthesis", *Chem. Eur. J.* **2020**, 26, 2067-2072.
- [21] O. M. ten Kate, T. Vranken, E. van der Kolk, A. P. J. Jansen, H. T. Hintzen, "Optical properties of $\text{Eu}^{2+}/\text{Eu}^{3+}$ mixed valence, silicon nitride based materials", *J. Solid State Chem.* **2014**, 213, 126-131.
- [22] M. Zeuner, S. Pagano, P. Matthes, D. Bichler, D. Johrendt, T. Harmening, R. Pöttgen, W. Schnick, "Mixed Valence Europium Nitridosilicate Eu_2SiN_3 ", *J. Am. Chem. Soc.* **2009**, 131, 11242-11248.
- [23] W. Schnick, V. Schultz-Coulon, " Ca_2PN_3 - A Novel Phosphorus(V) Nitride with One-Dimensional Infinite Chains of Corner-Sharing PN_4 Tetrahedra", *Angew. Chem.* **1993**, 105, 308-309; *Angew. Chem. Int. Ed. Engl.* **1993**, 32, 280-281.
- [24] H. Jacobs, U. Fink, "Über natrium- und kaliumamidometallate des calciums, strontiums und europiums", *J. Less Common Met.* **1979**, 63, 273-286.
- [25] A. Stuhr, H. Jacobs, R. Juza, "Amide of Yttrium", *Z. Anorg. Allg. Chem.* **1973**, 395, 291-300.
- [26] D. Peters, H. Jacobs, "Ammonothermalsynthese von kristallinem siliciumnitridimid, $\text{Si}_2\text{N}_2\text{NH}$ ", *J. Less Common Met.* **1989**, 146, 241-249.
- [27] The term *zweier* single chain was coined by Liebau and is derived from the German word "zwei" by suffixing "er" to the numeral; a *zweier* chain can be described as two polyhedra within one repeating unit of the linear part of the chain.
- [28] F. Liebau, "*Structural Chemistry of Silicates*", Springer, Berlin, **1985**.
- [29] T. Schlieper, W. Milius, W. Schnick, "Nitrido-silicate. II: Hochtemperatur-Synthesen und Kristallstrukturen von $\text{Sr}_2\text{Si}_5\text{N}_8$ und $\text{Ba}_2\text{Si}_5\text{N}_8$ ", *Z. Anorg. Allg. Chem.* **1995**, 621, 1380-1384.
- [30] C. Maak, R. Niklaus, O. Oeckler, W. Schnick, " $\text{Y}_{23}\text{Sr}_{17}[\text{Si}_{38}\text{O}_{18}\text{N}_{67}]\text{O}_9$ – An Oxonitridosilicate Oxide with a Unique Layered Structure", *Z. Anorg. Allg. Chem.* **2019**, 645, 182-187.
- [31] Z. A. Gál, P. M. Mallinson, H. J. Orchard, S. J. Clarke, "Synthesis and Structure of Alkaline Earth Silicon Nitrides: BaSiN_2 , SrSiN_2 , and CaSiN_2 ", *Inorg. Chem.* **2004**, 43, 3998-4006.
- [32] F. Ottinger, R. Nesper, "Synthesis and Crystal Structure of the Nitridosilicates $\text{Ca}_5[\text{Si}_2\text{N}_6]$ and $\text{Ca}_7[\text{NbSi}_2\text{N}_9]$ ", *Z. Anorg. Allg. Chem.* **2005**, 631, 1597-1602.
- [33] W. H. Baur, "Effective Ionic Radii in Nitrides", *Crystallogr. Rev.* **1987**, 1, 59-83.
- [34] R. Hoppe, "Madelung Constants", *Angew. Chem.* **1966**, 78, 52-63; *Angew. Chem. Int. Ed. Engl.* **1966**, 5, 95-106.
- [35] R. Hoppe, "The Coordination Number – an "Inorganic Chameleon"", *Angew. Chem.* **1970**, 82, 7-16; *Angew. Chem. Int. Ed. Engl.* **1970**, 9, 25-34.
- [36] R. Hübenthal, *Maple, Program for the Calculation of MAPLE values, version 4*; University of Gießen, Germany, 1993.

- [37] C. P. Kempter, N. H. Krikorian, J. C. McGuire, "The Crystal Structure of Yttrium Nitride", *J. Phys. Chem.* **1957**, *61*, 1237-1238.
- [38] E. Parthe, "The crystal structure of YSi and $\text{Hf}_5\text{Ge}_3(\text{C})$ ", *Acta Crystallogr.* **1959**, *12*, 559-560.
- [39] G. M. Sheldrick, *SADABS, Multi-Scan Absorption Correction*, v.2, Bruker-AXS, Madison, WI, USA, **2012**.
- [40] G. M. Sheldrick, *SHELXS-97: A program for crystal structure solution*, University of Göttingen, Germany, **1997**.
- [41] G. M. Sheldrick, *SHELXL-97: A program for crystal structure refinement*, University of Göttingen, Germany, **1997**.
- [42] A. Coelho, *TOPAS Academic, Version 6*, Coelho Software, Brisbane (Australia), **2016**.

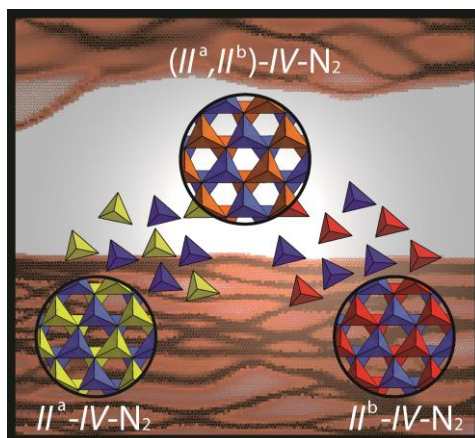
8 Summary

The main objectives of this thesis were the ammonothermal synthesis of Grimm-Sommerfeld analogous nitride semiconductors and the characterization of their optical and electronic properties, as well as the further development of the ammonothermal method in terms of number, structural diversity and crystal growth behavior of ammonothermally accessible (oxide) nitride materials. Details of the results achieved within this thesis are summarized below.

1. Solid Solutions of Grimm-Sommerfeld Analogous Nitride Semiconductors $II-IV-N_2$ ($II = \text{Mg, Mn, Zn}$; $IV = \text{Si, Ge}$): Ammonothermal Synthesis and DFT Calculations

Mathias Mallmann, Robin Niklaus, Tobias Rackl, Maximilian Benz, Thanh Giang Chau, Dirk Johrendt, Ján Minár, and Wolfgang Schnick

Chem. Eur. J. **2019**, *25*, 15887 - 15895.



Solid solutions of Grimm-Sommerfeld analogous $II-IV-N_2$ nitride semiconductors with the general formula $(II^{a_{1-x}}II^{b_x})-IV-N_2$ with $x \approx 0.5$ ($II = \text{Mg, Mn, Zn}$; $IV = \text{Si, Ge}$) were successfully synthesized starting from the corresponding metals, using supercritical NH_3 as solvent. NaNH_2 and KNH_2 were used as mineralizers, in order to increase the solubility of the starting materials through the formation of intermediate species. All six solid solutions crystallize in wurtzite-type superstructures in orthorhombic space group $Pna2_1$ (no. 33), which was confirmed by powder X-ray diffraction, and are therefore structurally related to group 13 nitrides. Diffuse reflectance UV/Vis spectroscopy indicated the optical bandgaps to range from 2.6 to 3.5 eV for the Ge-compounds and from 3.6 to 4.4 eV for the Si-compounds. In addition, magnetic measurements of Mn-containing compounds were conducted to indicate the magnetic behavior

of the solid solutions. In order to corroborate the experimental findings, DFT calculations were conducted to calculate the trends of electronic, optical and magnetic properties. For this purpose, the Korringa-Kohn-Rostoker Green's function method was used to account the mixed occupied phases. These results demonstrate the possibility to tune the bandgaps of the respective boundary phases by the formation of solid solutions, marking another step of *II-IV-N₂* compounds towards next-generation semiconductors as alternatives for commonly used group 13 nitrides.

2. Ammonothermal Synthesis, Optical Properties and DFT Calculations of Mg_2PN_3 and Zn_2PN_3

Mathias Mallmann, Christian Maak, Robin Niklaus, and Wolfgang Schnick

Chem. Eur. J. **2018**, *24*, 13963 - 13970.



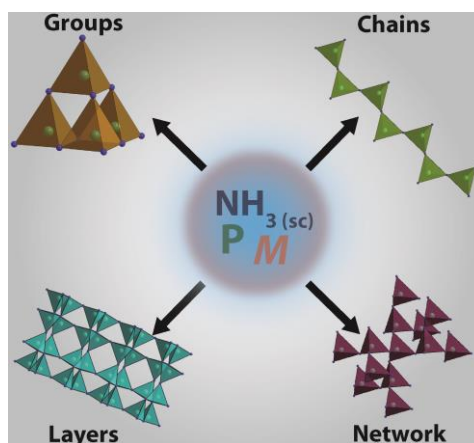
The ammonothermal approach was used to synthesize the phosphorus nitrides Mg_2PN_3 and Zn_2PN_3 , starting from P_3N_5 and the corresponding metals. To increase the solubility of the starting materials, the alkali metal amides NaNH_2 for the synthesis of Mg_2PN_3 , and KNH_2 for the synthesis of Zn_2PN_3 were employed as ammonobasic mineralizers. Thus, needle shaped single crystals of Mg_2PN_3 with length up to $30\ \mu\text{m}$ were obtained at $1070\ \text{K}$ and $140\ \text{MPa}$ for the first time. To obtain insights into the crystallization behavior of Mg_2PN_3 , dissolution experiments were conducted, suggesting a solution-based growth mechanism. Due to the fact that Zn_2PN_3 already decomposes at these conditions, only submicron-sized crystallites were obtained at $800\ \text{K}$ and $200\ \text{MPa}$. Both compounds crystallize in orthorhombic space group Cmc_2_1 (no. 36) in a wurtzite-type superstructure and are structurally related to group 13 nitrides, which was confirmed by single crystal XRD (Mg_2PN_3 : $a = 9.7234(16)$, $b = 5.6562(9)$, $c = 4.7083(7)\ \text{\AA}$, $Z = 4$) and PXRD (Zn_2PN_3 : $a = 9.4177(5)$, $b = 5.4399(3)$, $c = 4.9477(2)\ \text{\AA}$, $Z = 4$). As Zn_2PN_3 was predicted as possible wide bandgap semiconductor, the optical bandgaps of both compounds were estimated to be $5.0\ \text{eV}$ (Mg_2PN_3) and $3.8\ \text{eV}$ (Zn_2PN_3) using diffuse reflectance spectroscopy. To verify the experimental values and to obtain insights into the electronic properties, DFT calculations were carried out indicating indirect bandgaps for both compounds. Altogether, the presented results provide first experimental

information about the semiconducting properties of Mg_2PN_3 and Zn_2PN_3 and indicate these phosphorus nitrides as auspicious candidates for application in optoelectronics or photovoltaics.

3. Crystalline Nitridophosphates by Ammonothermal Synthesis

Mathias Mallmann, Sebastian Wendl, and Wolfgang Schnick

Chem. Eur. J. **2020**, *26*, 2067 - 2072.

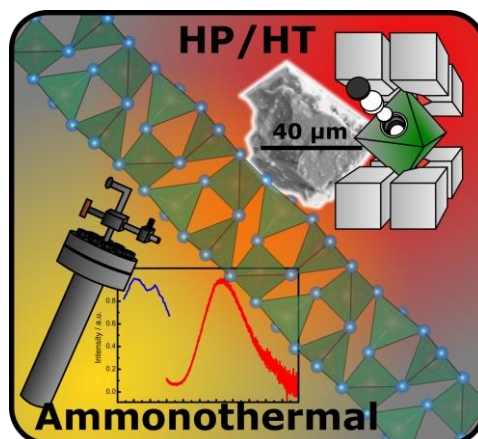


The six nitridophosphates $\alpha\text{-Li}_{10}\text{P}_4\text{N}_{10}$, $\beta\text{-Li}_{10}\text{P}_4\text{N}_{10}$, $\text{Li}_{18}\text{P}_6\text{N}_{16}$, Ca_2PN_3 , $\text{SrP}_8\text{N}_{14}$ and LiPN_2 were synthesized under ammonobasic conditions at temperatures and pressures up to 1070 K and 200 MPa, establishing the ammonothermal method as a versatile synthetic tool to access nitridophosphates. Moreover, red phosphorus was established as starting material for nitridophosphate synthesis, making commonly used and not readily available precursors such as P_3N_5 dispensable. In this context, a possible reaction mechanism as well as possible involved intermediates were discussed. All compounds were analyzed by powder X-ray diffraction and energy dispersive X-ray spectroscopy measurements. The absence of any NH_x functionality in Li containing nitridophosphates was confirmed by Fourier transformed infrared spectroscopy. The synthesized nitridophosphates cover degrees of condensation κ between $1/3$ and $4/7$, featuring different structural motifs ranging from PN_4 tetrahedra groups over infinite PN_4 tetrahedra chains and layered substructures to highly condensed frameworks. Thus, a major extension of the structural diversity of ammonothermally accessible nitrides was achieved, which was hitherto limited mainly to wurtzite-type derivatives and oxide nitride perovskites. In addition, using simple starting materials and yielding large sample-volumes, in contrast to commonly used high-pressure techniques, the ammonothermal method facilitates a more detailed characterization of materials properties of nitridophosphates.

4. $\text{Sr}_3\text{P}_3\text{N}_7$: Complementary Approach of Ammonothermal and High-Pressure Methods

Mathias Mallmann, Sebastian Wendl, Philipp Strobel, Peter J. Schmidt, and Wolfgang Schnick

Chem. Eur. J. **2020**, *26*, 6257 - 6263.



A complementary approach of high-pressure and ammonothermal methods as a powerful tool for a detailed characterization was used for the preparation of the novel nitridophosphate $\text{Sr}_3\text{P}_3\text{N}_7$. While single crystals could only be obtained using the multianvil approach following Equation 8.1, ammonothermal synthesis with SrH_2 , P_3N_5 and NaN_3 as starting materials yielded phase-pure crystalline powders for a detailed characterization of materials properties.

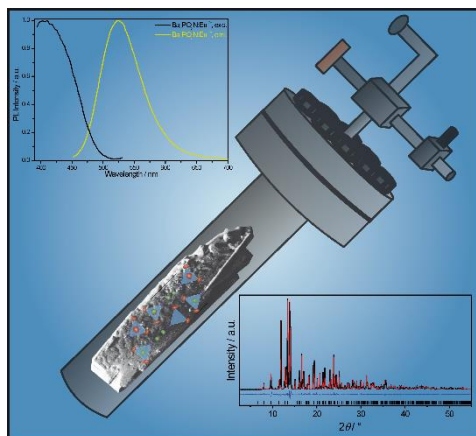


The structure was elucidated by single-crystal XRD and confirmed by Rietveld refinement. $\text{Sr}_3\text{P}_3\text{N}_7$ crystallizes in monoclinic space group $P2_1/c$ (no. 13) ($a = 6.882(8)$, $b = 7.416(9)$, $c = 7.036(8)$ Å, $\beta = 104.96(3)^\circ$, $Z = 2$) and is built up from unprecedented *dreier* double chains, extending the class of ternary alkaline earth nitridophosphates by the degree of condensation of $\kappa = 3/7$. The chemical composition was verified by energy dispersive X-ray spectroscopy. The absence of any NH_x functionality was confirmed by Fourier transformed infrared spectroscopy. $\text{Sr}_3\text{P}_3\text{N}_7$ exhibits an optical bandgap of 4.4 eV and a deep-red to infrared luminescence ($\lambda_{\text{em}} = 681$ nm, $\text{fwhm} \approx 3402 \text{ cm}^{-1}$) upon doping with Eu^{2+} , when excited with UV to blue light. The internal quantum efficiency was determined to be 42%, making it practically interesting for a further improvement of luminescence efficiency with respect to possible commercial applications such as in horticultural lighting.

5. Ammonothermal Synthesis of $\text{Ba}_2\text{PO}_3\text{N}$ – An Oxonitridophosphate with Non-Condensed PO_3N Tetrahedra

Sebastian Wendl, Mathias Mallmann, Philipp Strobel, Peter J. Schmidt, and Wolfgang Schnick

Eur. J. Inorg. Chem. **2020**, 2020, 841 - 846.

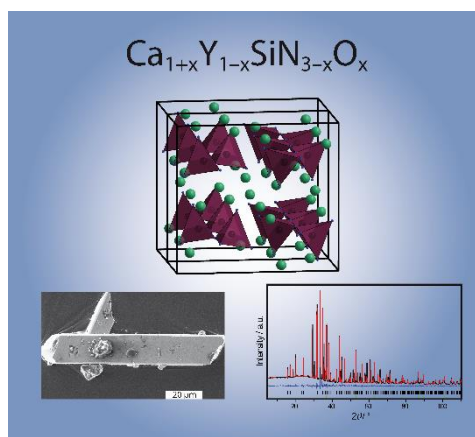


The *ortho*-oxonitridophosphate $\text{Ba}_2\text{PO}_3\text{N}$ was synthesized under ammonobasic conditions ($T = 1070 \text{ K}$, $p = 120 \text{ MPa}$) starting from red phosphorus, BaO , NaN_3 and KOH . Thus, single crystals with sizes up to $\sim 600 \mu\text{m}$ grew at the upper part of the used Ta-liner, suggesting a solution-based growth mechanism. The crystal structure was elucidated with single-crystal XRD ($Pnma$ (no. 62), $a = 7.596(2)$, $b = 5.796(1)$, $c = 10.212(3) \text{ \AA}$, $Z = 4$) and verified by Rietveld refinement. Energy dispersive X-ray and Fourier Transformed Infrared spectroscopy as well as bond-valance sums (BVS), lattice energy calculations (MAPLE) and charge distribution (CHARDI) corroborate the crystal structure. $\text{Ba}_2\text{PO}_3\text{N}$ crystallizes in the $\beta\text{-K}_2\text{SO}_4$ structure type, is isotypic to its lighter homologues $\text{Ca}_2\text{PO}_3\text{N}$ and $\text{Sr}_2\text{PO}_3\text{N}$ and is built up from non-condensed $[\text{PO}_3\text{N}]^{4-}$ ions, extending the range of ammonothermally accessible degrees of condensations for (oxo)nitridophosphates to $1/4 \leq \kappa \leq 4/7$. The bandgap was estimated using diffuse reflectance UV/Vis spectroscopy to be 4.3 eV . Eu^{2+} doped samples show green luminescence ($\lambda_{\text{em}} = 534 \text{ nm}$, $\text{fwhm} = 85 \text{ nm}/2961 \text{ cm}^{-1}$) when irradiated with UV light. However, low temperature measurements indicated a strong thermal quenching of the luminescence even at room temperature.

6. Ammonothermal Synthesis and Crystal Growth of the Chain-type Oxonitridosilicate $\text{Ca}_{1+x}\text{Y}_{1-x}\text{SiN}_{3-x}\text{O}_x$ ($x > 0$)

Mathias Mallmann, Christian Maak, and Wolfgang Schnick

Z. Anorg. Allg. Chem. **2020**, DOI: 10.1002/zaac.202000018.



The oxonitridosilicate $\text{Ca}_{1+x}\text{Y}_{1-x}\text{SiN}_{3-x}\text{O}_x$ with $x > 0$ was synthesized ammonothermally ($T = 1070$ K, $p = 140$ MPa) using CaH_2 , intermetallic YSi and NaN_3 as starting material. Intermetallic YSi was used to prevent an increased formation of YN as side-phase. Oxygen may originate from oxide layers of the autoclave and liner wall or from oxygen impurities of the starting materials. NaN_3 , which decomposes in situ and forms NaNH_2 , increases the solubility of the other starting materials by the formation of intermediate species, which facilitates the crystal growth process. Thus, rod shaped single crystals with sizes up to $200 \mu\text{m}$ were obtained. The crystal structure was elucidated by single-crystal XRD (*Cmce* (no. 64) with $a = 5.331(2)$, $b = 10.341(4)$, $c = 11.248(4)$ Å and $Z = 8$), which was supported by Rietveld-refinement, energy dispersive X-ray spectroscopy and MAPLE calculations. $\text{Ca}_{1+x}\text{Y}_{1-x}\text{SiN}_{3-x}\text{O}_x$ is isostructural to Ca_2PN_3 and Eu_2SiN_3 and is built up from infinite *zwei* single chains, running along [100]. These results may serve as a suitable starting point for future explorative screenings targeting novel (oxo)nitridosilicates and may trigger a future transfer of the ammonothermal approach to other (oxide) nitride systems.

9 Conclusion and Outlook

This thesis presents fundamental and applied investigations on (oxide) nitride materials that have been prepared by the ammonothermal method. Within the first part, the syntheses and examination of semiconducting nitrides are reported in Chapter 2 and 3. Here, the ammonothermal technique was used to synthesize solid solutions of Grimm-Sommerfeld analogous $II-IV-N_2$ nitrides ($II = \text{Mg, Mn, Zn}$; $IV = \text{Si, Ge}$) to investigate the bandgap tunability of these compounds. Moreover, the optical and electronic properties of the semiconducting phosphorus nitrides Mg_2PN_3 and Zn_2PN_3 were examined on the basis of ammonothermally synthesized bulk samples. Within the second part, Chapters 4–6 report on the development of an ammonothermal access to (oxo)nitridophosphates, which significantly expands the structural diversity of ammonothermally accessible nitrides and emphasizes the great potential of the ammonothermal method itself for (oxide) nitride synthesis. In Chapter 7, finally, the lessons learned were used for further methodical development in terms of the ammonothermal synthesis of an oxonitridosilicate, representing a case study for future preparation of other (oxide) nitride materials. Within the following sections the presented results are briefly discussed in their scientific context and prospects for future investigations are provided that concern the field of ammonothermal synthesis.

9.1 Grimm-Sommerfeld Analogous Nitride Semiconductors

Ga and In belong to the technology-critical elements, with application in state-of-the-art optoelectronic semiconductors, for instance.^[1] The steadily increasing demand of optoelectronic semiconductors in combination with the limited availability of Ga and In, however, triggers research for earth-abundant alternatives. Various theoretical calculations indicated Grimm-Sommerfeld analogous $II-IV-N_2$ and II_2-V-N_3 compounds as promising semiconductors. These materials are suspected to feature auspicious optical, electronic, and chemical properties, including good bandgap tunability, low carrier effective masses, as well as high chemical and thermal stability.^[2, 3] Therefore, $II-IV-N_2$ and II_2-V-N_3 nitrides appear as very interesting candidates for different application fields such as photovoltaics, photocatalysis, UV detectors or power electronics.^[4, 5] Experimental investigations on these compounds, however, had been rather scarce as their syntheses appeared quite challenging. For instance, Zn-IV-N_2 ($IV = \text{Si, Ge, Sn}$) could only be prepared using either metalorganic vapor-phase epitaxy, or high-temperature high-pressure methods. Since both methods only provide small sample volumes, a detailed characterization of chemical and physical properties has been hindered.^[6–10]

Prior to this thesis, the ammonothermal approach was introduced as a promising synthetic tool for the bulk synthesis of Grimm-Sommerfeld analogous nitrides such as above mentioned $II-IV-N_2$ ($II = \text{Mg, Mn, Zn}$; $IV = \text{Si, Ge}$), $I-IV-N_3$ ($I = \text{Li}$; $IV = \text{Si, Ge}$), or CaGaSiN_3 .^[11-13] At moderate temperatures and pressures NH_3 is reacted in a solution-based process, which hinders thermal decomposition and may facilitate crystal growth of the targeted compounds. Within this thesis, the research on $II-IV-N_2$ compounds was further expanded by synthesizing solid solutions with the general formula $(II^a_{1-x}II^b_x)-IV-N_2$ ($II = \text{Mg, Mn, Zn}$; $IV = \text{Si, Ge}$; $x \approx 0.5$). Optical measurements as well as corresponding DFT calculations suggest that bandgap tunability is achieved. Furthermore, the family of ammonothermally accessible Grimm-Sommerfeld analogous nitride semiconductors was extended by the synthesis of the II_2-V-N_3 nitrides Mg_2PN_3 and Zn_2PN_3 . Altogether, the $II-IV-N_2$ and the II_2-V-N_3 nitrides cover a bandgap range from 2.5 to 5.3 eV, which is already more than 50% of the energy range of group 13 nitrides (0.7 to 6.2 eV).^[14] There is, however, still room for improvement, especially in the narrow bandgap range, as is illustrated in Figure 9.1. To specifically access this bandgap range, future investigations may deal with the ammonothermal synthesis of $II-\text{Sn}-N_2$ compounds and their solid solutions ($II = \text{Mg, Mn, Zn}$).^[2, 9, 10, 15] Here, the synthesis of InN under ammononeutral conditions that uses InCl_3 and KNH_2 as starting materials could serve as a possible starting point ($T = 773 \text{ K}$, $p = 280 \text{ MPa}$).^[16] Thus, a similar approach starting from SnF_4 , ZnF_2 , and KNH_2 appears conceivable targeting ZnSnN_2 , for instance. Since ZnSnN_2 and MgSnN_2 have only been prepared at high pressures ($p > 5.5 \text{ GPa}$) thus far,^[10, 15] pressures above 300 MPa may be required under ammonothermal conditions, as well. Such pressures, however, are out of the range of the current autoclave equipment, in turn necessitating further mechanical improvements such as internally heated capsules.^[17] Moreover, future investigations on Sn containing intermediate species may support the screening of suitable synthesis parameters for ammonothermal synthesis of $II-\text{Sn}-N_2$ compounds. In contrast to Sn, intermediates of the nitridation of Zn, Mg or Mn have already been extensively studied in both, ammonobasic (e.g. $\text{Li}_4[\text{Zn}(\text{NH}_2)_4](\text{NH}_2)_2$, $\text{Na}_2[\text{Mn}(\text{NH}_2)_4]$, $\text{K}_2[\text{Zn}(\text{NH}_2)_4]$, $\text{K}_2[\text{Mg}(\text{NH}_2)_4]$, $\text{Cs}_2[\text{Zn}(\text{NH}_2)_4]$), and ammonoacidic environments (e.g. $\text{Zn}(\text{NH}_3)_3\text{F}_2$, $[\text{Zn}_2(\text{NH}_3)_2(\text{NH}_2)_3]\text{Cl}$, $[\text{Zn}(\text{NH}_3)_2(\text{NH}_2)]\text{Br}$).^[18-24]

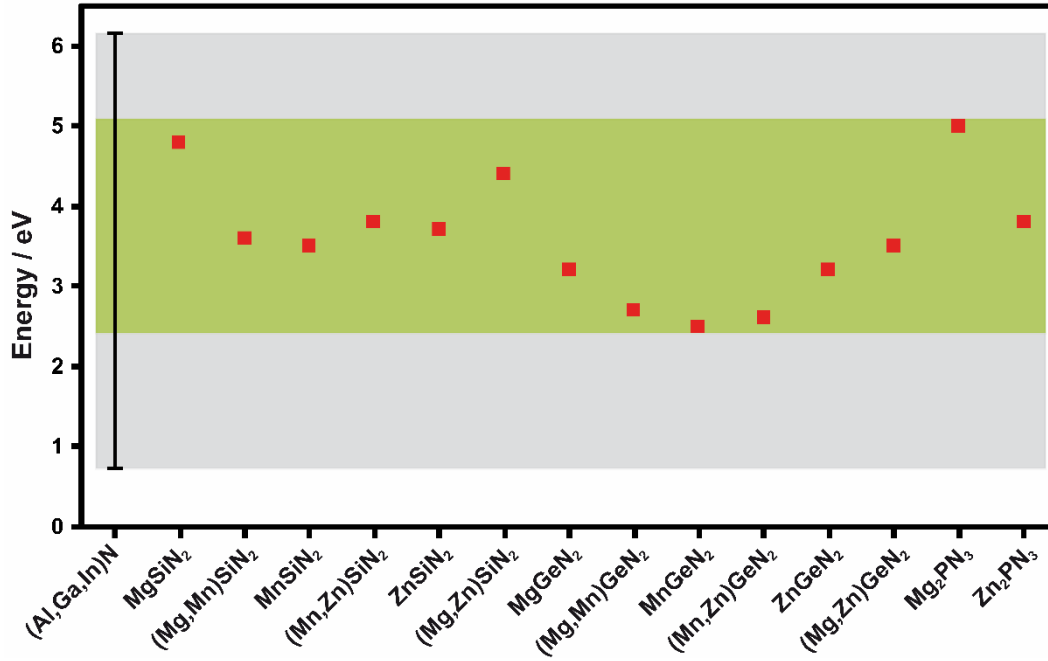


Figure 9.1. Optical bandgaps of ammonothermally synthesized Grimm-Sommerfeld analogous $II-IV-N_2$ and II_2-V-N_3 compounds together with the accessible bandgap range of $(Al,Ga,In)N$ solid solutions. Red squares are values obtained from diffuse reflectance UV/Vis spectroscopy, the area illustrates the bandgap range of group 13 nitrides, and the green area highlights the accessible bandgap range of $II-IV-N_2$ and II_2-V-N_3 compounds.^[11, 12]

To replace group 13 nitrides by Grimm-Sommerfeld analogous nitrides in semiconducting devices as a long-term goal, the growth of single crystals is indispensable. Therefore, future examinations of the crystallization behavior of $II-IV-N_2$ compounds appear essential. For this purpose, in situ methods such as X-ray imaging experiments are of decisive importance. Exemplarily, this method has successfully been used for in situ investigations on the ammonothermal crystallization process of GaN, and recently insights in the dissolution behavior of $ZnGeN_2$ have been obtained.^[11, 25, 26] Accordingly, $ZnGeN_2$ dissolves at temperatures around 670 K, while its formation proceeds at 870 K. This information is crucial for a successful solution-based crystal growth and may pave the way to further solid solutions with general formula $II-(IV^a_{1-x}IV^b_x)-N_2$ ($II = Mg, Mn, Zn$; $IV = Si, Ge, Sn$), which are hardly accessible due to different synthesis temperatures of the ternary compounds.

In a next step, the optical and electronic properties of Grimm-Sommerfeld analogous nitrides may be examined in terms of their electronic bandgap, defect concentration, as well as charge carrier concentration, lifetime, and mobility. Furthermore, doping experiments would provide further information on their semiconducting properties. Theoretical calculations concerning $ZnGeN_2$ already indicated possible p-type dopants such as Li, Al or Ga.^[27]

Recapitulating, the ammonothermal synthesis of Grimm-Sommerfeld analogous nitride semiconductors as well as the subsequent characterization of their optical and electronic properties, presented in the first part of this thesis, is a further step towards the development of possible alternatives for group 13 nitride semiconductors. Based on these results, the ammonothermal method seems promising for the further synthesis of theoretically predicted wurtzite-type semiconductors such as ZnTiN_2 , Zn_2VN_3 , Zn_2TaN_3 , and Zn_3WN_4 .^[3]

9.2 Extension of Ammonothermally Accessible (Oxide) Nitrides

Although the ammonothermal approach has been developed continuously for over 60 years, the number of synthesized ternary and multinary (oxide) nitrides, as well as their structural diversity has been rather limited, prior to this thesis. The successful synthesis of HPN_2 , $\text{K}_3\text{P}_6\text{N}_{11}$, Mg_2PN_3 , and Zn_2PN_3 , however, inspired to do systematic investigations on the ammonothermal synthesis of nitridophosphates, within this thesis.^[28, 29] Accordingly, the nitridophosphates known from literature, $\alpha\text{-Li}_{10}\text{P}_4\text{N}_{10}$, $\beta\text{-Li}_{10}\text{P}_4\text{N}_{10}$, $\text{Li}_{18}\text{P}_6\text{N}_{16}$, Ca_2PN_3 , $\text{SrP}_8\text{N}_{14}$, and LiPN_2 , were for the first time synthesized under ammonothermal conditions. Hence, a huge variety of structures is now accessible, including PN_4 tetrahedra groups, infinite PN_4 tetrahedra chains, layered substructures, and highly condensed frameworks.^[30–35] Moreover, red phosphorus was established as a starting material for nitridophosphate synthesis, making inconvenient precursors such as P_3N_5 , PCl_5 or $(\text{PNCl}_2)_3$ dispensable.^[36] The ammonothermal approach even allowed to expand the (oxo)nitridophosphate compound class by the preparation of the *ortho*-oxonitridophosphate $\text{Ba}_2\text{PO}_3\text{N}$, with single crystal sizes up to 600 μm in diameter, and the chain-type nitridophosphate $\text{Sr}_3\text{P}_3\text{N}_7$. Thus, both the total number, as well as the overall structural diversity of ammonothermally accessible multinary (oxide) nitrides have significantly been extended.

In addition to the explorative screenings, future investigations may shine a light on the reaction mechanism of nitridophosphate crystallization. Especially, the mobilization of red phosphorus in supercritical ammonia might be considered of interest for nitride material research. Jacobs and co-workers already succeeded in the synthesis of various soluble compounds, such as $\text{P}_3\text{N}_3(\text{NH}_2)_6$, $\text{Na}_{10}[\text{P}_4(\text{NH})_6\text{N}_4](\text{NH}_2)_6(\text{NH}_3)_{0.5}$, and $\text{Cs}_5[\text{P}(\text{NH})_4](\text{NH}_2)_2$, which may be conceived as intermediate species in a solution-based crystallization process.^[37–39] Prospective in situ Raman and UV/Vis investigations, as well as ultrasonic velocity measurements may provide additional information on possible intermediates and their concentrations, respectively.^[40, 41]

(Oxo)Nitridophosphates are commonly prepared employing high-pressure high-temperature techniques, which however provide rather limited sample volumes.^[36] In contrast, the novel straightforward ammonothermal syntheses of (oxo)nitridophosphates yield large-volume samples, which

enable a detailed characterization of their materials properties. Accordingly, bulk samples of ammonothermally synthesized $\text{Ba}_2\text{PO}_3\text{N}:\text{Eu}^{2+}$ and $\text{Sr}_3\text{P}_3\text{N}_7:\text{Eu}^{2+}$ were investigated within the scope of this thesis. Featuring a broad red to IR emission ($\lambda_{\text{em}} = 681 \text{ nm}$, $\text{fwhm} = 162 \text{ nm}/3402 \text{ cm}^{-1}$, $\text{IQE} = 42\%$), $\text{Sr}_3\text{P}_3\text{N}_7:\text{Eu}^{2+}$ turned out as an intriguing phosphor for future optimization, as such infrared emitters are currently discussed for commercial applications in horticultural lighting, for instance. Thus, the ammonothermal technique was introduced as an innovative approach for (oxo)nitridophosphate synthesis, which may enable mid-term applications of P/N based materials.

Deducing from the lessons learned, the chain-type oxonitridosilicate $\text{Ca}_{1+x}\text{Y}_{1-x}\text{SiN}_{3-x}\text{O}_x$ ($x > 0$) was synthesized in supercritical NH_3 , and single crystals of several hundred μm in length were obtained. This exemplary synthesis of an oxonitridosilicate will serve as a suitable starting point for future explorative screenings targeting novel (oxo)nitridosilicates. Moreover, this case study may trigger future transfer of the ammonothermal approach to other (oxide) nitride systems such as (oxo)nitridogermanates, (oxo)nitridoaluminates or (oxo)nitridogallates. For the latter two, the deep knowledge on the ammonothermal synthesis of group 13 nitrides in general could certainly be helpful.

Furthermore, noncentrosymmetric (oxo)nitridosilicates are discussed as possible nonlinear optical (NLO) materials, as they exhibit a high chemical and thermal stability.^[42] However, the investigation of such nonlinear optics requires large single crystals, which are hardly feasible with conventional high-temperature techniques. With respect to the herein reported growth of large $\text{Ba}_2\text{PO}_3\text{N}$ and $\text{Ca}_{1+x}\text{Y}_{1-x}\text{SiN}_{3-x}\text{O}_x$ ($x > 0$) single crystals, the ammonothermal method could be a promising approach for the crystal growth of such NLO materials.

9.3 Final Remarks

Within this thesis, the ammonothermal technique was improved in terms of fundamental and applied investigations on (oxide) nitride materials. Through systematic investigations on suitable reaction conditions, new starting materials, and possible mineralizers, compounds that had previously not been studied ammonothermally could be accessed. Moreover, these investigations allowed for ammonothermal synthesis of large single crystals of ternary and multinary (oxide) nitrides for the first time, which may provide promising insights for a future ammonothermal preparation of functional materials. Recapitulating, this thesis further established the ammonothermal method in the field of preparative solid-state chemistry, and may therefore pave the way to the future synthesis and crystal growth of numerous (oxide) nitride materials.

9.4 References

- [1] A. Cobelo-García, M. Filella, P. Croot, C. Frazzoli, G. Du Laing, N. Ospina-Alvarez, S. Rauch, P. Salaun, J. Schäfer, S. Zimmermann, "COST action TD1407: network on technology-critical elements (NOTICE)—from environmental processes to human health threats", *Environ. Sci. Pollut. Res.* **2015**, *22*, 15188-15194.
- [2] P. Narang, S. Chen, N. C. Coronel, S. Gul, J. Yano, L. W. Wang, N. S. Lewis, H. A. Atwater, "Bandgap Tunability in Zn(Sn,Ge)N₂ Semiconductor Alloys", *Adv. Mater.* **2014**, *26*, 1235-1241.
- [3] Y. Hinuma, T. Hatakeyama, Y. Kumagai, L. A. Burton, H. Sato, Y. Muraba, S. Iimura, H. Hiramatsu, I. Tanaka, H. Hosono, F. Oba, "Discovery of earth-abundant nitride semiconductors by computational screening and high-pressure synthesis", *Nat. Commun.* **2016**, *7*, 11962.
- [4] T. Suehiro, M. Tansho, T. Shimizu, "Quaternary Wurtzitic Nitrides in the System ZnGeN₂–GaN: Powder Synthesis, Characterization, and Potentiality as a Photocatalyst", *J. Phys. Chem. C* **2017**, *121*, 27590-27596.
- [5] Y. Zou, Y. Zhang, Y. Hu, H. Gu, "Ultraviolet Detectors Based on Wide Bandgap Semiconductor Nanowire: A Review", *Sensors* **2018**, *18*, 2072.
- [6] T. Endo, Y. Sato, H. Takizawa, M. Shimada, "High-pressure synthesis of new compounds, ZnSiN₂ and ZnGeN₂ with distorted wurtzite structure", *J. Mater. Sci. Lett.* **1992**, *11*, 424-426.
- [7] T. Cloitre, A. Sere, R. L. Aulombard, "Epitaxial growth of ZnSiN₂ single-crystalline films on sapphire substrates", *Superlattices Microstruct.* **2004**, *36*, 377-383.
- [8] T. Misaki, A. Wakahara, H. Okada, A. Yoshida, "Epitaxial growth and characterization of ZnGeN₂ by metalorganic vapor phase epitaxy", *J. Cryst. Growth* **2004**, *260*, 125-129.
- [9] P. C. Quayle, K. He, J. Shan, K. Kash, "Synthesis, lattice structure, and band gap of ZnSnN₂", *MRS Commun.* **2013**, *3*, 135-138.
- [10] F. Kawamura, N. Yamada, M. Imai, T. Taniguchi, "Synthesis of ZnSnN₂ crystals via a high-pressure metathesis reaction", *Cryst. Res. Technol.* **2016**, *51*, 220-224.
- [11] J. Häusler, S. Schimmel, P. Wellmann, W. Schnick, "Ammonothermal Synthesis of Earth-Abundant Nitride Semiconductors ZnSiN₂ and ZnGeN₂ and Dissolution Monitoring by In Situ X-ray Imaging", *Chem. Eur. J.* **2017**, *23*, 12275-12282.
- [12] J. Häusler, R. Niklaus, J. Minár, W. Schnick, "Ammonothermal Synthesis and Optical Properties of Ternary Nitride Semiconductors Mg-IV-N₂, Mn-IV-N₂ and Li-IV₂-N₃ (IV=Si, Ge)", *Chem. Eur. J.* **2018**, *24*, 1686-1693.

- [13] J. Häusler, L. Neudert, M. Mallmann, R. Niklaus, A.-C. L. Kimmel, N. S. A. Alt, E. Schlücker, O. Oeckler, W. Schnick, "Ammonothermal Synthesis of Novel Nitrides: Case Study on CaGaSiN_3 ", *Chem. Eur. J.* **2017**, *23*, 2583-2590.
- [14] J. Wu, W. Walukiewicz, "Band gaps of InN and group III nitride alloys", *Superlattices Microstruct.* **2003**, *34*, 63-75.
- [15] F. Kawamura, M. Imura, H. Murata, N. Yamada, T. Taniguchi, "Synthesis of a Novel Rocksalt-Type Ternary Nitride Semiconductor MgSnN_2 Using the Metathesis Reaction Under High Pressure", *Eur. J. Inorg. Chem.* **2020**, *2020*, 446-451.
- [16] J. Hertrampf, P. Becker, M. Widenmeyer, A. Weidenkaff, E. Schlücker, R. Niewa, "Ammonothermal Crystal Growth of Indium Nitride", *Cryst. Growth Des.* **2018**, *18*, 2365-2369.
- [17] D. Ehrentraut, R. T. Pakalapati, D. S. Kamber, W. Jiang, D. W. Pocius, B. C. Downey, M. McLaurin, M. P. D'Evelyn, "High Quality, Low Cost Ammonothermal Bulk GaN Substrates", *Jpn. J. Appl. Phys.* **2013**, *52*, 08JA01.
- [18] T. M. M. Richter, N. S. A. Alt, E. Schlücker, R. Niewa, "Ammonothermal Synthesis and Characterization of $\text{Li}_4[\text{Zn}(\text{NH}_2)_4](\text{NH}_2)_2$ ", *Z. Anorg. Allg. Chem.* **2015**, *641*, 1016-1023.
- [19] G. Kreiner, H. Jacobs, "Magnetische Struktur von $\eta\text{-Mn}_3\text{N}_2$ ", *J. Alloys Compd.* **1992**, *183*, 345-362.
- [20] T. M. M. Richter, S. Zhang, R. Niewa, "Ammonothermal synthesis of dimorphic $\text{K}_2[\text{Zn}(\text{NH}_2)_4]$ ", *Z. Kristallogr.* **2013**, *228*, 351-358.
- [21] H. Jacobs, J. Birkenbeul, J. Kockelkorn, "Darstellung und eigenschaften der amidomagnesate des kaliums und rubidiums $\text{K}_2[\text{Mg}(\text{NH}_2)_4]$ - und $\text{Rb}_2[\text{Mg}(\text{NH}_2)_4]$ -Verbindungen mit isolierten $[\text{Mg}(\text{NH}_2)_4]^{2-}$ -tetraedern", *J. Less Common Met.* **1984**, *97*, 205-214.
- [22] T. M. M. Richter, N. S. A. Alt, E. Schlücker, R. Niewa, "Ammonothermal Synthesis and Characterization of $\text{Cs}_2[\text{Zn}(\text{NH}_2)_4]$ ", *Z. Anorg. Allg. Chem.* **2016**, *642*, 1207-1211.
- [23] T. M. M. Richter, S. LeTonquesse, N. S. A. Alt, E. Schlücker, R. Niewa, "Trigonal-Bipyramidal Coordination in First Ammoniates of ZnF_2 : $\text{ZnF}_2(\text{NH}_3)_3$ and $\text{ZnF}_2(\text{NH}_3)_2$ ", *Inorg. Chem.* **2016**, *55*, 2488-2498.
- [24] T. M. M. Richter, S. Strobel, N. S. A. Alt, E. Schlücker, R. Niewa, "Ammonothermal Synthesis and Crystal Structures of Diamminetriamidodizinc Chloride $[\text{Zn}_2(\text{NH}_3)_2(\text{NH}_2)_3]\text{Cl}$ and Diamminemonoamidozinc Bromide $[\text{Zn}(\text{NH}_3)_2(\text{NH}_2)]\text{Br}$ ", *Inorganics* **2016**, *4*, 41.
- [25] S. Schimmel, M. Lindner, T. G. Steigerwald, B. Hertweck, T. M. M. Richter, U. Künecke, N. S. A. Alt, R. Niewa, E. Schlücker, P. J. Wellmann, "Determination of GaN solubility in supercritical ammonia with NH_4F and NH_4Cl mineralizer by in situ x-ray imaging of crystal dissolution", *J. Cryst. Growth* **2015**, *418*, 64-69.

- [26] S. Schimmel, M. Koch, P. Macher, A.-C. L. Kimmel, T. G. Steigerwald, N. S. A. Alt, E. Schlücker, P. Wellmann, "Solubility and dissolution kinetics of GaN in supercritical ammonia in presence of ammonoacidic and ammonobasic mineralizers", *J. Cryst. Growth* **2017**, 479, 59-66.
- [27] N. L. Adamski, Z. Zhu, D. Wickramaratne, C. G. V. d. Walle, "Strategies for p-type doping of ZnGeN₂", *Appl. Phys. Lett.* **2019**, 114, 032101.
- [28] H. Jacobs, R. Nymwegen, S. Doyle, T. Wroblewski, W. Kockelmann, "Crystalline Phosphorus(V) Nitride Imide, HPN₂ and DPN₂, respectively, – Structure Determination with X-Ray, Synchrotron, and Neutron Radiation", *Z. Anorg. Allg. Chem.* **1997**, 623, 1467-1474.
- [29] H. Jacobs, R. Nymwegen, "Synthesis and Crystal Structure of a Potassium Nitridophosphate, K₃P₆N₁₁", *Z. Anorg. Allg. Chem.* **1997**, 623, 429-433.
- [30] W. Schnick, U. Berger, "Li₁₀P₄N₁₀ - A Lithium Phosphorus(V) Nitride with the Novel Complex Anion P₄N₁₀¹⁰⁻", *Angew. Chem.* **1991**, 103, 857-858; *Angew. Chem. Int. Ed. Engl.* **1992**, 31, 213-214.
- [31] E. M. Bertschler, C. Dietrich, T. Leichtweiß, J. Janek, W. Schnick, "Li⁺ Ion Conductors with Adamantane-Type Nitridophosphate Anions β-Li₁₀P₄N₁₀ and Li₁₃P₄N₁₀X₃ with X=Cl, Br", *Chem. Eur. J.* **2018**, 24, 196-205.
- [32] E.-M. Bertschler, C. Dietrich, J. Janek, W. Schnick, "Li₁₈P₆N₁₆ – A Lithium Nitridophosphate with Unprecedented Tricyclic [P₆N₁₆]¹⁸⁻ Ions", *Chem. Eur. J.* **2017**, 23, 2185-2191.
- [33] W. Schnick, V. Schultz-Coulon, "Ca₂PN₃ - A Novel Phosphorus(V) Nitride with One-Dimensional Infinite Chains of Corner-Sharing PN₄ Tetrahedra", *Angew. Chem.* **1993**, 105, 308-309; *Angew. Chem. Int. Ed. Engl.* **1993**, 32, 280-281.
- [34] S. Wendl, W. Schnick, "SrH₄P₆N₁₂ and SrP₈N₁₄: Insights into the Condensation Mechanism of Nitridophosphates under High Pressure", *Chem. Eur. J.* **2018**, 24, 15889-15896.
- [35] W. Schnick, J. Lücke, "On Lithium Phosphorus Nitride. Preparation and Refinement of the Crystal Structure of LiPN₂", *Z. Anorg. Allg. Chem.* **1990**, 588, 19-25.
- [36] S. D. Kloß, W. Schnick, "Nitridophosphates – A Success Story of Nitride Synthesis", *Angew. Chem.* **2019**, 131, 8015-8027; *Angew. Chem. Int. Ed.* **2019**, 58, 7933-7944.
- [37] F. Golinski, H. Jacobs, "Crystal Structure of Hexamine Cyclotriphosphazene, P₃N₃(NH₂)₆", *Z. Anorg. Allg. Chem.* **1994**, 620, 965-968.
- [38] H. Jacobs, S. Pollok, F. Golinski, "Synthesis and Crystal Structure of Na₁₀[P₄(NH)₆N₄](NH₂)₆(NH₃)_{0.5} with an Adamantane-like Anion [P₄(NH)₆N₄]⁴⁻", *Z. Anorg. Allg. Chem.* **1994**, 620, 1213-1218.
- [39] H. Jacobs, F. Golinski, "Synthesis and Crystal Structure of a Cesium-tetraimidophosphate-diamid, Cs₅[P(NH)₄](NH₂)₂ = Cs₃[P(NH)₄] · 2 CsNH₂", *Z. Anorg. Allg. Chem.* **1994**, 620, 531-534.

- [40] T. G. Steigerwald, J. Balouschek, B. Hertweck, A.-C. L. Kimmel, N. S. A. Alt, E. Schlücker, "In situ investigation of decomposing ammonia and ammonobasic solutions under supercritical conditions via UV/vis and Raman Spectroscopy", *J. Supercrit. Fluids* **2018**, *134*, 96-105.
- [41] H. Baser, W. Schwieger, D. Freitag, T. G. Steigerwald, E. Schlücker, "Solubility Studies of Sodium Azide in Liquid Ammonia by In Situ Ultrasonic Velocity Measurement", *Chem. Eng. Technol.* **2017**, *40*, 1101-1106.
- [42] H. Lutz, S. Joosten, J. Hoffmann, P. Lehmeier, A. Seilmeier, H. A. Höppe, W. Schnick, "Nonlinear optical susceptibilities $\chi^{(2)}$ of nitridosilicate powders", *J. Phys. Chem. Solids* **2004**, *65*, 1285-1290.

A Supporting Information for Chapter 2

Mathias Mallmann, Robin Niklaus, Tobias Rackl, Maximilian Benz, Thanh Giang Chau, Dirk Johrendt, Ján Minár, and Wolfgang Schnick

Chem. Eur. J. **2019**, *25*, 15887 - 15895.

A.1 Additional crystallographic data

Table A.1. Wyckoff positions and atomic coordinates of $\text{Mg}_{1-x}\text{Mn}_x\text{SiN}_2$ ($x \approx 0.543$) obtained from powder X-ray diffraction, standard deviations in parentheses.

Atom	Wyckoff	<i>x</i>	<i>y</i>	<i>z</i>	SOF	<i>U</i> _{iso}
Mg1	4a	0.0810(4)	0.6251(6)	-0.0116(5)	0.457(12)	0.0127
Mn1	4a	0.0810(4)	0.6251(6)	-0.0116(5)	0.543(12)	0.0127
Si1	4a	0.0646(5)	0.1356(6)	0.0082(7)	1	0.0127
N1	4a	0.0468(12)	0.0799(15)	0.3611(11)	1	0.0127
N2	4a	0.1235(9)	0.6388(17)	0.4167(12)	1	0.0127

Table A.2. Wyckoff positions and atomic coordinates of $\text{Mg}_{1-x}\text{Zn}_x\text{SiN}_2$ ($x \approx 0.515$) obtained from powder X-ray diffraction, standard deviations in parentheses.

Atom	Wyckoff	<i>x</i>	<i>y</i>	<i>z</i>	SOF	<i>U</i> _{iso}
Mg1	4a	0.08133(16)	0.6226(3)	0.0043(3)	0.485(3)	0.0127
Zn1	4a	0.08133(16)	0.6226(3)	0.0043(3)	0.515(3)	0.0127
Si1	4a	0.0742(3)	0.1225(5)	0.0048(7)	1	0.0214(5)
N1	4a	0.0560(7)	0.1010(11)	0.3610(5)	1	0.0127
N2	4a	0.1086(6)	0.6528(10)	0.4168(5)	1	0.0127

Table A.3. Wyckoff positions and atomic coordinates of $\text{Mn}_{1-x}\text{Zn}_x\text{SiN}_2$ ($x \approx 0.53$) obtained from powder X-ray diffraction, standard deviations in parentheses.

Atom	Wyckoff	<i>x</i>	<i>y</i>	<i>z</i>	SOF	U_{iso}
Mn1	4 <i>a</i>	0.08166(18)	0.6227(4)	0.9652(5)	0.47(2)	0.0127
Zn1	4 <i>a</i>	0.08166(18)	0.6227(4)	0.9652(5)	0.53(2)	0.0127
Si1	4 <i>a</i>	0.0709(4)	0.1213(9)	0.9672(17)	1	0.0171(1)
N1	4 <i>a</i>	0.1097(12)	0.6601(15)	0.3690(8)	1	0.0127
N2	4 <i>a</i>	0.0397(14)	0.1082(19)	0.3118(8)	1	0.0127

Table A.4. Wyckoff positions and atomic coordinates of $\text{Mg}_{1-x}\text{Mn}_x\text{GeN}_2$ ($x \approx 0.625$) obtained from powder X-ray diffraction, standard deviations in parentheses.

Atom	Wyckoff	<i>x</i>	<i>y</i>	<i>z</i>	SOF	U_{iso}
Mg1	4 <i>a</i>	0.0827(3)	0.6217(7)	0.0880(10)	0.375(6)	0.0127
Mn1	4 <i>a</i>	0.0827(3)	0.6217(7)	0.0880(10)	0.625(6)	0.0127
Ge1	4 <i>a</i>	0.0711(2)	0.1267(4)	0.0814(6)	1	0.0265(4)
N1	4 <i>a</i>	-0.0621(14)	-0.0877(12)	-0.0476(12)	1	0.0127
N2	4 <i>a</i>	0.1065(11)	0.6248(18)	0.4827(11)	1	0.0127

Table A.5. Wyckoff positions and atomic coordinates of $\text{Mg}_{1-x}\text{Zn}_x\text{GeN}_2$ ($x \approx 0.545$) obtained from powder X-ray diffraction, standard deviations in parentheses.

Atom	Wyckoff	<i>x</i>	<i>y</i>	<i>z</i>	SOF	U_{iso}
Mg1	4 <i>a</i>	0.0843(3)	0.6251(7)	0.9629(7)	0.455(4)	0.0127
Zn1	4 <i>a</i>	0.0843(3)	0.6251(7)	0.9629(7)	0.545(4)	0.0127
Ge1	4 <i>a</i>	0.07434(19)	0.1261(5)	0.9691(4)	1	0.0203(3)
N1	4 <i>a</i>	0.0745(14)	0.125(2)	0.3342(9)	1	0.0127
N2	4 <i>a</i>	0.0954(13)	0.6515(14)	0.3697(9)	1	0.0127

Table A.6. Wyckoff positions and atomic coordinates of $\text{Mn}_{1-x}\text{Zn}_x\text{GeN}_2$ ($x \approx 0.45$) obtained from powder X-ray diffraction, standard deviations in parentheses.

Atom	Wyckoff	x	y	z	SOF	U_{iso}
Mn1	4a	0.0839(3)	0.6255(10)	0.9900(11)	0.55(2)	0.0127
Zn1	4a	0.0839(3)	0.6255(10)	0.9900(11)	0.45(2)	0.0127
Ge1	4a	0.0733(3)	0.1277(9)	0.9922(8)	1	0.0137(1)
N1	4a	0.0743(19)	0.117(5)	0.3587(19)	1	0.0127
N2	4a	0.0998(18)	0.652(3)	0.3886(19)	1	0.0127

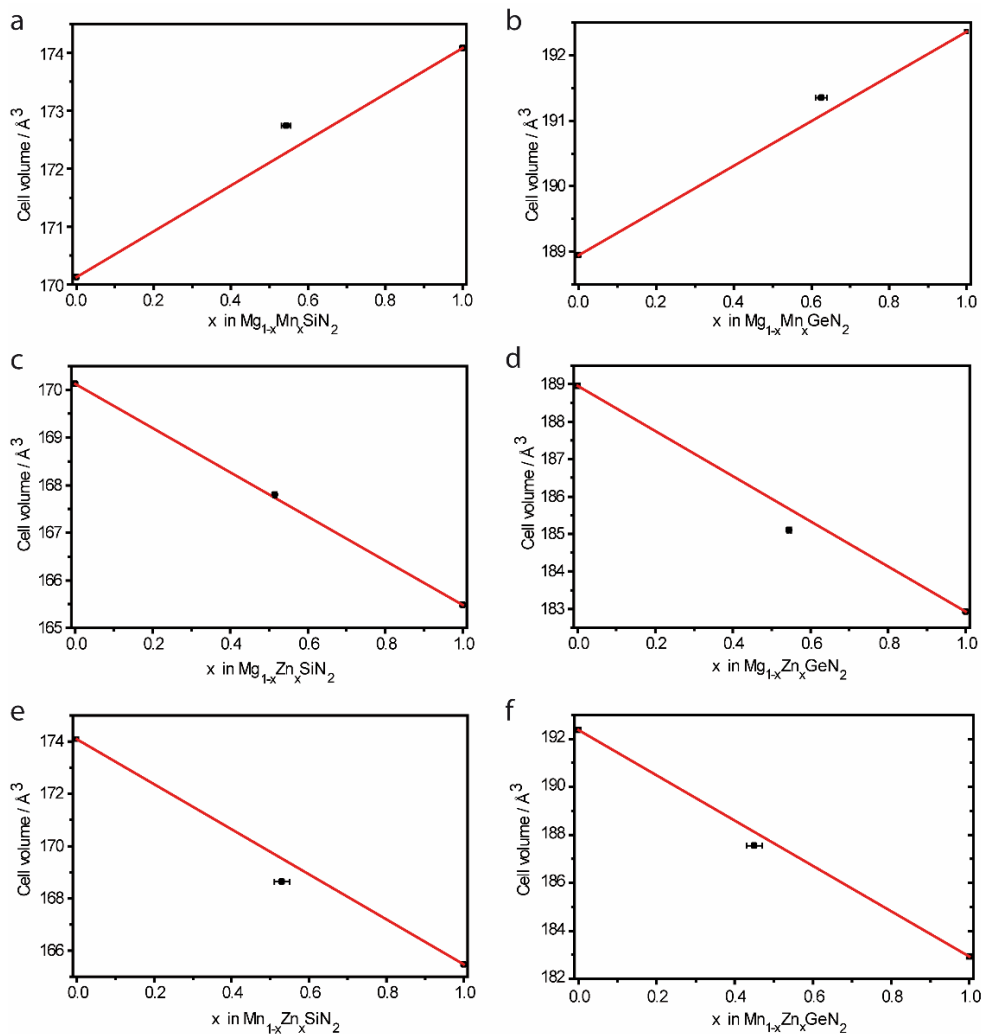


Figure A.1. Comparison of the cell volumes of the solid solutions $\text{Mg}_{1-x}\text{Mn}_x\text{SiN}_2$ (a), $\text{Mg}_{1-x}\text{Mn}_x\text{GeN}_2$ (b), $\text{Mg}_{1-x}\text{Zn}_x\text{SiN}_2$ (c), $\text{Mg}_{1-x}\text{Zn}_x\text{GeN}_2$ (d), $\text{Mn}_{1-x}\text{Zn}_x\text{SiN}_2$ (e) and $\text{Mn}_{1-x}\text{Zn}_x\text{GeN}_2$ (f) with the cell volumes of their corresponding edge phases.^[1, 2] Error bars represent the standard deviations obtained from Rietveld refinement. The red lines were interpolated using Vegard's rule.

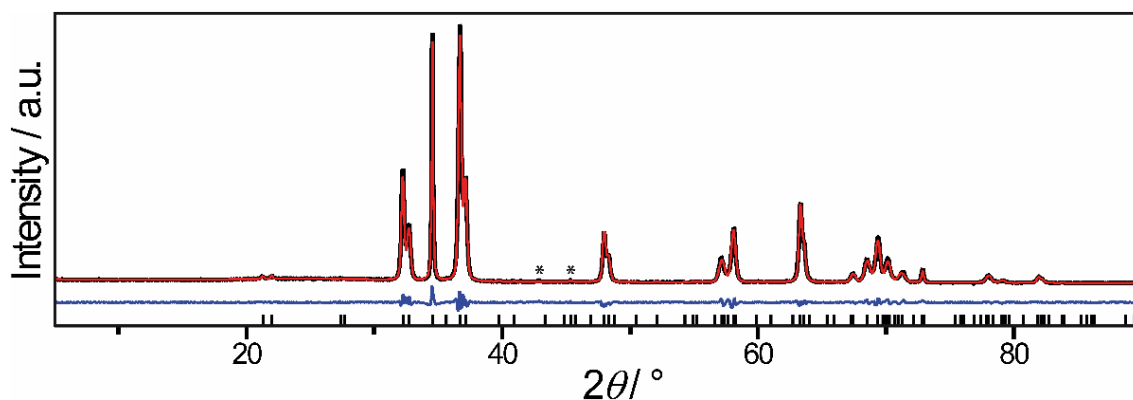


Figure A.2. Rietveld refinement of PXRD pattern (Cu- $K_{\alpha 1}$) of solid solution of $\text{Mg}_{1-x}\text{Zn}_x\text{GeN}_2$ ($x \approx 0.826$) with experimental data (black line), calculated data (red line), difference profile (blue lines), and reflection positions (black bars). Asterisks mark reflections from unknown phases.

Table A.7. Wyckoff positions and atomic coordinates of $\text{Mn}_{1-x}\text{Zn}_x\text{GeN}_2$ ($x \approx 0.826$) obtained from powder X-ray diffraction, standard deviations in parentheses.

Atom	Wyckoff	x	y	z	SOF	U_{iso}
Mg1	$4a$	0.0785(4)	0.6273(7)	0.9696(6)	0.174(6)	0.0127
Zn1	$4a$	0.0785(4)	0.6273(7)	0.9696(6)	0.826(6)	0.0127
Ge1	$4a$	0.0802(4)	0.1249(7)	0.9719(7)	1	0.0528(5)
N1	$4a$	0.1161(12)	0.093(2)	0.3733(13)	1	0.0127
N2	$4a$	0.0567(15)	0.645(3)	0.3334(13)	1	0.0127

Table A.8. Crystallographic data of $\text{Mg}_{1-x}\text{Zn}_x\text{GeN}_2$ ($x = 0.826$) obtained by Rietveld refinement.

Formula	$\text{Mg}_{0.174}\text{Zn}_{0.826}\text{GeN}_2$
Crystal system	orthorhombic
Space group	$Pna2_1$ (no. 33)
$a / \text{\AA}$	5.47260(10)
$b / \text{\AA}$	6.44130(13)
$c / \text{\AA}$	5.18932(10)
Cell volume / \AA^3	182.927(6)
Density / $\text{g}\cdot\text{cm}^{-3}$	5.766(6)
Formula units / cell	4
T / K	293(2)
Diffractometer	STOE STADI P
Radiation / \AA	$\text{Cu-K}\alpha_1$ ($\lambda = 1.5406$)
2θ range / $^\circ$	$5.0 \leq 2\theta \leq 90$
Profile function	fundamental parameters model
Background function	Shifted Chebyshev
Data points	5668
Number of reflections	89
Refined parameters	56
R values	$R_p = 0.0539$ $R_{wp} = 0.0699$ $R_{\text{Bragg}} = 0.0161$
Goodness of fit	1.52

A.2 Details on scanning electron microscopy

All EDX measurements showed small amounts of impurities like Na, K and O which originate from residual mineralizer as well as washing steps with ethanol and acetic acid. For the quantification of the composition of the compounds, the peaks of Na, K and O were deconvoluted.

Table A.9. SEM EDX measurements of Si-compounds.

$\text{Mg}_{1-x}\text{Mn}_x\text{SiN}_2$	Mg	Mn	Si	N
measurement 1:	11.3	10.6	23.7	54.4
measurement 2:	11.8	12.0	25.7	50.5
measurement 3:	11.9	12.1	25.7	50.3
measurement 4:	11.3	11.8	24.3	52.6
\emptyset	11.6	11.6	24.9	51.9

$\text{Mg}_{1-x}\text{Zn}_x\text{SiN}_2$	Mg	Zn	Si	N
measurement 1:	13.1	14.9	26.9	45.1
measurement 2:	11.4	13.2	27.1	48.3
measurement 3:	14.4	11.3	28.1	46.2
measurement 4:	12.4	10.4	27.0	50.2
\emptyset	12.8	12.5	27.3	47.4

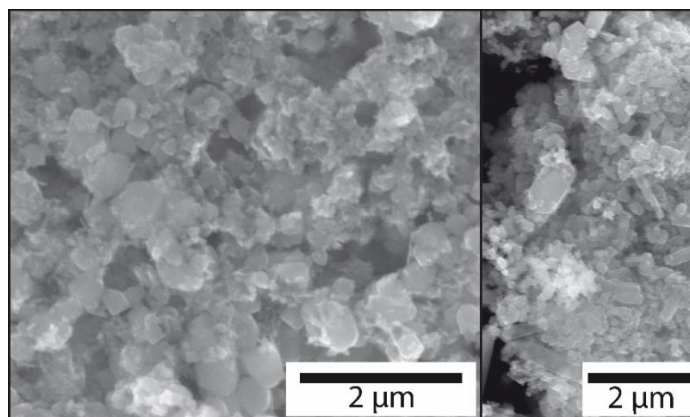
$\text{Mn}_{1-x}\text{Zn}_x\text{SiN}_2$	Mn	Zn	Si	N
measurement 1:	12.6	12.4	27.9	47.1
measurement 2:	12.6	12.4	28.0	47.0
measurement 3:	11.5	11.3	25.9	51.3
measurement 4:	12.0	9.4	26.6	52.0
\emptyset	12.2	11.4	27.1	49.3

Table A.10. SEM EDX measurements of Ge-compounds.

$\text{Mg}_{1-x}\text{Mn}_x\text{GeN}_2$	Mg	Mn	Ge	N
measurement 1:	12.5	11.8	22.7	53.0
measurement 2:	12.2	11.2	21.8	54.8
measurement 3:	12.8	12.8	23.8	50.6
measurement 4:	13.6	12.9	24.3	49.2
\emptyset	12.8	12.2	23.1	51.9

$\text{Mg}_{1-x}\text{Zn}_x\text{GeN}_2$	Mg	Zn	Ge	N
measurement 1:	14.6	13.0	22.7	49.7
measurement 2:	14.6	14.8	25.5	45.1
measurement 3:	13.6	13.8	24.8	47.8
measurement 4:	13.3	13.9	27.1	45.7
\emptyset	14.0	13.9	25.0	47.1

$\text{Mn}_{1-x}\text{Zn}_x\text{GeN}_2$	Mn	Zn	Ge	N
measurement 1:	10.8	11.2	25.4	52.6
measurement 2:	13.3	12.5	25.6	48.6
measurement 3:	14.2	12.8	28.8	44.2
measurement 4:	10.9	10.4	23.0	55.7
\emptyset	12.3	11.7	25.7	50.3

**Figure A.3.** SEM images of $\text{Mn}_{1-x}\text{Zn}_x\text{SiN}_2$ (left) and $\text{Mn}_{1-x}\text{Zn}_x\text{GeN}_2$ (right).

A.3 Details on UV/Vis reflectance spectroscopy

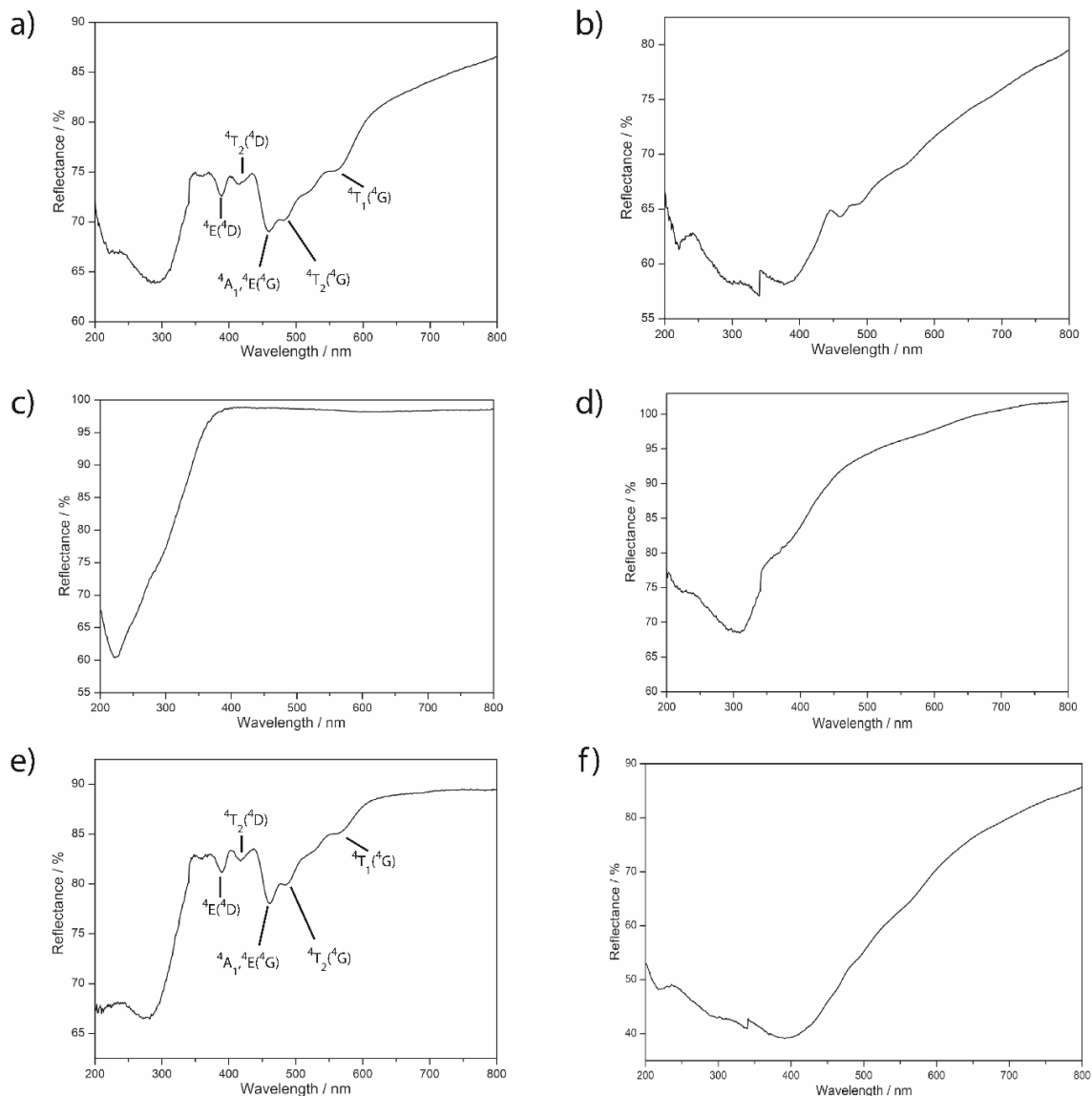


Figure A.4. Diffuse reflectance spectra of $\text{Mg}_{1-x}\text{Mn}_x\text{SiN}_2$ (a), $\text{Mg}_{1-x}\text{Mn}_x\text{GeN}_2$ (b), $\text{Mg}_{1-x}\text{Zn}_x\text{SiN}_2$ (c), $\text{Mg}_{1-x}\text{Zn}_x\text{GeN}_2$ (d), $\text{Mn}_{1-x}\text{Zn}_x\text{SiN}_2$ (e) and $\text{Mn}_{1-x}\text{Zn}_x\text{GeN}_2$ (f). Sub-bandgap absorption bands in the case of $\text{Mg}_{1-x}\text{Mn}_x\text{SiN}_2$ (a) and $\text{Mn}_{1-x}\text{Zn}_x\text{SiN}_2$ (e) can be attributed to the absorption of Mn^{2+} (transition of the ground state ${}^6\text{A}_1({}^6\text{S})$ to the excited states ${}^4\text{T}_1({}^4\text{G})$, ${}^4\text{T}_2({}^4\text{G})$, ${}^4\text{A}_1, {}^4\text{E}({}^4\text{G})$, ${}^4\text{T}_2({}^4\text{D})$ and ${}^4\text{E}({}^4\text{D})$ according to literature.^[3]

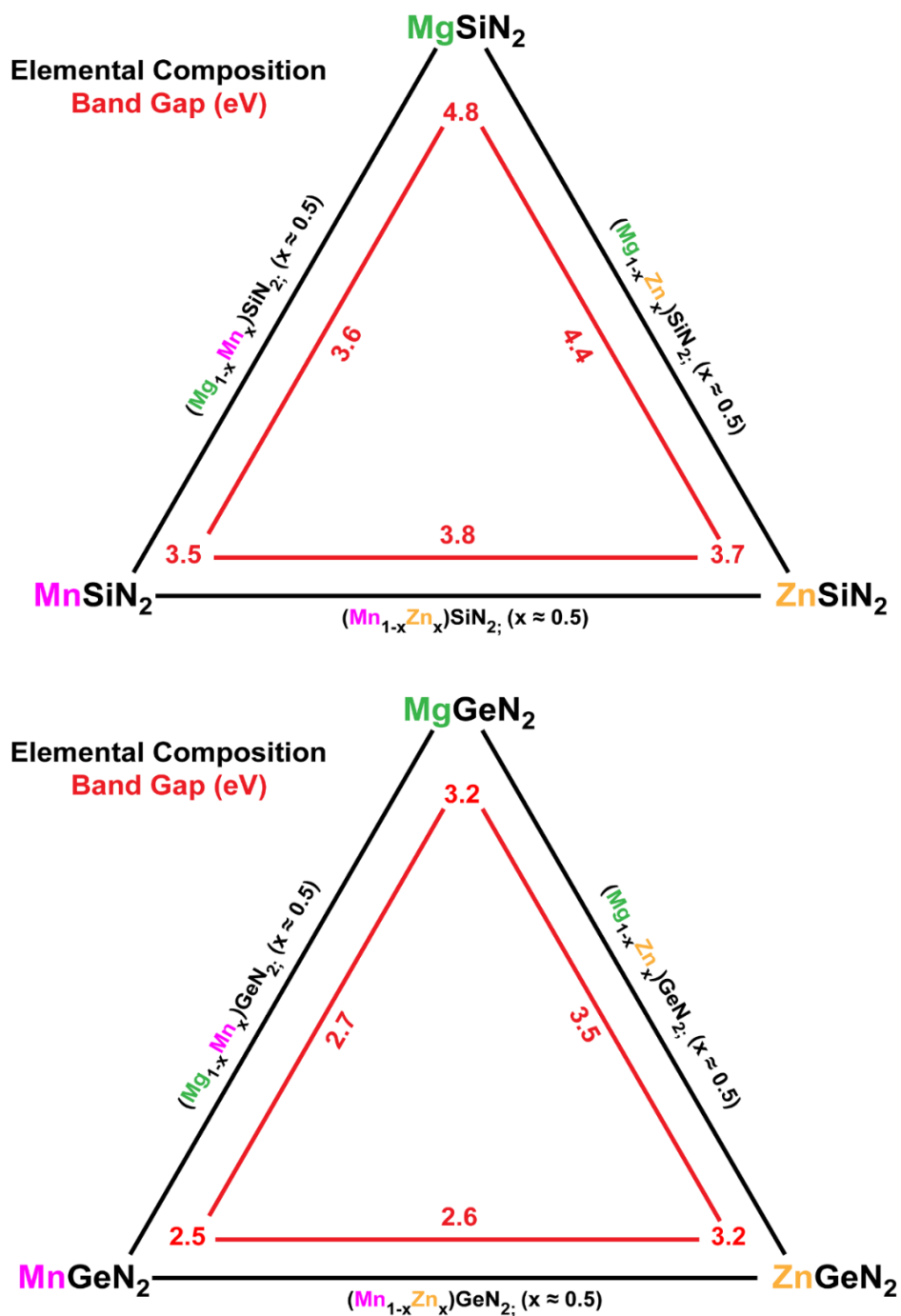


Figure A.5. Evaluated bandgaps (E_g^{exp}) of the mixed occupancy ($II^B_{1-x}II^A_x$)- $IV-N_2$ compound series. Top: Si-series, bottom Ge-series. Bandgaps of edge phases were taken from literature.^[1, 2]

A.4 Additional data of DFT calculations

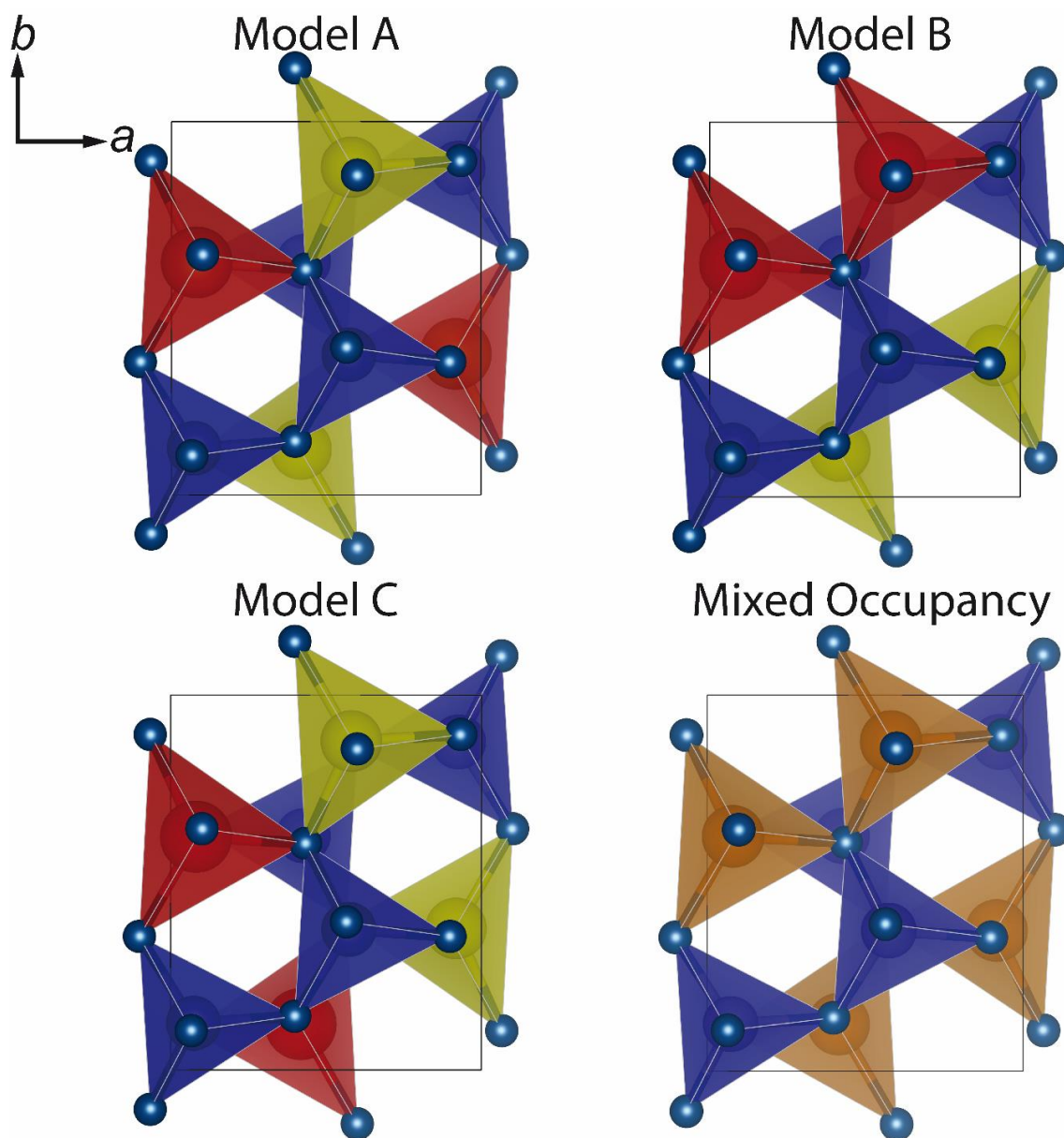


Figure A.6. Different ordering variants (A-C) and model for mixed occupation of divalent cations in $(I^{P_{1-x}}I^P_x)-IV-N_2$ ($x = 0.5$). I^P-N_4 tetrahedra are depicted in red, I^P-N_4 tetrahedra in yellow, $IV-N_4$ in blue and mixed occupied $I^{P/b}-N_4$ tetrahedra in orange.

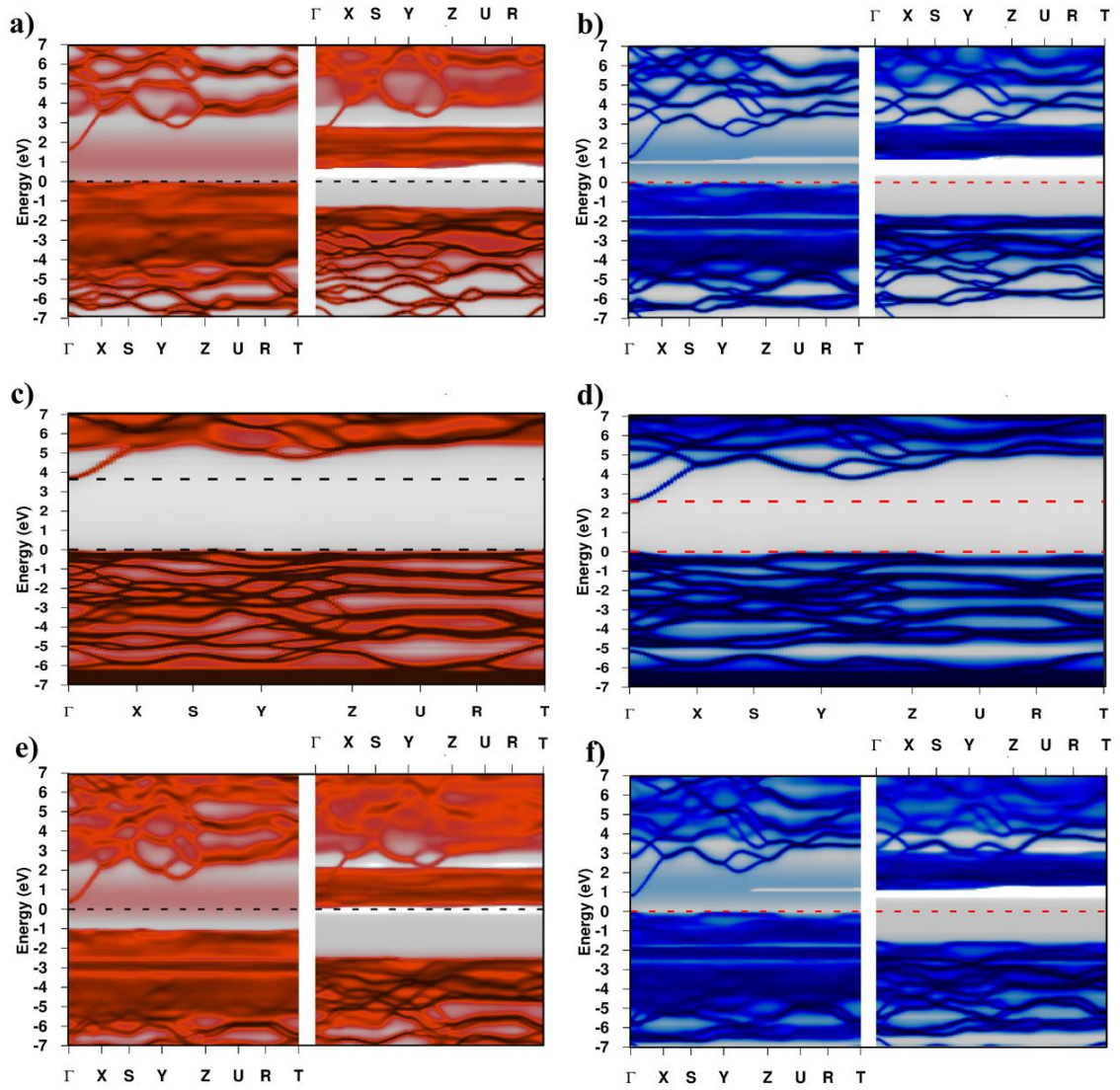


Figure A.7. Bloch spectral functions as calculated by the SPRKKR formalism (EV-GGA) of $(\text{Mg}_{0.5}\text{Mn}_{0.5})\text{SiN}_2$ (a) (left: \uparrow /right: \downarrow), $(\text{Mg}_{0.5}\text{Mn}_{0.5})\text{GeN}_2$ (b) (left: \uparrow /right: \downarrow), $(\text{Mg}_{0.5}\text{Zn}_{0.5})\text{SiN}_2$ (c), $(\text{Mg}_{0.5}\text{Zn}_{0.5})\text{GeN}_2$ (d), $(\text{Mn}_{0.5}\text{Zn}_{0.5})\text{SiN}_2$ (e) (left: \uparrow /right: \downarrow) and $(\text{Mn}_{0.5}\text{Zn}_{0.5})\text{GeN}_2$ (f) (left: \uparrow /right: \downarrow).

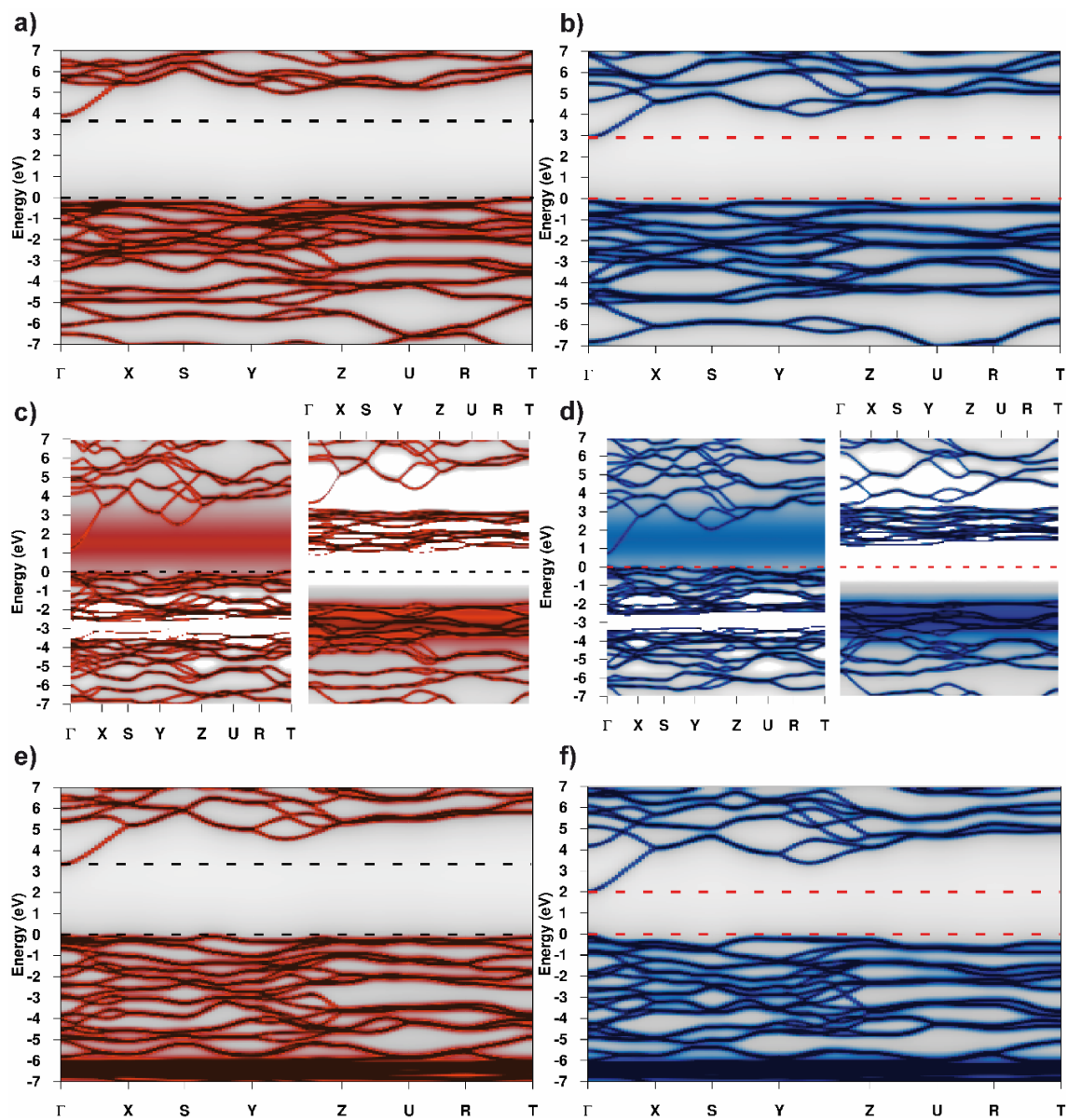


Figure A.8. Bloch spectral functions as calculated by the SPRKKR formalism (EV-GGA) of MgSiN₂ (a), MgGeN₂ (b), MnSiN₂ (c) (left: \uparrow /right: \downarrow), MnGeN₂ (d) (left: \uparrow /right: \downarrow), ZnSiN₂ (e) and ZnGeN₂ (f).

Table A.11. Bandgap values [eV] for the different ($I^P_{1-x}I^P_x$)-Si-N₂ compounds from experiment and theory in comparison to values of preceding literature.

	^{a)} mBJ-GGA \bar{O}^{A+B+C}	^{a)} KKR ^{EV-GGA}	QSGW $0.8\bar{\Sigma} + \Delta_0 (+ E_{xb})$		EXP.
Transition	\uparrow to \uparrow \uparrow to \downarrow direct \approx indirect	\uparrow to \uparrow \uparrow to \downarrow direct \approx indirect	direct	indirect	
MgSiN ₂		4.1	6.28 ^[4]	5.84 ^[4]	4.8–5.6 ^[2, 5, 6]
Mg _{0.5} Mn _{0.5} SiN ₂	2.78 2.28	1.65 0.63			^{a)} 3.6
MnSiN ₂		1.2 0.85			3.5–4.3 ^[2, 7]
Mn _{0.5} Zn _{0.5} SiN ₂	2.44 2.4	1.4 1.1			^{a)} 3.8
ZnSiN ₂		3.45	5.66 ^[8]	5.44 ^[8]	3.7–4.4 ^[1, 9–11]
Mg _{0.5} Zn _{0.5} SiN ₂	4.55	3.7			^{a)} 4.4
MgSiN ₂		4.1	6.28 ^[4]	5.84 ^[4]	4.8–5.6 ^[2, 5, 6]

^{a)} Bandgap values from this work**Table A.12.** Bandgap values [eV] for the different ($I^P_{1-x}I^P_x$)-Ge-N₂ compounds from experiment and theory in comparison to values of preceding literature.

	^{a)} mBJ-GGA \bar{O}^{A+B+C}	^{a)} KKR ^{EV-GGA}	QSGW $0.8\bar{\Sigma} + \Delta_0 (+ E_{xb})$		EXP.
Transition	\uparrow to \uparrow \uparrow to \downarrow direct \approx indirect	\uparrow to \uparrow \uparrow to \downarrow direct \approx indirect	direct		
MgGeN ₂		3.1	5.14 ^[4]		3.2 ^[2]
Mg _{0.5} Mn _{0.5} GeN ₂	1.42 1.8	1.3 1.15			^{a)} 2.7
MnGeN ₂		0.7 1.1			2.5 ^[2]
Mn _{0.5} Zn _{0.5} GeN ₂	1.09 1.43	0.75 1.1			^{a)} 2.6
ZnGeN ₂		2.0	3.42 ^[8]		3.1–3.5 ^[1, 10–13]
Mg _{0.5} Zn _{0.5} GeN ₂	3.14	2.6			^{a)} 3.5
MgGeN ₂		3.1	5.14 ^[4]		3.2 ^[2]

^{a)} Bandgap values from this work

A.5 Magnetic measurements

A.5.1 Experimental

Magnetic measurements were performed with a Quantum Design PPMS-9 using the vibrating sample magnetometer (VSM) option. Temperature dependent magnetization measurements were carried out between 2 and 400 K with applied fields of 0.01 and 3 T. The isothermal magnetization was determined at 2 and 400 K with variable fields of $B = \pm 5$ T.

A.5.2 Results and Discussion

The magnetic properties of MnSiN_2 and MnGeN_2 have been reported in literature. Both compounds order anti-ferromagnetically with Néel temperatures of $T_N = 453$ K (MnSiN_2) and $T_N = 448$ K (MnGeN_2).^[14, 15] The magnetic structure of MnSiN_2 was determined from neutron powder diffraction and magnetization data. Above 500 K the nitride appeared to be paramagnetic with strong antiferromagnetic fluctuations. Antiferromagnetic order occurs below 490 K, which changes into a canted antiferromagnetic state with spin tilting disorder at 442 K.^[16]

We first reinvestigated the magnetic behavior of MnSiN_2 synthesized via solid state methods or via ammonothermal reactions with and without mineralizer, according to literature.^[2, 16] In the range between 300 and 400 K, we find linearly decreasing susceptibility for MnSiN_2 from solid state and ammonothermal synthesis without mineralizer, both in agreement with the antiferromagnetic state reported in literature (Figs. A.9, A.10).^[16] The upturn at lower temperatures is probably caused by paramagnetic impurities. Samples prepared with KNH_2 in the ammonothermal reaction reveal increasing paramagnetic susceptibility over the whole temperature range. This is probably caused by higher amounts of paramagnetic impurities like K_3MnO_4 (see Figure 2.2), which has an effective moment of $2.80\mu_B$.^[17] It is also possible that the samples contain amorphous proportions of potassium manganites. Thus the magnetic measurements of all samples synthesized with mineralizer are mainly affected by impurity phases and therefore of limited significance.

The solid solutions $\text{Mg}_{1-x}\text{Mn}_x\text{SiN}_2$, $\text{Mn}_{1-x}\text{Zn}_x\text{SiN}_2$, $\text{Mg}_{1-x}\text{Mn}_x\text{GeN}_2$ and $\text{Mn}_{1-x}\text{Zn}_x\text{GeN}_2$ ($x \approx 0.5$) were synthesized using a mineralizer. The susceptibility data are similar to those of magnetic MnSiN_2 synthesized via the same synthetic method. Consequently, the magnetism of the solid solutions are also mainly affected by paramagnetic impurity phases (see Figure A.12-A.15), which impedes a reliable determination of the intrinsic magnetic properties. However, the data shown in Figs. A.12-A.15 are compatible with antiferromagnetism in the solid solutions similar to the boundary phases MnSiN_2 and MnGeN_2 .

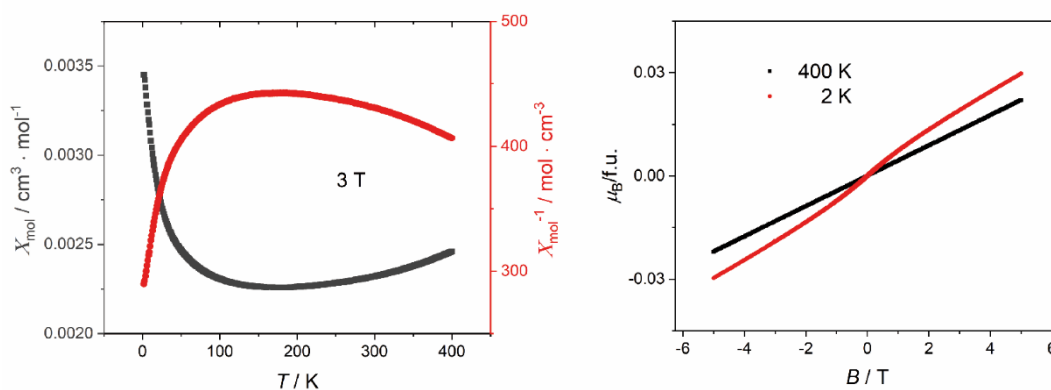
MnSiN₂ (solid state reaction)

Figure A.9. Magnetic measurements of MnSiN₂. **Left:** Susceptibility and inverse susceptibility (red) at 3 T in the temperature range of 2 – 400 K. **Right:** Magnetization isotherms at 2 (red) and 400 K (black).

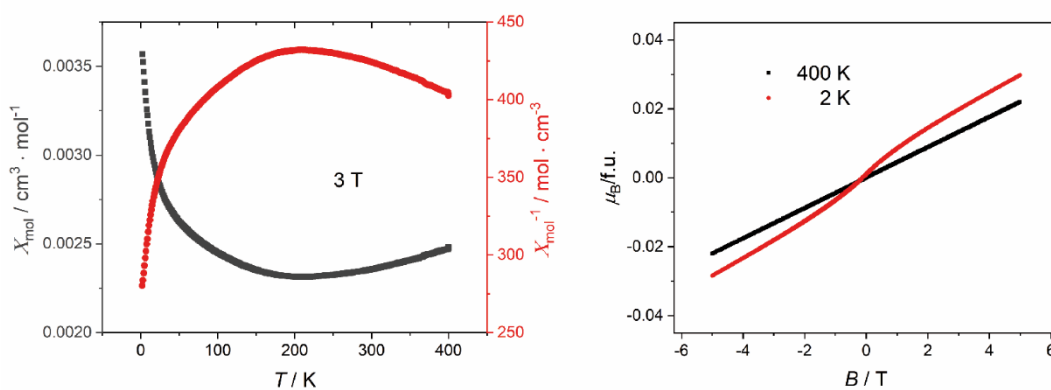
MnSiN₂ (Ammonothermal without mineralizer)

Figure A.10. Magnetic measurements of MnSiN₂. **Left:** Susceptibility and inverse susceptibility (red) at 3 T in the temperature range of 2 – 400 K. **Right:** Magnetization isotherms at 2 (red) and 400 K (black).

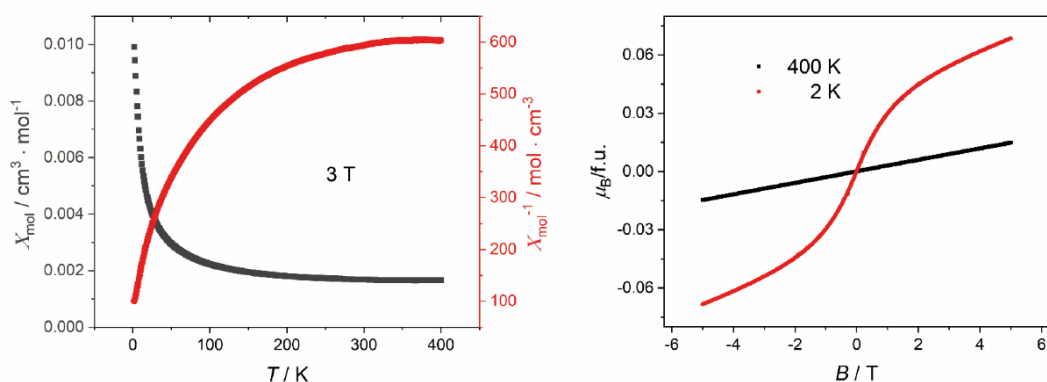
MnSiN₂ (Ammonothermal with mineralizer)

Figure A.11. Magnetic measurements of MnSiN₂. **Left** Susceptibility and inverted susceptibility (red) at 3 T in the temperature range of 2 – 400 K. **Right:** Magnetization isotherms at 2 (red) and 400 K (black).

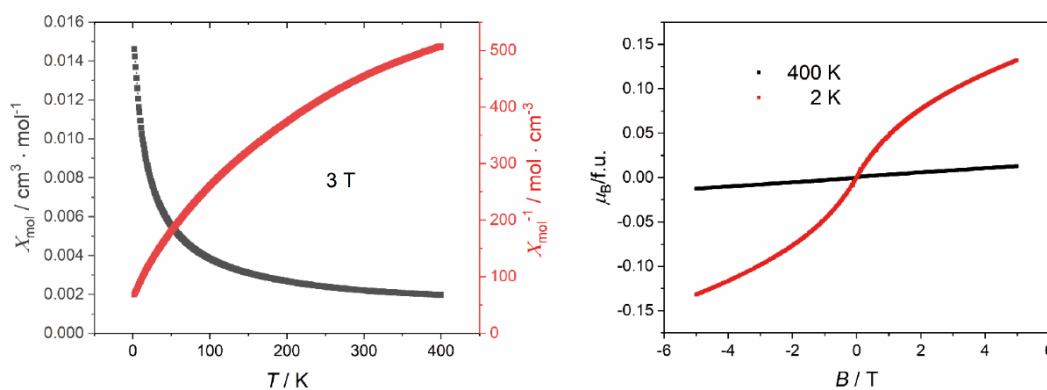
Mg_{0.457}Mn_{0.543}SiN₂

Figure A.12. Magnetic measurements of Mg_{0.457}Mn_{0.543}SiN₂. **Left:** Susceptibility and inverted susceptibility (red) at 3 T in the temperature range of 2 – 400 K. **Right:** Magnetization isotherms at 2 (red) and 400 K (black).

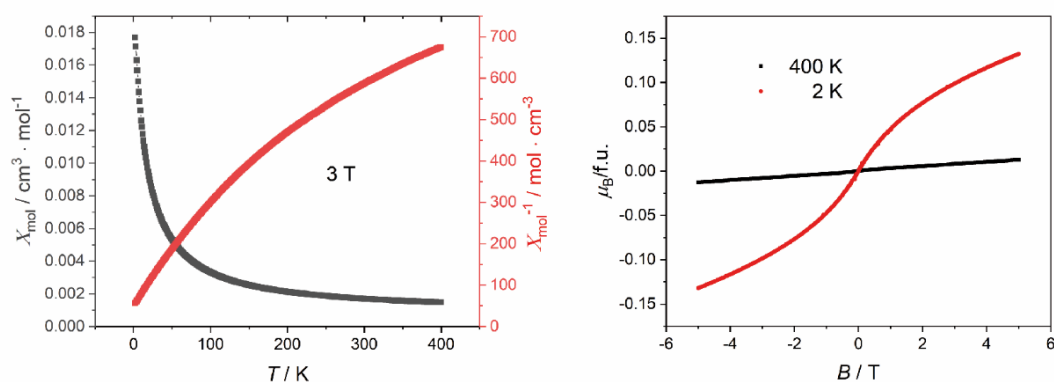
$\text{Mn}_{0.47}\text{Zn}_{0.53}\text{SiN}_2$ 

Figure A.13. Magnetic measurements of $\text{Mn}_{0.47}\text{Zn}_{0.53}\text{SiN}_2$. **Left:** Susceptibility and inverted susceptibility (red) at 3 T in the temperature range of 2 – 400 K. **Right:** Magnetization isotherms at 2 (red) and 400 K (black).

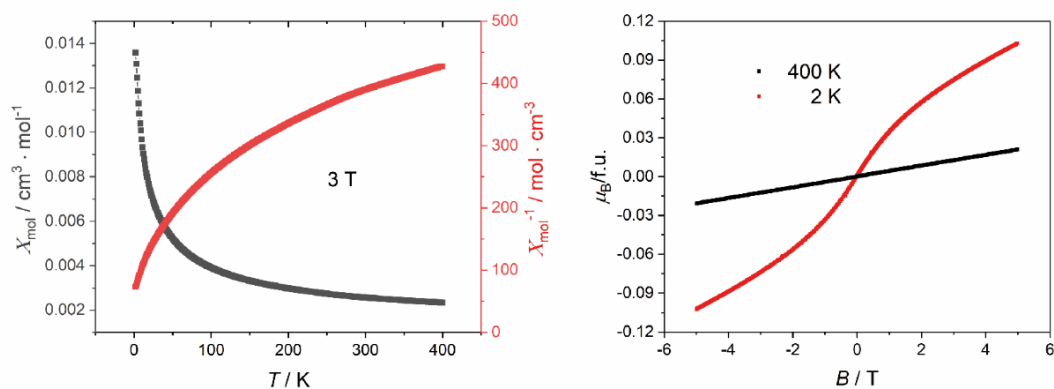
 $\text{Mg}_{0.375}\text{Mn}_{0.625}\text{GeN}_2$ 

Figure A.14. Magnetic measurements of $\text{Mg}_{0.375}\text{Mn}_{0.625}\text{GeN}_2$. **Left:** Susceptibility and inverted susceptibility (red) at 3 T in the temperature range of 2 – 400 K. **Right:** Magnetization isotherms at 2 (red) and 400 K (black).

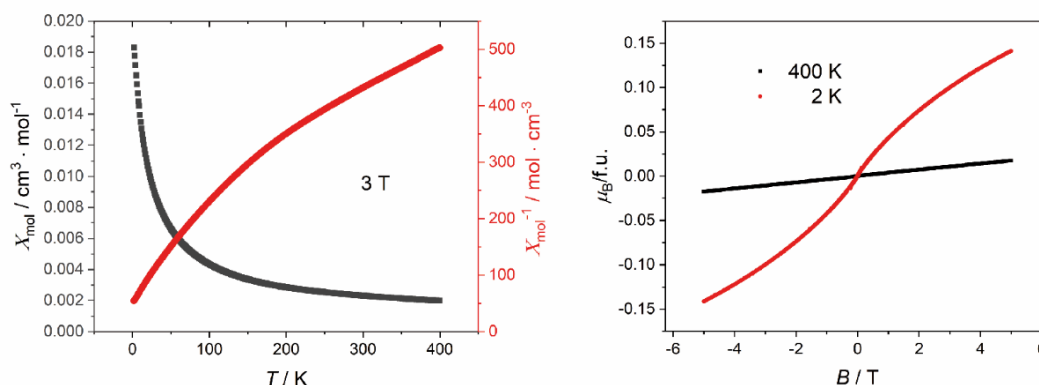
Mn_{0.45}Zn_{0.55}GeN₂

Figure A.15. Magnetic measurements of Mn_{0.45}Zn_{0.55}GeN₂. **Left:** Susceptibility and inverted susceptibility (red) at 3 T in the temperature range of 2 – 400 K. **Right:** Magnetization isotherms at 2 (red) and 400 K (black).

A.6 References

- [1] J. Häusler, S. Schimmel, P. Wellmann, W. Schnick, "Ammonothermal Synthesis of Earth-Abundant Nitride Semiconductors ZnSiN₂ and ZnGeN₂ and Dissolution Monitoring by In Situ X-ray Imaging", *Chem. Eur. J.* **2017**, *23*, 12275-12282.
- [2] J. Häusler, R. Niklaus, J. Minár, W. Schnick, "Ammonothermal Synthesis and Optical Properties of Ternary Nitride Semiconductors Mg-IV-N₂, Mn-IV-N₂ and Li-IV₂-N₃ (IV = Si, Ge)", *Chem. Eur. J.* **2018**, *24*, 1686-1693.
- [3] Y. Tanabe, S. Sugano, "On the Absorption Spectra of Complex Ions. I", *J. Phys. Soc. Jpn.* **1954**, *9*, 753-766.
- [4] A. P. Jaroenjittichai, W. R. L. Lambrecht, "Electronic band structure of Mg-IV-N₂ compounds in the quasiparticle-self-consistent GW approximation", *Phys. Rev. B* **2016**, *94*, 125201.
- [5] C. M. Fang, R. A. d. Groot, R. J. Bruls, H. T. Hintzen, G. d. With, "Ab initio band structure calculations of Mg₃N₂ and MgSiN₂", *J. Phys.: Condens. Matter* **1999**, *11*, 4833-4842.
- [6] T. de Boer, T. D. Boyko, C. Braun, W. Schnick, A. Moewes, "Band gap and electronic structure of MgSiN₂ determined using soft X-ray spectroscopy and density functional theory", *Phys. Status Solidi RRL* **2015**, *9*, 250-254.
- [7] C. J. Duan, A. C. A. Delsing, H. T. Hintzen, "Red emission from Mn²⁺ on a tetrahedral site in MgSiN₂", *J. Lumin.* **2009**, *129*, 645-649.
- [8] A. Punya, W. R. L. Lambrecht, M. van Schilfgaarde, "Quasiparticle band structure of Zn-IV-N₂ compounds", *Phys. Rev. B* **2011**, *84*, 165204.

- [9] T. Endo, Y. Sato, H. Takizawa, M. Shimada, "High-pressure synthesis of new compounds, $ZnSiN_2$ and $ZnGeN_2$ with distorted wurtzite structure", *J. Mater. Sci. Lett.* **1992**, *11*, 424-426.
- [10] A. Osinsky, V. Fuflyigin, L. D. Zhu, A. B. Goulakov, J. W. Graff, E. F. Schubert, in *Proc. 2000 IEEE/ Cornell Conference on High Performance Devices*, **2000**, pp. 168-172.
- [11] J. Muth, A. Cai, A. Osinsky, H. Everitt, B. Cook, I. Avrutsky, "Optical Properties of II-IV- N_2 Semiconductors", *Mater. Res. Soc. Symp. Proc.* **2005**, *831*, E11.45.11-15.
- [12] T. Misaki, A. Wakahara, H. Okada, A. Yoshida, "Optical properties of $ZnGeN_2$ epitaxial layer", *Phys. Status Solidi C* **2003**, *0*, 2890-2893.
- [13] M. Shang, J. Wang, J. Fan, H. Lian, Y. Zhang, J. Lin, " $ZnGeN_2$ and $ZnGeN_2:Mn^{2+}$ phosphors: hydrothermal-ammonolysis synthesis, structure and luminescence properties", *J. Mater. Chem. C* **2015**, *3*, 9306-9317.
- [14] M. Wintenberger, J. Guyader, M. Maunaye, "Etude cristallographique et magnetique de $MnGeN_2$ par diffraction neutronique", *Solid State Commun.* **1972**, *11*, 1485-1488.
- [15] M. Wintenberger, R. Marchand, M. Maunaye, "Etude cristallographique et magnetique de $MnSiN_2$ par diffraction des neutrons", *Solid State Commun.* **1977**, *21*, 733-735.
- [16] S. Esmailzadeh, U. Hålenius, M. Valldor, "Crystal Growth, Magnetic, and Optical Properties of the Ternary Nitride $MnSiN_2$ ", *Chem. Mater.* **2006**, *18*, 2713-2718.
- [17] R. Olazcuaga, J.-M. Reau, G. Leflem, P. Hagenmuller, "Préparation, Propriétés Cristallographiques et Magnétiques des Phases K_3XO_4 ($X = V, Cr, Mn$)", *Z. Anorg. Allg. Chem.* **1975**, *412*, 271-280.

B Supporting Information for Chapter 3

Mathias Mallmann, Christian Maak, Robin Niklaus, and Wolfgang Schnick

Chem. Eur. J. **2018**, *24*, 13963 - 13970.

B.1 Additional crystallographic data of Mg₂PN₃

Table B.1. Wyckoff positions and atomic coordinates of Mg₂PN₃ obtained from single-crystal X-ray diffraction, standard deviations in parentheses.

Atom	Wyckoff	<i>x</i>	<i>y</i>	<i>z</i>	<i>U</i> _{iso}
Mg1	8 <i>b</i>	0.66317(9)	0.83405(13)	0.9773(4)	0.0068(3)
P1	4 <i>a</i>	1	0.83886(15)	0.99993(10)	0.0041(3)
N1	8 <i>b</i>	0.8598(2)	0.6970(4)	0.9297(6)	0.0059(5)
N2	4 <i>a</i>	1	0.8911(6)	0.3539(9)	0.0051(7)

Table B.2. Anisotropic displacement parameters [\AA^2] occurring in Mg₂PN₃ obtained from single-crystal X-ray diffraction, standard deviations in parentheses.

Atom	<i>U</i> ₁₁	<i>U</i> ₂₂	<i>U</i> ₃₃	<i>U</i> ₂₃	<i>U</i> ₁₃	<i>U</i> ₁₂
Mg1	0.0052(4)	0.0062(4)	0.0089(6)	-0.0003(5)	-0.0003(4)	-0.0004(3)
P1	0.0047(4)	0.0034(4)	0.0042(5)	-0.0001(4)	0	0

Table B.3. Selected interatomic distances [\AA] occurring in Mg₂PN₃ obtained from single-crystal X-ray diffraction, standard deviations in parentheses.

P1 – N1	1.616(2)
P1 – N1	1.616(2)
P1 – N2	1.675(3)
P1 – N2	1.693(4)
Mg1 – N1	2.075(2)
Mg1 – N1	2.077(2)
Mg1 – N2	2.116(3)
Mg1 – N1	2.149(4)

Table B.4. Crystallographic data of Mg₂PN₃ obtained by Rietveld refinement.

Crystal system	orthorhombic
Space group	<i>Cmc</i> 2 ₁ (no. 36)
<i>a</i> / Å	9.70545(4)
<i>b</i> / Å	5.64482(2)
<i>c</i> / Å	4.70160(2)
Cell volume / Å ³	257.58(2)
Formula units / cell	4
Density / g cm ⁻³	3.136
<i>T</i> / K	293
Diffractometer	Stoe STADI P
Radiation / Å	Cu- <i>K</i> _{α1} (1.5406)
2θ range / °	5.0 ≤ 2θ ≤ 100.5
Profile function	fundamental parameters approach
Background function	Shifted Chebyshev
Data points	6365
Number of reflections	86
Refined parameters	34
<i>R</i> _p	0.0453
<i>R</i> _{wp}	0.0589
<i>R</i> _{Bragg}	0.0122
Goodness of Fit	1.191

B.2 Additional crystallographic data of Zn₂PN₃

Table B.5. Crystallographic data of Zn₂PN₃ obtained by Rietveld refinement.

Crystal system	orthorhombic
Space group	<i>Cmc</i> 2 ₁ (no. 36)
<i>a</i> / Å	9.4177(5)
<i>b</i> / Å	5.4399(3)
<i>c</i> / Å	4.9477(2)
Cell volume / Å ³	253.48(2)
Formula units / cell	4
Density / g cm ⁻³	5.340
<i>T</i> / K	293(2)
Diffractometer	Stoe STADI P
Radiation / Å	Cu-K _{α1} (1.5406)
2θ range / °	9.9 ≤ 2θ ≤ 110.5
Profile function	fundamental parameters approach
Background function	Shifted Chebyshev
Data points	6702
Number of reflections	98
Refined parameters	45
<i>R</i> _p	0.0338
<i>R</i> _{wp}	0.0458
<i>R</i> _{Bragg}	0.0088
Goodness of Fit	1.511

Table B.6. Wyckoff positions and atomic coordinates of Zn_2PN_3 obtained from powder X-ray diffraction, standard deviations in parentheses. Isotropic displacement parameters for P and N were restrained to typical values for solids.

Atom	Wyckoff	<i>x</i>	<i>y</i>	<i>z</i>	<i>B</i> _{iso}
Zn1	8b	0.1698(2)	0.3380(2)	0.9823(4)	1.07(5)
P1	4a	0	0.1632(4)	0.475(1)	0.7
N1	8b	0.1451(5)	0.3143(7)	0.3826(5)	0.7
N2	4a	0	0.1175(9)	0.8165(7)	0.7

Because of the poor crystallinity of the product and the resulting overlap of the peaks in the PXRD, distance restraints were applied during refinement. These are limitations on the distances between nearby anions and cations that should vary within a reasonable range (restraints: P-N distances: 1.6 - 1.8 Å and Mg-N distances: 1.95 - 2.2 Å).

Table B.7. Selected interatomic distances [Å] occurring in Zn_2PN_3 obtained from powder X-ray diffraction data, standard deviations in parentheses.

P1 – N1	1.659(5)
P1 – N1	1.659(5)
P1 – N2	1.708(6)
P1 – N2	1.717(6)
Zn1 – N1	1.969(4)
Zn1 – N1	1.992(5)
Zn1 – N1	1.998(3)
Zn1 – N2	2.161(3)

B.3 Details on scanning electron microscopy

Table B.8. SEM EDX measurements of Mg_2PN_3 .

Mg_2PN_3	Mg	P	N	O
measurement 1:	32.3	16.3	48.1	3.3
measurement 2:	31.4	15.4	50.7	2.5
measurement 3:	35.5	18.6	43.7	2.2
measurement 4:	32.8	17.1	47.6	2.5
\emptyset	33.0	16.9	47.5	2.6
calculated	33.3	16.7	50.0	-

EDX measurements of Zn_2PN_3 showed small amounts of impurities like Na, K or Cl, which originate from residual mineralizer, washing steps with HCl or impurities of the autoclave. For the quantification of Zn, P, and N the peaks of Cl, Na, and K were deconvoluted.

Table B.9. SEM EDX measurements of Zn_2PN_3 .

Zn_2PN_3	Zn	P	N	O
measurement 1:	32.5	15.0	45.8	6.7
measurement 2:	29.7	15.8	46.6	7.9
measurement 3:	29.0	16.9	46.3	7.7
\emptyset	30.4	15.9	46.2	7.4
calculated	33.3	16.7	50.0	-

B.4 UV/Vis spectra

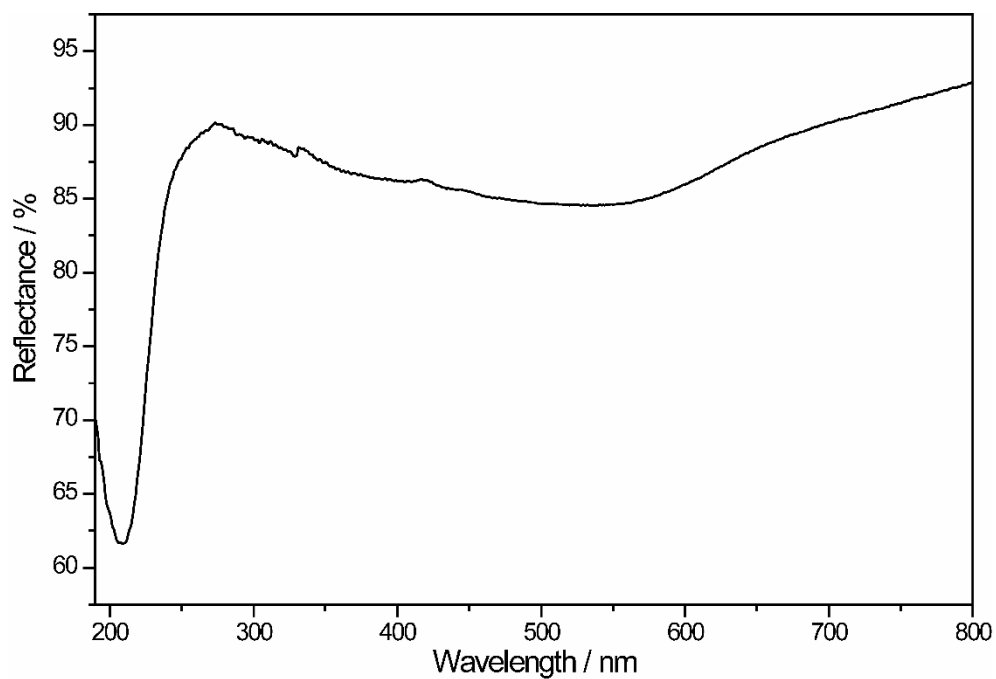


Figure B.1. Diffuse reflectance spectrum of Mg₂PN₃.

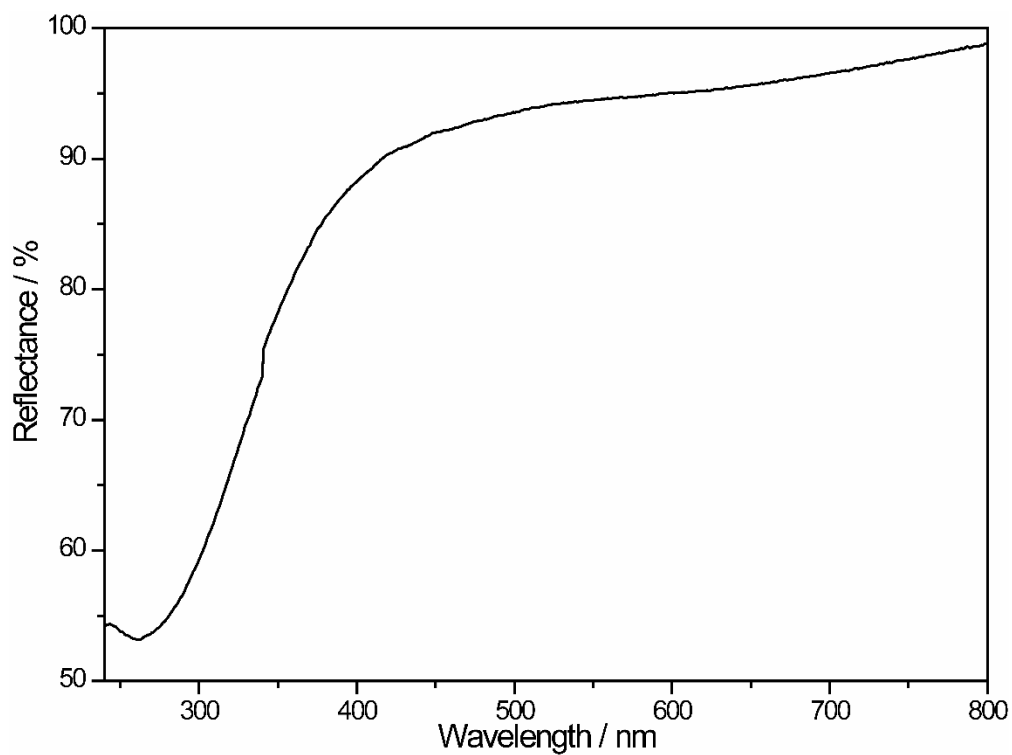


Figure B.2. Diffuse reflectance spectrum of Zn₂PN₃.

C Supporting Information for Chapter 4

Mathias Mallmann, Sebastian Wendl, and Wolfgang Schnick

Chem. Eur. J. **2020**, *26*, 2067 - 2072.

C.1 α -Li₁₀P₄N₁₀, β -Li₁₀P₄N₁₀ and Li₁₈P₆N₁₆

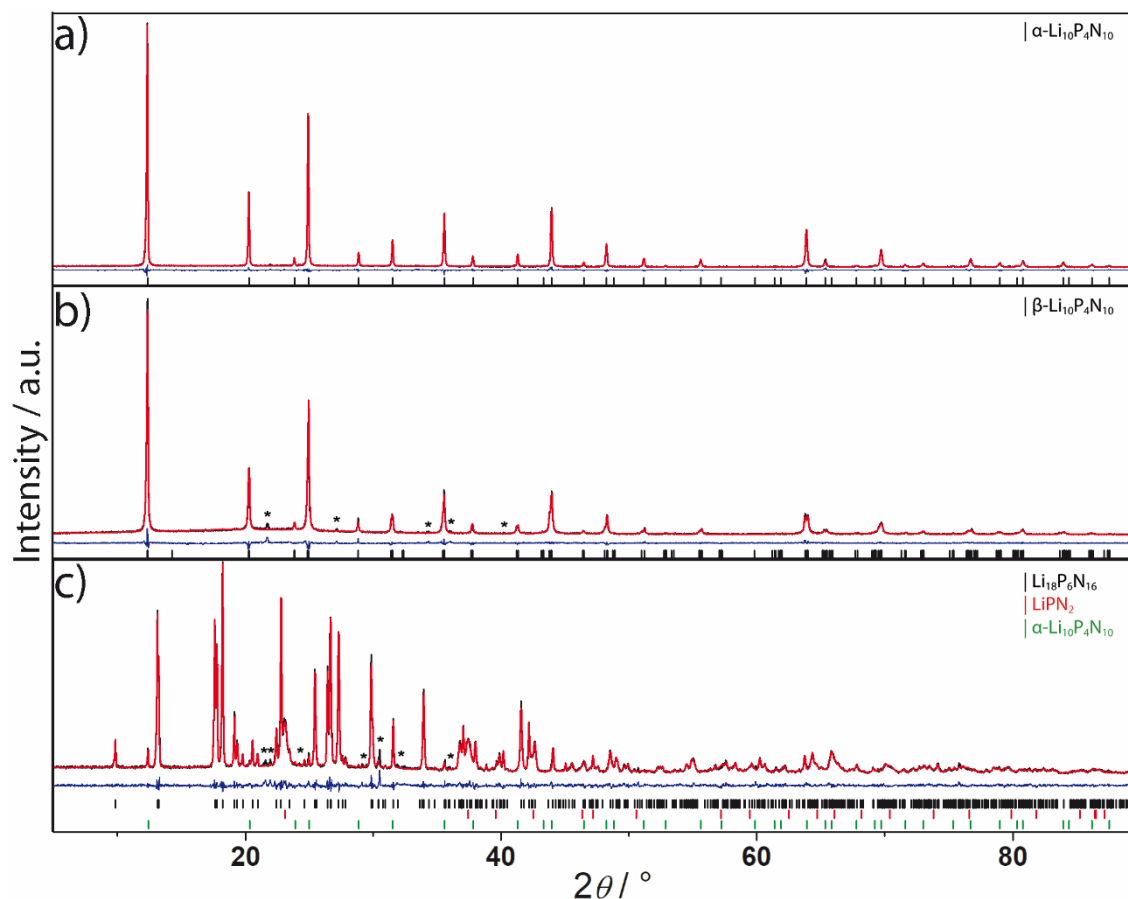


Figure C.1. Rietveld refinements of α -Li₁₀P₄N₁₀ (a), β -Li₁₀P₄N₁₀ (b) and Li₁₈P₆N₁₆ (c). Experimental and calculated data are displayed in black and red lines, and difference profiles are shown as blue lines. Vertical bars mark Bragg reflections of the refined phases. Unknown side phases are marked with asterisks. Start values for Rietveld refinement were taken from literature.^[1–3]

Table C.1. Crystallographic data of α -Li₁₀P₄N₁₀, β -Li₁₀P₄N₁₀ and Li₁₈P₆N₁₆ obtained by Rietveld refinement, standard deviations in parentheses. Li sites were not refined for all three compounds.

Formula	α -Li ₁₀ P ₄ N ₁₀	β -Li ₁₀ P ₄ N ₁₀	Li ₁₈ P ₆ N ₁₆
Crystal system	cubic	trigonal	triclinic
Space group	$Fd\bar{3}m$ (no. 227)	$R3$ (no. 146)	$P\bar{1}$ (no. 2)
$a / \text{\AA}$	12.35331(8)	8.72293(2)	5.3986(1)
$b / \text{\AA}$			7.4837(2)
$c / \text{\AA}$		21.4622(7)	9.8333(2)
$\alpha / ^\circ$			108.933(1)
$\beta / ^\circ$			99.118(1)
$\gamma / ^\circ$			104.942(1)
Cell volume / \AA^3	1885.17(4)	1414.26(7)	350.11(1)
Density / $\text{g}\cdot\text{cm}^{-3}$	2.34922(4)	2.34922(4)	2.53625(10)
Formula units / cell	8	6	1
T / K		293(2)	
Diffractometer		STOE STADI P	
Radiation / \AA		Cu- $K_{\alpha 1}$ ($\lambda = 1.5406$)	
2θ range / $^\circ$		$5.0 \leq 2\theta \leq 90$	
Profile function		fundamental parameters model	
Background function		Shifted Chebyshev	
Data points		5668	
Number of reflections	51	249	569
Refined parameters	25	60	139
R values	$R_p = 0.0608$	$R_p = 0.0716$	$R_p = 0.0548$
	$R_{wp} = 0.0865$	$R_{wp} = 0.0941$	$R_{wp} = 0.0755$
	$R_{\text{Bragg}} = 0.0173$	$R_{\text{Bragg}} = 0.0299$	$R_{\text{Bragg}} = 0.0133$
Goodness of fit	0.977	1.252	1.218

Table C.2. Wyckoff positions and atomic coordinates of α -Li₁₀P₄N₁₀ obtained from Rietveld refinement, standard deviations in parentheses.

Atom	Wyckoff	x	y	z	SOF	U _{iso}
Li1	16d	1/2	1/2	1/2	1	0.0089
Li2	8a	1/8	1/8	1/8	1	0.0089
Li3	48f	0.3154	1/8	1/8	0.96	0.0089
Li4	32e	0.9628	0.9628	0.9628	0.31	0.0089
P1	32e	0.29376(6)	0.29376(6)	0.29376(6)	1	0.0089
N1	48f	0.47223(19)	1/8	1/8	1	0.0089
N2	32e	0.21844(12)	0.21844(12)	0.21844(12)	1	0.0089

Table C.3. Wyckoff positions and atomic coordinates of β -Li₁₀P₄N₁₀ obtained from Rietveld refinement, standard deviations in parentheses.

Atom	Wyckoff	x	y	z	SOF	U _{iso}
Li1	9b	0.905	0.159	0.4168	1	0.0089
Li2	9b	0.850	0.173	0.2720	1	0.0089
Li3	3a	1/3	2/3	0.140	1	0.0089
Li4	9b	0.785	0.211	0.1305	1	0.0089
Li5	9b	0.155	0.805	0.3556	1	0.0089
Li6	9b	0.787	0.191	0.8688	1	0.0089
Li7	3a	0	0	0.7137	1	0.0089
Li8	3a	0	0	0.101	1	0.0089
Li9	9b	0.212	1.018	0.6158	2/3	0.0089
P1	3a	0	0	0.9062(16)	1	0.0089
P2	9b	0.885(2)	0.0448(2)	0.3490(10)	1	0.0089
P3	3a	0	0	0.3153(18)	1	0.0089
P4	9b	0.121(2)	0.559(2)	0.8766(11)	1	0.0089
N1	9b	0.129(6)	0.575(7)	0.705(3)	1	0.0089
N2	9b	0.882(5)	0.439(5)	0.2645(17)	1	0.0089
N3	3a	0	0	0.833(3)	1	0.0089
N4	9b	0.888(6)	0.791(6)	0.186(3)	1	0.0089
N5	9b	0.735(4)	0.200(5)	0.620(2)	1	0.0089
N6	3a	2/3	1/3	0.724(4)	1	0.0089
N7	9b	0.885(6)	0.138(7)	0.518(3)	1	0.0089
N8	9b	0.121(6)	0.871(6)	0.707(2)	1	0.0089

Table C.4. Wyckoff positions and atomic coordinates of $\text{Li}_{18}\text{P}_6\text{N}_{16}$ obtained from Rietveld refinement, standard deviations in parentheses.

Atom	Wyckoff	<i>x</i>	<i>y</i>	<i>z</i>	SOF	U_{iso}
Li1	2i	0.1297	0.0264	0.4033	1	0.0117
Li2	2i	0.202	0.2786	0.7920	1	0.0183
Li3	2i	0.0785	0.1228	0.1450	1	0.0219
Li4	2i	0.3342	0.3953	0.3881	1	0.0188
Li5	2i	0.3710	0.0989	0.9653	1	0.0247
Li6	2i	0.6624	0.3295	0.1917	1	0.0271
Li7	2i	0.0638	0.4199	0.5862	1	0.0328
Li8	2i	0.392	0.4440	0.0551	0.6	0.039
Li9	2i	0.268	0.4588	0.0951	0.5	0.030
Li10	2i	0.130	0.465	0.113	0.35	0.036
Li11	2i	0.022	0.429	0.152	0.54	0.066
P1	2i	0.5435(11)	0.2598(7)	0.6374(5)	1	0.0098
P2	2i	0.2168(13)	0.8143(8)	0.1188(5)	1	0.0220
P3	2i	0.6871(11)	0.1306(7)	0.3461(5)	1	0.0108
N1	2i	0.546(3)	0.5268(17)	0.2702(13)	1	0.0089
N2	2i	0.193(3)	0.746(2)	0.2672(14)	1	0.0089
N3	2i	0.055(3)	0.2098(19)	0.9829(15)	1	0.0089
N4	2i	0.576(3)	0.269(2)	0.4832(14)	1	0.0089
N5	2i	0.063(2)	0.7343(18)	0.6664(12)	1	0.0089
N6	2i	0.326(3)	0.6745(16)	0.0186(15)	1	0.0089
N7	2i	0.430(2)	0.035(2)	0.1862(11)	1	0.0089
N8	2i	0.278(3)	0.0591(18)	0.6218(12)	1	0.0089

Table C.5. SEM EDX measurements of α -Li₁₀P₄N₁₀, β -Li₁₀P₄N₁₀ and Li₁₈P₆N₁₆. Oxygen impurities could be due to hydrolysis during sample preparation.

α-Li₁₀P₄N₁₀	P	O	N
measurement 1:	25.1	17.6	57.3
measurement 2:	23.1	19.6	57.3
measurement 3:	22.7	9.5	67.8
\emptyset	24(1)	16(5)	60(6)
ratio	4	2.7	10
ideal	4	0	10
β-Li₁₀P₄N₁₀	P	O	N
measurement 1:	24.2	5.0	70.8
measurement 2:	31.4	6.8	61.8
measurement 3:	25.2	6.2	68.6
\emptyset	27(4)	6(1)	67(5)
ratio	4	0.9	9.9
ideal	4	0	10
Li₁₈P₆N₁₆	P	O	N
measurement 1:	25.5	17.3	57.2
measurement 2:	22.7	18.6	58.7
measurement 3:	23.2	17.6	59.2
\emptyset	24(1)	18(1)	58(1)
ratio	6	4.5	14.5
ideal	6	0	16

The vibration bands below 1400 cm^{-1} are attributed to P–N framework vibrations. There are no significant stretching vibrations in the region around 3000 cm^{-1} where N–H vibrations would be expected.^[4–6] Weak signals can be explained by surface hydrolysis of the product during washing treatment.

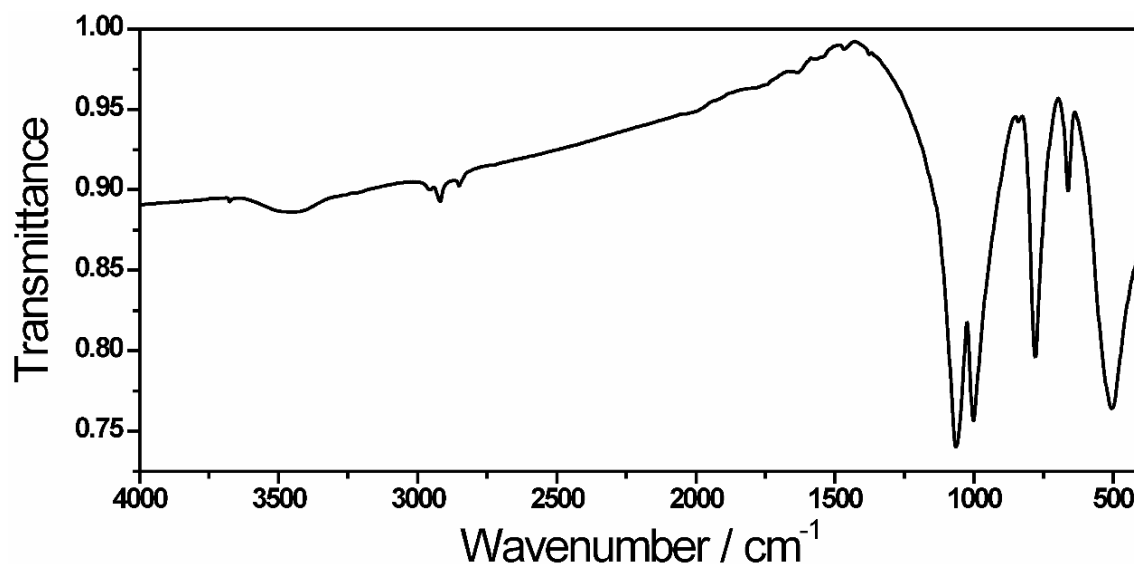


Figure C.2. FTIR spectrum of $\alpha\text{-Li}_{10}\text{P}_4\text{N}_{10}$.

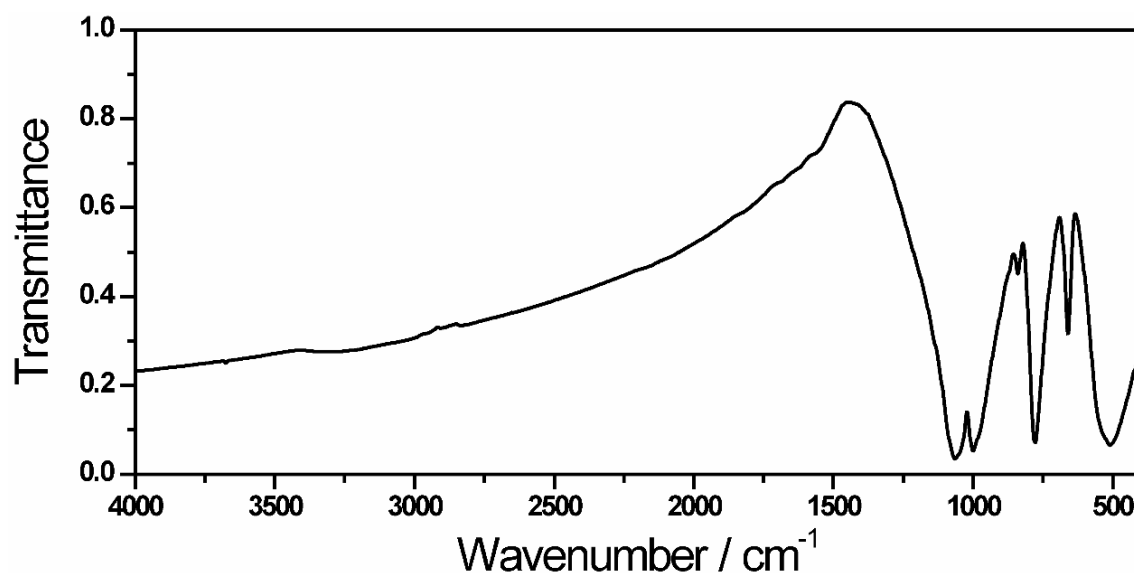


Figure C.3. FTIR spectrum of $\beta\text{-Li}_{10}\text{P}_4\text{N}_{10}$.

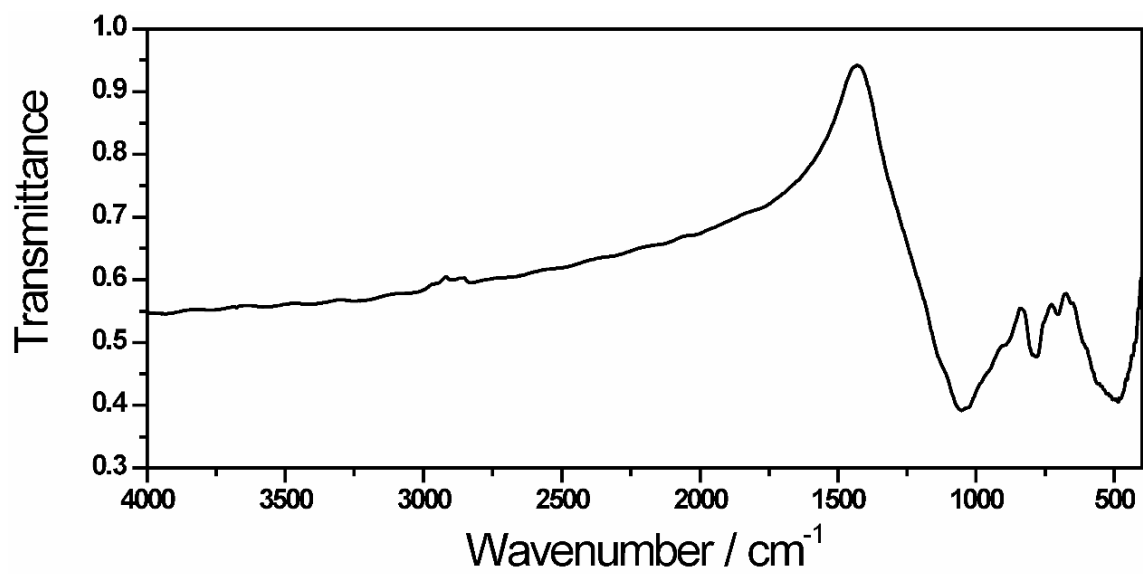


Figure C.4. FTIR spectrum of $\text{Li}_{18}\text{P}_6\text{N}_{16}$.

C.2 Ca₂PN₃**Table C.6.** Crystallographic data of Ca₂PN₃ obtained from Rietveld refinement, standard deviations in parentheses.

Formula	Ca ₂ PN ₃
Crystal system	orthorhombic
Space group	<i>Cmce</i> (no. 64)
<i>a</i> / Å	5.18798(6)
<i>b</i> / Å	10.31927(14)
<i>c</i> / Å	11.28164(12)
Cell volume / Å ³	603.976(12)
Density / g·cm ⁻³	3.36847(7)
Formula units / cell	8
<i>T</i> / K	293(2)
Diffractometer	STOE STADI P
Radiation / Å	Cu-K _{α1} ($\lambda = 1.5406$)
2 θ range /°	10 ≤ 2 θ ≤ 90
Profile function	fundamental parameters model
Background function	Shifted Chebyshev
Data points	5332
Number of reflections	146
Refined parameters	57
R values	$R_p = 0.0407$ $R_{wp} = 0.0540$ $R_{Bragg} = 0.0160$
Goodness of fit	0.707

Table C.7. Wyckoff positions and atomic coordinates of Ca_2PN_3 obtained from powder X-ray diffraction, standard deviations in parentheses.

Atom	Wyckoff	<i>x</i>	<i>y</i>	<i>z</i>	SOF	U_{iso}
Ca1	8 <i>f</i>	0	0.05150(13)	0.14303(11)	1	0.0190(5)
Ca2	8 <i>f</i>	0	0.36211(10)	0.07499(10)	1	0.0089(4)
P1	8 <i>f</i>	0	0.24233(17)	0.33300(15)	1	0.0092(5)
N1	8 <i>f</i>	0	0.3371(4)	0.4484(3)	1	0.0060(6)
N2	8 <i>f</i>	0	0.0889(4)	0.3583(4)	1	0.0060(6)
N3	8 <i>e</i>	1/4	0.2865(4)	1/4	1	0.0060(6)

Table C.8. SEM EDX measurements of Ca_2PN_3 . All EDX measurements showed amounts of impurities (O, Na) which originate from washing treatment, residual mineralizer and hydrolysis during sample preparation. For the quantification of the composition of the compounds, Na was not taken into account.

Ca_2PN_3	Ca	P	O	N
measurement 1:	15.9	9.6	46.3	28.1
measurement 2:	15.5	10.0	44.8	29.7
measurement 3:	17.2	11.3	44.8	26.7
\emptyset	17(1)	10(1)	45(1)	28(2)
ratio	1.7	1	4.5	2.8
ideal	2	1	0	3

C.3 $\text{SrP}_8\text{N}_{14}$

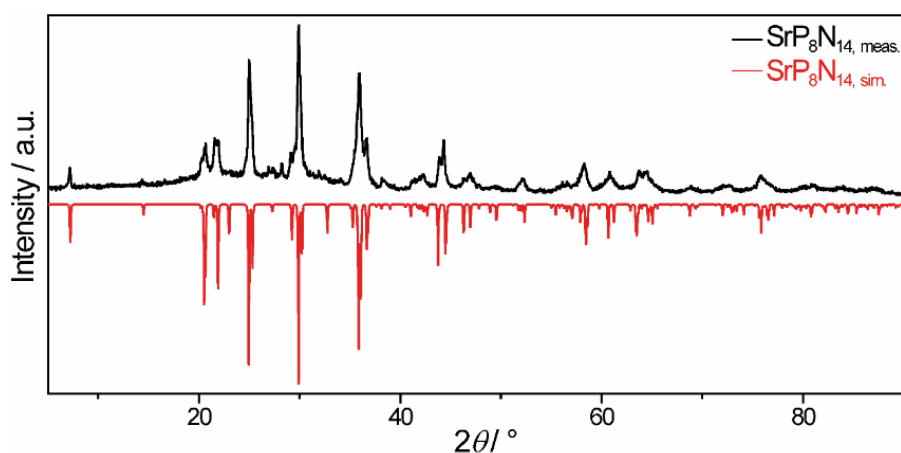
**Figure C.5.** Experimental PXRD pattern of $\text{SrP}_8\text{N}_{14}$ (black) and simulated pattern (red) taken from literature.^[5]

Table C.9. SEM EDX measurements of $\text{SrP}_8\text{N}_{14}$. The atomic ratios deviate from calculated ones, possibly due to an amorphous side phase (see PXRD). Traces of oxygen may originate from washing treatment with H_2O and HCl .

$\text{SrP}_8\text{N}_{14}$	Sr	P	O	N
measurement 1:	7.4	31.4	6.9	54.3
measurement 2:	5.7	20.1	19.1	55.1
measurement 3:	7.8	23.4	16.6	52.2
\emptyset	7(1)	25(6)	14(6)	54(2)
ratio	2.2	8	4.5	17.3
ideal	1	8	0	14

C.4 LiPN_2

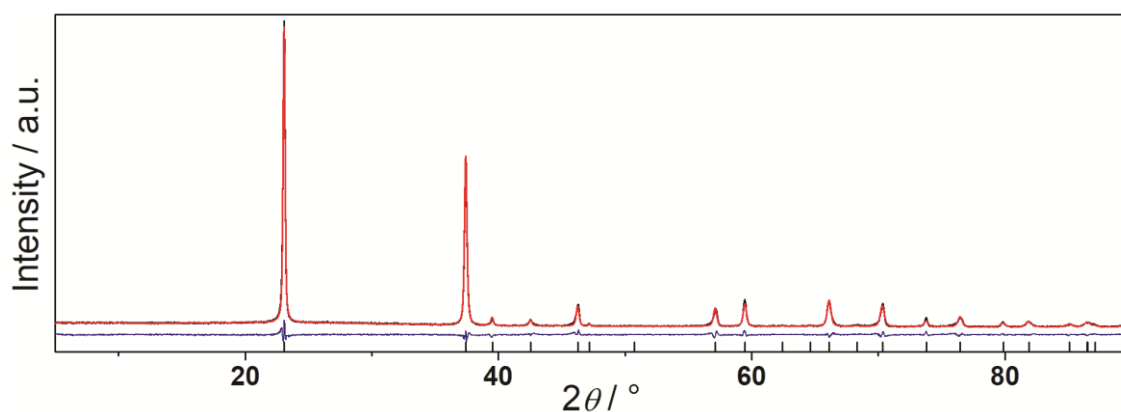


Figure C.6. Rietveld refinement of PXRD pattern of LiPN_2 with experimental data (black line), calculated data (red line), difference profile (blue line) and reflection positions (black bars). Start values were taken from literature.^[6]

Table C.10. Crystallographic data of LiPN₂ obtained by rietveld refinement, standard deviations in parentheses.

Formula	LiPN ₂
Crystal system	tetragonal
Space group	$\bar{I}42d$ (no. 122)
$a / \text{\AA}$	4.55609(10)
$c / \text{\AA}$	7.1945(2)
Cell volume / \AA^3	149.343(8)
Density / $\text{g}\cdot\text{cm}^{-3}$	2.93214(16)
Formula units / cell	4
T / K	293(2)
Diffractometer	STOE STADI P
Radiation / \AA	Cu- $K_{\alpha 1}$ ($\lambda = 1.5406$)
2θ range / $^\circ$	$5.0 \leq 2\theta \leq 90$
Profile function	fundamental parameters model
Background function	Shifted Chebyshev
Data points	5668
Number of reflections	24
Refined parameters	26
R values	$R_p = 0.0692$ $R_{wp} = 0.0942$ $R_{\text{Bragg}} = 0.0270$
Goodness of fit	1.283

Table C.11. Wyckoff positions and atomic coordinates of LiPN₂ obtained from powder X-ray diffraction, standard deviations in parentheses.

Atom	Wyckoff	x	y	z	SOF	U_{iso}
Li1	$4b$	0	0	1/2	1	0.0127
P1	$4a$	0	0	0	1	0.0084(5)
N1	$8d$	0.1637(6)	1/4	1/8	1	0.0089

Table C.12. SEM EDX measurements of LiPN₂. All EDX measurements showed small amounts of impurities (O, Cl) which originate from washing treatment with HCl. For the quantification of the composition of the compounds, Cl was not taken into account.

LiPN ₂	P	O	N
measurement 1:	34.4	7.1	58.5
measurement 2:	36.2	1.7	62.1
measurement 3:	35.4	2.2	62.4
∅	35(1)	4(3)	61(2)
ratio	1	0.1	1.7
ideal	1	0	2

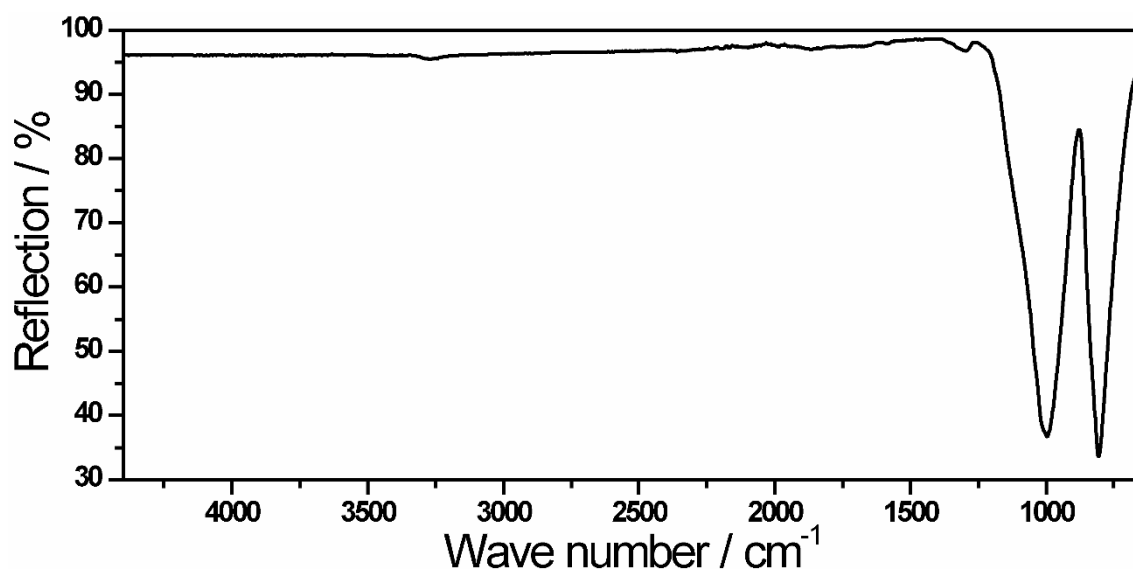


Figure C.7. FTIR (ATR) spectrum of LiPN₂. The two vibration bands at 998 and 808 cm⁻¹ are attributable to PN framework vibrations. There is no significant valance vibration in the region around 3000 cm⁻¹ where N-H-vibrations would be expected.^[4, 5] A weak signal can be explained by surface hydrolysis of the product during washing treatment.

C.5 References

- [1] E. M. Bertschler, C. Dietrich, T. Leichtweiß, J. Janek, W. Schnick, "*Li⁺ Ion Conductors with Adamantane-Type Nitridophosphate Anions β -Li₁₀P₄N₁₀ and Li₁₃P₄N₁₀X₃ with X = Cl, Br*", *Chem. Eur. J.* **2018**, *24*, 196-205.
- [2] W. Schnick, U. Berger, "*Li₁₀P₄N₁₀ - A Lithium Phosphorus(V) Nitride with the Novel Complex Anion P₄N₁₀¹⁰⁻*", *Angew. Chem.* **1991**, *103*, 857-858; *Angew. Chem. Int. Ed. Engl.* **1992**, *31*, 213-214.
- [3] E. M. Bertschler, C. Dietrich, J. Janek, W. Schnick, "*Li₁₈P₆N₁₆—A Lithium Nitridophosphate with Unprecedented Tricyclic [P₆N₁₆]¹⁸⁻ Ions*", *Chem. Eur. J.* **2017**, *23*, 2185-2191.
- [4] A. Marchuk, V. R. Celinski, J. Schmedt auf der Günne, W. Schnick, "*MH₄P₆N₁₂ (M = Mg, Ca): New Imidonitridophosphates with an Unprecedented Layered Network Structure Type*", *Chem. Eur. J.* **2015**, *21*, 5836-5842.
- [5] S. Wendl, W. Schnick, "*SrH₄P₆N₁₂ and SrP₈N₁₄: Insights into the Condensation Mechanism of Nitridophosphates under High Pressure*", *Chem. Eur. J.* **2018**, *24*, 15889-15896.
- [6] W. Schnick, J. Lücke, "*On Lithium Phosphorus Nitride. Preparation and Refinement of the Crystal Structure of LiPN₂*", *Z. Anorg. Allg. Chem.* **1990**, *588*, 19-25.

D Supporting Information for Chapter 5

Mathias Mallmann, Sebastian Wendl, Philipp Strobel, Peter J. Schmidt, and Wolfgang Schnick

Chem. Eur. J. **2020**, *26*, 6257 - 6263.

D.1 Additional crystallographic data

Table D.1. Wyckoff positions and atomic coordinates of Sr₃P₃N₇ obtained from single-crystal X-ray diffraction, standard deviations in parentheses.

Atom	Wyckoff	x	y	z	$U_{\text{eq}} [\text{\AA}^2]$
Sr1	2f	1/2	0.46228(16)	1/4	0.0188(3)
Sr2	4g	0.73739(16)	0.89636(11)	0.45130(11)	0.01718(19)
P1	4g	0.1749(3)	0.7068(3)	0.4251(3)	0.0158(4)
P2	2e	0	0.3684(4)	1/4	0.0165(6)
N1	2e	0	0.8006(13)	1/4	0.0177(19)
N2	4g	0.1711(9)	0.4873(9)	0.4010(9)	0.0147(13)
N3	4g	0.3899(9)	0.7822(10)	0.4302(9)	0.0190(14)
N4	4g	0.1178(10)	0.2307(10)	0.1330(9)	0.0198(14)

Table D.2. Anisotropic displacement parameters [\AA^2] of Sr₃P₃N₇, standard deviations in parentheses.

Atom	U_{11}	U_{22}	U_{33}	U_{23}	U_{13}	U_{12}
Sr1	0.0172(5)	0.0269(6)	0.0145(5)	0	0.0081(4)	0
Sr2	0.0154(3)	0.0225(4)	0.0159(3)	-0.0013(3)	0.0081(3)	-0.0009(3)
P1	0.0157(9)	0.0208(11)	0.0131(9)	-0.0010(8)	0.0080(8)	0.0000(8)
P2	0.0161(13)	0.0224(17)	0.0138(12)	0	0.0088(11)	0
N1	0.022(5)	0.021(5)	0.010(4)	0	0.005(4)	0
N2	0.007(3)	0.024(4)	0.011(3)	-0.002(2)	0.000(2)	0.000(2)
N3	0.018(3)	0.026(4)	0.015(3)	-0.002(3)	0.008(3)	0.001(3)
N4	0.022(3)	0.024(4)	0.017(3)	0.002(3)	0.013(3)	0.001(3)

Table D.3. Selected interatomic distances [Å] and angles [°] occurring in Sr₃P₃N₇ obtained from single-crystal X-ray diffraction, standard deviations in parentheses.

Sr1 – N1	2.740(9)	P1 – N1	1.631(8)	N1 – P1 – N1	115.0(4)
Sr1 – N1	2.740(9)	P1 – N1	1.575(10)	N1 – P1 – N3	112.3(5)
Sr1 – N2	2.846(9)	P1 – N3	1.646(10)	N1 – P1 – N3	106.7(5)
Sr1 – N2	2.846(9)	P1 – N3	1.646(10)	N1 – P1 – N3	106.7(5)
Sr1 – N2	2.883(10)	P2 – N2	1.575(10)	N1 – P1 – N3	112.3(5)
Sr1 – N2	2.883(10)	P2 – N4	1.638(6)	N3 – P1 – N3	103.3(5)
Sr1 – N1	2.895(7)	P2 – N1	1.642(9)	N2 – P2 – N4	111.4(5)
Sr1 – N1	2.895(7)	P2 – N3	1.683(10)	N2 – P2 – N1	110.2(5)
Sr1 – N3	3.068(10)			N2 – P2 – N3	108.2(5)
Sr1 – N3	3.068(10)			N4 – P2 – N1	111.1(5)
Sr2 – N2	2.504(10)			N4 – P2 – N3	104.5(5)
Sr2 – N4	2.665(4)			N1 – P2 – N3	111.3(5)
Sr2 – N2	2.726(9)				
Sr2 – N2	2.740(10)				
Sr2 – N3	2.772(9)				
Sr2 – N3	2.793(10)				
Sr2 – N3	2.978(9)				
Sr2 – N1	3.030(9)				
Sr2 – N4	3.283(10)				

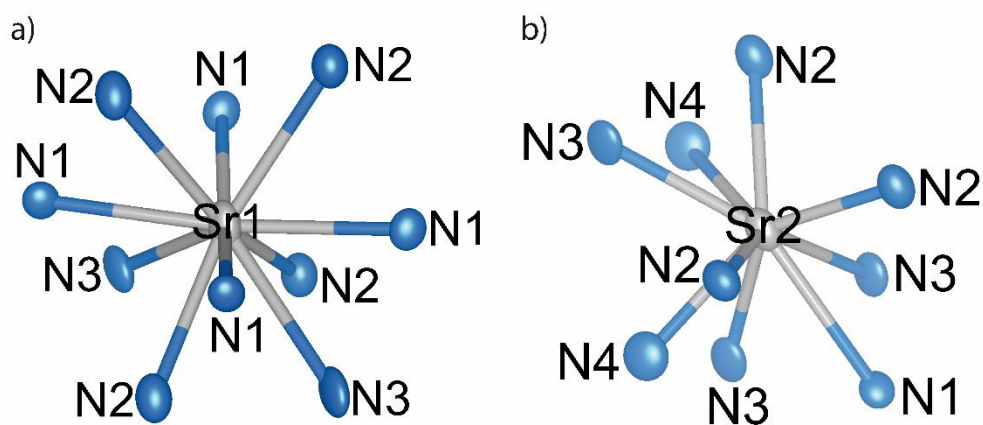
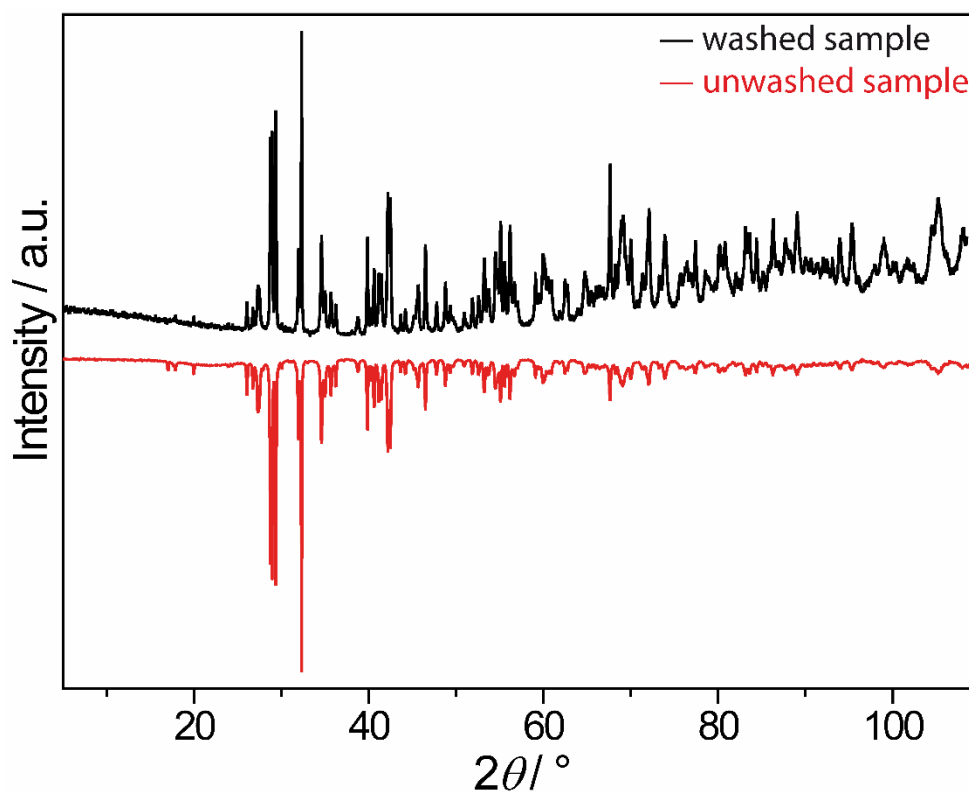
**Figure D.1.** Coordination polyhedra of Sr atoms (Sr1 (a) and Sr2 (b)) in Sr₃P₃N₇. Sr atoms are depicted in gray, nitrogen atoms in blue. Thermal ellipsoids are depicted at 90% probability.

Table D.4. Crystallographic data of ammonothermally synthesized $\text{Sr}_3\text{P}_3\text{N}_7$ obtained by Rietveld refinement, standard deviations in parentheses.

Formula	$\text{Sr}_3\text{P}_3\text{N}_7$
Crystal system	monoclinic
Space group	$P2/c$ (no. 13)
$a / \text{\AA}$	6.8970(4)
$b / \text{\AA}$	7.4289(4)
$c / \text{\AA}$	7.0693(4)
$\beta / ^\circ$	104.9555(11)
Cell volume / \AA^3	349.94(3)
Formula units / cell	2
Density / $\text{g}\cdot\text{cm}^{-3}$	4.3070(4)
T / K	293
Diffractometer	Stoe STADI P
Detector	Mythen 1K
Monochromator	Ge(111)
Radiation / \AA	$\text{Cu-}K_{\alpha 1}$ (1.5406)
2θ range / $^\circ$	$5.0 \leq 2\theta \leq 109.5$
Profile function	fundamental parameters approach
Background function	Shifted Chebyshev
Data points	6968
Number of reflections	442
Refined parameters	97
R_p	0.056
R_{wp}	0.073
R_{Bragg}	0.021
Goodness of Fit	1.19

Table D.5. Wyckoff positions and atomic coordinates of $\text{Sr}_3\text{P}_3\text{N}_7$ obtained from Rietveld refinement, standard deviations in parentheses.

Atom	Wyckoff	x	y	z	$U_{\text{iso}} [\text{\AA}^2]$
Sr1	$2f$	1/2	0.4601(3)	1/4	0.0191(11)
Sr2	$4g$	0.7372(2)	0.8960(2)	0.4557(2)	0.0191(11)
P1	$4g$	0.1729(5)	0.7081(5)	0.4218(7)	0.0184(14)
P2	$2e$	0	0.3709(8)	1/4	0.0184(14)
N1	$2e$	0	0.814(2)	1/4	0.017(2)
N2	$4g$	0.1646(17)	0.4822(13)	0.400(2)	0.017(2)
N3	$4g$	0.3883(16)	0.7946(17)	0.4309(17)	0.017(2)
N4	$4g$	0.1128(16)	0.2332(15)	0.1242(18)	0.017(2)

**Figure D.2.** Comparison of PXRD data of washed (black line) and unwashed (red line) $\text{Sr}_3\text{P}_3\text{N}_7$ samples synthesized ammonothermally.

D.2 Detailed Information on scanning electron microscopy

Table D.6. SEM EDX measurements of $\text{Sr}_3\text{P}_3\text{N}_7:\text{Eu}^{2+}$.

$\text{Sr}_3\text{P}_3\text{N}_7:\text{Eu}^{2+}$	Sr	P	N	Eu	O
measurement 1:	20.8	19.9	58.5	0.8	-
measurement 2:	24.2	24.4	47.2	0.7	3.5
measurement 3:	19.9	21.0	50.9	0.7	7.5
measurement 4:	19.5	23.3	56.7	0.5	-
\emptyset	21.1	22.1	53.3	0.7	2.8
calculated	22.6	23.1	53.8	0.5	-

D.3 Detailed information on IR spectroscopy

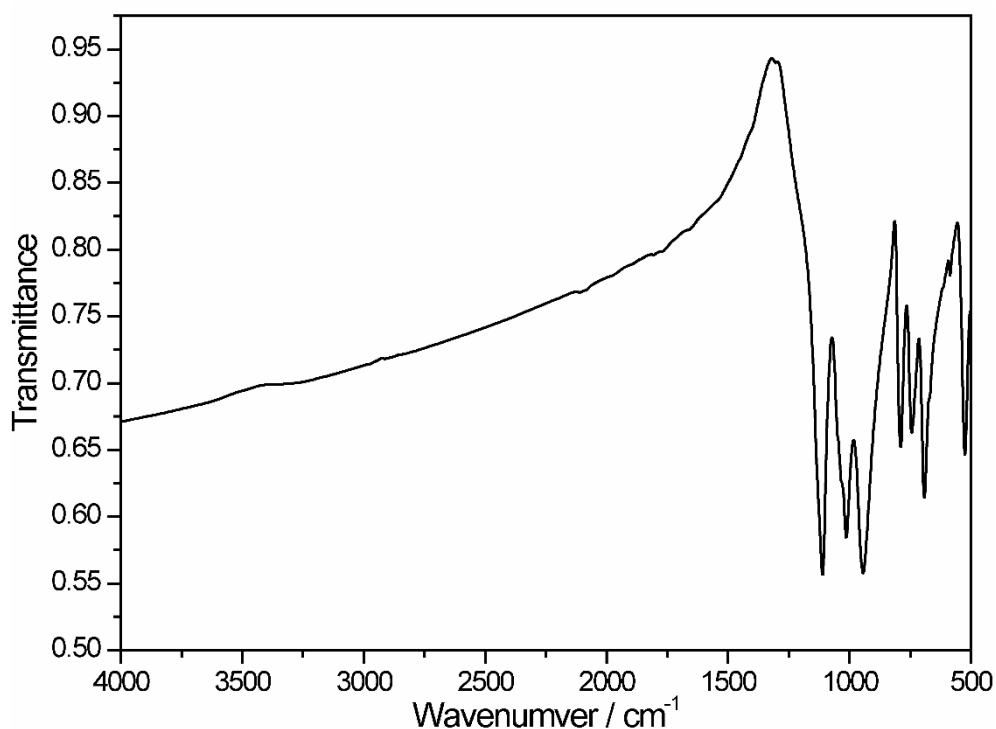


Figure D.3. FTIR spectrum of ammonothermally synthesized $\text{Sr}_3\text{P}_3\text{N}_7$, measured using the KBr pellet method.

D.4 Detailed information on UV/Vis spectroscopy

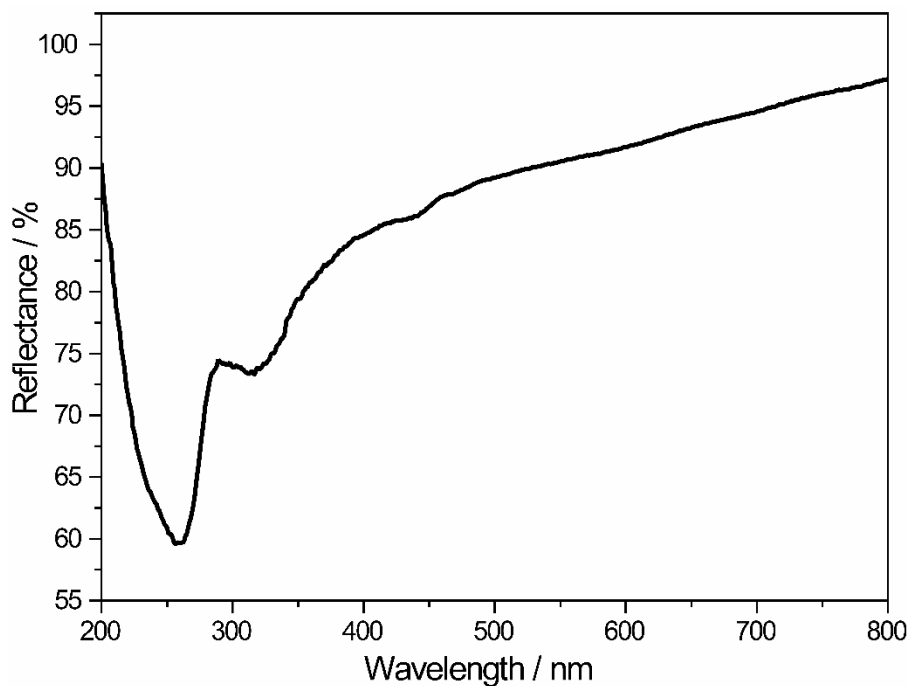


Figure D.4. Diffuse reflectance spectrum of ammonothermally synthesized $\text{Sr}_3\text{P}_3\text{N}_7$. The lamp switch causes the artifact around 340 nm.

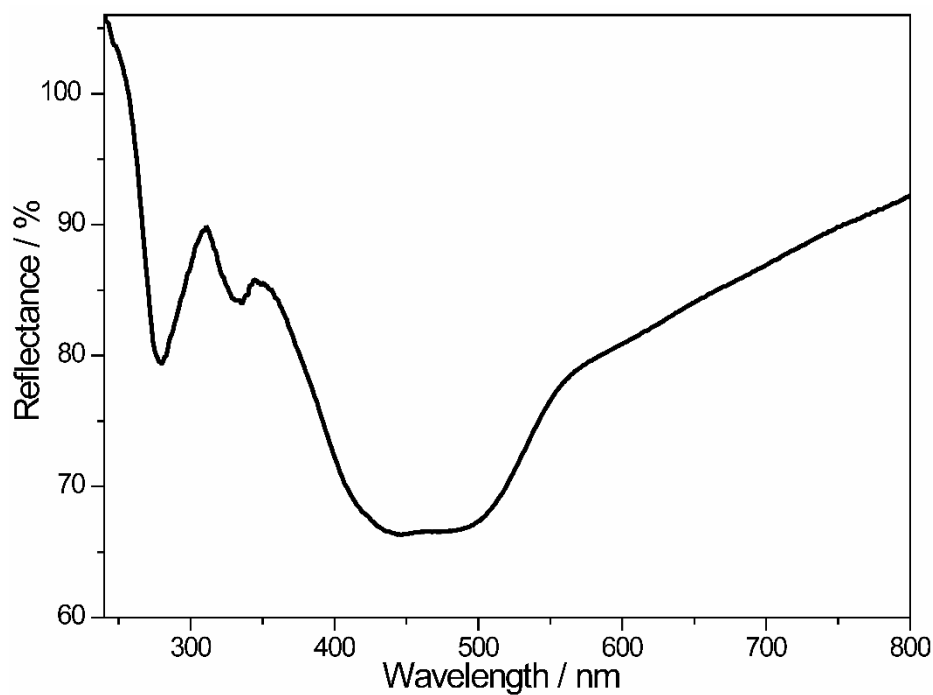


Figure D.5. Diffuse reflectance spectrum of ammonothermally synthesized $\text{Sr}_3\text{P}_3\text{N}_7:\text{Eu}^{2+}$. The lamp switch causes the artifact around 340 nm.

D.5 Luminescence properties

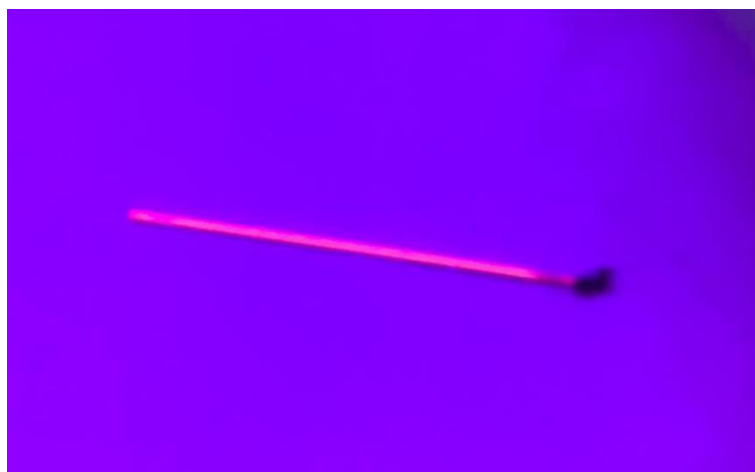


Figure D.6. Photograph of ammonothermally synthesized red luminescence $\text{Sr}_3\text{P}_3\text{N}_7:\text{Eu}^{2+}$ powder in a glass capillary when irradiated with UV light.

E Supporting Information for Chapter 6

Sebastian Wendl, Mathias Mallmann, Philipp Strobel, Peter J. Schmidt, and Wolfgang Schnick

Eur. J. Inorg. Chem. **2020**, 2020, 841 - 846.

E.1 Additional crystallographic data

Table E.1. Wyckoff positions and atomic coordinates of Ba₂PO₃N obtained from single-crystal X-ray diffraction, standard deviations in parentheses.

Atom	Wyckoff	<i>x</i>	<i>y</i>	<i>z</i>	<i>U</i> _{eq} [Å ²]
Ba1	4c	0.15869(3)	3/4	0.58252(2)	0.01504(5)
Ba2	4c	0.49595(2)	3/4	0.30557(2)	0.01158(4)
P1	4c	0.73340(10)	3/4	0.58127(8)	0.0087(1)
O1	8 <i>d</i>	0.7994(3)	0.5307(3)	0.6576(2)	0.0201(4)
O2	4c	0.5226(3)	3/4	0.5847(3)	0.0213(5)
N1	4c	0.8089(4)	3/4	0.4373(2)	0.0117(5)

Table E.2. Anisotropic displacement parameters [Å²] of Ba₂PO₃N, standard deviations in parentheses.

Atom	<i>U</i> ₁₁	<i>U</i> ₂₂	<i>U</i> ₃₃	<i>U</i> ₂₃	<i>U</i> ₁₃	<i>U</i> ₁₂
Ba1	0.01388(8)	0.01275(8)	0.01849(9)	0	0.00218(7)	0
Ba2	0.00967(7)	0.01371(8)	0.01135(8)	0	0.00015(6)	0
P1	0.0085(3)	0.0085(3)	0.0092(3)	0	0.0002(2)	0
O1	0.0219(9)	0.0160(8)	0.0224(8)	0.0074(7)	-0.0031(7)	0.0011(7)
O2	0.0126(10)	0.029(2)	0.0223(12)	0	0.0003(9)	0
N1	0.0126(10)	0.0150(12)	0.0074(10)	0	0.0025(8)	0

Table E.3. Selected interatomic distances [\AA] and angles [$^\circ$] occurring in $\text{Ba}_2\text{PO}_3\text{N}$ obtained from single-crystal X-ray diffraction, standard deviations in parentheses.

Ba1 – O2	2.764(2)	Ba2 – O1	2.711(2)	P1 – O1	1.573(2)
Ba1 – N1	2.9156(8)	Ba2 – O1	2.711(2)	P1 – O1	1.573(2)
Ba1 – N1	2.9156(8)	Ba2 – N1	2.731(3)	P1 – N1	1.578(2)
Ba1 – O1	2.960(2)	Ba2 – O1	2.797(2)	P1 – O2	1.602(2)
Ba1 – O1	2.960(2)	Ba2 – O1	2.797(2)		
Ba1 – N1	3.043(3)	Ba2 – O2	2.858(3)	O1 – P1 – O1	107.81(9)
Ba1 – O1	3.107(2)	Ba2 – N1	2.858(2)	O1 – P1 – N1	110.23(7)
Ba1 – O1	3.107(2)	Ba2 – O2	3.110(1)	O1 – P1 – O2	107.93(8)
Ba1 – O1	3.131(2)	Ba2 – O2	3.110(1)	N1 – P1 – O2	112.6(2)
Ba1 – O1	3.131(2)				

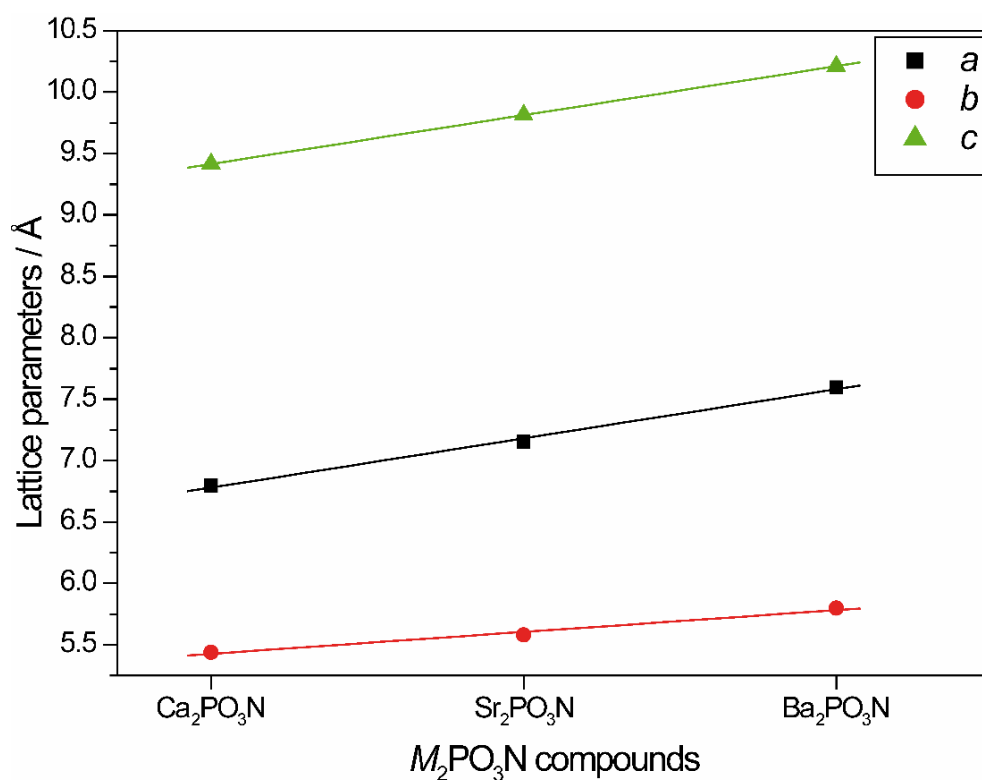
**Figure E.1.** Comparison of lattice parameters of $M_2\text{PO}_3\text{N}$ ($M = \text{Ca}, \text{Sr}, \text{Ba}$) compounds.

Table E.4. Results of MAPLE calculations [kJ/mol] for Ba₂PO₃N. Partial MAPLE values, total MAPLE value and deviation to sum of total MAPLE values of binary ionic compounds, forming Ba₂PO₃N in a hypothetical reaction (structural data were taken from literature).^[1, 2]

Ba1 ²⁺	Ba2 ²⁺	P1 ⁵⁺	O1 ^{[1]2-}	O2 ^{[1]2-}	N1 ^{[1]3-}	total MAPLE
1685	1912	14550	2606	2588	5036	30983
2 · BaO + PON _(cristobalite)						
2 · 3519 + 24142						31180
						Δ ≈ 0.63%

Typical partial MAPLE values [kJ/mol]:^[3]

Ba²⁺: 1500-2000

P⁵⁺: 14422-15580

N^{[1]3-}: 4300-5000

O^{[1]2-}: 2000-2800

Table E.5. Bond-valance sums for Ba₂PO₃N.

	Ba1	Ba2	P	O1	O2	N1
	1.876	2.407	4.686	2.064	1.781	3.063
oxidation state	2	2	5	2	2	3

Table E.6. Results of CHARDI calculations for Ba₂PO₃N.

Ba1	Ba2	P	O1	O2	N1
2.022	1.985	4.993	-2.350	-1.880	-2.420

Table E.7. Crystallographic data of Ba₂PO₃N obtained by Rietveld refinement, standard deviations in parentheses.

Formula	Ba ₂ PO ₃ N
Crystal system	orthorhombic
Space group	<i>Pnma</i> (no. 62)
<i>a</i> / Å	7.5896(2)
<i>b</i> / Å	5.78984(9)
<i>c</i> / Å	10.1969(2)
Cell volume / Å ³	448.08(1)
Formula units / cell	4
Density / g·cm ⁻³	5.4496(2)
<i>T</i> / K	293
Diffractometer	Stoe STADI P
Radiation / Å	Mo-K _{α1} (0.71073)
Detector	Mythen 1K
Monochromator	Ge(111)
2θ range / °	2.5 ≤ 2θ ≤ 56.26
Profile function	fundamental parameters approach
Background function	Shifted Chebyshev
Data points	3584
Number of reflections	618
Refined parameters	44
<i>R</i> _p	0.0426
<i>R</i> _{wp}	0.0699
<i>R</i> _{Bragg}	0.0190
Goodness of Fit	2.66

Table E.8. Wyckoff positions and atomic coordinates of Ba₂PO₃N obtained from Rietveld refinement, standard deviations in parentheses. Isotropic displacement parameters of P, O and N were taken from single-crystal XRD measurement.

Atom	Wyckoff	<i>x</i>	<i>y</i>	<i>z</i>	<i>U</i> _{iso} [Å ²]
Ba1	4 <i>c</i>	0.1598(2)	3/4	0.58443(12)	0.0138(4)
Ba2	4 <i>c</i>	0.4959(2)	3/4	0.30508(11)	0.0073(3)
P1	4 <i>c</i>	0.7335(6)	3/4	0.5777(7)	0.00872
O1	8 <i>d</i>	0.7986(10)	0.537(1)	0.6562(9)	0.0201
O2	4 <i>c</i>	0.526(1)	3/4	0.5883(11)	0.0213
N1	4 <i>c</i>	0.809(1)	3/4	0.440(1)	0.0117

E.2 Detailed information on scanning electron microscopy

Table E.9. SEM EDX measurements of Ba₂PO₃N:Eu²⁺.

Ba ₂ PO ₃ N:Eu ²⁺	Ba	P	O	N	Eu
measurement 1:	31.7	15.1	38.1	14.5	0.6
measurement 2:	32.3	15.4	38.1	13.7	0.5
measurement 3:	32.0	15.1	38.3	14.1	0.5
measurement 4:	31.6	15.6	37.5	14.9	0.4
∅	31.9	15.3	38.0	14.3	0.5
calculated	28.3	14.3	42.8	14.3	0.3

E.3 Detailed information on IR spectroscopy

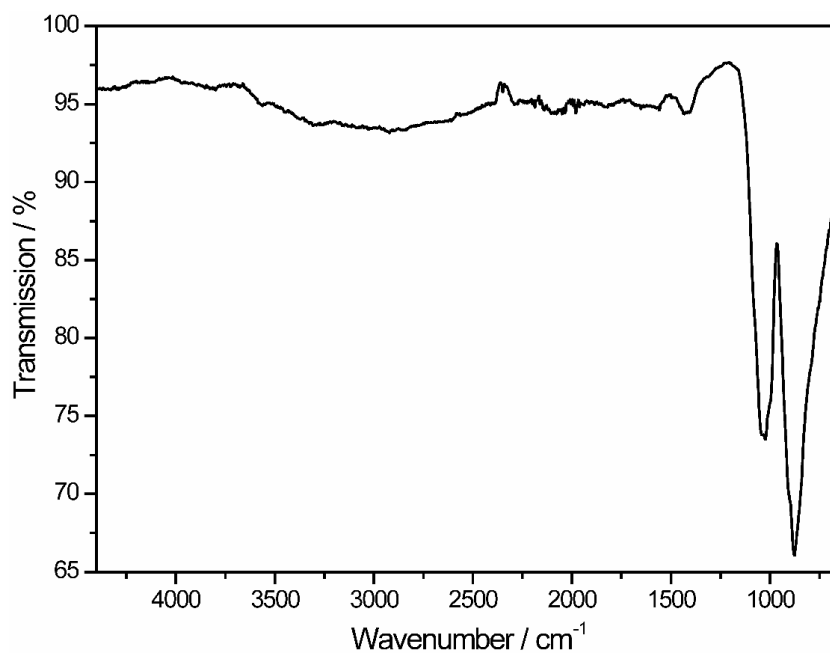


Figure E.2. FTIR (ATR) spectrum of Ba₂PO₃N.

E.4 Detailed information on UV/Vis spectroscopy

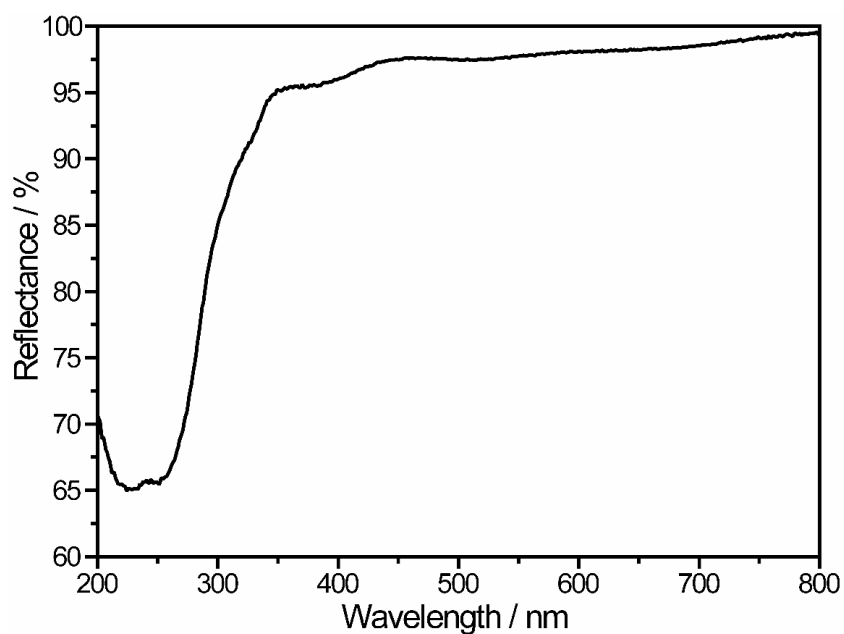


Figure E.3. Diffuse reflectance spectrum of Ba₂PO₃N. The lamp switch causes the artifact around 340 nm.

E.5 Luminescence properties

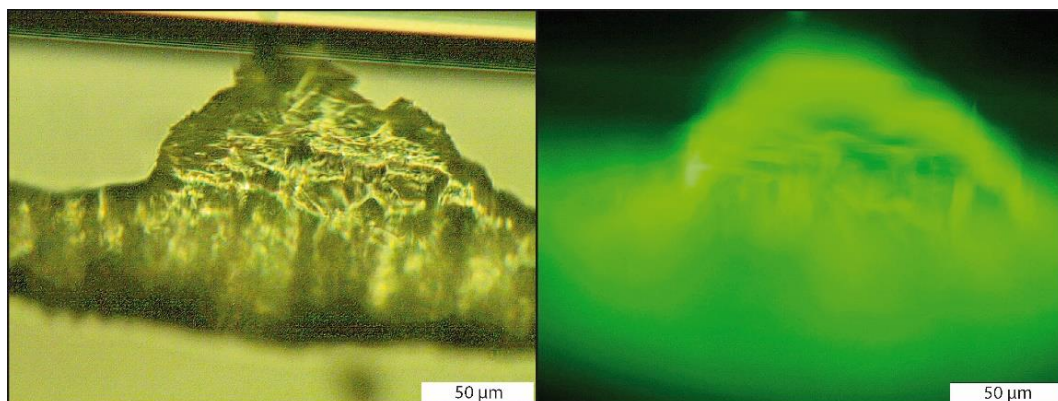


Figure E.4. Comparison of a Ba₂PO₃N:Eu²⁺ single-crystal irradiated with white light (left) and UV light (right).

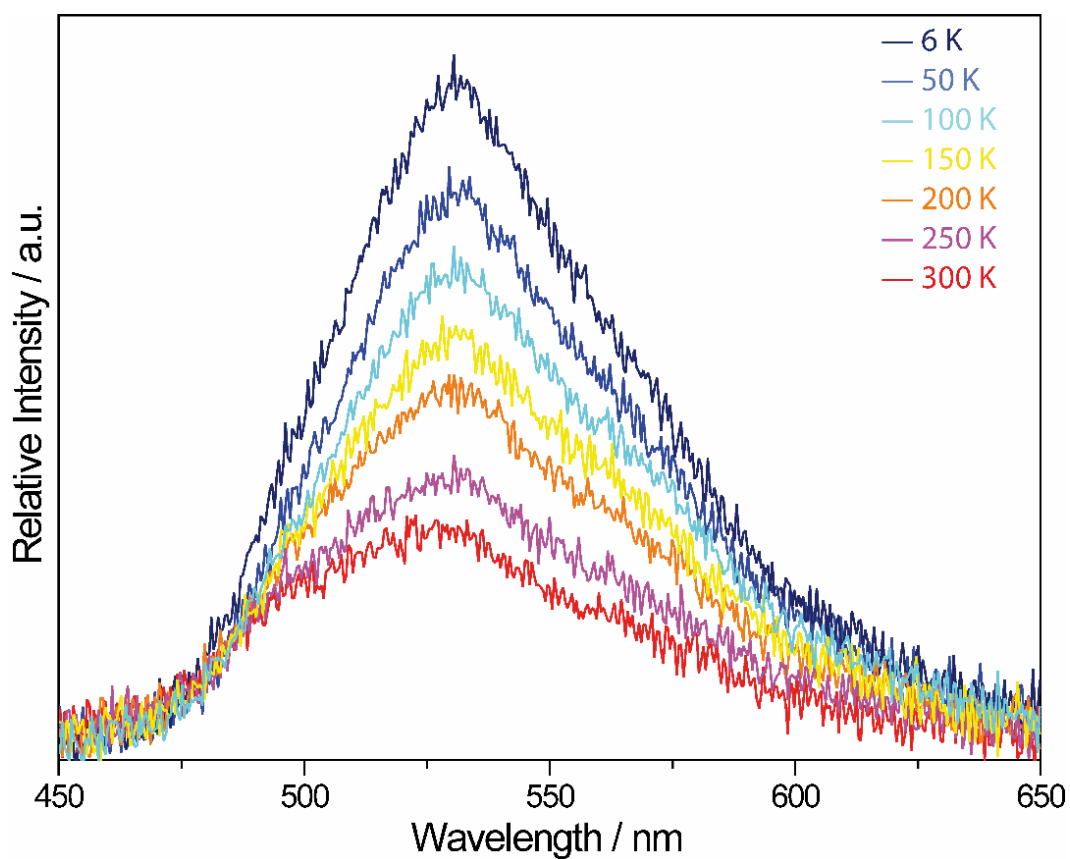


Figure E.5. Luminescence spectra of Ba₂PO₃N:Eu²⁺ powder at temperatures ranging from 6 to 300 K.

E.6 References

- [1] W. Gerlach, "Die Gitterstruktur der Erdalkalioxyde", *Z. Phys.* **1922**, 9, 184-192.
- [2] J. M. Léger, J. Haines, C. Chateau, G. Bocquillon, M. W. Schmidt, S. Hull, F. Gorelli, A. Lesauze, R. Marchand, "Phosphorus oxynitride PON, a silica analogue: structure and compression of the cristobalite-like phase; *P-T* phase diagram", *Phys. Chem. Miner.* **2001**, 28, 388-398.
- [3] M. Zeuner, S. Pagano, W. Schnick, "Nitridosilicates and Oxonitridosilicates: From Ceramic Materials to Structural and Functional Diversity", *Angew. Chem.* **2011**, 123, 7898-7920; *Angew. Chem. Int. Ed.* **2011**, 50, 7754-7775.

F Supporting Information for Chapter 7

Mathias Mallmann, Christian Maak, and Wolfgang Schnick

Z. Anorg. Allg. Chem. **2020**, DOI: 10.1002/zaac.202000018.

F.1 Additional crystallographic data

Table F.1. Anisotropic displacement parameters [\AA^2] of $\text{Ca}_{1+x}\text{Y}_{1-x}\text{SiN}_{3-x}\text{O}_x$ ($x > 0$), standard deviations in parentheses.

Atom	U11	U22	U33	U23	U13	U12
Ca1/Y1	0.0168(2)	0.0081(2)	0.0089(2)	-0.00019(18)	0	0
Ca2/Y2	0.0173(5)	0.0114(4)	0.0114(4)	0.0007(3)	0	0
Si1	0.0090(6)	0.0077(6)	0.0097(6)	0.0002(4)	0	0
N1/O1	0.0162(18)	0.0106(17)	0.0104(16)	-0.0012(14)	0	0
N2/O2	0.018(2)	0.0124(18)	0.0113(17)	-0.0014(14)	0	0
N3	0.0110(19)	0.0174(19)	0.0105(16)	0	-0.0038(15)	0

Table F.2. Selected interatomic distances [\AA] occurring in $\text{Ca}_{1+x}\text{Y}_{1-x}\text{SiN}_{3-x}\text{O}_x$ ($x > 0$) obtained from single-crystal X-ray diffraction, standard deviations in parentheses.

Y1 – N2/O2	2.321(4)	Y2 – N1/O1	2.396(4)	Si1 – N3	1.714(1)
Y1 – N1/O1	2.416(4)	Y2 – N1/O1	2.459(4)	Si1 – N3	1.714(1)
Y1 – N2/O2	2.429(4)	Y2 – N2/O2	2.544(4)	Si1 – N1/O1	1.726(4)
Y1 – N3	2.484(1)	Y2 – N2/O2	2.6889(11)	Si1 – N2/O2	1.736(4)
Y1 – N3	2.484(1)	Y2 – N2/O2	2.6889(11)		
Y1 – N1/O1	2.7086(11)	Y2 – N3	3.036(4)		
Y1 – N1//O1	2.7086(11)	Y2 – N2	3.036(4)		

Table F.3. *R* values for single-crystal XRD refinements with different occupation models of the two (mixed) Ca/Y sites.

Occupation	theoretical composition	<i>R</i> 1 ($F2 > 2\sigma(F2)$); <i>R</i> 1 (all data)	<i>wR</i> 2 ($F2 > 2\sigma(F2)$); <i>wR</i> 2 (all data)
Ca1/Y1: refined (21% / 79%) Ca2/Y2: refined (95% / 5%)	Ca _{1.16} Y _{0.84} SiN _{2.84} O _{0.16}	0.0257; 0.0373	0.0447; 0.0465
Ca1/Y1: fixed (0% / 100%) Ca2/Y2: refined (85% / 15%)	not charge-neutral	0.0298; 0.0403	0.0664; 0.0677
Ca1/Y1: refined (26% / 74%) Ca2/Y2: fixed (100% / 0%)	Ca _{1.26} Y _{0.74} SiN _{2.74} O _{0.26}	0.0261; 0.0366	0.0510; 0.0527
Ca1/Y1: fixed (0% / 100%) Ca2/Y2: fixed (100% / 0%)	CaYSiN ₃	0.0413; 0.0519	0.1004; 0.1013

Table F.4. Results of MAPLE calculations [kJ/mol] for Ca_{1+x}Y_{1-x}SiN_{3-x}O_x with *x* assumed to be 0.16. Partial MAPLE values, total MAPLE value and deviation to sum of total MAPLE values of binary ionic compounds, forming Ca_{1.16}Y_{0.84}SiN_{2.84}O_{0.16} in a hypothetical reaction (structural data were taken from literature).^[1-4]

Ca1 ²⁺ /Y1 ³⁺	Ca2 ²⁺ /Y2 ³⁺	Si1 ⁴⁺	N1 ^{[1]3-} /O1 ^{[1]2-}	N2 ^{[1]3-} /O2 ^{[1]2-}	N3 ^{[2]3-}	total MAPLE
(21.2%/78.8%)	(94.6%/5.4%)		(92.1%/7.9%)	(92.1%/7.9%)		
3673	1996	9722	4749	4793	5460	30393
0.39 · Ca ₃ N ₂ + 0.05 · Y ₂ O ₃ + 0.73 · YN + 0.33 · α-Si ₃ N ₄						
0.39 · 14125 + 0.05 · 15270 + 0.73 · 8946 + 0.33 · 52989						30289
						$\Delta \approx 0.34\%$

Typical values in nitridosilicates [kJ/mol]:^[5]

Ca²⁺: 1700-2200

RE³⁺: 3500-5100

Si⁴⁺: 9000-10200

N^{[1]3-}: 4300-5000

O^{[1]2-}: 2000-2800

N^{[2]3-}: 4600-6000

Table F.5. Crystallographic data of $\text{Ca}_{1+x}\text{Y}_{1-x}\text{SiN}_{3-x}\text{O}_x$ with x assumed to be 0.16 obtained by Rietveld refinement, standard deviations in parentheses.

Formula	$\text{Ca}_{1+x}\text{Y}_{1-x}\text{SiN}_{3-x}\text{O}_x$
Crystal system	orthorhombic
Space group	<i>Cmce</i> (no. 64)
$a / \text{\AA}$	5.34388(10)
$b / \text{\AA}$	10.3487(2)
$c / \text{\AA}$	11.2628(2)
Cell volume / \AA^3	622.86(2)
Density / $\text{g}\cdot\text{cm}^{-3}$	4.0883(2)
Formula units / cell	8
T / K	293(2)
Diffractometer	STOE STADI P
Detector	Mythen 1K
Monochromator	Ge(111)
Radiation / \AA	$\text{Cu-}K_{\alpha 1}$ ($\lambda = 1.5406$)
2θ range / $^\circ$	$5.0 \leq 2\theta \leq 110$
Profile function	fundamental parameters model
Background function	Shifted Chebyshev
Data points	7001
Number of reflections	229
Refined parameters (thereof background)	83 (12)
R values	$R_p = 0.0323$ $R_{wp} = 0.0455$ $R_{\text{Bragg}} = 0.0150$
Goodness of fit	1.700

Table F.6. Wyckoff positions and atomic coordinates of $\text{Ca}_{1+x}\text{Y}_{1-x}\text{SiN}_{3-x}\text{O}_x$ with x assumed to be 0.16, obtained from Rietveld refinement, standard deviations in parentheses.

Atom	Wyckoff	x	y	z	SOF	$U_{\text{iso}} [\text{\AA}^2]$
Ca1	8 <i>f</i>	1/2	0.14089(7)	0.57706(7)	0.788	0.01128
Y1	8 <i>f</i>	1/2	0.14089(7)	0.57706(7)	0.212	0.01128
Ca2	8 <i>f</i>	1/2	0.4538(2)	0.64527(12)	0.946	0.0134
Y2	8 <i>f</i>	1/2	0.4538(2)	0.64527(12)	0.054	0.0134
Si1	8 <i>f</i>	1/2	0.2402(2)	0.3380(2)	1	0.0088
N1	8 <i>f</i>	1/2	0.3365(5)	0.4600(4)	0.921	0.0124
O1	8 <i>f</i>	1/2	0.3365(5)	0.4600(4)	0.079	0.0124
N2	8 <i>f</i>	1/2	0.0741(5)	0.3694(5)	0.921	0.0139
O2	8 <i>f</i>	1/2	0.0741(5)	0.3694(5)	0.079	0.0139
N3	8 <i>e</i>	1/4	0.2835(5)	1/4	1	0.0130

F.2 References

- [1] O. Reckeweg, F. J. DiSalvo, "About Binary and Ternary Alkaline Earth Metal Nitrides", *Z. Anorg. Allg. Chem.* **2001**, 627, 371-377.
- [2] M. G. Paton, E. N. Maslen, "A refinement of the crystal structure of yttria", *Acta Crystallogr.* **1965**, 19, 307-310.
- [3] C. P. Kempter, N. H. Krikorian, J. C. McGuire, "The Crystal Structure of Yttrium Nitride", *J. Phys. Chem.* **1957**, 61, 1237-1238.
- [4] P. Yang, H.-K. Fun, I. A. Rahman, M. I. Saleh, "Two phase refinements of the structures of α - Si_3N_4 and β - Si_3N_4 made from rice husk by Rietveld analysis", *Ceram. Int.* **1995**, 21, 137-142.
- [5] M. Zeuner, S. Pagano, W. Schnick, "Nitridosilicates and Oxonitridosilicates: From Ceramic Materials to Structural and Functional Diversity", *Angew. Chem.* **2011**, 123, 7898-7920; *Angew. Chem. Int. Ed.* **2011**, 50, 7754-7775.

G Miscellaneous

G.1 List of publications within this thesis

1. Solid Solutions of Grimm-Sommerfeld Analogous Nitride Semiconductors $II-IV-N_2$ ($II = Mg, Mn, Zn$; $IV = Si, Ge$): Ammonothermal Synthesis and DFT Calculations

Mathias Mallmann, Robin Niklaus, Tobias Rackl, Maximilian Benz, Thanh Giang Chau, Dirk Johrendt, Ján Minár, and Wolfgang Schnick

Chem. Eur. J. **2019**, *25*, 15887 -15895.

Literature research, sample syntheses and formal analyses were performed by Mathias Mallmann. Maximilian Benz and Thanh Giang Chau helped in conducting the ammonothermal syntheses under supervision of Mathias Mallmann. DFT calculations and evaluation of data were conducted by Robin Niklaus under the supervision of Ján Minár. Tobias Rackl performed magnetic measurements of the samples as well as their interpretation under the supervision of Dirk Johrendt. Writing of the main part of the manuscript was carried out by Mathias Mallmann. Robin Niklaus wrote the computational calculations section. The Graphical material was created by Mathias Mallmann and Robin Niklaus. The project was supervised by Wolfgang Schnick. All authors revised the manuscript.

2. Ammonothermal Synthesis, Optical Properties and DFT Calculations of Mg_2PN_3 and Zn_2PN_3

Mathias Mallmann, Christian Maak, Robin Niklaus, and Wolfgang Schnick

Chem. Eur. J. **2018**, *24*, 13963 - 13970.

For this manuscript, literature research, ammonothermal syntheses, formal analyses, creation of graphical material and writing of the major part of the manuscript were performed by Mathias Mallmann. Christian Maak supported the formal analysis. DFT calculations were carried out by Robin Niklaus. The project was supervised by Wolfgang Schnick. All authors revised the manuscript.

3. **Crystalline Nitridophosphates by Ammonothermal Synthesis**

Mathias Mallmann, Sebastian Wendl, and Wolfgang Schnick

Chem. Eur. J. **2020**, *26*, 2067 - 2072.

Literature research, ammonothermal syntheses, formal analyses, preparation of graphical material and writing of the main part of the article were performed by Mathias Mallmann and supported by Sebastian Wendl. Wolfgang Schnick supervised the project. All authors revised the manuscript.

4. **Sr₃P₃N₇: Complementary Approach of Ammonothermal and High-Pressure Methods**

Mathias Mallmann, Sebastian Wendl, Philipp Strobel, Peter J. Schmidt, and Wolfgang Schnick

Chem. Eur. J. **2020**, *26*, 6257 - 6263.

For this contribution, Mathias Mallmann and Sebastian Wendl equally carried out the experimental syntheses, literature research, formal analyses, preparation of graphical material and writing of the manuscript. Luminescent measurements were performed by Philipp Strobel. Philipp Strobel and Peter J. Schmidt helped with the interpretation of the luminescence data. Wolfgang Schnick supervised the project. All authors revised the manuscript.

5. **Ammonothermal Synthesis of Ba₂PO₃N – An Oxonitridiophosphate with Non-Condensed PO₃N Tetrahedra**

Sebastian Wendl, Mathias Mallmann, Philipp Strobel, Peter J. Schmidt, and Wolfgang Schnick

Eur. J. Inorg. Chem. **2020**, *2020*, 841 - 846.

For this article, the experimental syntheses, literature research, formal analyses, preparation of graphical material and writing of the manuscript were performed equally by Sebastian Wendl and Mathias Mallmann. Philipp Strobel measured the luminescent properties of the sample. Interpretation of the luminescence data was supported by Philipp Strobel and Peter J. Schmidt. Wolfgang Schnick supervised the project. All authors revised the manuscript.

6. Ammonothermal Synthesis and Crystal Growth of the Chain-type Oxonitridosilicate $\text{Ca}_{1+x}\text{Y}_{1-x}\text{SiN}_{3-x}\text{O}_x$ ($x > 0$)

Mathias Mallmann, Christian Maak, and Wolfgang Schnick

Z. Anorg. Allg. Chem. **2020**, DOI: 10.1002/zaac.202000018.

Ammonothermal syntheses, literature research, formal analyses, preparation of graphical material and writing of the manuscript for this purpose were carried out by Mathias Mallmann and supported by Christian Maak. The project was supervised by Wolfgang Schnick. All authors revised the manuscript.

G.2 Other publications

1. Electronic Structure Investigation of Wide Band Gap Semiconductors – Mg_2PN_3 and Zn_2PN_3 : Experiment and Theory

Md Fahim Al Fattah, Muhammad Ruhul Amin, Mathias Mallmann, Safa Kasap, Wolfgang Schnick, and Alexander Moewes

J. Phys.: Condens. Matter **2020**, 32, 405504.

2. Ammonothermal Synthesis of Alkali-Alkaline Earth Metal and Alkali-Rare Earth Metal Carbodiimides: $\text{K}_{5-x}\text{M}_x(\text{CN}_2)_{2+x}(\text{HCN}_2)_{1-x}$ ($\text{M} = \text{Sr}, \text{Eu}$) and $\text{Na}_{4.32}\text{Sr}_{0.68}(\text{CN}_2)_{2.68}(\text{HCN}_2)_{0.32}$

Mathias Mallmann, Jonas Häusler, Niklas Cordes, and Wolfgang Schnick

Z. Anorg. Allg. Chem. **2017**, 643, 1956 - 1961.

3. Ammonothermal Synthesis of Novel Nitrides: Case Study on CaGaSiN_3

Jonas Häusler, Lukas Neudert, Mathias Mallmann, Robin Niklaus, Anna-Carina L. Kimmel, Nicolas S. A. Alt, Eberhard Schlücker, Oliver Oeckler, and Wolfgang Schnick

Chem. Eur. J. **2017**, 23, 2583 - 2590.

4. Ammonothermal Synthesis of Novel Nitrides: Case Study on CaGaSiN₃ (Cover Picture)

Jonas Häusler, Lukas Neudert, Mathias Mallmann, Robin Niklaus, Anna-Carina L. Kimmel, Nicolas S. A. Alt, Eberhard Schlücker, Oliver Oeckler, and Wolfgang Schnick

Chem. Eur. J. **2017**, *23*, 2479.

5. Investigation on the Sodium and Potassium Tetrasalts of 1,1,2,2-Tetranitraminoethane

Maximilian Born, Martin A. C. Härtel, Thomas M. Klapötke, Mathias Mallmann, and Jörg Stierstorfer

Z. Anorg. Allg. Chem. **2016**, *642*, 1412 - 1418.

G.3 Conference Contributions

1. Ammonothermalsynthese ternärer und multinärer Nitride (talk)

Mathias Mallmann, and Wolfgang Schnick

3. Obergurgl-Seminar für Festkörperchemie, Obergurgl (Austria), January 23 – 26, 2018.

2. Mischphasen im System II-IV-N₂ (II = Mg, Mn, Zn; IV = Si, Ge) (talk)

Mathias Mallmann, and Wolfgang Schnick

4. Obergurgl-Seminar für Festkörperchemie, Obergurgl (Austria), January 29 – February 01, 2019.

3. Ammonothermal Synthesis of Solid Solutions of Ternary Nitride Semiconductors II-IV-N₂ (II = Mg, Mn, Zn; IV = Si, Ge) (poster presentation)

Mathias Mallmann, Robin Niklaus, Ján Minár, and Wolfgang Schnick

10th International Symposium on Nitrides, Barcelona (Spain), June 9 – 13, 2019.

4. Ammonothermal Synthesis of Ternary Grimm-Sommerfeld Analogous Nitride Semiconductors $II-IV-N_2$ ($II = Mg, Mn, Zn$; $IV = Si, Ge$) (poster presentation)

Florian Engelsberger, Mathias Mallmann, Jonas Häusler, and Wolfgang Schnick

1st e-conversion Conference, Venice (Italy), September 9 – 13, 2019.

5. Ammonothermal Synthesis of Solid Solutions of Ternary $II-IV-N_2$ ($II = Mg, Mn, Zn$; $IV = Si, Ge$) (poster presentation)

Thanh Giang Chau, Mathias Mallmann, and Wolfgang Schnick

Undergraduate Research Conference on Molecular Sciences (URCUP), Kloster Irsee (Germany), October 19 – 20, 2019.

6. $Sr_3P_3N_7$: Ammonothermal- und Hochdrucksynthese (talk)

Mathias Mallmann, and Wolfgang Schnick

5. Obergurgl-Seminar für Festkörperchemie, Obergurgl (Austria), January 28 – 31, 2020.

G.4 Deposited Crystallographic Data

Crystallographic data (CIF) of investigated compounds were deposited at the Fachinformationszentrum (FIZ) Karlsruhe, 76344 Eggenstein-Leopoldshafen, Germany (fax: +49-7247-808-666, e-mail: crysdata@fizkarlsruhe.de) or at the Cambridge Crystallographic Data Centre via www.ccdc.cam.ac.uk/structures and are available on quoting the following CSD depository numbers.

Compound	CSD-Number
$\text{Mg}_{0.375}\text{Mn}_{0.625}\text{GeN}_2$	1903084
$\text{Mg}_{0.455}\text{Zn}_{0.545}\text{GeN}_2$	1903085
$\text{Mn}_{0.55}\text{Zn}_{0.45}\text{GeN}_2$	1903088
$\text{Mg}_{0.457}\text{Mn}_{0.543}\text{SiN}_2$	1903087
$\text{Mg}_{0.515}\text{Zn}_{0.485}\text{SiN}_2$	1903086
$\text{Mn}_{0.47}\text{Zn}_{0.53}\text{SiN}_2$	1903089
Mg_2PN_3	434689
Zn_2PN_3	434690
$\text{Sr}_3\text{P}_3\text{N}_7$	1975990
$\text{Ba}_2\text{PO}_3\text{N}$	1975933
$\text{Ca}_{1+x}\text{Y}_{1-x}\text{SiN}_{3-x}\text{O}_x$ ($x > 0$)	1975994